University of Massachusetts Amherst
ScholarWorks@UMass Amherst

Doctoral Dissertations 1896 - February 2014

1-1-1977

Small angle x-ray scattering studies of the deformation of Polyethylene.

Stanley K. Baczek
University of Massachusetts Amherst

Follow this and additional works at: https://scholarworks.umass.edu/dissertations_1

Recommended Citation
Baczek, Stanley K., "Small angle x-ray scattering studies of the deformation of Polyethylene." (1977). *Doctoral Dissertations 1896 - February 2014*. 620.
https://scholarworks.umass.edu/dissertations_1/620

This Open Access Dissertation is brought to you for free and open access by ScholarWorks@UMass Amherst. It has been accepted for inclusion in Doctoral Dissertations 1896 - February 2014 by an authorized administrator of ScholarWorks@UMass Amherst. For more information, please contact scholarworks@library.umass.edu.

SMALL ANGLE X-RAY SCATTERING STUDIES OF THE DEFORMATION OF POLYETHYLENE

A Dissertation Presented

by

Stanley K. Baczek

Submitted to the Graduate School of the
University of Massachusetts in partial fulfillment
of the requirements for the degree of

DOCTOR OF PHILOSOPHY

July, 1977

Polymer Science and Engineering Department

© STANLEY K. BACZEK 1977

All Rights Reserved

SMALL ANGLE X-RAY SCATTERING STUDIES OF THE DEFORMATION OF POLYETHYLENE

A Dissertation Presented
by
Stanley K. Baczek

Approved as to style and content by:

Richard S. Stein, Chairperson of Committee

Richard J. Farris, Member

William J. MacKnight, Member

Isaac C. Sanchez, Member

William J. MacKnight, Head
Polymer Science and Engineering

Dedicated to

My wife, Sandy, for her patience,
singleness of purpose, and her prayers

and to

My children, Lisa and David,

for their joy.

Inspirational

Bring the full tithes into the storehouse, that there may be food in my house; and thereby put me to the test, says the Lord of hosts, if I will not open the windows of heaven for you and pour down for you an overflowing blessing. I will rebuke the devourer for you, so that it will not destroy the fruits of your soil; and your vine in the field shall not fail to bear, says the Lord of hosts.

Malachi 3:10,11

ACKNOWLEDGMENTS

My sincere appreciation is extended to Dr. R. S. Stein, thesis director, for producing an atmosphere of guided freedom in which to work and for the concern of the various dimensions of my own and my family's lives.

Acknowledgment and gratitude is extended to the other members of my thesis committee, Drs. R. J. Farris, W. J. MacKnight, and I. C. Sanchez, each of whom contributed by their knowledge and their interest to the completion of this project.

A special thank you to Dr. R. W. Hendricks and his staff, Drs. D. Carlson and J. S. Lin, at the Oak Ridge National Laboratories, without which none of the SAXS pin hole data would have been obtained.

Invaluable discussions concerning SAXS were held with Drs. A. Wasiak, F. P. Warner, R. E. Wetton and W. Wenig, all visiting scientists from other countries. My thanks to them.

The author appreciated the assistant of Mr. D. A. Keedy and Mr. C. Napikoski of the technical shops. Also, the use of Dr. G. Orsten's photographic equipment for reduction of optical diffraction masks and his discussions were stimulating. A very special thank you to Mrs. Sandy Baczek for preparations of the masks.

Finally, thank you Sophia for typing this manuscript.

This work was supported in part by grants from the National Science Foundation, the Army Research Office (Durham), the Oak Ridge Associated Universities, and the Materials Research Laboratory of the University of Massachusetts.

Computer calculations were carried out at the University of Massachusetts Research Computing Center.

ABSTRACT

SMALL ANGLE X-RAY SCATTERING STUDIES OF THE DEFORMATION OF POLYETHYLENE

July 1977

Stanley K. Baczek, B.S., Southeastern Massachusetts University
M.S., University of Massachusetts
Ph.D., University of Massachusetts

Directed by: Professor Richard S. Stein

Previous attempts to elucidate deformation mechanisms of crystalline polymers by small-angle x-ray scattering (SAXS) using long slit geometries have met with limited success since current desmearing procedures are not rigorous for anisotropic scattering. Use of the ORNL 10 meter SAXS spectrometer which utilizes pin hole collimation has alleviated this problem. Intensities from uniaxially strained (90%) low density polyethylene (LDPE), and (25%) high density polyethylene (HDPE), and (40%) special texture (parallel lamellae stretched perpendicular to lamellar planes) LDPE have been analyzed at specific azimuthal angles, reflecting angular positions within the spherulites, by assuming the linear paracrystalline Hosemann scheme. Results indicate onset of fiber formation or microscopic yielding long before any macroscopic effects are observed. Lamellar orientation functions are calculated and compared to various model predictions. Effects of lamellar twisting and c-axis chain tilting are considered. A

mechanism of lamellar buckling and interleaving for those perpendicular to the stretch direction is proposed while amorphous compression and interlamellar slip for those lamellae parallel to the strain is advanced. Crystalline lamellar thicknesses are found to remain constant within experimental error with strain irrespective of their initial positions within the spherulite. Total scattering intensities are measured and swelling experiments performed. These indicate the absence of microvoid formation during deformation in LDPE. Some evidence for its existence in HDPE is apparent.

TABLE OF CONTENTS

	Page
CHAPTER 1 - INTRODUCTION	1
CHAPTER 2 - THEORETICAL	7
A. General Theory of SAXS	7
B. Hosemann Linear Paracrystalline Model	9
C. Vonk Correlation Function Approach	24
D. Tsvankin/Buchanan Model	29
E. The Total Integral-Invariant	33
F. Swelling Studies - The Invariant	38
G. The Elliptically Symmetric Invariant	53
H. Small Angle Light Scattering (SALS)	58
CHAPTER 3 - EXPERIMENTAL	63
A. Sample Preparation	63
B. Small-Angle X-Ray Scattering	64
1. Slit Geometry	64
a. Apparatus	64
b. Desmearing Procedures	66
c. Absolute Intensity Determinations	73
2. Point-Like Geometry	75
a. Apparatus	75
b. Absolute Intensity	80

3. SAXS Data Reduction 83

a. Background Corrections 83

b. The "Lorentz" Factor 84

c. Correlation Function Tables 90

d. Buchanan Analysis 91

C. Other Methods 92

1. Wide-Angle X-Ray Diffraction 92

2. Differential Scanning Calorimetry 92

3. Density Determinations 92

4. Small-Angle Light Scattering 93

CHAPTER 4 - RESULTS AND DISCUSSION 95

A. Spherulitic Morphology 95

1. Two-Dimensional Contour Plots 95

2. Qualitative Investigation of Intensity Data 105

3. Comparisons from Point-Like and Slit Geometries 109

4. SAXS Curve Analyses 112

5. Total Integrals and Swelling 119

B. Parallel Lamellar Morphology 127

C. On the Deformation Mechanisms 132

1. Parallel Lamellar Sheets 132

2. Spherulitic Morphology 139

3. Relationship to Mechanical Observations 148

4. Conclusions 149

D. Future Experiments 150

TABLES 157

FIGURES 191

GLOSSARY OF SAXS TERMS 274

REFERENCES 276

APPENDIX 287

I. Scattering from Angularly-Disordered Rods 287

II. Effects of Lamellar Twisting on SAXS 297

A. "The Venetian Blind Problem" 297

B. A Semi-Empirical Approach to Lamellae Twisting 308

III. Optical Diffraction Analogs 313

IV. Additional Computer Programs 318

CHAPTER 1

INTRODUCTION

The mechanical responses of polymeric materials have been the focus of a significant volume of research from both scientific and engineering viewpoints for many years. They are understood quite well for crosslinked rubbery and linear amorphous polymers above their glass transition temperatures (1,2). However, the presence of crystalline structures sufficiently complicates the response to stress so that only very approximate theories of mechanical behavior may be applied (3,4).

It is well known (5) that the actual morphology of many semicrystalline polymers is lamellar, in which the crystalline regions exist as thin sheets of the order of 100Å thickness and in which there is chain orientation perpendicular to the lamellar plane. Interlamellar regions presumably consist of "amorphous" structures in which a more-or-less random ordering of chains exists. Less-ordered regions may occur within crystals as defects (6). Deformation of these "amorphous" zones depends upon whether they are inter- or intralamellar in nature and upon the orientation of lamellae with respect to the stress. As Stein has observed (7), "If the lamellae orient with their planes perpendicular to the stress as in Figure 1a, then the interlamellar regions act in series with the crystallites (see References 7 and 8 for definitions of series and parallel models), whereas if the stress is parallel to the lamellae (Figure 1b), the interlamellar deformation is in parallel to that of the crystalline lamellae. Here the interlamellar zones experience a tensile deformation. However, if lamellae are tilted with respect

to the stress, they tend to slide with respect to each other since the interlamellar regions experience a shear stress (Figure 1c). Thus, the deformational response of the disordered regions of a crystalline polymer depends upon the nature of the regions and the local orientation of lamellae with respect to the stress."

Microscopy and light scattering experiments have verified that in certain cases the lamellae are organized into a superstructure in which there is correlation of their orientations over rather large regions of space. A spherulite is a particular case of this organization in which, ideally, the lamellae are arranged with their planes radially emanating from a central point. Sasaguri, et al. (9), showed that the tensile deformation of polybutene-1 films containing a spherulitic morphology involved the cooperative motion of lamellae such that an initially-spherical structure transformed to an ellipsoidal one. The ratio of the deformed to undeformed length of the spherulite was approximately equal to the macroscopic elongation ratio of the sample (10). This has not been observed for all polymers similarly studied (11,12) suggesting variations in their deformation mechanisms.

Several model theories of the responses of semicrystalline polymers comprised of spherulitic or lamellar morphologies have been proposed. A usual starting point is that of the affine scheme originally proposed by Kuhn and Grun (13) for the characterization of the optical anisotropy of rubbers. Affine deformation assumes that the microscopic strain on each particular element, e.g. chains, crystals, lamellae, spherulites, etc., is equivalent to the macroscopic strain of the sample.

Kuhn and Grun applied the affine deformation to chain segments. Kratky (14) extended this on to the affine displacement of rods imbedded in an amorphous matrix. Since the shapes of the rods remained constant but were positionally and angularly displaced from their initial state within the matrix, the deformation was termed "pseudo-affine".

Others have applied this general phenomonological model to semi-crystalline polymers to explain results of birefringence (15-17), light scattering (18,19), and x-ray diffraction experiments (17,20). Wilchinsky (17) extended the affine description to spherulites as a whole. The affine treatment is, of course, an oversimplification in that it has been recognized that deformation is often positionally dependent due to localized stresses at the various levels of structure (12,21,22).

An extension of the generalized Hooke's law for anisotropic elastic solids to anisotropic linear viscoelastic solids was proposed by Takanayagi (23) to explain the mechanical behavior of a series of oriented polyethylene sheets. Recently, the treatment of polymer spherulites by composite theories has been somewhat successful in describing the mechanical responses to stress. Specifically, application of Halpin-Kardos (24,25) theory by Phillips (26) in a rather simple manner, and by T. T. Wang (27) using the more complex continuum approach, has yielded mechanical responses at the three levels of lamellae, spherulites, and the bulk sample. A theory of the mechanical properties of spherulites was also presented in this laboratory by Kawaguchi (28). Other theories also exist (29,30) and the list continues. However, a major obstacle has been the fact that there is very little direct experimental evidence

as to the nature of the elastic deformation on the scale of the lamellae which are obviously involved in the processes. Therefore, the object of this work is not to add another theory of semicrystalline polymer deformation, but rather to use an experimental approach to measure the changes associated with the crystalline and amorphous regions in their relative spatial positions within the spherulites during uniaxial deformation and to test some of the existing models with the results. Appropriately, then, the technique of small angle x-ray scattering (SAXS) has been mainly utilized since data interpretation has yielded information regarding the nature and sizes of lamellar and interlamellar regions.

Figure 2 shows the photographic SAXS patterns generated from point geometry for low density polyethylene at various stages of uniaxial strain. In the unstretched state, a symmetric pattern is obtained while at varying degrees of elastic or plastic deformation, the anisotropic patterns are observed. Presumably, proper analysis of the intensity profile along any given azimuthal angle will yield information regarding those structures which scatter into that particular azimuth. It is well established that a lamellar morphology exists for polyethylene. Since the lamellae can be treated as x-ray reflecting planes, we know from the Ewald construction (e.g. see References 31 and 32) that they must be perpendicular to the direction of the analyzed azimuth. For a good qualitative description of the geometry of SAXS processes from lamellae, see pp. 404 and 405 of Reference 33. Thus, for the unstrained case the lamellae are symmetrically distributed and generate a circularly-symmetric scattering pattern. However, application of a strain changes the spatial

distribution, and positionally-dependent average long spacings are reflected in the anisotropic patterns. The fundamental idea, then, is to obtain intensity profiles at particular azimuths to learn something of the structures generating them. Their angular variations will be tested at various states of strain. Finally, the absolute intensity of SAXS is monitored to gain information regarding electron densities in the phases at various strains and spatial positions.

Two attempts to do a study very similar in some respects to this one deserve mention. In the first, Labarbe, this author, et al. (20), using similar samples to those analyzed here (Monsanto experimental low density polyethylene, LDPE), a long-slit geometry SAXS spectrometer, and application of Tsvankin/Buchanan (34-36) theory found that long periods and crystalline thicknesses varied with elongation. Specifically, the long period (crystalline plus amorphous thickness) decreased for lamellae parallel to the strain while it increased for those perpendicular to it. The crystalline lamellar and amorphous interlamellar dimensional responses were similar but of differing magnitudes. However, crystallinities remained constant over the entire azimuthal range and with total macroscopic strain (up to 60%). This latter result is to be compared with the second study which is that of Schultz (37,38). He reported a decrease in overall crystallinity with strain (up to 20%) and a slowly-increasing long period for lamellae perpendicular to the strain, and concluded that lamellar thinning occurs for those lamellae perpendicular to the strain axis during deformation. This conclusion is found to be in direct contradiction with that of Labarbe, et al. The discrepancy justifies further study.

An inherent assumption, especially in the Labarbe work, is that the scattering anisotropy at a particular strain is small and for all practical purposes can be treated as if it were spherically symmetric. Spherical symmetry is a primary consideration for the application of existing desmearing procedures (39,40). The ideal pinhole geometry with our Rigaku-Denki spectrometer could not be fully utilized for the practical consideration of the long counting times involved. However, the photographic evidence of Figure 2 reveals a highly-anisotropic scattering pattern even at the lower strains. Assuming a spherical scattering symmetry would be very approximate indeed. This fact, along with the interpretation of his results, casts serious doubt as to the validity of the assumption.

To overcome these deficiencies we have used the 10-Meter SAXS spectrometer (41,42) located at the Oak Ridge National Laboratory (ORNL) in cooperation with Dr. R. W. Hendricks and his colleagues. This spectrometer utilizes a rotating anode generator to produce a high incident x-ray flux, a monochromator, point geometry and a two-dimensional position sensitive proportional counter. All azimuthal data is acquired simultaneously at a given strain and is processed and corrected using a dedicated computer. Rapid data acquisition and the ability to process intensities without the constraint of having to correct for slit smearing effects make this instrument invaluable for accurate results on these deformed systems.

CHAPTER 2

THEORETICAL

A. General Theory of SAXS

It is well known that if we consider a system of thin parallel plates separated by a distance, d, and a wave plane of wavelength, λ, incident upon them, the condition for constructive interference of the scattered rays over the plane normal to them is given by Bragg's law

$$n\lambda = 2d \sin\theta$$

where θ is the angle between the incident beam and the platelet and n is the order of the reflection (n = 1, 2, 3 . . .). It is also known that most semicrystalline polymers give rise to rather broad scattering maxima in the SAXS region (ca. $< 3^{o}$). These maxima have generally been ascribed to periodic fluctuations of structural order of tens to hundreds of Angstroms within the sample. Interpretations based on two phase models of alternating crystalline and amorphous regions and application of Bragg's law have met with varied successes when results are compared to electron microscopy (EM) studies (43,44) or to the line broadening techniques (45,46) of wide angle x-ray diffraction (WAXD). Actually, Guinier (Reference 40, pp. 140-148) demonstrates the limitations of Bragg's law to SAXS by focusing on its original derivation and ways in which SAXS

spectra deviate from this. Basically, Bragg's law is derived for equi-spaced lattice planes and well-defined internal structural parameters extending over an infinite array. Most polymer systems exhibit a broad SAXS maximum with few, if any, observable subsidiary maxima reflecting a distribution of lattice planes over a finite space and probably varying structural patterns. Thus, a complete knowledge of the distribution of scattering centers as well as structural parameters must be known. Only average quantities can be reported. Therefore, Bragg's law cannot be rigorously applied to determine "spacings" in SAXS patterns. However, its use is often illustrative of trends and, therefore, values are still cited in the literature and will be reported here bearing in mind the limitations set forth above. Crist (47) refers to the evidence that since quantitative agreement is lacking in the majority of cases studied by EM and that polyethylene, polypropylene, and polyoxymethylene frequently show two SAXS maxima which cannot simply be related by Bragg's law to order effects, work has proceeded to refine or expand the scattering calculations from the simple two-phase model. Three such models will be discussed herein to various depths and for various reasons which will become clear later in the text. Since our work has shown that among the Hosemann, Vonk, and Tsvankin/Buchanan models the former is the more general for the systems studied, it will be described in greater detail than the others. A table (Table 1) comparing the major similarities and differences between the three models is included.

B. Hosemann Linear Paracrystalline Model

The variation of SAXS intensity with angle for a lattice whose entire distribution of scattering centers can be described if the distribution law for nearest neighbors is known was derived by Zernicke and Prins (48) and Hermans (49) and generalized by Hosemann (50). The subsequent derivations follow those of References 33, Chapter 5, and 51, Chapter 5.

The statistical representation of paracrystalline lattice points can be derived with reference to Figure 3 as follows. (A paracrystalline lattice differs from a crystalline lattice in that in the former the arrangement of lattice points is not perfect. Lattice points may fluctuate about some mean value in position.) Considering a one-dimensional system, let the lattice points in the x direction be A_1, A_2, etc., where A_1 is the nearest neighbor to an arbitrary origin, O. If the probability of locating A_1 by a vector $\underset{\sim}{y}$ from the origin is $H_1(\underset{\sim}{y})$, then the probability that A_2 is located by an independent vector $\underset{\sim}{z}$ from the end of $\underset{\sim}{y}$ is given by $H_1(\underset{\sim}{y}) \cdot H_1(\underset{\sim}{z})$. The total probability, $H_2(\underset{\sim}{x})$, that A_2 will lie at the end of a single vector $\underset{\sim}{x} = \underset{\sim}{y} + \underset{\sim}{z}$ from the origin is given by

$$H_2(\underset{\sim}{x}) = \int_0^\infty H_1(\underset{\sim}{y})\, H_1(\underset{\sim}{x}-\underset{\sim}{y})\, dy = H_1(\underset{\sim}{x}) * H_1(\underset{\sim}{x}) \qquad (1)$$

if we assume no statistical correlation between the vectors $\underset{\sim}{y}$ and $\underset{\sim}{z}$. The symbol (*) denotes the convolution process which is defined in Equation (1). $H_1(\underset{\sim}{x})$ is given in Figure 3 and represents the distribution law for first neighbors. From (1) we see that the distribution function for the next nearest neighbors, $H_2(\underset{\sim}{x})$, is given by that for the first neighbors. The mean distance between neighbors, $\overline{\ell}$, is given by

$$\overline{\ell} = \int_0^\infty \underset{\sim}{x}\, H_1(\underset{\sim}{x})\, dx \qquad (2)$$

and since the resulting interference function will be referred to one scattering unit, $H_1(\underset{\sim}{x})$ must satisfy the normalization condition.

$$\int_0^\infty H_1(\underset{\sim}{x})\, dx = 1 \qquad (3)$$

Physically the convolution of $H_1(\underset{\sim}{x})$ with itself means that $H_1(\underset{\sim}{x})$, describing a certain displacement from the origin and a certain width, is once more displaced and broadened so that the result is a broader function of lower peak height. The convolution process of Equation (1) is readily generalized to

$$H_m(\underset{\sim}{x}) = H_1 * H_1 \ldots\ldots H_1 \quad \text{[the (m-1) convolution of } H_1\text{]} \qquad (4)$$

where m is the number of points in the lattice. The lattice extends in both the (+) and (-) directions and is centrosymmetric such that $H_m(\underset{\sim}{x}) = H_{-m}(-\underset{\sim}{x})$. $H_m(\underset{\sim}{x})$ is sometimes represented as $\overset{m}{\frown}{H_1}$.

If we specify a distribution function $W(\underset{\sim}{x})$ which describes the random distribution of points in $A(\underset{\sim}{x})$, it will fully define the diffraction properties of the linear array which is dependent on the location of scattering units. Then

$$Z(\underset{\sim}{x}) = \frac{W(x)}{N} = H_0 + H_{+1} + H_{-1} + \overset{2}{\frown}{H_1} + \overset{2}{\frown}{H_{-1}} + \ldots$$

$$\overset{m}{\frown}{H_1} + \overset{m}{\frown}{H_{-1}} + \ldots$$

$$= H_0 + \sum_{m=1}^{\infty} [\overset{m}{\frown}{H_1} + \overset{m}{\frown}{H_{-1}}] \qquad (5)$$

where N is the number of points in the lattice. $Z(\underset{\sim}{x})$ is, therefore, the distribution function per unit scattering center.

The definition of a Fourier transform or actually a Fourier transform pair is given in Equation (6).

$$F(\underset{\sim}{X}) = \int_{-\infty}^{\infty} G(\underset{\sim}{Y})\, e^{2\pi i(\underset{\sim}{X}\cdot\underset{\sim}{Y})}\, dv_y$$

$$G(\underset{\sim}{Y}) = \int_{-\infty}^{\infty} F(\underset{\sim}{X})\, e^{-2\pi i(\underset{\sim}{X}\cdot\underset{\sim}{Y})}\, dv_x \qquad (6)$$

or

$$F(\underset{\sim}{X}) = F\,[G(\underset{\sim}{Y})]$$

$$G(\underset{\sim}{Y}) = F^{-1}\,[F(\underset{\sim}{X})] \qquad (7)$$

in which F and F^{-1} represent the Fourier transform operators as defined in Equation (6).

This, along with the theorem that

$$F[G_1(\underset{\sim}{X}) * G_2(\underset{\sim}{X})] = F[G_1(\underset{\sim}{X})]\; F[G_2(\underset{\sim}{X})]$$

$$= F_1(\underset{\sim}{Y})\, F_2(\underset{\sim}{Y}) \qquad (8)$$

or that the Fourier transform of a convolution is the product of the transforms of the convoluted functions, enables us to write

$$F[Z(\underset{\sim}{x})] = Z(\underset{\sim}{X}) = F[H_0] + \sum_{m=1}^{\infty} [F^m + F^{*m}] \tag{9}$$

where

$$F^m = F^m(\underset{\sim}{X}) = F[H_m(\underset{\sim}{x})] = F[\overbrace{H_1(x)}^{m}]$$

and

$$F^{*m} = F^{*m}(\underset{\sim}{X}) = F[H_{-m}(\underset{\sim}{x})] = F[\overbrace{H_1(-\underset{\sim}{x})}^{m}]$$

$Z(\underset{\sim}{X})$ is the interference function for x-ray scattering.

It is useful to point out at this point that F, the structure factor or amplitude is of universal application in that, in general, it extends the concept of scattering from a single point to any physical scattering unit such as the lamellae considered here. Also, the intensity of scattering is proportional to the square of its modulus or the product of the amplitude, F, and its complex conjugate, F*.

Summing the series in Equation (9) and realizing that $F[H_0] = 1$, results in

$$Z(\underset{\sim}{X}) = 1 + \frac{F}{1-F} + \frac{F^*}{1-F^*}$$

$$= 1 + 2\mathrm{Re}\left[\frac{F}{1-F}\right] = \mathrm{Re}\left[\frac{1+F}{1-F}\right] \qquad (10)$$

since (9) contains conjugate quantities of the same form and the system is centrosymmetric. Re represents the real part of the term and $\underset{\sim}{X}$ is any general scattering vector.

Either the interference function, $Z(\underset{\sim}{X})$, or a shape amplitude factor, $S(\underset{\sim}{X})$, determines the shape of the intensity maximum depending on whether the lattice is large or small, respectively. The shape amplitude factor describes the shape in reciprocal space of the scattering regions and is the Fourier transform of the shape function, $\Phi(\underset{\sim}{x})$ in real space defined by

$$\Phi(\underset{\sim}{x}) = \begin{cases} 1 \text{ inside object} \\ \\ 0 \text{ outside object} \end{cases} \qquad (11)$$

To avoid complications introduced by the shape factor, it is meaningful to consider the distribution function and its transform for finite N rather than infinite N. In Equation (5), $Z(\underset{\sim}{x}) = W(\underset{\sim}{x})/N$ and all $H_m(\underset{\sim}{x})$ are normalized to unity by (3). However, for a finite N, $H_m(\underset{\sim}{x})$ must be normalized to N-|m|, thus in place of (5),

$$Z(\underset{\sim}{X})_N = N + \sum_{m=1}^{N} (N-|m|) \left[F^m + F^{*m}\right] \qquad (12)$$

which after summation and rearrangement leads to

$$Z(\underset{\sim}{X})_N = N \text{ Re} \left[\frac{1+F}{1-F}\right] - 2 \text{ Re} \left[F \frac{1-F^N}{(1-F)^2}\right] \qquad (13)$$

The subscript, N, refers to scattering from a finite array. The second term in (13) has been shown to be similar to the Laue function (Reference 33, p. 129) which for small N broadens the intensity versus angle curve. The form of the distribution functions, F, has not been specified here.

More recently, Bramer (52) utilized this concept for scattering from a finite one-dimensional stack of lamellae separated by amorphous

interlamellar regions. Following Hosemann's formulation (50), he termed these stacks "clusters" and distributed them randomly in space as shown in Figure 4. Wenig (53,54) added the contribution to scattering by a finite transition zone thickness between the crystalline and amorphous layers. A shematic is shown in Figure 5.

Let us assume that the lamellae are larger in their lateral dimensions than in their thicknesses. Clusters are the aggregation of alternating crystalline and amorphous or intercrystalline regions and they completely fill the sample volume. Sizes along the crystalline and amorphous thicknesses are given by $L = Nx_d$ where x_d is the average long spacing given by $x_c + x_a$, where x_c and x_a are the thicknesses of the crystalline and amorphous layers, respectively. N is the number of lamellae within a cluster. The average structure factor for the cluster is given by

$$\langle |F|^2 \rangle = \int_0^\infty |F|^2 \, H(\xi) \, d\xi \tag{14}$$

and

$$H(\xi)_{cluster} = \overbrace{\Big|\Big|}^{N}_{n=1} \; H_a\,(x_{an}) \cdot H_c\,(x_{cn}) \tag{15}$$

where $H_a(x_{an})$ and $H_c(x_{cn})$ are the thickness distribution functions for the crystalline and amorphous phases, $H(\xi)_{cluster}$ is the resulting thickness

distribution of the cluster, and F is the structure factor for the particular cluster. The x direction is taken along a line perpendicular to the lateral lamellar dimensions and the line encounters regions of alternating high and low electron density when passing through crystalline and amorphous regions, respectively, as shown in Figure 5. The average structure factor in Equation (14) is obtained by integrating over all the clusters in space. The thickness distribution of a crystalline and amorphous layer together, H_d, is given by the convolution theorem of Equation (1) as

$$H_d(x_{dn}) = \int_0^\infty H_a\,(x_{an}) \cdot H_c(x_{dn} - x_{an})\, dx_{an} = H_a * H_c \qquad (16)$$

The relationships between the average values, $\overline{x_d}$, and the squared fluctuations about the averages, $\overline{(\Delta x_\alpha)^2}$, are

$$\overline{x}_a + \overline{x}_c = \overline{x}_d; \quad \overline{\alpha} = \int_0^\infty \alpha\, H_\alpha(\alpha)\, d\alpha;\ \alpha = x_a,\ x_c,\ x_d \qquad (17)$$

and

$$\overline{(\Delta x_a)^2} + \overline{(\Delta x_c)^2} = \overline{(\Delta x_d)^2};\ \overline{(\Delta\alpha)^2} = \int_0^\infty (\alpha - \bar{\alpha})^2\ H_\alpha(\alpha)\ d\alpha;$$

$$\alpha = x_a,\ x_c,\ x_d \tag{18}$$

The average square intensity is given by combining Equations (14) and (15)

$$\overline{I(s)} = \langle |F|^2 \rangle = \int_0^\infty |F|^2\ [H_a(x_{a1})\ dx_{a1} \cdots H_a(x_{an})\ dx_{an}$$

$$H_c(x_{c1})\ dx_{c1} \cdots H_c(x_{cn})\ dx_{cn}] \tag{19}$$

where $s = (2/\lambda)\ \sin\theta$.

Let

$$F_\alpha = \int_0^\infty H_\alpha(\alpha)\ e^{-2\pi i\ s\alpha} d\alpha,\ \alpha = x_a,\ x_c,\ x_d$$

and

$$F_a \cdot F_c = F_d \tag{20}$$

Substituting and performing the Fourier operations similarly as in Equations (5-13) yields the final result that

$$\overline{I(s)} = \frac{K}{s^2} \, Re\left\{ N \frac{(1-F_a)(1-F_c)}{(1-F_d)} + F_c \left(\frac{1-F_a}{1-F_d}\right)^2 (1-F_d^N) \right\} \qquad (21)$$

where K is a constant of proportionality used primarily as a scaling factor in curve fitting. Here, N is an explicit parameter which after integration is the mean number of parallel lamellae averaged over the clusters in the entire array. This differs from the N in Equation (13) since there, the averaging over clusters was not performed.

The generalized thickness distribution functions for the crystalline and amorphous phases are given by Gaussians as

$$H_\alpha(\alpha) = \frac{1}{\left[2\pi \overline{(\Delta x_\alpha)^2}\right]^{1/2}} \exp\left[- \frac{(x-x_\alpha)^2}{2\overline{(\Delta x_\alpha)^2}} \right] \qquad (22)$$

where α is c or a depending on whether the crystalline or amorphous distributions are to be specified. For purposes of simplification and computer programming, the mean squared fluctuations can be represented by

$$\overline{(\Delta x_\alpha)^2} = g_\alpha \overline{x_\alpha}^2 \qquad (23)$$

where g_α is now the deviation about the mean value and is a parameter specified in the calculations.

Equation (21) is identical to Equation (8) of Reference 50, page 413. The first term in brackets is known as the diffuse or Babinet, $\overline{I}_B$, component since it is symmetrical in F_a and F_c. It follows Babinet's reciprocity law (Reference 50, page 540) exactly, and is proportional to the average number of lamellae in the cluster. The second term is called the crystalline component, $\overline{I}_C$. It is small compared to $\overline{I}_B$ when N is large and at angles where the zero order component is negligible. The zero order scattering is that arising from the cluster size L. Hosemann (50) has shown that for large N, and in the limit of very small angles, $\overline{I}_C$ reduces to

$$\lim_{s\to 0} \overline{I}_C = \phi^2 \overline{L^2}$$

where ϕ is volume fraction crystallinity or the mean packing density of the material. Thus, in the region of SAXS, $\overline{I}_C$ should not be neglected.

The above model assumes no interference effects from the arrangement of the clusters due to their polydispersity and, therefore, the shape of the SAXS curve is determined only by the inner structure of the domains. Also, it is assumed that the lamellae are distributed statistically with respect to their thicknesses over all the domains so that each lamellar thickness can be found in every domain according to its probability specified by the thickness distribution function. Thus, any two clusters of the model are indistinguishable.

At this point we shall investigate the meaning of the parameter, N. Obviously in the derivation N is taken to mean an absolute real number describing the average value of parallel lamellae within a cluster. Because of our preliminary results and those of others (53-55), the actual values of N were often found to be below 2.0. Obviously 1.2 lamellae, for example, cannot give rise to any interference and this number has no physical significance. To test this problem, we calculated the scattering from an array of parallel rods allowing for a statistical fluctuation from parallelness to occur at specified intervals. The actual details of the calculation and the computer program are given in Appendix I. After a certain small angular deviation was reached, the intensity at the maximum remained constant even with the introduction of greater amounts of angular deviation. Figure 6 shows the results of the intensity at the maximum vs. the number of parallel rods N. This number was varied from 2 to 50 to generate the curve. Then 50 rods were assembled with the introduction of angular deviation at specified intervals as designated by limits surrounding numbers generated randomly.

Thus, allowing 10% of the rods to vary at some angle with respect to the other parallel rods, on the average, every 6th rod would be expected to be non-parallel. We can see, however, that the scattering obtained here is much greater than that obtained from 5 parallel rods alone. Other examples along with numbers are given in Appendix I. Also, the intensity was calculated at the very exact angle of 90 degrees to the lamellar planes. Experimentally, one cannot achieve this due in least part to finite detector or detector element sizes and, in fact, a distribution of scattering planes is observed. This effect would tend to reduce the accuracy of the average N probably by raising it somewhat since lamellae at slightly different angles could scatter into the particular range of azimuth. However, the values reported here and in the Bramer and Wenig works tend to approach 1.2 for LDPE. The average value would, thus, have to be even lower. Despite this, the N parameter is not used in any quantitative fashion in any experiments reported to date and only trends and qualitative judgments concerning the structures are deduced.

Now we can consider the stack of four lamellae shown in Figure 7. The average number of parallel rods is 1.5 but, according to the conclusions reached from the model calculations, this stack could scatter coherently as if it contained between two and four parallel rods. One can envision low or high density polyethylene (LDPE or HDPE) stacks comprised of many approximately-parallel lamellae. However, the average number of exactly-parallel lamellae would be rather low, possibly 1.2, due to lamellae branching effects, etc. Scanning electron microscopic evidence of Keller (unpublished results) of spherulite fracture surfaces supports the rather low values of N which have been reported here.

Finally, the initial statement that 1.2 lamellae cannot give rise to any interference is a perfectly true one unless one realizes that this number is an average value relating the average number of parallel lamellae within a larger cluster and is derived as such.

We now return to the addition of an electron density transition zone in the calculation of SAXS from a finite number of lamellae as described by the cluster model. Consider the electron density profile (projection of electron density on the fibrillar axis) of Figure 5. According to Tsvankin (34), the amplitude of scattering due to the transition zone is given by

$$F(s) = \int_0^{x_E} \frac{x}{x_E} \exp(-kx)\, dx + \int_x^{x_E+x_c} \exp(-kx)\, dx + \int_{x_E+\bar{x}}^{x_c+2x_E} \frac{x - x_c - 2x_E}{x_E} \exp(-kx)\, dx \qquad (23)$$

where $k = 2\pi i s$ and x_E, the transition zone thickness.

Solution of these integrals and averaging appropriately as done by Wenig (53) results in a factor $Z_1(S)$ where

$$Z_1(S) = \frac{1}{(2\pi i s)^2 x_E} \left| 1 - \exp(-2\pi i s\, x_E) \right|^2 \qquad (24)$$

which, when multiplied by the average intensity of Equation (21), yields the final intensity from a cluster model including the finite transition zones:

$$\overline{I(s)} = \left(\frac{K}{s^2}\right) \text{Re} \quad \{N \frac{(1-F_a)(1-F_c)}{(1-F_d)} + F_c \left(\frac{1-F_a}{1-F_d}\right)^2 (1 - F_d^N)\} \cdot Z_1(s) \tag{25}$$

This equation was used in all the calculations and a computer program (TCSC) was written (see Appendix) to compare theoretical and experimental scattering curves. The basic parameters governing the shape of the structural part of the SAXS curves are, therefore, the average crystalline, $\bar{x}_c$ or c, and amorphous, $\bar{x}_a$ or a, thicknesses, and their distributions, g_c and g_a, the transition zone thickness, $\bar{x}_E$ or E, and the average number of parallel lamellae within a cluster, N. More will be said concerning the nature of the program and the parameters used in the Experimental section.

C. Vonk Correlation Function Approach

The correlation function was originally defined by Debye, et al. (50,57), and by Porod (58) as:

$$\gamma(r) = \frac{\langle \Delta n_1 \, \Delta n_2 \rangle_r}{\langle \Delta \eta^2 \rangle} \tag{26}$$

where $\Delta n_i = \rho_i - \bar{\rho}$ and represents the local deviations in electron density of the various phases, ρ_i, from the average value, $\bar{\rho}$, at positions 1 and 2 separated by a distance r. The correlation function can be calculated for various models and compared to that determined by Fourier transformation of the experimental curve. Vonk, et al. (59,60), applied this concept to analyze the structures of bulk polymers. Since then, others have also utilized this technique (61-63). According to the Vonk approach, the relationship between the desmeared or point-like intensity and the one-dimensional correlation function is given by

$$\gamma(r) = \frac{\int_0^\infty s^2 I(s)_e \cos 2\pi\, r \cdot s\, ds}{\int_0^\infty s^2 I(s)_e\, ds} \qquad (27)$$

in which $\gamma(r)$ is normalized to give a value of 1.0 when $r = 0$ and 0 when $r = \infty$. $I(s)_e$ is the experimentally-determined intensity distribution as a function of the scattering vector, s. The position of the first maximum in $\gamma(r)$ corresponds approximately to the average long period. It is termed a one-dimensional function since it is confined to a central line perpendicular to the alternating crystalline and amorphous layers. Details of the determination of $\gamma(r)$ will be given in the next chapter.

The theoretical correlation function derived by Vonk and Kortleve (59) is based on a linear two phase model of randomly-oriented alternating high (crystalline) and low (amorphous) electron density regions much like that of the Hosemann treatment. Independent thickness distribution functions $P_c(r_c)$ and $P_a(r_a)$ represent the distribution of crystalline and amorphous layer thicknesses r_c and r_a whose mean values are c and a, respectively. The one-dimensional calculated correlation function is then given by:

$$\gamma(r) = \frac{\phi}{1-\phi}\left[(1-\phi)^2 \int_0^\infty (r_c - r)\, P_c\,(r_c)\, dr_c + P_{cac} + P_{cacac} + \ldots - 1\right] \qquad (28)$$

where ϕ is the volume fraction of lamellae,

$$\phi = \frac{c}{c + a} \qquad (29)$$

Equation (29) represents a linear crystallinity in that it is calculated strictly on the basis of the widths of the crystalline and amorphous regions. P_{cac} and P_{cacac} are the overall probability functions dependent

upon P_a and P_c such that the coordinate vector r has both of its ends in a crystalline phase and traverses through on one (P_{cac}) or two (P_{cacac}) amorphous layers. P_a and P_c are normalized such that

$$\int_0^\infty P_c(r)\, dr = \int_0^\infty P_a(r)\, dr = 1 \qquad (30)$$

and, therefore, P_{cac} and P_{cacac} are also normalized functions. In fitting the calculated correlation function to the experimental one, the unit of length in the experimental curve is first equated to the value of r at the first maximum. Then the parameters ϕ, B_a and B_c are adjusted to give the best correspondence. B_c and B_a represent the widths of the distribution functions P_a and P_c which themselves can be represented by either Gaussian [Equation (31)] or log-normal [Equation (32)] functions.

$$P(r) = \frac{1}{B\sqrt{2\pi}} \exp\left[-(r-\phi)^2/2B^2\right] \qquad (31)$$

$$P(r) = \left[\exp\left(\frac{B^2}{2}\right)/\phi\ B\sqrt{\pi}\ \right] \exp\left\{\left[3B^2/4 + \ln\left(\frac{r}{\phi}\right)\right]^2/B^2\right\} \qquad (32)$$

Similar to Reference 64, combinations of these distribution functions were used so that one was not confined to describing both phases by the same distribution function. Negative values of r were obviously not allowed and in cases of broad distribution, in order to compensate for any cut-off at r = 0, the entire function was renormalized to 1.0 and recalculated. Brown, et al. (64), concluded that the choice of a particular distribution function is not critical for highly-crystallized samples ($\phi > 0.5$) where the distribution widths would be expected to be lower. However, for samples of lower crystallinities where rather broad functions would be appropriate, their type becomes sensitive and significant upon the final fit of the experimental and calculated correlation function.

In comparing the Vonk and Hosemann calculations, Gaussian distributions must be used for both phases in the former calculation. Also in relating the distribution parameters g_α and B of the Hosemann and Vonk treatment, references to Equations (22), (23) and (31) reveal that

$$(\Delta x_a)^2 = B^2$$

Therefore,

$$g_\alpha = \frac{\overline{(\Delta x_\alpha)^2}}{\overline{x_\alpha}} = \frac{B^2}{\overline{x_\alpha}^2} \qquad (33)$$

Thus, direct comparison of the two Gaussian distribution parameters can be made. However, one must also keep in mind that the major difference in the two approaches as described here is that the Hosemann scheme analyzes clusters of finite width lamellae while the Vonk treatment assumes an infinite one-dimensional stack. Also, in Vonk's derivation, disorder of the first kind is used while that of the second kind, described previously, is used by Hosemann. In the first kind, the scattering centers are located then crystalline thicknesses built up around them. Negative amorphous thicknesses are possible but are generally corrected for by careful choice of distribution parameters. No such problem exists in the latter case. Also, in the physical building of the system, the former seems the more likely to occur and thus define the statistics.

D. Tsvankin/Buchanan Model

The Buchanan (35) model is basically a correction and extension of the Tsvankin (34,36) scheme which consists again of a one-dimensional model of alternating crystalline (high electron density) and amorphous (low electron density) layers. Scattering from such an assembly consists of calculating the projection of electron density on to a line as was done for the two prior cases.

The general relationship for the diffracted intensity from a system of N scattering objects of varying lengths is given by

$$I(s) \propto N[\overline{|F^2|} - |\overline{F}|^2] + |\overline{F}|^2 \{N + \sum_{i \neq k}^{N} \sum \exp (i\underset{\sim}{s}_T \cdot \underset{\sim}{z}_{ik})\} \qquad (34)$$

where F is the Fourier transform of the electron density distribution within the crystal, $|s_T| = 4\pi \sin\theta/\lambda$, and $\underset{\sim}{z}_{ik}$ is the vector joining the i^{th} and k^{th} crystals. A rectangular distribution of crystallite sizes of mean dimension c varying between $c - \Delta < c < c + \Delta$, plus the following substitutions

$$y = s_T a = 2\pi a \sin 2\theta/\lambda \qquad (35)$$

$$\alpha_T = c/a$$

$$\beta = \Delta/a$$

$$a = d - c$$

where again d is the long period, and a is the mean amorphous length, led the authors to derive an analytical expression for I_1, where

$$I_1 = (\beta^2 y^2 + \beta^2 y^4 - \sin^2 \beta y)/(\sin^2 \beta y + \beta^2 y^2 + \beta^2 y^4$$

$$- 2\beta y \cos\alpha_T y \sin\beta y + 2\beta y^2 \sin\alpha_T y \sin\beta y) \qquad (36)$$

and is derived from Equation (34) where

$$|\overline{F}|^2 \cdot I_1 = |\overline{F}|^2 \{N + \sum_{i \neq k}^{N} \sum \exp (i \underset{\sim}{s}_T \cdot \underset{\sim}{z}_{ik})\} \qquad (37)$$

Next, inclusion of a trapezoidal electron density profile within a crystal similar to that of Figure 5 and use of Zernicke-Prins (48) statistics to locate the average positions of the scattering centers (a one-dimensional disorder of the first kind) allowed the calculation of the scattering amplitudes $|\overline{F}|^2$ and $|\overline{F^2}|$ and, therefore, the total scattered intensity per unit scattering object, $\overline{I(s)}/N$. In order to establish relationships between the calculated and experimental scattering curves, a set of calibration curves based on the calculated scattering intensities was generated. The quantity relating these two, $\psi(p)$, is given by

$$\psi(p) = p/X_m = d_e q \tag{38a}$$

and

$$p = dq;\ X_m = d/d_e \tag{38b}$$

where X_m and d_e are the calculated and experimental peak positions, respectively, and p and q are the calculated and experimental half widths at half height, respectively. Tsvankin found that the transition width parameter, E, only slightly influenced the calculated intensity distributions. However, the β/α_T parameter describing the dispersion of crystallite lengths about their mean value very strongly influenced the results. Thus, β/α_T, α_T, and E, along with the running variable, p, were systematically varied to generate the calibration curves. Typical calibration curves can be found in References 20 and 36. From these considerations, values of the mean long period, the crystallite length, and the amorphous dimensions were obtained from Equation (38) and

$$c = \phi d \tag{39}$$

where ϕ is the linear crystallinity defined as in the Hosemann and Vonk treatment. ϕ and X_m are obtained directly from the calibration curves.

Thus the application of the Tsvankin/Buchanan model is a rather convenient one to use since only the peak position and half-width at half-maximum are needed to fully characterize the scattering morphology. The full width at half maximum is used by some (65) but this depends obviously on the way in which calibration curves are generated. More will be said concerning this method in subsequent sections including numerous criticisms.

E. The Total Integral-Invariant

The only parameter which can be determined with no a priori assumptions concerning the nature of the inhomogeneities giving rise to the scattering is the mean squared electron density fluctuation, $\overline{(\rho - \bar{\rho})^2}$. This has been termed the scattering power of the particular system (38,58,66) and it is related to the total integral scattering intensity

$$\int_0^\infty s^2 I(s)\, ds = Q, \text{ point geometry}$$

or

$$\int_0^\infty s\, \tilde{I}(s)\, ds = \tilde{Q}, \text{ slit geometry} \qquad (40)$$

where I(s) and Q, and $\tilde{I}(s)$ and $\tilde{Q}$ are calculated from point-like or infinite slit (smeared) geometry, respectively.

For a system of evenly-distributed electron densities in two phases separated by a sharp bounday, we can write

$$\overline{(\rho - \bar{\rho})^2} = \phi_1 (\rho_1 - \bar{\rho})^2 + \phi_2 (\rho_2 - \bar{\rho})^2 \qquad (41)$$

where

$$\bar{\rho} = \phi_1 \rho_1 + \phi_2 \rho_2$$

$$\phi_1 + \phi_2 = 1.0$$

ϕ_1 and ϕ_2 are the volume fractions of material in the phases.

Making the proper substitutions and rearranging terms leads to the well-known expression, where

$$\overline{(\rho - \bar{\rho})^2} = (\rho_1 - \rho_2)^2 \phi_1 \phi_2 = \langle \Delta\eta^2 \rangle \qquad (42)$$

We must keep in mind that the ρ's are electron densities in these equations as opposed to mass densities normally thought of. $\overline{(\rho - \bar{\rho})^2}$ will be replaced by the more conventional terminology $\langle \Delta\eta^2 \rangle$.

Concerning the evaluation of the invariants, Q and $\tilde{Q}$, obviously it is not possible to experimentally evaluate the integral over the whole angular range from zero to infinity. The low angle region may be obtained by a plot of $s\,\tilde{I}(s)$ vs. s and extrapolation of the linear position to zero angle. Conversely, extrapolation to higher angles must be done accurately since it may account for over 10% of the final result. Use of Porod's law (58) which states that for a two-phase system $s^4\, I(s)$ or $s^3\, \tilde{I}(s)$ should assume constant values in the high angle regions away from any obvious structural portions of the curve will allow evaluation to infinity, as follows. The invariant may be divided into two parts:

$$\tilde{Q} = \tilde{Q}' + \tilde{Q}'' \tag{43}$$

where

$$\tilde{Q}' = \int_0^{s'} s\,\tilde{I}(s)\,ds \tag{44}$$

and is evaluated numerically, while

$$Q'' = \int_{s'}^{\infty} s\,\tilde{I}(s)\,ds \tag{45}$$

where s' is the scattering vector at which Porod's law begins to be invoked. [A plot of $s^2\,\tilde{I}(s)$ or $s^4\,I(s)$ may first have to be corrected for diffuse boundary effects (59,67).] Considering only the slit-smeared case,

$$s^3\,\tilde{I}(s) = \text{Const.}$$

and

$$s\,\tilde{I}(s) = \frac{K}{s^2} \tag{46}$$

Substitution of (46) into (45) results in

$$\tilde{Q}'' = \int_{s'}^{\infty} \frac{K}{s^2}\,ds = \frac{K}{s'} \tag{47}$$

Finally, substituting Equations (47) and (44) into (43) gives the result we sought.

The observed or corrected total integrals are related to the mean squared electron density fluctuation by

$$\tilde{Q}(s) = \frac{r_T^2 \lambda N_A^2 P_s t_s \langle \Delta\eta^2 \rangle}{2\pi r_{sd}} \qquad (48)$$

where r_T^2 is the Thomson scattering factor, N_A is Avagadro's number, P_s the sample attenuated intensity of the primary beam, t_s the sample thickness, and r_{sd} is the sample-to-detector distance in centimeters. The energy of the incident beam must be determined experimentally. This has been done using a Lupolen (polyethylene) calibration standard (68,69) supplied to us by Professor O. Kratky. The energy per cm length of incident beam after sample attenuation is given by Equation (49).

$$P_s = \frac{K_s \cdot I_s \cdot r_{sd} \cdot A}{F_s} \qquad (49)$$

where K_s is the calibration constant supplied, A is the sample attenuation factor measured experimentally, F_s is the counting tube slit area, and I_s is the intensity of scattering from the standard sample at the particular calibration angle. Since $\tilde{Q}$ involves a measured intensity, the values of F_s and r_{sd} need not be determined for the calculation of $\langle \Delta\eta^2 \rangle$. More will be said concerning the details of these calculations in the Experimental section.

F. Swelling Studies - The Invariant

Swelling techniques have been used by Porod, et al. (58a,70) to elucidate the structure of regenerated cellulose. Air-swollen and dried samples showed striking differences and the authors concluded that the swollen matrix could be represented by a dilute system while the dried one by a densely-packed colloidal system. The agreement with the absolute scattering intensity was very good.

More recently, Sakai, et al. (71), used iodine (solvent) uptake in conjunction with SAXS to study the density of the amorphous intercrystalline regions of poly(ethylene terephthalate). By experimental determination of the ratios of peak intensities with and without iodine present and to varying degrees, and comparison with model calculations, they were able to conclude that sorption sites were more numerous near the crystal surface than in the interior of the amorphous phase. They postulated that this was due to a lower density region at the extremities of the amorphous phase rather than the interior.

In a slightly different study concerning SALS , Rhodes and Stein (72) were able to show that light scattering patterns (V_V) from stretched polyethylene were not affected by swelling in trichlorobenzene or heptane. They concluded that refractive index heterogeneity at the fibril boundary is a result of orientation fluctuations of the optic axes rather than a density discontinuity. Blackadder, et al. (73,74) have shown that solvent uptake alone can be a powerful technique for morphological investigations.

In order to evaluate the validity of the two-phase model for the stretched and unstretched samples in this study, specifically with respect to voids or void formation, the technique of evaluating $\langle \Delta\eta^2 \rangle$ in the swollen and unswollen cases and comparing the results to model calculations was employed. The basic idea is that if a void exists and is characterized by essentially zero electron density and a fluid subsequently is allowed to penetrate that volume, the relative electron density will have increased. Since the total integral is proportional to the difference in electron densities of the phases, swelling will decrease this difference and the intensity should drop rather dramatically. If no voids were present initially, then the drop should not be as significant.

In the subsequent derivations, it is assumed that a void will scatter x-rays coherently. The swollen amorphous phase which initially had voids will now scatter as one new phase. The major possible situations are considered independently and compared as follows.

Case I. No Voids, Unswollen.

We shall assume that the crystalline and amorphous regions have uniform densities and that they are separated by a sharp boundary. This is just the case presented in Equations (41) and (42), changing subscripts 1 and 2 to c and a for the crystalline and amorphous phases, respectively.

Case II. Voids, Unswollen.

This consists of a three-phase system comprised of crystals of uniform electron density and voids within the amorphous zones. The general equation for the mean squared electron density fluctuations of a system containing n homogeneous phases is by definition

$$\langle \Delta\eta^2 \rangle = \sum_{i=1}^{n} (\rho_i - \bar{\rho})^2 \phi_i ,$$

$$\bar{\rho} = \sum_{i=1}^{n} \rho_i \phi_i , \text{ and } \sum_{i=1}^{n} \phi_i = 1 \qquad (50)$$

Thus application to the three-phase system here yields

$$\langle \Delta\eta^2 \rangle_v = \phi_{cv} (\rho_c - \bar{\rho})^2 + \phi_{av} (\rho_a - \bar{\rho})^2 + \phi_v (\rho_v - \bar{\rho})^2 \qquad (51)$$

where

$$\phi_{cv} + \phi_{av} + \phi_v = 1.0, \; \rho_v = 0.0 \tag{52}$$

and

$$\bar{\rho} = \phi_{cv} \rho_c + \phi_{av} \rho_a + \phi_v \rho_v \tag{53}$$

Again, ϕ represents the volume fraction of material in the system. ϕ_{cv}, ϕ_{av} and ϕ_v are those volume fractions of crystalline and amorphous phases adjusted for the presence of voids (the extra subscript v).

In these calculations, values of ϕ_v must be assumed. Substitution of Equations (52) and (53) into (51) and rearrangement gives

$$\langle \Delta\eta^2 \rangle_v = \phi_{cv} \phi_{av} (\rho_c - \rho_a)^2 + \phi_v (\phi_{cv} \rho_c^2 + \phi_{av} \rho_a^2) \tag{54}$$

In the limiting cases, when $\phi_v = 0$, Equation (54) reduces to (42), whereas, when $\phi_v = 1.0$, $\phi_{cv} = \phi_{av} = 0$ and $\langle \Delta\eta^2 \rangle_v = 0$, which is the expected result.

At this point we must examine the work of Heikens (75) and Hermans, et al. (76), who derived an expression for $\langle \Delta\eta^2 \rangle$ for a three-phase system containing voids using the relation

$$\langle \Delta\eta^2 \rangle = \frac{1}{2} \sum_{i=1}^{n} \sum_{j=1}^{n} (\rho_i - \rho_j)^2 \phi_i \phi_j \qquad (55)$$

which is presented as an alternative form of Equation (50), and is basically a generalization from results of the two phase system. Thus for a three-phase system (n=3) containing voids, the above equation expands to

$$\langle \Delta\eta^2 \rangle = (\rho_1 - \rho_2)^2 \phi_1 \phi_2 + (\rho_1 - \rho_3)^2 \phi_1 \phi_3 + (\rho_2 - \rho_3)^2 \phi_2 \phi_3$$

It is presented here as a test of the validity of Equation (55) using subscripts 1, 2, and 3 to denote phases to keep the solution completely general. Hence, generalizing Equation (51),

$$\langle \Delta\eta^2 \rangle = \phi_1(\rho_1 - \bar{\rho})^2 + \phi_2 (\rho_2 - \bar{\rho})^2 + \phi_3 (\rho_3 - \bar{\rho})^2 \qquad (57)$$

where

$$\bar{\rho} = \phi_1 \rho_1 + \phi_2 \rho_2 + \phi_3 \rho_3$$

and

$$\phi_1 + \phi_2 + \phi_3 = 1.0$$

Performing the subtractions in parentheses yields

$$\rho_1 - \bar{\rho} = \phi_2 (\rho_1 - \rho_2) + \phi_3 (\rho_1 - \rho_3)$$

$$\rho_2 - \bar{\rho} = \phi_1 (\rho_2 - \rho_1) + \phi_3 (\rho_2 - \rho_2)$$

$$\rho_3 - \bar{\rho} = \phi_1 (\rho_3 - \rho_1) + \phi_2 (\rho_3 - \rho_2)$$

Substituting and squaring the terms, along with factoring terms in $(\rho_i - \rho_j)$ leads to

$$\langle \Delta\eta^2 \rangle = \phi_1 \phi_2 (1 - \phi_3) (\rho_1 - \rho_2)^2 + \phi_1 \phi_3 (1 - \phi_2) (\rho_1 - \rho_3)^2$$

$$+ \phi_2 \phi_3 (1 - \phi_1) (\rho_2 - \rho_3)^2 + 2 \phi_1 \phi_2 \phi_3 [\rho_1^2 + \rho_2^2$$

$$+ \rho_3^2 - \rho_1 \rho_2 - \rho_1 \rho_3 - \rho_2 \rho_3]$$

Rearrangement and cancellation of cross-products leads directly to Equation (56). Thus, at least for the three-phase system, Equation (55) is completely rigorous. When $\rho_3 = 0$, Equation (56) reduces to (54).

Case III. No Voids, Swollen.

Here it is assumed that the swelling only takes place in the amorphous phase and that the liquid distributes itself homogeneously throughout. The crystalline phase remains unaffected. The general equation for $\langle \Delta\eta^2 \rangle$ is given by

$$\langle \Delta\eta^2 \rangle_s = \phi_{cs} (\rho_c - \bar{\rho})^2 + \phi'_{as} (\rho_{as} - \bar{\rho})^2 \qquad (58)$$

where the s denotes the swollen case and

$$\phi'_{as} = \phi_{as} + \phi_s$$

$$\phi_{cs} + \phi_{as} + \phi_s = 1.0 \qquad (59)$$

By definition,

$$\rho_{as} = \frac{W_a + W_s}{V_a + V_s} \tag{60}$$

$$\phi_s = \frac{V_s}{V_{cs} + V_{as} + V_s} \quad ; \; W_a = \rho_a V_a$$

$$\phi_{as} = \frac{V_{as}}{V_{cs} + V_{as} + V_s} \quad ; \; W_s = \rho_s V_s \tag{61}$$

where W_a, W_s and V_a, V_s denote the weights and volumes of the amorphous and solvent phases, and ρ_{as} is the electron density of the swollen amorphous phase. Substituting (61) into (60) and again rearranging,

$$\rho_{as} = \frac{\phi_{as} \rho_a + \phi_s \rho_s}{1 - \phi_{cs}} \tag{62}$$

Finally,

$$\bar{\rho} = \phi_{cs} \rho_c + \phi_{as} \rho_a + \phi_s \rho_s \tag{63}$$

In this case, it is simpler to calculate Equations (59), (62) and (63) explicitly and substitute the results directly into (58) rather than try to simplify the expression. The volume fraction of solvent imbibbed is found from swelling measurements or from results of SAXS model calculations. We will see that the two techniques agreed to within experimental error.

Case IV. Voids, Swollen.

Here it is assumed that the voids no longer exist after swelling since the swollen amorphous phase completely replaces any space previously occupied by the voids. It, therefore, assumes that the crystallinity values used are completely free from the influence of voids. Therefore, we can write down Equation (64)

$$\langle \Delta\eta^2 \rangle = \phi_{csv} (\rho_c - \bar{\rho})^2 + \phi'_{asv} (\rho_{asv} - \bar{\rho})^2 \qquad (64)$$

where

$$\phi'_{asv} = \phi_{asv} + \phi_s + \phi_v$$

$$\phi_{csv} + \phi_{asv} + \phi_s + \phi_v = 1.0 \qquad (65)$$

and using similar definitions as in Case II,

$$\rho_{asv} = \frac{W_a + W_s}{V_a + V_s + V_v} \tag{66}$$

where

$$W_s = \rho_s \, (V_s + V_v)$$

$$W_a = \rho_a \, V_a \tag{67}$$

and

$$\phi_i = \frac{V_i}{V_T}$$

where

$$V_T = \sum_i V_i \; ; \; i = a, \, s, \, v$$

Substituting Equations (67) into (66) and rearranging,

$$\rho_{asv} = \frac{\phi_a \, \rho_a + \rho_s \, (\phi_s + \phi_v)}{1 - \phi_c} \tag{68}$$

and is the electron density of the swollen amorphous phase which initially included voids. Finally,

$$\overline{\rho} = \phi_{csv}\,\rho_c + (\phi_{asv} + \phi_v)\,\rho_{asv} + \phi_s\,\rho_s \qquad (69)$$

Calculation of Equations (65), (68) and (69) and substitution into (64) gives the desired result. Use of an electronic, programmable, scientific calculator makes these calculations quite manageable.

Case V. No Voids, Unswollen. A Finite Transition Width.

Here a two phase system is treated where the electrons are distributed uniformly in each of their respective phases but rather than a sharp separating boundary, a linear transition zone is introduced. This calculation was originally performed by Blundell (77) and subsequently by Vonk (60) and Khambatta (78), where the result is given by

$$\langle \Delta\eta^2 \rangle_E = (\rho_c - \rho_a)^2 \left(\phi_c\phi_a - \frac{ES}{6V}\right) \qquad (70)$$

The subscript E denotes the finite transition width. E denotes the width of the transition zone in Angstroms, and S/V is the specific surface area of the phase boundary. Vonk showed that for layer structures

such as lamellae, S/V = 2/d where d is the long period. Substitution into Equation (70) leads to the final result that

$$\langle \Delta n^2 \rangle_E = (\rho_c \rho_a)^2 \left(\phi_c \phi_a - \frac{E}{3d}\right) \tag{71}$$

E/3d is actually equal to the volume fraction of this third phase, ϕ_E, describing the contribution of the finite transition width.

Case VI. No Voids, Swollen, Finite Transition Width.

Here we assume the same as in Case III and also that the transition width swells uniformly with solvent. We could also assume that the transition width goes to zero with swelling and this reduces to Case III. We can write

$$\langle \Delta \eta^2 \rangle_{sE} = \phi'_{csE} (\rho_c - \bar{\rho})^2 + \phi^*_{asE} (\rho_{asw} - \bar{\rho})^2 + \phi_E (\rho_3(x) - \bar{\rho})^2 \tag{72}$$

where

$$\phi'_{csE} = \phi_{csw} - \frac{\phi_E}{2}$$

$$\phi^*_{asE} = \phi_{asw} - \frac{\phi_E}{2} + \phi_s \qquad (73)$$

and

$$\overline{\rho} = \phi_{csE}\,\rho_c + (\phi_{asE} + \phi_s)\,\rho_{asE}$$

$$\overline{\rho} = \phi_{csE}\,\rho_c + \phi^{II}_{asE}\,\rho_{asE} \qquad (74)$$

where

$$\phi^{II}_{asE} = \phi'_{asE} + \phi_s + \frac{\phi_E}{2}\,.$$

and

$$\phi'_{asE} = \phi_{asE} - \frac{\phi_E}{2}$$

Let $\rho_3(x)$ be the linear gradient of electron density,

$$\rho_3(x) = \rho_{csE} + (\rho_{asE} - \rho_c)\frac{x}{E} \tag{75}$$

where x is the distance parameter along the thickness of the transition zone, E. If we define

$$\eta_3 = \rho_{csE} + (\rho_{asE} - \rho_c)\frac{x}{E} - \bar{\rho} \tag{76}$$

and substitute (74)

$$\eta_3 = (\rho_{asE} - \rho_c)\left(\frac{x}{E} - \phi^{\Pi}_{asE}\right) \tag{77}$$

Now averaging

$$\langle \eta_3 \rangle = \frac{1}{E} \int_0^E (\rho_{asE} - \rho_c)^2 \left(\frac{x}{E} - \phi_{asE} \right)^2 dx \qquad (78)$$

and performing the integration of (78) yields,

$$\langle \eta_3^2 \rangle = (\rho_{asE} - \rho_c)^2 \left(\frac{1}{3} - \phi_{asE}^{II} \phi_{csE} \right) \qquad (79)$$

and where

$$\rho_{asE} = \frac{\phi_{asE} \rho_a + \phi_s \rho_s}{\phi_{asE} + \phi_s} \qquad (80)$$

and

$$\phi_{csE} + \phi_{asE} + \phi_s = 1.0 \qquad (81)$$

Combining the relevant equations leads to the final result that

$$\langle \Delta\eta^2 \rangle_{sE} = \phi'_{csE} (\rho_c - \bar{\rho})^2 + \phi^*_{asE} (\rho_{asE} - \bar{\rho})^2 + \phi_E \langle \eta_3^2 \rangle \qquad (82)$$

Again it is easier to calculate the separate terms and feed them into (82) rather than trying to simplify it.

Other cases or combinations could have been pursued but, because of the nature of the experiments and their accuracy, only these six, very distinguishable cases were analysed.

G. The Elliptically Symmetric Invariant

Due to the fact that the scattering from the elastically-strained samples exhibited elliptically-symmetric scattering patterns in some cases (see Results) and that the 10 Meter ORNL spectrometer could easily monitor the absolute scattered intensity, the total integral was derived with the hopes of obtaining two major pieces of information.

The first is the determination of the invariant, previously derived for spherically-symmetric scattering patterns (see e.g. Reference 31). If the shape of the scattering pattern is something other than spherically symmetric, then the calculation of the invariant is meaningless, unless its shape is known and is mathematically expressed properly, or unless a two-dimensional experimental integration is possible. The second reason is to study deviations from the analytically expressed scattering shape and to, therefore, characterize the system more fully. The derivation is as follows.

In the spherical coordinate system

$$Q = \int_{v_s} I(\underset{\sim}{s})\, dv_s = 2\pi \int_{\psi=0}^{\pi} \int_{s=0}^{\infty} s^2\, I(s) \sin\psi\, ds\, d\psi \tag{83}$$

assuming cylindrical symmetry about θ, where now θ is the space coordinate in the spherical coordinate system (not to be confused with the scattering angle), v_s is the total volume of reciprocal space over which the integration is performed, and ψ is the azimuthal angle.

For elliptically-symmetric iso-intensity contours (generated by the computer ORNL processing of SAXS spectrometer data)

$$I(s) = I'(s, \psi) \tag{84}$$

and the integration of (83) can go no further. However, if we allow s to vary elliptically, cylindrically symmetric about an axis, then I(s) is regenerated and

$$s^2 = \frac{a^2 b^2}{a^2 \sin^2\psi + b^2 \cos^2\psi} = \frac{a^2}{k^2 \sin^2\psi + \cos^2\psi} \qquad (85)$$

where $k = a/b$ = major/minor axes, obtained directly from the iso-intensity contours. Here, a is not to be confused with the amorphous thickness parameters.

Thus

$$s = \frac{a}{(k^2 \sin^2\psi + \cos^2\psi)^{1/2}} \qquad (86)$$

$$ds = \frac{da}{(k^2 \sin^2\psi + \cos^2\psi)^{1/2}} \qquad (87)$$

and

$$I'(s, \psi) = I(a)$$

Substituting (86) and (87) into (83),

$$Q = \int_{a=0}^{\infty} \int_{\phi=0}^{\pi} I(a) \frac{a^2 \sin\psi}{(k^2 \sin^2\psi + \cos^2\psi)^{3/2}} \, d\psi \, da \qquad (88)$$

Solution of (88) is performed by a propitious change of variables

$$x = \sin\psi$$

$$y = \cos\psi$$

which leads to an integral of the form

$$\int \frac{dx}{(ax^2 + c)^{3/2}} = \frac{x}{c(ax^2 + c)^{1/2}}$$

resulting in

$$Q = 4\pi \int_{a=0}^{\infty} \frac{a^2}{k^2} I(a) \, da \qquad (89)$$

Substituting Equations (85) and (87), results in the final equation,

$$Q = \frac{4\pi}{k^2} \left(k^2 \sin^2\psi + \cos^2\psi\right)^{3/2} \int_{s=0}^{\infty} s^2 I(s)\, ds \qquad (90)$$

Note that this is identical to the case of spherical symmetry except for the scaling due to the elliptical terms.

If we allow the strain to be along the y axis, and k = 2.0, at $\psi = 0^o$, a y axis average, Equation (90) gives

$$Q = \pi \int_0^{\infty} s^2 I(s)\, ds$$

while at $\psi = 90^o$, an x average, it reduces to

$$Q = 8\pi \int_0^{\infty} s^2 I(s)\, ds$$

A slightly-different approach was used by Hendricks (79) and similar results were obtained. Combining the two derivations has yielded

a more general relationship (Reference 79) than Equation (90) where any given ellipsoid can be considered, not only the prolate one assumed above. Thus

$$Q = 4\pi \frac{k_3}{k_2} (k_2^2 \sin^2\psi + \cos^2\psi)^{3/2} \int_0^\infty s^2 I(s)\, ds \qquad (91)$$

where $k_3 = b/a$, $k_2 = c/a$ and describe the shape of the triaxial ellipse (scaling factors). For a prolate ellipsoid, $k_3 = k_1 = 1$ (revolution about the y, k_2 axis) and (91) reduces to (90).

Deviations in Q from different azimuthal slices will indicate deviations from the elliptical symmetry predicted from the affine scheme (see Discussion).

H. Small Angle Light Scattering (SALS)

The interpretations of (SALS) by deformed spherulites has been the topic of a considerable research effort both in this laboratory (7,10,15,16,18,19,21,81) and in others (11,29,30,82,83). Specifically, Van Aartsen and Stein (19) calculated the H_V (crossed polaroids) light scattering patterns for uniaxially deformed three dimensional spherulites assuming an affine deformation of the total spherulite. Thus a point with coordinates (x, y, z) will assume coordinates (x', y', z') after deformation, where $x' = \lambda_1 x$, $y' = \lambda_2 y$, and $z' = \lambda_3 z$ where λ_i's are

the strain ratios along the given directions. For uniaxial deformation $\lambda_1 = \lambda_2$ and the major strain direction is along λ_3 or the z axis. The optic axis of a scattering element lying at an arbitrary angle with respect to the radius is allowed to vary during the course of deformation in a manner that depends upon its angular location within the spherulite and according to some empirically assumed equation. Two general models are considered. In the first, a constant density of scattering elements is preserved (Model I) while in the second, (Model II), the radial density of scattering elements remains constant but the angular distribution changes affinely. Constant volume deformation is considered. Also, twisting of lamellae about their radii is considered. During deformation, the twist may remain unchanged from the undeformed case (random) or may preferentially twist or detwist depending upon the location within the spherulite relative to the strain. Finally, the variation of the optic axis angle with respect to the radius is considered. It can either allign itself more nearly parallel to the strain direction or else remain constant. Both the lamellar twisting and the optic axis variations are described by semi-empirical compliance parameters.

The authors found that with increasing spherulite elongation, the absolute maximum in intensity with respect to both the reduced scattering angle, U, and the azimuthal angle, μ, moved to slightly higher U values and appreciably higher μ values; i.e., toward the equatorial regions of the pattern. They also found that experimental separation of models I and II was impossible due to the small angular variations which would have to be measured. The influence of a

non-random lamellar twist during deformation appears to increase the overall intensity without appreciably changing the shape of the pattern. Quantitative intensity measurements would have to be made here. Finally, there seems to be little effect from the reorientation of the optic axes.

Because of the first observation, models I and II were combined to give an average model from which, mathematics being simplified, the intensity was calculated where

$$I_{H_V} = \sin^2\varepsilon \cos^2\varepsilon \, [4 \sin U^* - U^* \cos U^* - 3\mathrm{Si}U^*]^2 \, (U^*)^{-6} \qquad (92)$$

where

$$U^* = U \left[\lambda_2^{\,2} \sin^2\left(\frac{\theta}{2}\right) + \cos^2\left(\frac{\theta}{2}\right) (\lambda_2^{\,2} \sin^2\mu + \lambda_3^{\,2} \cos^2\mu)\right]^{1/2}$$

$$U = 4\pi \left(\frac{R}{\lambda}\right) \sin\left(\frac{\theta}{2}\right)$$

$$\cos\varepsilon = \lambda_3 \cos\left(\frac{\theta}{2}\right) \cos\mu\left(\frac{U}{U^*}\right)$$

and

$$\lambda_2^2 \lambda_3 = 1 \quad \text{(cylindrical symmetry)}$$

Finally, the spherulite radius is R, the wavelength of light within the medium is λ, and $\theta/2$ is the scattering angle exiting the medium.

Maximizing the intensity as $(\partial I/\partial \mu)_U$ and $(\partial I/\partial U)_\mu$ simultaneously predicts that the maximum intensity is to be found at

$$U^* = 4.09 \text{ and } \cos^2\mu = [(\lambda_3^3 + 1)\cos^2 \frac{\theta}{2}]^{-1}$$

where λ_3 is the elongation ratio along the stretch direction. Thus for small scattering angles we have the approximate relations

$$\tan^2\mu_{max} = \lambda_3^3 \tag{93}$$

and

$$U_{max} = 4.00 \tag{94}$$

Thus, a knowledge of the azimuthal angle at which the maximum in H_V scattering occurs either by photographic or photometric techniques will characterize the elongation of the spherulite within the sample.

The above theory proves to be very useful in determining the relationships between macroscopic and microscopic (spherulitic) deformation characteristics. For polyethylene, when spherulite sizes are too small to be successfully monitored by optical microscopy, it is especially revealing. An important limitation, however, is due to the contribution of background scattering which cannot always be successfully subtracted and which, in fact, may vary with sample elongation. The source of background scattering is probably due to spherulite imperfections arising from boundary regions, internal disorder, or inter-spherulitic interference.

CHAPTER 3

EXPERIMENTAL

A. Sample Preparation

Low-Density Polyethylene: The samples studied were Monsanto experimental M8011 (LDPE). Pertinent physical characterization properties are given in Table 2. Thick films were prepared by melting pellets sandwiched between aluminum foil covered, cold-rolled steel platens and subjecting the melt to 12000 psi in a bench-size Carver press. Melting times, t_m, and temperatures, T_m, pressing times, t_p, and temperatures, T_p, as well as sample thicknesses are given in Table 3. Slowly-cooled (SC) samples were prepared by allowing the pressed films to cool at the natural cooling rate of the press. Quenched (Q) samples were prepared by rapidly transferring the sample and platens into an ice-water bath.

High-Density Polyethylene: The samples studied were Monsanto MPE 200/17942 high density polyethylene (HDPE). Again, the pertinent physical characterization parameters are given in Table 2 while the film preparation data are given in Table 3. The notation and preparation of slowly-cooled and quenched samples is the same as for the LDPE.

Special-Texture LDPE: Monsanto M8011,Q was used in the preparation of the parallel lamellae morphologies as described by Keller (84,85). Strips 3" x 0.5" were cut from the polyethylene sheets and clamped into an Instron. They were drawn through the yield and necking region to a total strain of about 500 percent. They recovered to about 300% total strain after removal from the clamps as estimated by distances measured

between fiducial marks. The necked portions were then passed several times in the same direction through a two-roll mill at room temperature until the thickness was about 60% of the original. Finally, annealing of the strips between glass cover slips in a silicone oil bath at 115°C for about 15 seconds produced the desired parallel lamellae morphology as evidenced by photographic SAXS. Typical two-point patterns were evident. Annealing at higher temperatures or longer times randomized the orientation so that diffuse SAXS patterns were obtained.

B. Small-Angle X-Ray Scattering.

1. Slit Geometry.

a. Apparatus.

A Rigaku-Denki Small Angle X-Ray Diffractometer (Catalog No. 2202) utilizing slit geometry and a scintillation counter detector with pulse height analyzer was used for studies of the undeformed and swollen samples. Analysis of stretched samples was performed for a slit height study and for comparison with results of point geometry data. The schematic of Figure 8 illustrates the collimation system. Slits s_1 and s_2 collimate the x-rays prior to impingement on the sample, while s_3 serves to remove excess parasitic scattering from the s_2 slit edges. The sample is located directly behind s_3. Scattered x-rays exit from the sample and travel along the flight path through an evacuated chamber to the scattering, s_4, and receiving, s_5, slits, and finally to the detector. Slit widths and their arrangement are given in Table 4.

Cu K_α x-rays were generated at 40 kVolts and 1.5 m amps with a G.E. CA8-F fine focus tube and G.E. XRD-6 generator. Cu K_β radiation was removed by a standard nickel filter. A Harshaw Chemical Company Na I(Tℓ) scintillation counter (type K968SHG32K) including the NB-18A preamplifier was used to detect scattered radiation in conjunction with a Digital Automation Company (DAC) Model 200 Spectrometer equipped with a pulse height analyzer. Spectrometer settings were determined according to the procedures outlined in References 31, p. 119, and 86. Table 5 includes settings and conditions of the spectrometer for future reference. A styrene-butadiene-styrene (SBS) block copolymer (Shell Kariflex 101) with a sharp, strong reflection at 0.25^{o} was used as a secondary standard and also for transmission determinations. At the settings listed in Table 5, this sample gave an average intensity of 79 counts per second (cps), with a natural background of 0.9 cps. The natural background is measured with the x-ray shutter closed. Also, a standard x-ray source, ^{129}I (NES-1865 from New England Nuclear) taped to the detector face gave an average reading of 16.8 cps.

The detector was supplied by the manufacturer with a metal collimator consisting of a 1/8" x 1/2" slot. This was mounted on the face of the detector directly in front of the Beryllium (Be) window. It was replaced by a brass collimator containing a circular hole 0.7" in diameter; approximately the size of the Be window on the detector face. Thus, alignment of the detector was simple and uncritical and reduced the probability of scattering from the metal slot edges. Possible fluorescence

from copper in the brass collar is minimized by the large diameter of the bored hole. The same collar should be used in any intensity comparisons especially with the ^{129}I source since this is taped directly to it.

Experimental scanning intervals were typically 0.05^{o}. Also, 10,000 counts were usually obtained at each scattering angle through the maximum of the scattering curve, giving rise to a precision of about $\pm$ 1%. Precision in this case is defined as $\pm 100X\sqrt{N_c}/N_c$ where N_c is the preset count. About $\pm$ 5% precision was obtained at the tails of the curve due to lower counting rates. The precision of background scans, the major source of error, typically ranged from $\pm$ 1% near zero angle to about $\pm$ 10% at angles of 0.2^{o} or more. The extremely-low counting rates were the major causes.

The above equipment was integrated with a PDP-8 minicomputer to store data and to direct the scanning and counting operations. A teletype equipped with a paper tape punch and reader served as the communications link to the PDP-8. Scattering data was output directly to punched tape which was then fed into the CDC Cyber 70 computer at the University of Massachusetts Computing Center.

b. Desmearing Procedures.

The theories of SAXS presented in the Theoretical section are derived primarily on the basis of a point-like cross-section of the incident beam which can be closely achieved by collimation with very

small pinholes. In fact, most theoretical treatments assume this geometry unless otherwise specifically stated.

The need for greater intensity in the small angle regions has prompted the use of slit collimators. Thus two approaches have resulted in order to understand the data generated. The first has been to correct the experimental curves to give the corresponding point-like pattern. This has been termed "desmearing". The second approach has majored on theoretical development of models including the effects of smearing. Both methods assume an a priori knowledge of the shape of the scattering pattern. However, the former method has been employed here since, according to Alexander (Reference 31, p. 287), the second method suffers from the deficiency that the "smeared" theory does not yield the complete scattering curves for particles of various shapes and size distributions. The former method suffers from certain approximations needed to solve the equations which will become evident in the subsequent derivations.

Guinier (Reference 40, Chapter 3) has shown that for slits of arbitrary height (length), but of negligible width, the experimental intensity curve, $I_e(s)$ is related to the equivalent intensity function for point collimation, $I(s)$ by

$$I_e(s) = \int_0^\infty w(\phi)\ I(\sqrt{s^2 + \phi^2})\ d\phi \qquad (95)$$

where $w(\phi)$ is a weighting function describing the shape of the main beam intensity profile along the length of the slit, depends on the collimating system and x-ray source, and is normalized according to

$$\int_0^\infty w(\phi)\, d\phi = 1 \qquad (96)$$

The definition of the "height" of the beam relative to the slit length and sample scattering can be clarified by the following considerations. First, the general criterion for the "infinite" slit height approximation is that the main beam must have a height at least equal to the diameter of the circularly-symmetric interference ring. Another more-easily determinable criterion (Reference 63, Sec. 2.4.5) is that an infinitely-high beam must satisfy the condition that $L > 2m + d$, where L is the height of the homogeneous part of the beam at the receiving slit, d is the height of that slit, and m is the angular distance measured in the plane of registration. Thus, the infinite beam approximation is not only a function of the geometry of the spectrometer and sample, but also the angle to which data can be recorded. If any two of these criteria are not met, then the slits are considered of finite height.

Since this laboratory is in possession of the Schmidt desmearing program (87,88) which desmears on the basis of a finite slit geometry,

the details of these criteria were not, for the most part, important. See the Appendix for the Fortran IV program SAXSC. However, some work of Warner and Russell (private communation) in this laboratory showed that desmearing as finite slit heights in cases where the infinite criterion held showed insignificant differences in the resulting curves.

Kratky, Porod, and Kahovec (89) showed that for slits of arbitrary height and a Gaussian approximation to $w(\phi)$, i.e., $w(\phi) = 2p\pi^{-1/2} \exp(-p^2 \phi^2)$,

$$I(s) = - \frac{\exp (p^2 s^2)}{p\pi^{1/2}} \int_0^\infty \frac{N' (t^2 + s^2)\, dt}{(t^2 + s^2)^{1/2}} \qquad (97)$$

where p is determined by the slit height with perfect collimation corresponding to the limit of infinite p, and with the weighting function for infinite slit height being obtained by letting p=0 in the exponential function followed by assignment of a convenient factor by which the function is multiplied. t is an arbitrary parameter of integration. N'(s) is the first derivative of the intensity function, N(s), where

$$N(s) = I_e(s) \exp (-p^2 s^2)$$

To find I(s) by Equation (101), the experimental data must be differentiated numerically and, because of this, the relative error in I(s) may be greater than the relative error in $I_e(s)$.

Without going into the mathematical detail of the Schmidt method (87) alluded to earlier, basically the analysis involves the numerical differentiation of N(s) which is determined by least squares fitting a cubic polynomial taking six experimental points at a time to determine a smooth function which can be precisely differentiated. The experimentally-determined curve is "hand" smoothed by plotting experimental points with their error bars on large, 1 x 1 m, graph paper and drawing smooth curves through them. Large "ships" curves similar to "French" curves are perfect for drawing smooth curves for the sizes and shapes of the scattering curves encountered.

The slit-corrected intensity is, then, given as a sum of terms which are the products of the experimental intensity values and constants which depend only on the collimation system and which are the same for all scattering curves measured under the same collimation conditions. The sum is taken to be infinite, but must be truncated due to the finite number of points in the experimental curve. This is a major deficiency of the method.

Calculation of the weighting function, $w(\phi)$, is carried out according to the method of Hendricks and Schmidt (90). The Beeman four-slit system is assumed and defined in Reference (90). Schmidt found that the collimation errors are relatively insensitive to the fine details of the form

of the weighting function and that approximate functions can be used in most cases. Therefore, the Gaussian weighting function

$$W(u) = W(o) \exp (-p^2 u^2) \tag{98}$$

with the normalization condition of Equation (96) is used. u is related to ϕ and to the geometry of the spectrometer. W(o) is determined by Equation (31c) of Reference 90 for the system in this laboratory.

Since calculations were done as a function of slight height in a series of experiments, the appropriate values of W(o) and p where

$$p = \sqrt{\pi}\, W(o) \tag{99}$$

are given in Table 6.

These experiments were performed in an attempt to experimentally determine the accuracy of the desmearing procedures on the deformed samples. The weighting functions of Table 6 were used as slits s_1, s_2 and s_5 were systematically varied in their heights. An unstretched and a 30% stretched LDPE were characterized. Intensity versus scattering

angle curves were obtained at 0, 30, 60 and 90 degree azimuthal angles for the stretched samples. A plot of W(u) vs. u shown in Figure 9 calculated from Equation (31c) of Reference 90 at various slit heights shows that small variations in spectrometer geometry which may slightly change μ would greatly influence the value of the weighting function at small slit heights. Conversely, due to the broad function displayed for the longest slits, small variations in geometry would not affect the results as dramatically. These variations may occur as a result of imperfect alignment or non-parallelness of slits along the flight path.

The smearing due to the slit width has been shown to be rather insignificant (91) with respect to that from the height and, therefore, has been omitted in these calculations.

An inherent assumption in these calculations is that of a circularly or spherically symmetric true scattering pattern. The intensity I(s) depends only on scattering angle and not on any azimuthal dependence. Generalizations to any scattering shapes have been treated by Kranjc (92) and by Synecek (93). The intensity distribution in the direct beam cross-section must be accurately known in the former, while accurate integrated intensities along various azimuthal angles must be determined or the infinite beam approximation must be ensured in the latter. These generalizations prove intriguing to this work. However, the availability of the ORNL-10 meter spectrometer, to be subsequently described, alleviates the necessity for these elaborate mathematical corrections and they were, therefore, not pursued.

c. Absolute Intensity Determinations.

A description of the equations needed for determination of the total integrated scattered intensities is given in Section 2, Equations (43) - (49). Some details concerning the calculations are given here.

In using the Kratky Lupolen [designated (17/4)] calibration standard, Equations (48) and (49) combine to give

$$\langle \Delta\eta^2 \rangle = \frac{\int_0^\infty \tilde{I}(\theta)\ \theta\ d\theta}{P_s} \qquad (100)$$

where the scattering vector, s, has been converted to the scattering angle θ to conform to Kratky's (68,69) notation. Also, the scattered intensity, $I(\theta)$, is given in terms of counts/min. rather than the more conventional cps. For the "17/4" standard provided, Equation (49) reduces to

$$P_s = 68.7 \cdot I_s \cdot r_{sd} \cdot A \qquad (101)$$

where r_{sd} is 27.0 cm. The value of I_s is found for the standard and the

spectrometer by placing the standard into the scattering position and counting the intensity at 0.589^{o}. An average of five readings at a preset count of 1000 was determined at the beginning and end of each run, then averaged again. Drift could be, thereby, detected. The effect of parasitic scattering was determined by placing the calibration standard at the detector position, recounting, and subtracting this value from the above reading. Finally, the natural background (no x-rays) was subtracted and I_s determined. The sample attenuation factor, A, was obtained by determining the scattering intensity from an SBS block copolymer (Shell Kariflex 101) at 0.25^{o} with, $\tilde{I}_{A,2}$, and without, $\tilde{I}_{A,1}$, the test specimen at the absorbing position on the detector head. Thus,

$$A = \tilde{I}_{A,2}/\tilde{I}_{A,1}$$

Again, this was measured five times and the values averaged.

The integrated intensity in Equation (100) was calculated according to Equation (43). $\tilde{Q}'$ of (44) was determined by application of Simpson's rule using a Hewlett Packard programmable, HP-55, calculator.

Determination of $\langle \Delta\eta^2 \rangle$ for swollen samples included subtraction of the scattering from the solvent as well. A special sample holder consisting of mica windows and a thick teflon gasket was prepared for

these measurements. Scattering from an equivalent volume of solvent was approximated by using a second gasket reduced in thickness by that of the swollen polymer itself.

2. Point-Like Geometry.

a. Apparatus.

The spectrometer described here is located at the Oak Ridge National Laboratories (ORNL), Oak Ridge, Tennessee, and was principally built by Dr. R. W. Hendricks (41). It is referred to as the ORNL 10-Meter SAXS Spectrometer. A schematic is given in Figure 10.

The spectrometer utilizes a 6 kw Rigaku-Denki rotating anode generator (Cu K_α), graphite crystal monochromator and incident beam monitor to produce the desired high intensity, monochromatic, and monitored radiation. The collimation system consists of two pinholes separated by 5 meters. The first slit is a 1 mm diameter hole in a lead sheet mounted on an X-Y (perpendicular to incident x-rays, i.e., along Z axis) positioning stage at the front of the beam path. The second contains four specially-polished tungsten edges to make a 1 mm square hole also mounted on an X-Y positioning stage. The specimen compartment consists of a 30 x 30 x 35 cm vacuum chamber containing externally-operated X-Y positioning devices for both the second slit and the specimen holder. Scattered radiation emerges at the end of the flight path through a 30 cm diameter, specially-supported, 0.5 mm thick beryllium window. The entire flight path from the first pinhole to the exit window is evacuated to 20 μm of mercury.

The detector is a Borkowski and Kopp (95) two-dimensional position sensitive proportional counter which operates on the rise-time method of processing the signal (see Reference 96 for details). Basically, when a scattered x-ray strikes a certain position on the detector, a high resistance wire, a signal is generated in both directions from that point. The difference in time required to detect it in traveling through two symmetric systems of electronics locates its position along the wire. The intensity is determined by the strength of the signal. A good illustration is given in Figure 2 of Reference 96 for the case of a one-dimensional detectoe.

The area detector is 40 cm in diameter and weighs approximately 25 kg. It is mounted on an X-Y-Z positioning stage designed for individual adjustments. An incident beam stop is mounted on a thin finger in the 20 x 20 cm active detector area and just touches the Be window on the flight path. Data are processed via a Modular Computer System Modcomp II/220 CP and results are displayed on a Tektronix Model 4014 Graphics terminal. Among other capabilities, results can be displayed both during and after data acquisition as two-dimensional contour maps, angular perspectives or azimuthally cross-sectional or averaged intensity profiles. A computer program to extract the azimuthally cross-sectional data was written by D. Carlson (ORNL) and myself and is part of the ORNL system. Data is stored either in on-line disk storage or the ORNL 360/91 computer. Data handling and processing can be done either on-line (Modcomp II) or in the batch mode using the IBM 360/91. The Modcomp II

is hard-wired directly to the IBM facility.

Resolution of the spectrometer is varied by simply inserting or removing sections of the beam line and adjusting the detector appropriately. Following Hendricks, the resolution of the collimation system is defined as

$$R = \gamma + e \tag{102}$$

where γ = maximum angular deviation in the incident beam and e = maximum angular deviation of the rays recorded in the detector resolution element.

For square pinholes of dimensions $a_1 \times a_1$ and $a_2 \times a_2$ separated by a distance, L_1, and a detector with a resolving element of size $a_3 \times a_3$ separated by L_2 from the specimen located directly behind the second slit,

$$\gamma = (a_1 + a_2)/2L_1 \tag{103}$$

and

$$e = (a_2 + a_3)/2L_2 \tag{104}$$

Since a_1, a_2, and a_3 are determined by the constraints of the focal spot size, specimen size, and detector element size, only L_1 and L_2 are adjustable parameters. The aim is to optimize the system by maximizing the power into a detector element. It turns out that this maximum is obtained when

$$\gamma = e = R/2$$

given by Equations

$$L_1 = (a_1 + a_2)/R \tag{105}$$

and

$$L_2 = (a_2 + a)/R \tag{106}$$

Using the examples cited by Hendricks, in order to achieve a resolution of 0.5 mrad, if a_1 = 0.5 mm and a_2 = 1.5 mm and a_3 = 2.0 mm, the optimum focal spot to specimen distance, L_1, is 4 m while the optimum specimen-to-detector distance, L_2 is 7 m. Therefore, for a 20 x 20 cm detector area, a total angular range of 0.5 mrad to 24 mrad is covered.

Larger angles can be obtained by decreasing L_1 and L_2 while maintaining constant pinhole sizes. For the geometry which was used for these experiments, the active detector area was electronically sectioned into a 64 x 64 array and the maximum attainable resolution was approximately 0.5 mrad or about 3000Å for Cu K_α radiation. The latter value is lowered slightly when one considers effects of parasitic scattering and its incomplete elimination.

The incident beam has a diameter of about 1.5 mm at the sample plane. Very small specimens may therefore be observed. Concurrently, the sample chamber is large and suggests the possibility of sophisticated heating and stretching apparatuses, etc. A small sample stretcher was used so as to ensure that the same sampling area was maintained at the various elongations, i.e., the sample was simultaneously stretched from both sides by hand - first one side then the other by the same amount of screw turns. Typically, 15 minutes were needed to stretch the sample about 2 mm so as to ensure complete orientation of the material within and also to prevent premature necking of the specimen.

Typical experiment times of 50 minutes per elongation yielded all the necessary data to analyze lamellae in their various spatial configurations. This is to be compared to approximately 80 hours of similar data acquisition in the case of the conventional slit spectrometer described previously. Data handling such as background subtractions and transmission corrections have not been included in the latter estimate. Precision was slightly lower, however, for a 50 minute run than a typical 8 hour

slit geometry run where a total of 10,000 events per scattering angle were detected. Typically, an average of 200 counts per channel were recorded with the ORNL facility leading to a precision of about 7%.

b. Absolute Intensity.

In order to determine the absolute intensity to calculate the invariants, the following is considered. For point geometry where slit smearing effects may be neglected, the power detected in a given detector element is given by (see Reference 96)

$$P(s, \psi) = \Psi F_s \Delta\Omega_1 t_s e^{-\mu_s t_s} \frac{d\Sigma}{d\Omega} (s, \psi) \Delta\Omega_2 \qquad (107)$$

where Ψ = photons per second per unit area per unit solid angle emanating from the effective source (the graphite crystal monochromator); F_s = area of entrance slit; $\Delta\Omega_1$ = solid angle subtended by the second slit; t_s = sample thickness, in cm; μ_s = sample linear absorption coefficient, in cm^{-1}, $\frac{d\Sigma}{d\Omega}$ = sample total scattering cross-section = $r_T^2 I_{eu}$; r_T^2 = Thomson scattering factor (7.94×10^{-26} cm^2); I_{eu} = absolute intensity in electron units/cm^3, or eu/cm^3; and $\Delta\Omega_2$ = solid angle subtended by a detector element.

The number of photons incident on the specimen, P_o, is given by

$$P_o = \Psi F_s \Delta\Omega_1 \tag{108}$$

By using the foil attenuation method (97), P_o was determined to be 3×10^5 photons/sec at 45 kV and 30 m amps. The detector solid angle, $\Delta\Omega_2$, is $(2.553)^2/(5108)^2$ for a 1 x 1 channel element. Thus to convert data to absolute units

$$I_{eu}(s, \psi) = \frac{P(s, \psi)}{P_o t_s e^{-\mu_s t_s} \cdot n \Delta\Omega_2 r_T^2} \tag{109}$$

where n is the number of detector elements in the azimuthal slice. All of my data is normalized to one detector element; therefore, n = 1. Equation (109) gives I_{eu} in eu/cm^3. The more traditional value of eu/molecule is determined by dividing Equation (109) by the number of polyethylene molecules/cm^3. However, since I have calculated mean squared electron densities in eu/Å^3 from theoretical treatments of Section 2F, data will be reported consistently in terms of the latter dimensions.

As mentioned previously, the main beam power was monitored and recorded for each experiment along with the total scattered intensity, $I(s, \psi)$, detected by the area proportional counter. Also, sample transmission, T_s, was determined with Equation (110) where $I(s, \psi)_{standard+sample}$ and $I(s, \psi)_{standard}$ are the average (3 runs) total intensities scattered into the area detector with the sample in and out of the scattering position. The standard is a piece of glassy carbon which intensely scatters x-rays in the small angle region. Thus,

$$T_s = \frac{I(s, \psi)_{standard+sample}}{I(s, \psi)_{standard}} \qquad (110)$$

Typically, $I(s, \psi)$ was determined in 100 seconds with about 9×10^5 events recorded giving $\pm$ 0.1% precision.

Scattered intensities were corrected for slight fluctuations in the main beam intensity. These fluctuations were, however, usually slight and could be ignored in most cases.

Also, all scattering curves presented except where noted are background subtracted and sensitivity corrected. This entails the automatic point-by-point (detector element-by-element) subtraction of the results for a run of only the main beam without any sample present from the desired curve. Adjustment for sample transmission and main beam fluctuations is automatically included as well as correction for

the sensitivity fluctuations of each detector element and for the shadowing effect of the aluminum grid which supports the Be window. The latter is done by placing an x-ray source (1 mCi ^{55}Fe) at the sample position and allowing it to evenly illuminate the detector for a long period of time, usually overnight. Thus, the sensitivity of each detector element is determined, assuming the even x-ray saturation over the entire active detector area.

3. SAXS Data Reduction.

a. Background Corrections.

Warner (63, Section 2.4.2) has discussed various sources of "background" scattering in terms of four factors, including

a. natural background radiation and noise detected with the x-ray shutter closed,

b. parasitic scattering from the edges of the collimating slits,

c. liquid scattering from the sample, and

d. foreign particle scattering from dust or other inhomogeneities such as residual catalysts or initiators.

The first two have been removed as corrected by the techniques described in the previous sections for slit and point geometries. The problem of parasitic scattering from the ORNL 10 meter spectrometer has been minimized by the use of specially-machined and polished edges at the second pinhole. For the slit system, scanning with the sample in the absorbing position in front of the detector and subtraction from the experimental curve reduces these effects.

Removal of the liquid scattering background from the slit-smeared curves was performed according to the method of Vonk, et al. (60,94). A straight line of zero slope was extrapolated from the very high angle (about 2.5^{o}) asymptotic regions to zero angle after corrections for a and b. The entire area below this line was subtracted from the experimental curve. The technique could not be applied to data from the ORNL spectrometer since in the high resolution mode data was recorded to only about 1.1 degrees. However, since the procedure is only important for the accurate determination of invariants, it was not used for analysis of intensity shapes or distributions by the model theories.

Correction for the effects of foreign particles includes a subtraction of the scattering from the sample in the molten state, especially at very small angles where these presumably large particles would scatter. Since this work includes studies of scattering from solvent-swollen systems and this correction would be impractical, if not impossible, it was not pursued. Also, in stretched samples, the asperities could deform. Treatment of this problem would also be difficult since molten, stretched samples would have to be studied, assuming that temperature had no effect on the nature, positions, or shapes of the asperities.

b. The "Lorentz" Factor.

According to Alexander (31, p. 284), for a system containing spherically-symmetric particles whose nature may be described by the structure factor, $F(\underset{\sim}{s})$, the intensity of SAXS may be expressed as

$$I(s) = \overline{L\,[F(\underset{\sim}{s})]^2} \qquad (111)$$

where L is somewhat analogous to the Lorentz factor of classical x-ray crystallography. The classical Lorentz factor is dependent on the time in which a given family of crystal planes reflects x-rays under a certain set of experimental conditions and arises in part from the lack of truly parallel and monochromatic x-rays in the incident beam. It takes a different form, for instance, for a rotating single crystal or a randomly-oriented crysalline powder and is dependent upon the position of the reflection.

In SAXS, the "Lorentz factor", or L, also depends on the geometry of the experimental conditions and the nature of the scattering entities. Crist (47b) has shown that L for point-like scattering from a disk-like model which exhibits spherically-symmetric SAXS is $2\pi s^2$. His reasoning is as follows.

The intensity increment, dI(s), along a line of scattering in reciprocal space arising from a thin disk of uniform electron density in the limit of an infinite radius can be defined as

$$dI(s) = 2I(s)_{calc}\, ds \qquad (112)$$

where $I(s)_{calc}$ can be readily calculated for an infinite plane of a given thickness. The factor of 2 arises from the +s and -s scattering directions. If we now distribute this disk over all possible orientations, the resulting intensity is spherically symmetric in reciprocal space and dI(s) resides in a spherical shell of radius s. Since the measured intensity is that in a fixed volume element of reciprocal space, we can now equate the linear and averaged cases to obtain

$$dI(s) = 2I(s)_{calc}\, ds = 4\pi s^2\, I(s)_{obs}\, ds \qquad (113)$$

or

$$I(s)_{calc} = 2\pi s^2\, I(s)_{obs} \qquad (114)$$

Thus, the L factor for the isotropic scattering system is the well-known s^2 times the scaling factor 2π. For curve fitting, only s^2 need be considered. The $4\pi s^2$ in Equation (113) is derived from volume element considerations in spherical coordinates.

Now, is L the same over the azimuthal range of a deformed system exhibiting elliptically-symmetric scattering? Rephrasing the question, by what L should the intensity versus scattering angle curves at various azimuthal angles be multiplied to ensure accurate results? Reasoning on

similar lines as given above, we have shown that the total integrated intensity for any triaxial ellipsoid is given by Equation (90). Thus, analogous to Equation (113),

$$dI(s) = 4\pi \frac{k_3}{k_2^2} (k_2^2 \sin^2\psi + \cos^2\psi)^{3/2} s^2 I(s)_{ob} ds \qquad (115)$$

Equating (115) and (112),

$$I(s)_{calc} = 2\pi \frac{k_3}{k_2^2} (k_2^2 \sin^2\psi + \cos^2\psi)^{3/2} s^2 I(s)_{obs} \qquad (116)$$

All the necessary terms have been defined previously. Therefore, the result of Equation (116) reduces again to the familiar s^2 multiplied by a scaling factor which now varies with the particular azimuthal angle at which the curve is integrated. This factor varies between $2\pi\ k_3\ k_2^{-2}$ at $\psi = 0^o$ and $2\pi\ k_2\ k_3$ at $\psi = 90^o$. Again, in the curve fitting procedures, the scaling factors may be ignored.

The result is that the "Lorentz factor" for curve-fitting purposes is the same at any azimuthal angle as it is for undeformed spherically-symmetric systems, namely, s^2. It should also be emphasized that in the derivation for the deformed system, it is assumed that the scattering can be uniquely described by an elliptical symmetry. This is obviously

not the case in some of the more highly-deformed specimens.

Finally, we must ask whether the "Lorentz" correction is the same for a system of highly-oriented lamellae, as in the case of the Keller-type special morphology samples studied here. Again, Crist (47b) states without rigorous proof that "for orders of one reflection, the 'Lorentz' factor for an imperfectly-oriented sample having fiber symmetry is the same as that for an isotropic specimen." This would lead us to believe that multiplication by s^2 of intensity profiles from two-point patterns is appropriate. This procedure generates unrealistic intensity curves and results in the lack of any reasonable curve fitting with the Hosemann analysis. However, if the procedure is not adopted but rather multiplication by 1 is assumed, then reasonable parameters and very good correspondence in fits are obtained.

The solution to the discrepancy lies in the derivation of Equation (113). It is here that the observed scattering shape is assumed and derived in the spherical coordinate system. In the corresponding Cartesian coordinate system, Equation (113) has the form

$$dI(x,y,z) = I(x,y,z)_{obs}\, dx\, dy\, dz \qquad (117)$$

while if we consider the scattering from the infinitely-extended disk of a given thickness to be concentrated along the z axis, then Equation (112) converts to

$$dI(z) = 2\ I(z)_{calc}\ dz \tag{118}$$

Since we have concentrated the intensity in the ideal real system along the z axis only, then no intensity exists in the x and y spaces, and equating (117) and (118) as with (112) and (113),

$$dI(x,y,z) = dI(z) = 2I(z)_{calc}\ dz = I(x,y,z)_{obs}\ dx\ dy\ dx$$

or

$$2I(z)_{calc} = I(x,y,z)_{obs} = I(z)_{obs} \tag{119}$$

Therefore, there exists no L factor (or L = 1) for a perfect two-point pattern, only the scaling factor, 2. Theory and experiment can be directly compared in this case. Experimentally perfect two-point patterns do not exist, but azimuthally-broadened patterns are generally revealed. In analysis of data long the "z" axis, no L factor has been used since it is assumed that scattering in this region is due solely to lamellae

whose normals are perfectly aligned to the "z" axis. The quotations are used about z since this is considered the y axis in the ORNL equipment from which these data are taken. Replacement of z by s is straightforward.

Recently, Kawai, et al. (98), used similar reasoning in deriving the proper form of Porod's law for a system of completely-oriented lamellae microdomains. Extension of their equation to derive the L factor leads to the same result as above.

c. Correlation Function Tables.

In order to simplify the curve-fitting procedures for the calculated and experimental correlation functions, a series of tables (Table 7) were prepared by Dr. F. P. Warner from which the possible choices of crystallinity, ϕ, and distribution parameters B_a and B_c could be narrowed. The numbers in the table were produced by generating theoretical correlation functions then determining the defining parameters which are the values of the minimum (absolute) and maximum in $\gamma(r)$ and the ratio of their positions, r_{min}/r_{max}. These are shown in the box below according to the manner in which they appear in Table 7.

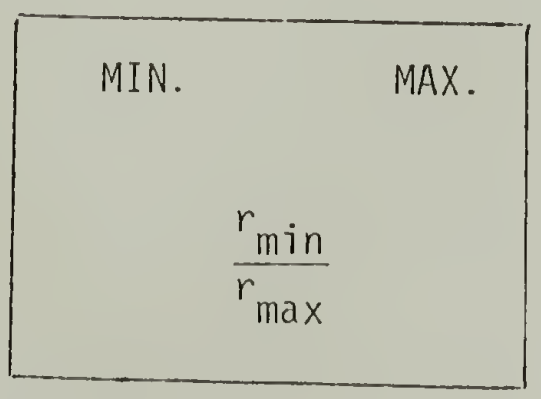

One calculates the experimental $\gamma(r)$ as in Equation (27) and program "ECF1" and determines these parameters. Next, the choice of Gaussian or log-normal distributions is made and values most closely representing those obtained experimentally are found in the tables. Finally, the corresponding values of ϕ, B_a, and B_c are plugged into the theoretical correlation function program, "TCF1", and the curves plotted on the same graph. Minor adjustments in parameters can be done to ensure the best possible fit between the two curves. Programs "ECF1" and "TCF1" are given in the Appendix. One will observe that in interpretation of Table 7 crystallinities of ϕ or $(1 - \phi)$ cannot be distinguished due to Babinet's theorem. External evidence must be supplied to make a choice between the two. Table 7 is published by permission of Dr. F. P. Warner.

d. Buchanan Analysis.

Figure 11 gives the calibration curves used to calculate the various physical sample parameters from SAXS intensities according to the method of Buchanan (35). The experimental half-width at half-maximum intensity, q, is obtained by dividing the full-width of the "Lorentz" corrected curve by two. This quantity and the position of the maximum, d_e, must obviously be determined in the same units. They are multiplied as in Equation (38). Other parameters are determined in a straightforward manner from the figure.

C. Other Methods

1. Wide-Angle X-Ray Diffraction (WAXD).

WAXD was used to determine initial crystallinities of undeformed samples by the method of Ruland (99,100) using a homemade diffractometer, a Phillips generator, Nickel-filtered Cu K_α radiation and scintillation counter. A Canberra Model 1701 spectrometer with pulse-height analyzer was used to detect the scattered radiation. A PDP-8 minicomputer was used to perform spectrometer functions and to output data on a paper tape. Details of the spectrometer, operations, and calculations can be found in the thesis of R. Cembrola (in preparation).

2. Differential Scanning Calorimetry (DSC).

A Perkin-Elmer Model 1B DSC was used to determine crystallinities of the undeformed polyethylene samples. Heats of fusion were measured from areas under the melting endotherms referred to an Indium (ΔH_f = 6.80 cal/gm) standard. ΔH_f^o, the heat of fusion of a perfectly-crystalline polyethylene is taken as 66 cal/gm from References 101 and 102. Areas under the melting endotherms were determined by paper weighing.

3. Density Determinations.

Crystallinities were also determined by the method of fluid displacement, or application of Archimedes principle. This involved weighing samples in air then in a suitable liquid (ethanol/water) whose density was accurately known. The sample density, d_p, is then determined by

$$d_p = W_{\ell d}/(W_{p\ell}/d_\ell) \qquad (120)$$

where $W_{\ell d}$ is the weight of liquid displaced determined by measuring the polymer in air and in the liquid and subtracting the two values, $W_{p\ell}$ is the weight of sample in the liquid and d_ℓ is the density of the liquid. d_ℓ is determined in a similar manner with reference to standard glass beads of known density.

Densities of stretched samples were obtained similarly. Tensile strips 1/4" x 2" were stretched on the Instron at 0.05 in/min. A small aluminum sample holder (1 x 2.5 in) was fabricated to secure the specimens in a stretched state during the weighing measurements. Tare weight of the holder including the compressed portions of the sample at the jaws was typically 7.8 gm while the total weight of the sample and holder averaged about 8.3 gm. This ensured the needed precision for accurate analysis. An automatic Mettler analytical balance with $\pm$0.0001 gm precision was used throughout, removing the sample pan and weighing from a tared wire. The wire was retared when weighing in liquid due to the buoyant force of the liquid.

4. Small-Angle Light Scattering (SALS).

Photographic SALS was used to determine spherulite deformation. A He-Ne red laser was used as a sourse of coherent parallel light. The H_V (crossed polaroids) mode was used throughout and the

sample was stretched along the direction of the polarizer (V). Polaroid type 52 film was used to record the patterns. The maximum in scattered intensity was estimated in each of the four lobes on the photographs and angles were measured and averaged. Error bars were determined from the deviation in the measured angles.

CHAPTER 4

RESULTS AND DISCUSSION

A. Spherulitic Morphology

This section deals with the bulk of the experimental information gathered and its interpretation regarding low and high density polyethylene, designated LDPE, SC; LDPE, Q; and HDPE, respectively.

1. Two-Dimensional Contour Plots.

Computer generated two-dimensional SAXS iso-intensity contour plots obtained at ORNL for LDPE, SC at various stages of strain are given in Figure 12. These have been corrected for background scattering, sensitivity of the various detector elements, sample transmission, and main beam fluctuations.

In each plot, the space between the outermost and next-to-outermost contour lines defines a region where the intensity is 16 $\pm$ 8 counts per second (cps). The intensity corresponding to the space between successive contour lines is incremented by a factor of two. Intensity increments can also be varied, but for all the plots presented in this report, the above holds true. Also, the odd-shaped central contours, removed in a and b by simply erasing for the sake of simplicity, are due to incomplete subtraction of the high background intensities about the beam stop. The sample stretch direction is horizontal, along x. The y axis is vertical.

Figure 13 shows the iso-intensity SAXS plot roughly comparable to Figure 12a before corrections for sensitivity, background, and sample transmission. One notes the strong centrally, cross-shaped parasitic scattering pattern indicative of the square pin holes used in the spectrometer. Other than a guide in aligning the instrument, this pattern is of no practical use and data are reported, henceforth, as in Figure 12. A similar series of plots is presented in Figure 14a-d for quenched LDPE.

For both LDPE, SC and LDPE, Q we observe a circularly symmetric pattern in the unstretched material. On straining at various levels, the patterns gradually change from circular to elliptical to symmetrically distorted. If we assume that the scattering at any given azimuthal angle originates from lamellae lying perpendicular to this angle as discussed previously, then application of Bragg's law at the approximate peak positions* (limitations discussed in Chapter 2) should yield information regarding the separation of lamellae at their relative orientations. Within the level of approximations already present in the Bragg formulation as applied to SAXS, simply taking the ratios of the major (M_1) to minor (M_2) axes of the innermost non-parasitic iso-intensity ellipse gives information regarding the deformation characteristics of lamellae

*Observation of iso-intensity contours alone can be misleading since a given space between successive contour lines may correspond to an increase or decrease in intensity. Perspective plots (see Chapter 3, Section II and Figure 43) or I(s) vs. s plots verify maxima and minima.

perpendicular and parallel, respectively, to the stretch direction. The ratios, M_1/M_2, for LDPE, SC are plotted as a function of sample stretch ratio, λ_s, in Figure 15, along with those predicted for similar orientations from the affine deformation mechanism considering constant volume on deformation. Thus $(M_1)_a = M_0\lambda_s$ and $(M_2)_a = M_0\lambda_s^{-1/2}$ where the subscript a denotes the affine calculation, M_0 being the diameter of the innermost contour line of the unstretched sample. Results show a good correspondence through an elongation ratio of about 1.4 after which a strong deviation is apparent. Also, the elliptical shapes seen in Figure 12 and 14 break down at strains of 50% or greater. Reasons for these deviations will be explored after a full treatment of the data has been presented.

Another illuminating piece of information can be obtained by direct analysis of the contour plots by the Herman's type (103,104) orientation function, f_ℓ, of lamellae defined as

$$f_\ell = \frac{3 \langle \cos^2\alpha \rangle - 1}{2} \qquad (121)$$

where α is the angle between the stretch direction and the lamellae, and

$$\langle \cos^2 \alpha \rangle = \frac{\int_0^{\pi/2} I(\psi) \sin\psi \cos^2\psi \, d\psi}{\int_0^{\pi/2} I(\psi) \sin\psi \, d\psi} \qquad (122)$$

where ψ is the azimuthal angle measured perpendicular to the stretch direction. The brackets, < >, denote average values. Since, for averaging over a uniform spherical distribution, $\langle \cos^2 \alpha \rangle_{av} = 1/3$, $f_\ell = 0$ for random orientation. If the lamellae are oriented perfectly along the stretch direction, $\langle \cos^2 \alpha \rangle_{av} = 1$, and $f_\ell = 1$. Finally, if the lamellae are aligned perpendicularly to the stretch direction, then $\langle \cos^2 \alpha \rangle_{av} = 0$, and $f_\ell = -1/2$. For data presented in the format of Figures 12 and 14, an average orientation function can be obtained by simply placing a sheet of transparent polar coordinate paper over the contour plots and measuring the angles at which iso-intensity regions of a given magnitude intersect a circle through the peak intensity. The circle remains constant in measuring f_ℓ from the deformed patterns. The procedure is carried out in all four quadrants and then averaged. Due to its approximate nature a circle of almost any practical radius may be used as long as enough iso-intensity lines are intersected. A more rigorous procedure would be to calculate the integrated intensities along azimuthal angles and then sum these according to Equation (122). However, as will be seen in Figure 16, the results from the more simplified

procedure are remarkably accurate. These are plotted for LDPE, SC and LDPE, Q in Figure 16 along with the orientation function predicted for uniaxial extension using the affine assumption, $(f_\ell)_a$. $(f_\ell)_a$ is obtained from Equation (123) shown in Figure 20 and is given by

$$(f_\ell)_a = \frac{3\lambda_s^3}{2(\lambda_s^3 - 1)} \left\{ 1 - \frac{\tan^{-1}(\lambda_s^3 - 1)^{1/2}}{(\lambda_s^3 - 1)^{1/2}} \right\} - \frac{1}{2} \qquad (123)$$

where, again, λ_s is the macroscopic sample deformation or strain ratio. Equation (123) is derived on the basis that the affine assumption predicts

$$\langle \cos^2\theta_n \rangle_{av} = \frac{1}{N_0} \int_{\alpha=0}^{\pi/2} N(\alpha') \cos^2\alpha' \sin\alpha' \, d\alpha' \qquad (124)$$

where $N(\alpha') \sin\alpha' \, d\alpha'$ is the number of lamellae per cm^3 making angles between α' and $\alpha' + d\alpha'$ in the deformed state and N_0 is the total number of lamellae per cm^3. $N(\alpha')$ is given by the affine model as

$$N(\alpha') = \frac{(N_0/2)\ (\lambda_x/\lambda_y)^2}{[\cos^2\alpha' + (\lambda_x/\lambda_y)^2 \sin^2\alpha']^{3/2}} \qquad (125)$$

where λ_x and λ_y are the elongation ratios in the stretching and transverse directions. Finally, the constant volume approximation is made where $\lambda_y = \lambda_z = \lambda_x^{-1/2}$ which appears to be a good assumption (see Reference 7).

We observe that the two polyethylenes follow the affine prediction over their entire deformation ranges (up to $\lambda_s = 1.5$ for LDPE, Q and $\lambda_s = 1.87$ for LDPE, SC). This is in contrast to the first result showing a deviation in M_1/M_2 at about 40% strain. These results suggest an overall affine transformation of lamellae deformation within spherulites but localized, azimuthally dependent processes which deviate from affineness.

Overall affine transformation is supported by SALS experiments. Figure 17 shows the photographic SALS results of stretching LDPE, SC. The scattering maximum moves to appreciably higher azimuthal angle, μ, predicted in the Theoretical part of this thesis. Use of Equation (93) and location of the scattering maximum by eye in all four quadrants and averaging the results leads to the results shown in Figure 18. One can see that the overall spherulite (λ_3) versus sample (λ_s) extension for

LDPE, SC follows the affine prediction to at least 50% strain. Higher strains could not be accurately measured due to difficulties in locating the scattering maximum by observation. Use of a two-dimensional optical multichannel analyzer with proper signal display and data handling would be most beneficial for extension to higher strain ratios. Also, the accuracy of the experiment would probably be enhanced. However, Pakula and Kryszewski (29) applied a special rotating sector method to analyze SALS patterns from deformed low and high density polyethylene to $\lambda_s = 2.0$. In a plot similar to that of Figure 18 (Reference 29, Figure 5), they showed an essentially one-to-one correspondence with macroscopic and microscopic dimensional variations for the LDPE. A lower slope was seen for the HDPE with greater curvature at the higher elongations.

The iso-intensity SAXS contour plots for the HDPE, SC sample are given in Figure 19a,b. The sample was only measured at 0 and 25% strain due to lack of beam time at the ORNL facility. $M_1/M_2 = 1.04$ at $\lambda_s = 1.25$. Also, the orientation function, f_ℓ, could not be accurately determined by the graphical method due to the lack of sufficient anisotropy in the scattering pattern. These observations along with the SALS results for HDPE of Pakula and Kryszewski (29) can be accounted for by the rather low compliance of the material. More will be said concerning this point as we proceed.

For undeformed polyethylene the b crystal axis is aligned along the radius (7) and the c axis (chain axis) is perpendicular and randomly

oriented about the radius. If this were to remain so during deformation, then we should expect that the b axis orientation function, defined by

$$f_b = \frac{3\langle\cos^2\theta\rangle_b - 1}{2}$$

where θ_b is the angle between the b crystal axis and the stretching direction, should be equal to the lamellar oreintation function, f_ℓ. Comparison of Figure 15 and, e.g. Figure 4 of Reference 105, shows that this is not the case. In fact, while f_ℓ is always positive with strain, f_b becomes negative on stretching (105,106). This requires that the crystal axes rotate with respect to the spherulite radius. Various models for such rotation have been proprosed which involve lamellae twisting, chain tilting with respect to the lamellae, unfolding of folded chain crystals, etc. These processes are described by phenomenological theories (15,16,25,206-109) and are believed to occur to varying extents in different regions of the spherulites. For example, lamellar twisting would not be expected in the meridian region since the stress is parallel to the lamellae there, whereas chain tilting would be most prevalent since the chains are initially perpendicular to the stress. The relative changes of the orientation functions of the crystal axes depend upon contributions of these processes. For example, lamellar twisting about its b axis produces no change in f_b but will affect f_a and f_c, while chain

tilting will affect f_b. Consequently, the parameters of the orientation theories may be fitted to the observed changes in the orientation functions. Changes in lamellar orientation and interlamellar spacing will depend upon these parameters.

Figure 16 also includes the variation of f_ℓ with elongation ratio considering the correction derived in Appendix IIB for the effects of lamellar twisting. As mentioned there, since evidence exists for the fact that lamellae detwist when initially oriented perpendicular to the strain, while those parallel remain relatively unaffected, a correction factor, $F(\psi)$, must be included to compensate for the increased scattered intensity from the spherulite equator. Therefore, using Equation (A-14), $\langle\cos^2\alpha\rangle$ may be determined by

$$\langle\cos^2\alpha\rangle = \frac{\int_0^\pi [I(\psi)/F(\psi)] \cos^2\psi \sin\psi \, d\psi}{\int_0^\pi [I(\psi)/F(\psi)] \sin\psi \, d\psi} \qquad (126)$$

where all the terms have been previously defined. Equation (126) is substituted into (121) to yield the final orientation function. When $\eta = 0$ in Equation (A-14), $F(\psi) = 1$ and the affine case is apparent. f_ℓ is plotted with values of $\eta = 0.5$, 1.0, and 1.5. Yoon (106) determined from WAXD studies that $\eta = 1.2$ best described his data. We can see from Figure 16 that the experimental points favor the case of random twisting rather than

preferred twisting. However, due to the conclusive evidence for the variation of lamellar twist changes with strain and initial angular positions within the spherulite (106), other factors must be occurring which are uniquely observed by SAXS. For example, we know that WAXD is sensitive mainly to variations in orientation of the crystalline unit cell. SAXS, on the other hand, reflects the average lamellar/inter-lamellar habits. It is also to be noted that the calculation embodied in Equations (123-125) is equivalent to that of the Kratky floating rod model (165). Here, the crystals orient in the same way as the amorphous displacement vectors. However, their internal dimensions cannot vary. The model has, therefore, been described as a "pseudo-affine" deformation.

In light of the above considerations, the effects of lamellar twisting which produce the larger f_ℓ values at a given strain in Figure 16 are probably compensated for by effects such as lamellar bending or buckling and interleaving at the equator or c-axis orientation tending to orient the b-axis perpendicular to the strain near the poles. These mechanisms would tend to distribute the scattering over reciprocal space which would have the effect of decreasing the calculated f_ℓ.

It has been suggested that even at small deformations (10-20%) lamellar bending may occur (110). Peterlin (111-114), Hosemann (115) and Yeh (116) have proposed that at high strains lamellae dissociate into mosaic blocks which reassemble to form new fibrillar lamellae in the highly drawn state. These combined effects, then, tend to randomize

the lamellar orientation relative to that expected from the affine or pseudo-affine cases and explain the discrepancies noted above. Also, the decrease in intensities from the equatorial parts of the spherulite could be due to a decrease in the difference between electron densities of lamellar and interlamellar layers in these regions. If this is indeed the case, which can only be speculative at this point, then it would also tend to decrease the value of f_ℓ. Additional evidence will be presented for the validity of the mechanisms suggested.

2. Qualitative Investigation of Intensity Data.

Figure 20 shows the effects of background subtraction and "Lorentz" correction on the intensity curve for the LDPE, SC unstretched sample. This data was obtained from an azimuthal slice (four channels wide, normalized to one) of the contour plot similar to that of Figure 12a but of uncorrected data using routine CIRAV (see Experimental part, page 176). One notes the strong influence of the background on the very low angle regions. The "Lorentz" correction produces a dramatically different curve and shifts the peak position to a higher angle. These effects are well known (64,117). Since the data of this curve is not corrected for sensitivity of the detector elements, it is used here only for illustrative purposes.

Figure 21a,b shows the fully corrected scattering profiles of lamellae perpendicular and parallel to the stretch direction, respectively,

and at various strains for LDPE, SC. Figure 22a,b shows similar curves for LDPE, Q, while Figure 23 gives the curves for the HDPE. Some similar trends are observed for each of the curves. First, for lamellae oriented perpendicular to the strain we see a gradually decreasing intensity and shift of the maximum to lower angles with increasing strain. The latter effect is indicative of an increasing long spacing, while the former reflects a decrease in crystallinity or difference in electron density between the two phases. The intensity decrease may also be due to a decrease in the overall number of scattering centers within the scattering volume, or the fracture and disorientation of lamellar planes with respect to each other causing scattering at azimuthal angles other than zero degrees. Finally, lamellar detwisting predicted for this region would increase the intensity as described in Appendix II. Since this increase is not observed, the process may be minimal or there may be compensating effects such as those described above. These various possibilities will be explored.

One also notes the simultaneous increase in intensity and in the position of the scattering maximum with strain for lamellae parallel to the strain. Again, similar reasoning as above would suggest that an increase in the number of scattering centers could account for the intesity effects while a decreasing long spacing would account for the shift in the maximum. Since the two LDPE samples exhibit an initial crystallinity, ϕ_c, of about 0.5, then, according to Equation (42), any increase

or decrease would reflect in a decrease in intensity assuming $(\rho_1 - \rho_2)^2$ remained constant. Thus, the apparent increase in intensity for lamellae parallel to the strain direction must be due to some other effects. Since it is unlikely that during compression of the lamellae with simultaneous stretching a large variation in $(\rho_1 - \rho_2)^2$ should occur, this effect must be due primarily to an increase in the number of scattering centers parallel to the strain within a given volume.

As mentioned previously, the Yoon theory (106) of spherulite deformation predicts a lamellar detwisting in the equatorial region of the spherulite with strain. Presumably this would increase the number of lamellae which are oriented in such a manner as to constructively scatter x-rays. This alone would predict an increase in the observed intensity for lamellae perpendicular to the strain. The effect is not seen and suggests the complicated nature of the deformation processes. These processes alluded to earlier will be elucidated as we proceed.

Qualitatively the shapes of the scattering curves for the quenched and slowly cooled (annealed) samples are similar; the quenched sample having a slightly smaller long period. However, comparison with HDPE shows the dramatic variations of larger long period and narrower intensity distributions, i.e. the width at half height is much less for the HDPE. Also, the appearance of the second order maximum in HDPE is apparent. These qualitative differences have also been thoroughly discussed in the literature (see, e.g., Reference 59).

A plot of the reduced long spacing, d/d_0, versus strain ratio, $\lambda_s = L/L_0$, where d is the long spacing of the deformed structure either in the parallel or perpendicular orientations, and d_0 is that of the undeformed sample calculated by simple application of Bragg's law is given in Figure 24. $d_0 = 143\text{Å}$ for LDPE, SC, for example, while $d_0 = 271\text{Å}$ for HDPE. The plot also contains the predicted response according to the affine assumption utilizing constant volume deformation. We see that the affine prediction is not followed for lamellae perpendicular to the strain but is followed for those parallel. The quenched LDPE exhibits marked deviation although the shape of the response is similar to the affine prediction. The leveling off for lamellae parallel to strain at $\lambda_s = 1.4$ is intriguing because of the similarity in Figure 15. Due to the limited applicability of Bragg's law to SAXS data, mechanistic judgments will not be advanced on the basis of this figure. A similar plot will be presented after application of the SAXS model calculations.

The intensity versus scattering angle at various azimuthal angles for LDPE, SC at 30% strain is shown in Figure 25. One notes a rather constant intensity maximum but a shift to lower scattering angles in going from the cases of lamellae parallel and perpendicular to the strain direction. Multiplication of the intensities by $(2\theta)^2$ shifts the curves as in Figure 20 and also decreases the intensities for lamellae more perpendicular to the strain while increasing those more parallel. This effects is shown in Figure 26.

3. Comparisons from Point-Like and Slit Geometries.

It is appropriate at this point to compare the SAXS curves obtained for deformed and undeformed samples from the pinhole and slit geometries. In the Labarbe (20) study the data was gathered as mentioned in the Introduction and the assumption made as to the approximate spherical symmetry of the interference patterns from stretched samples. Data was, therefore, desmeared according to the Schmidt (39,40) procedure. In an attempt to justify this assumption, slits of decreasing height were used along with their appropriate weighting factors, as given in Table 6 and the Experimental part, and the results of peak position extrapolated to zero slit height, presumably yielding results free from slit height effects. Thus, appropriate correction factors could be utilized for data from finite slit heights.

Background subtracted, Lorentz corrected SAXS curves at various slit heights are given in Figure 27a-d for a 30% stretched LDPE, SC. Curves a to d represent the variations at azimuthal angles of 0, 30, 60 and 90 degrees. Intensities are normalized to a value of 1.0 at the peaks. We see that the peak positions vary slightly in going from 0 to 30 degrees but increase for the two larger azimuthal angles. A plot of the observed Bragg spacing versus slit height at the four azimuthal angles is given in Figure 28. The increase in long spacing with azimuthal angle is apparent and predicted. Also, because of the rather large error bars due to poor precision in locating the peak positions, an exact dependence

could not be specified for the larger azimuthal angles. The dependence for the two smaller angles suggests that measurements taken with the long slits would be accurate. However, more careful observation of the curves in Figure 28 reveals that not only the position of the maxima are difficult to locate but that the shapes of the curves vary. This is especially evident in the high angle regions. Similar curves obtained for the undeformed sample did not show this trend. These high angle regions are especially important in curve fitting procedures and analyses of total integrals. The conclusion reached from this study is that although the peak positions may not be altered by the desmearing procedure, the shape of the scattering certainly is. The peak position is suspect, also due to the lack of precision encountered. Finally, Figure 25d reveals unusually shaped curves at all three slit heights. This has been seen by the author for other cases of desmearing from anisotropic scattering patterns. Reference to Figure 21a shows the decrease in intensity scattered for lamellae perpendicular to the strain. Also, since the curves are very broad in these regions, slight fluctuations in the smoothed data will result in spurious peaks and bumps in the final desmeared data. The need for comparisons of the desmeared data from stretched samples and that from point-like geometry is apparent.

Figure 29 shows a plot of "Lorentz" corrected intensity versus scattering angle for an unstretched LDPE, SC sample obtained by the long slit geometry Rigaku-Denki spectrometer (desmeared) and a plot from the ORNL-10 Meter spectrometer (point-like geometry). The areas of the two

curves have been normalized. It is evident that the peak positions are coincident within experimental error. However, the desmeared (slit) curve is narrower than the point geometry curve suggesting either a broadening due to finite pinhole sizes or an overcorrection in the desmearing operation. Schelten and Hendricks (96) observed a similar situation in studies of Lupolen using the one-dimensional pinhole geometry spectrometer located at ORNL. They found that the effect was due primarily to an overcorrection of the desmearing procedure, showing that pinhole smearing was negligible by calculation of the collimation errors due to both the width and height of the square pinholes used. However, no rationalization was given for the overcorrection due to desmearing. The problem may lie in the calculation of the proper weighting function. Since point-like geometry facilities now exist and are readily available (one dimensional systems can be built for about $15,000), the proper weighting function could be determined by curve fitting the data from both systems or eliminating the slit system entirely.

Plots of corrected SAXS intensities versus scattering angle from slit desmeared and point-like geometries at azimuthal angles of 0^{o} and 90^{o} for a sample stretched 60% are given in Figure 30a,b. It can be readily seen that the peaks are shifted to higher angles for data from the slit systems and that the overall shapes are completely different at each azimuthal angle. Again we observe the odd shaped (double peak) curve from desmeared data at $\mu = 90^{o}$. Although this effect was not reported in

the Labarbe (20) work, re-examination of the original data revealed its presence. However, because of the nature of the Tsvankin analysis (see Chapter 2, Section D), it could be ignored. A smooth, average curve was used in its place.

We have verified experimentally, therefore, that desmearing of anisotropic scattering patterns leads to erroneous results. In the remainder of this work only anisotropic scattering patterns obtained from the ORNL facility will be analyzed.

4. SAXS Curve Analyses.

Analyses of the SAXS curves of stretched low and high density polyethylenes obtained with the ORNL-10 Meter spectrometer by the Tsvankin/Buchanan (Chapter 2, Section D) model are given in Tables 8 and 9 for LDPE, SC and HDPE, respectively. This data is to be compared with that obtained by Labarbe, et al. (extracted from Reference 20), in Table 10 for LDPE, SC. Both sets of data were obtained with reference to the calibration plots of Figure 11 where the $\beta/\alpha = 0.2$ and $\varepsilon = 0.2$. Comparison of Tables 8 and 10 shows that the initial long periods from the slit data are approximately equivalent and the crystallinities consistently higher than the ORNL data. Also, ϕ_c, remains relatively constant with strain in both sets of data confirming Labarbe's observation in this regard. However, the large increase in d with strain observed by Labarbe is not seen as dramatically in this work. This is probably due to the effects of desmearing the anisotropic data.

Studies of Warner, et al. (55), and Stein, et al. (118), have shown that Tsvankin analysis may lead to erroneous results. Specifically, when the parameters are used to regenerate scattering curves, poor correspondence results, suggesting an inadequacy in the method. Crist (47) has observed that the derivation of Tsvankin's final intensity expression [Equations (36) and (37)] is incorrect. In Equation (34), where the double sum within the second term accounts fully for the lattice statistics which cannot be affected by fluctuations in particle sizes, Tsvankin includes the distribution of particle sizes and performs the sums. This is in violation of the basic assumptions made in deriving Equation (34) and resulting in counting the distribution of lamellae sizes twice (once in the structure factor, F). The effect of this error is small if the distribution of crystal or long period sizes is small. However, we will see later that these distributions are in fact rather broad. Kortleve and Vonk (59), Strobl and Muller (119) Brown, et al. (64) and Wenig (53), as well as Crist, have reported broad thickness distributions for LDPE.

Studies of Warner, et al. (55), and Stein, et al. (118), also revealed some interesting observations regarding the usefulness of the Tsvankin/Buchanan and Vonk correlation function approaches for systems showing long range correlations (periodicities in the SAXS range) over only a few scattering entities. In the latter study SAXS of blends of isotactic polystyrene/atactic polystyrene, polystyrene/polyphenylene oxide, and polyvinyl

chloride/polycaprolactone along with polyethylene (Figures 31 and 32) were analyzed using the methods of Vonk, Tsvankin/Buchanan, and Hosemann. After correcting the original SAXS profiles for liquid and foreign particle scattering the curves were desmeared then "Lorentz" corrected and analyzed with the three models. Tsvankin/Buchanan parameters yielded calculated curves which did not agree well with the experimental ones. The Vonk correlation function, however, gave reliable fits in cases where a corresponding Hosemann analysis yielded a high value of N, the average number of parallel layers of alternating electron densities (see Appendix I). At lower values of N, the Hosemann model gave reasonable crystalline and amorphous thickness distributions, crystallinities, and transition zone thicknesses. Thus, it was concluded that for the systems investigated, the Hosemann analysis, with its additional parameter N, was the most versatile and yielded results consistent with other experimental techniques, namely thermal and WAXD methods.

Figure 31 shows the fit obtained by comparing the experimentally-obtained SAXS from ORNL for LDPE, unstretched and that calculated by using the Tsvankin/Buchanan parameters to generate the corresponding curves. The two are normalized at the peak height. Figure 32 gives the corresponding fit obtained for unstretched HDPE. We can see that the correspondences are good at the peak and half-widths at the higher angle. However, for both curves the low angle ends fit very poorly. In HDPE the second peak at about 12 mrad is very poorly reproduced. These plots,

as well as those mentioned in References 55 and 118, verify that Tsvankin/Buchanan analysis should be used only with reservation.

Because of the results presented here and in the Warner and Stein works, it was decided to do the remainder of the analyses in this study using the Hosemann paracrystalline model. However, for completeness, Figure 33, showing the correlation functions (both experimental and theoretical) of unstretched LDPE, SC from the Rigaku-Denki spectrometer is included. One notes the rather deep minimum, shallow maximum and rapid loss of oscillation at about r = 180Å. From the two works mentioned above, this response is typical for polymers showing lamellar structures with low values of N, or crystallinities about 50%. The theoretical curve was calculated using Table 7 for which log-normal distributions of the crystalline and amorphous regions were used. The crystallinity necessary for a good fit between the theoretical and experimental curves was 0.55 while $B_a = 0.05 \pm 0.02$ and $B_c = 0.32 \pm 0.02$. This crystallinity is somewhat large when compared to other techniques used in this study. Also, the crystalline thickness distribution is broad suggesting that for this polymer $c = 73 \pm 23$Å. This is consistent with results of Kortleve and Vonk (59) who also point out the difficulty of uniquely specifying the parameters of the fit for polymers whose crystallinities lie between 35% and 65%.

A plot of the "Lorentz" corrected SAXS intensity versus scattering angle for unstretched LDPE, SC using the ORNL facility is given in

Figure 34 along with the points calculated by the Hosemann analysis [Equation (25)]. The goodness of fit is measured by the parameter, Δ, calculated by

$$\Delta = \sum_{S_{min}}^{S_{max}} \frac{|I(s)_T - I(s)_E|}{I(s)_E}$$

i.e., the sum of the normalized differences between the theoretical, $I(s)_T$, and experimental, $I(s)_E$, intensity values calculated at discrete points. The criterion for an acceptable fit was $\Delta < 0.1$. Typically, Δ values of about 0.05 or 5% deviation were encountered. An 8% deviation is observed in Figure 34. Parameters extracted from this fit along with those for stretched LDPE, SC are given in Tables 11a,b for azimuthal angles of 0^o and 90^o. Table 12 gives those for HDPE, SC also obtained at the ORNL facility. Intensity profiles along with the Hosemann fits for HDPE, λ_s = 1.0, 1.25 at $\psi = 0^o$, 90^o are given in Figures 35a-c. We see that, contrary to the Tsvankin/Buchanan results, linear crystallinities vary dramatically on stretching (Figure 36) while crystal thicknesses remain relatively constant at the azimuthal angles tested. Most of the dimensional changes are reflected in the amorphous regions.

Overall crystallinity decreases of the samples on stretching have been shown to be small by Peiffer, et al. (123). From the SAXS

crystallinities obtained by Tsvankin analysis no overall crystallinity change would be predicted. Because of the variations observed from Hosemann analysis, the overall crystallinity of the spherulite, Φ_c, could be calculated from the linear crystallinities $\phi_c(\psi)$, obtained at azimuthal intervals from an equation such as

$$\Phi_c = 2 \int_0^{\pi/2} \phi_c(\psi) \sin\psi \, d\psi$$

However, linear crystallinities were only obtained at $\psi = 0^o$, 90^o, hence, the above equation could not be fully applied.

A plot of reduced dimensions d/d_o and a/a_o ($c/c_o = 1$ throughout) is given in Figure 37. For the LDPE, SC we see an increase in long spacing roughly following the affine prediction for lamellae perpendicular to the strain up to about $\lambda_s = 1.3$ with a leveling off followed by a subsequent decrease at $\lambda_s = 1.5$ to a value reaching $d/d_o = 1$ at the highest strain. A similar trend is observed for the amorphous components with an abrupt decrease at $\lambda_s = 1.5$ and a final value of $a/a_o = 1$ at the highest strain. This suggests that the lamellae initially separate. With additional strain a deformation process takes over causing the decreases seen. This process (processes) will be explored later. At the meridian, interlamellae material deforms as predicted by the affine model with a decrease in thickness caused by extensional and

compressional forces in this region.

The precision of the SAXS curves generated at the ORNL facility depends on the times used to obtain the plots. For 3000 seconds, the time used for most of the work presented here, the precision is about $\pm$ 7%. Therefore, generation of theoretical plots and their subsequent comparisons need not be any better. However, precision limits are given in Tables 13 and 14 based on the changes observed in repeated calculations such that the deviation, Δ, varies $\pm$ 1%. One can see that variations in g_a and g_c are large but do not change the final fit. Also, the transition width parameter may vary by $\pm$ 10Å without severely affecting the results. Its major influence is on the tails of the curves, being important for total integral work but only secondary for fitting procedures. Crystal and amorphous thicknesses vary by only a few Angstroms and N may deviate by about only $\pm$ 0.1 and is more specific as it decreases. Thus, the major parameters controlling the fits are c, a and N in this work. At higher values of N the thickness distribution parameters, g_a and g_c, become more sensitive as evidenced in Table 14. This work is, however, primarily concerned with the effects of tensile strain on c, a, and N.

A plot of N versus λ_s for LDPE, SC given in Figure 38 reveals a decrease in N for lamellae in the equatorial part of the spherulite while remaining relatively constant for those at the meridian. As discussed in Appendix I, this parameter may qualitatively suggest something of the relative ordering or disordering occurring within the spherulite

with strain. Thus, a decrease in the average parallelness of lamellae occurs for those oriented perpendicular to the strain. Those initially oriented parallel seem to remain unaffected in this regard. Table 12 shows that for HDPE N = 8. This is to be compared with N = 1.6 for LDPE, SC. These results are comparable to those of Wenig (53). Uniaxial strain of 25% decreases this value to N = 5 for those lamellae perpendicular to the strain while increasing to N = 10 for those parallel to it. Again, the lamellae are seen to order or disorder relative to each other when oriented parallel or perpendicular to the strain, respectively.

5. Total Integrals and Swelling.

As mentioned in Chapter 2, Sections E and F, the total integral or "invariant" in SAXS is used to elucidate the nature of the scattering phases within the system. The existence of voids (microvoids according to Peterlin, Reference 114) is also easily detected when combined with solvent swelling methods.

Figure 39 shows the corrected scattering curves for swollen and unswollen LDPE, SC. We see a change in shape of the curve on swelling and a loss of the second order peak. Also the maximum is shifted toward lower angles confirming that the swelling is occurring within the scattering phases. If there was much extra-spherulitic non-crystalline material present and the swelling occurred preferentially in these regions, the shift in maximum would not necessarily be observed.

The swelling solvent, ethylbenzene (EB), was chosen since Bettelheim and Stein (120) showed that the swelling ratio, q_s, at elongations up to 150% did not vary. Also, its electron density was sufficiently different from the amorphous regions so that an appreciable change in intensity could be observed (ρ_s = 0.285 eu/Å^3 versus ρ_a = 0.301 eu/Å^3 where ρ_s and ρ_a are electron densities of the solvent and amorphous phases.) Macroscopic sample swelling q_s was calculated by

$$q_s = \frac{V_p + V_s}{V_s} \tag{127}$$

where V_p and V_s are the volumes of polymer and solvent, respectively. At least ten days of swelling at room temperature was performed before SAXS measurements. Utilizing the relationship between weight, W, and volume, rearranges to

$$q_s = 1 + \frac{W_s/\rho_s'}{W_p/\rho_p'} \tag{128}$$

where W_s and W_p are the weights of the solvent and polymer, respectively, and ρ_s' and ρ_p' are the solvent and polymer densities in gm/cm^3. Primes

indicate mass densities. Thus, the swelling ratio is easily obtained by weighing the swollen polymer in a tared covered weighing bottle, drying the polymer then reweighing. For a LDPE, SC sample studied, S41B, Q = 1.143 $\pm$ 0.005, in agreement with the observations of Bettelheim and Stein. The volume fraction of solvent in the polymer, ϕ_s, used in the equations of Chapter 2, Section F, is easily obtained from these measurements and Equation (129).

$$\phi_s = \frac{V_s}{V_s + V_p} = \frac{1}{1 + \frac{W_p}{W_s}\frac{\rho_s}{\rho_p}} \qquad (129)$$

For S41B, ϕ_s = 0.11. If we now assume that all of the swelling is reflected in an increase of the amorphous thickness (no crystalline swelling or changes in lateral dimensions of lamellae or interlamellae regions), then for a polymer whose initial linear crystallinity is 47% and long period is 136Å the long period should increase to 146Å from $(c + q_s a)$. If, on the other hand, the swelling occurred to the same degree in both phases, i.e. $q_s(c+a)$, then the long period should increase to 155Å. Experimentally we find that d_s = 142Å lending credibility to the first assumption. This assumption can be expressed mathematically by

$$\frac{V_a}{V_a^o} = \frac{a}{a^o} \tag{130}$$

where V_a and V_a^o are the volumes of the amorphous regions in the swollen and unswollen states. Therefore, a more critical test is to determine a and a_o via a model calculation. This was accomplished using the Hosemann scheme and $a/a_o = 82\text{Å}/72\text{Å} = 1.12 \pm 0.02$. We see a very good agreement with q_s suggesting the reliability of Equation (130).

Using the equations of Section F, Chapter 2, the mean squared electron densities were calculated assuming $\rho_c = 0.347$ eu/Å^3 ($\rho_c' = 1.008$ gm/cm^3), $\rho_a = 0.301$ eu/Å^3 ($\rho_a' = 0.87$ gm/cm^3) (see Reference 59), and $\rho_s = 0.285$ eu/Å^3 ($\rho_s' = 0.867$ gm/cm^3). Crystallinities (unswollen) were determined by the gravimetric procedure outlined in Chapter 3, Section C.3, and are given in Table 13 for the polymers studied. Volume fraction crystallinities from density measurements were calculated by the equation,

$$\phi_c = \frac{\rho - \rho_a}{\rho_c - \rho_a}$$

Volume fractions of voids present were assumed and varied as shown in Table 14.

In calculating $\langle \Delta\eta^2 \rangle$ experimentally care was taken to subtract not only the liquid scattering of the polymer (see Section B.3, Chapter 3), but also that due to the excess solvent in the scattering cell of the swollen polymer. For this measurement the teflon gasket used in the sample holder was decreased in thickness by an amount equal to the thickness of the swollen sample. The scattering of the ethylbenzene was then recorded and subtracted from the sample scattering after proper correction for the sample attenuation. Equations (40) (slit-geometry) and (43) to (49) were then used to calculate $\langle \Delta\eta^2 \rangle$. Results are presented in Table 14. The important parameter here is the ratio of electron densities of the swollen to the unswollen cases (s/u). We can see that the ratios predicted in the cases of no voids or a finite transition width (columns 2 and 5) are greater than one, while those predicted for a sample initially containing 2% or 4% voids by volume are less than one. Also, the absolute values of $\langle \Delta\eta^2 \rangle$ for samples containing 2% and 4% voids are 5 to 9 times greater than that predicted for no voids. Experimentally we observe that the absolute values are in the range predicted for samples with no detectable voids. Also, the ratios are near a value of one indicating that these two LDPE samples contain few, if any, voids which are contributing to the observed scattering. If we take the smallest possible ratio considering the experimental error, i.e. s/u = 0.8, a back calculation using Equations (50) and (64) reveals the possibility of about 0.02% voids. This is a rather minor amount. Thus, we see that

voids, of the order of the sizes of the lamellae or much smaller (about 20Å) are not present in any effective amount in the starting material. Any microvoids detected during uniaxial sample stretching would have to arise from the deformation processes themselves.

A similar study was not performed with HDPE because of limited resolution of the Rigaku-Denki spectrometer. However, $\langle \Delta\eta^2 \rangle$ was calculated from the ORNL spectrometer using Equations (107) to (110) given in the Experimental part. Results are given in Table 15 which show a good agreement between the calculated and experimental values. In the determination of the experimental invariant, Porod's law was confirmed by the $s^4 I(s)$ versus s plot shown in Figure 40. Data extrapolated to zero scattering angle was performed according to the procedure set forth in the Experimental chapter. The fact that the calculated and experimental invariants agreed well and, in fact, that the calculated value was slightly higher suggests again that the starting material before stretching was free from voids at least of sizes on the order of the lamellae.

On stretching the sample 25%, the invariant was calculated using Equation (90) assuming Porod's law could be expressed similarly for the curves from deformed samples. From the iso-intensity contours of Figure 18, k = 1.04. We see excellent agreement with the unstretched case indicating the validity of Equation (90) and that void formation, if at all present, is rather slight. No calculated values are given in the

table. In order to obtain this, the entire thickness distribution of crystalline and amorphous phases would have to be known.

Similar calculations could not be performed on the LDPE samples because of the finite size of the area detector, i.e. the low angle portion of the curve where Porod's law is obeyed could not be obtained. In order to obtain this information, the sample to detector distance of the spectrometer would have to be reduced to a lower resolution mode. Curves from each spectrometer geometry would then be superimposed using suitable correction factors.

However, the ORNL spectrometer system has been programmed such that a quantity $\Sigma I(x,y)$ is monitored throughout the experiment [see Equation (134)]. X and Y are the detector coordinates in real space and $\Sigma I(X,Y)$ is the total scattered intensity in counts recorded by the detector. Although this is not the invariant of Equation 132,

$$Q = \int_{Vol} I(\underset{\sim}{x},\underset{\sim}{y},\underset{\sim}{z})\, d\underset{\sim}{x}\, d\underset{\sim}{y}\, d\underset{\sim}{z} \qquad (132)$$

where $\underset{\sim}{x}$, $\underset{\sim}{y}$, $\underset{\sim}{z}$ are reciprocal space vectors and the integration is performed over the entire reciprocal space, it can be used in a qualitative manner to study any gross changes in scattered intensity. A plot of $\Sigma I(X,Y)$ versus strain, corrected for sample transmission and beam

fluctuations is given in Figure 41 and shows a steadily decreasing curve. This effect could be the result of intensity spilling over the edges of the detector but does, however, suggest that void formation of the sizes of the deforming lamellae and interlamellar regions is not an integral part of the deformation mechanism.

For HDPE, SC, the change of $\Sigma I(X,Y)$ with strain varies as the invariant calculated explicitly in Table 15. This suggests the qualitative accuracy of $\Sigma I(X,Y)$.

Finally, the change in density on deforming LDPE (S41) was measured using the gravimetric technique described in Chapter 3, Section C.3. The plot of decreasing density versus λ_s is given in Figure 42. Peiffer, et al. (121), using WAXD also observed a decrease in crystallinity from 46 to 43% at $\lambda_s = 1.5$. The decrease observed here is from 48 to 41%. These are within the 2% experimental error often quoted for WAXD experiments (31, Chapter 3).

From the plot of Figure 42 one can calculate Poisson's ratio, μ_p, indicating any volume changes on stretching. Thus, by definition

$$\mu_p = \frac{1}{2}\left\{1 - \frac{1}{V}\frac{dV}{d\varepsilon}\right\} \tag{133}$$

where V is the specific sample volume and $dV/d\varepsilon$ is its change with

strain, ε. If $dV/dE = 0$, then $\mu = 0.5$ showing no volume change on stretching. Equation (133) is valid for small elastic strains; however, it can be applied to a first approximation. Thus at $\varepsilon = 0.5$, $\mu_p = 0.490$.

A better way to calculate μ_p for these strains is using the Hanke definition of strain where $\varepsilon = \ln (L/L_o)$. Here $\mu_p = 0.492$. These results suggest a slight volume dilatation during strain but for the level of precision of most of the analyses performed in this work the constant volume assumption is adequate. From mechanical studies, Darlington and Saunders (122) concluded that Poisson's ratio for highly drawn polyethylene sheets was approximately 0.5.

Thus, a small overall decrease in crystallinity with stretching is apparent for LDPE. This may describe the slight decrease seen in the $\Sigma I(X,Y)$ values but these effects from SAXS can only be fully realized when the entire scattering curves, including the Porod region, are obtained.

B. Parallel Lamellar Morphology

Special morphology polyethylene samples of parallel lamellar morphology, termed parallel lamellar sheets, were prepared and characterized as described in Chapter 3, Section A. Their geometry is given in Figure 43. In all cases studied, the x-ray beam path is along the X' axis and is to be differentiated from the X axis of the detector.

A unique capability of the ORNL spectrometer can be graphically displayed using these types of samples. Figure 44 shows a three-dimensional perspective plot of a parallel lamellar sheet designated S39. The two point pattern can be clearly seen in the three dimensions of intensity (vertical) and the X and Y axes of the recorder. The large central spikes are unsubtracted parasitic scattering. However, the usefulness of these types of data displays have not yet been fully developed.

Contour plots from two undeformed samples, designated H29 and S39, respectively, are given in Figures 45 and 46a. The machine direction (MD) is horizontal. They both confirm the results expected from photographic SAXS (see Reference 123, Chapter 9). However, H29 exhibits a much narrower overall distribution than S39. Calculation of the orientation of lamellar normals, f_ℓ, using Equation (121) in a manner similar to that for the spherulitic polymers reveals that $f_\ell = 0.89 \pm 0.01$ for H29 and $f_\ell = 0.68 \pm 0.02$ for S39 confirming the more highly ordered state of the former sample. Note that the azimuthal angles used in Equation 122 are measured from the axis through the two maxima, thus describing the orientation lamellar normals. Since the samples were both annealed at $115 \pm 0.5^{o}C$ the variability probably arises from the annealing times which were not carefully monitored.

Sample S39 was subjected to tensile stress along MD. SAXS patterns were recorded at strains of 10, 25 and 40% after which the sample failed catastrophically. Contour plots are given in Figure 46b-d. The variation

of f_ℓ with strain is given in Figure 47. A disordering of the lamellae reflected by the decrease in f_ℓ is apparent, consistent with the qualitative observations of Pope and Keller (85,124).

Sample stretching perpendicular to MD was attempted but the sample failed at less than 5% strain by a delamination parallel to the stretch direction. No SAXS experiments could be performed here.

The sharpness of the intensity versus scattering angle corrected for background and sensitivity for the scattering along the meridian (parallel to MD) in S39 can be readily observed in Figure 48. The position of the peak intensity decreases to smaller angles with strain indicating a deformation of the lamellar/interlamellar regions. The long spacing from Bragg's law for the undeformed material is 188Å. This is to be compared to 116Å for a quenched LDPE, S42Q, prior to stretching, rolling, and annealing indicating a thickening process in either of the two phases or both.

Results of the application of the Hosemann paracrystalline model are given in Table 16. In the unstretched state the initial crystallinity is similar to that of the starting material. $\phi_c = 0.42$ compared to $\phi_c = 0.41$ for S42Q from DSC. The crystal thickness remains constant during strain while the amorphous and transition zone thicknesses increase. The disorder parameter, N, decreases from a value of 2.5 at $\lambda_s = 1.0$ to 1.7 at $\lambda_s = 1.4$ while the distribution width parameters g_a and g_c remain constant within experimental error. As for the spherulitic

samples, N varies as f_ℓ with strain.

A plot of microscopic strain ratio $(d/d_o)_h$ and a/a_o, versus λ_s is given in Figure 49 for S39. The affine prediction is shown by the dashed curve. Within experimental error and up to the maximum strain tested, the deformation is taken up almost solely by the amorphous interlamellar phases according to the affine scheme. Pope and Keller (85,124) also concluded that stretching of these films in a direction perpendicular to the lamellar plane primarily increases the separation between lamellae.

It was also pointed out in References 85 and 124 that the increase in separation of parallel lamellae should lead to a decrease in density of interlamellar matter unless material can move in sidewards into the interlamellar space to occupy the volume created by the lamellar separation. If such density depletion should occur, say by microvoid formation, then this should lead to an appreciable increase in the total intensity of scattered x-rays. This was studied as with the LDPE samples using the total scattered intensity recorded by the area detector, $\Sigma I(X,Y)$. Values as a function of strain, corrected for sample transmission, T, detector, sensitivity, and main beam fluctuations, BM, are given below. SM is the sample monitor which records the total scattered intensity.

λ_s	BM	SM	T	$\Sigma I(X,Y)$ $\times 10^{-5}$
1.0	107044	419707	0.791	5.306
1.1	107125	444686	0.805	5.520
1.25	107734	434588	0.827	5.221
1.4	107214	394465	0.829	4.751

where

$$\Sigma I(X,Y) = \frac{(BM)_{\lambda_s=1.0}}{(BM)_{\lambda_s} T} \qquad (134)$$

It is seen that the relative value of $\Sigma I(X,Y)$ decreased by about 11% at 40% strain. Pope and Keller reported little change in intensity with stretching in agreement with this result. The slight decrease could be accounted for by the decrease in linear crystallinity. This alone would contribute a 9% drop in the total scattered intensity considering the two phase model. Incorporation of the variation in the transition width, although in this case overcorrecting could account for the rest of the difference.

Returning to the point of microvoids, it is inconceivable from this data to account for their presence because of the stretching process. Interlamellar density is preserved on deformation.

It is interesting that the sample failed just after 40% strain. Obviously, void formation had to occur about certain stress concentrations prior to failure. This observation needs to be studied further but it will be shown to be consistent with the mechanism of deformation put forth in the next section.

C. On the Deformation Mechanisms

1. Parallel Lamellar Sheets.

The major findings of this report for the parallel lamellar sheets uniaxially deformed perpendicular to the lamellar planes were:

1. a constant crystal lamellar thickness and a steadily increasing interlamellar thickness up to 40% strain,
2. a slight decreasing total scattering intensity,
3. a disordering of lamellar planes with respect to each other, and
4. failure between 40-50% strain.

WAXD and SAXS studies in this laboratory (123) have shown that at the annealing temperature of 115^{o}C used here, the lamellae have rotated to a position where they are perpendicular to the original draw direction. Here the shear stress for an interlamellar slip mechanism becomes zero. The chain axes (c-axes) have rotated via an intralamellar slip mechanism to give a final lamellar/chain axis picture given in Figure 11 of Reference 123, Chapter 9. For the sake of clarity, the lamellar normals

are measured by an angle ϕ to the machine direction while the chain axes are measured by the angle θ. We have seen in the previous section that in fact there is a rather broad distribution of lamellar normals about $\phi = 0^{o}$.

In the deformation work of Pope and Keller (124) no direct separation of crystalline and amorphous contributions to the long period was made. Rather, the long spacing was expressed by the formula

$$d = \ell \cos(\theta + \phi) + a \qquad (135)$$

where ℓ is the length of the chain in the crystal and the other symbols are as previously defined. The sum of $\theta + \phi$ is chain obliquity relative to the machine direction and can be determined from WAXD and SAXS experiments. Combining the results of Table 18 and Figure 10 of Reference 123, Chapter 9, into the above equation yields a crystal chain length of 112$\mathring{A}$ ($\phi = 0^{o}$, $\theta = 50^{o}$). If the strains are expressed by ε, then accordingly the existence of lamellar separation is identified in extension by the fact that $\varepsilon(d) > \varepsilon[\cos(\theta + \phi)]$; i.e. the strain reflected by the long spacing is greater than that seen by the crystal. The results of Table 16 directly obtained via the Hosemann model calculation

do indeed suggest the lamellar separation mechanism in agreement with the Pope and Keller findings.

It must be pointed out that the authors applied Bragg's law at the "center of gravity" of the scattering curves to calculate $\varepsilon(d)$. We have seen that application of the Hosemann paracrystalline model decreases the apparent d especially if the curves are broad. In calculating the strain in lamellar periodicity versus sample strain, they obtain a positive deviation from the affine prediction noted in Figure 49. We feel that our observations are quantitatively more accurate due to the application of the more sophisticated scatttering model.

Regarding the question of an increase in volume change on stretching these particular samples, the authors found a very slight increase (possibly too high due to preceding arguments) from their strain measurements. It was much less than that expected from the total strain of the sample. They proposed three types of explanations for this effect. Either (1) the samples are not completely filled with the lamellae which give rise to the scattering patterns, (2) lamellar separation involves a process leading to no increase in volume such as pulling chains through the lattice or (3) the interlamellar material somehow contracts laterally and microvoids formed at the edges of lamellae are filled either by extralamellar material or by the edges of other lamellae.

After various arguments including swelling studies by the authors and by Point, et al. (125) who showed that the maximum degree of swelling occurs in a direction parallel to the lamellar planes, it was concluded that explanation 3 was the most consistent with the experimental findings. We too agree with this mechanism.

A general mechanism consistent with these results and which will hold for the spherulitic lamellae similarly oriented is shown graphically in Figure 50. It is assumed that area, L x W in the y, z plane, is conserved on stretching while the third orthogonal dimension, x, is unaffected. Experimentally, the deformation up to about 40% strain is governed by the empirical equation

$$d = \lambda_s a_o + c$$

where the symbols have retained their prior meanings. Also

$$L \times W = nd \times W$$

where the total length of the stack L is nd and n is the number of lamellae. In Figure 50, n = 4. W is the width of the stack which, for purposes of illustration, is set equal to the probably unrealistically low value of W = L. Also, d_o = L/4 and c = a_o = d_o/2. Thus, the initial crystallinity of the stack is 50%. It is important to emphasize here that this illustration is meant only to justify the long period and total intensity results. It implies nothing directly of lamellar twisting, or lamellar deformation, only that the lamellae (b-axis as shown) are discontinuous along the spherulite radius and interleave upon stretching perpendicular to their b axes. Thus, we can see an increase in the long spacing between adjacent lamellae while material is moved sidewards to conserve the total electron density and therefore a constant SAXS invariant. Actually, the slight decrease seen may be related to an increase in the amorphous electron density due to the fact that crystals rather than other amorphous material are moving in between adjacent lamellae. At some point enough of the crystalline lamellae have interleaved to begin decreasing the apparent long period and the amorphous interlamellar width as seen in Figure 37. The point at which this phenomenon is observed is obviously dependent upon the initial thickness parameters and their distributions and upon the initial crystallinity of the sample. In the geometry of Figure 50, it can be estimated that this point occurs at λ_s = 1.7 since here the crystals overlap each other by half their lengths. Since the long period is averaged over the entire width of the central portion, it will tend to offset the increase

still apparent at the edges. If the lamellae were continuous along W and maintained their integrity during stretching, then the increase in long spacing would be continuous with strain and the scattering intensity would increase due to depletion of material in the interlamellar zones. We can see that this is the case at $\lambda_s = 1.0$ with further stretching.

In Chapter 4, Section B, a lamellar orientation function, f_ℓ, was calculated versus strain. It was assumed that the meridional spread in azimuthal intensity was caused by the disorientation of lamellae due to inhomogeneous strain fields. We must, however, examine more critically the observations and possible mechanisms which could produce them. The important parameters and observations are given in Table 17 along with predictions for three possible cases which could arise due to stretching. They are (1) fewer lamellae are present in scattering volume, (2) lamellae fracture but remain parallel to each other, and (3) lamellae disorient with respect to each other; a prior fracture may or may not be involved. We can see that the results (observations) can best be justified on the basis of the disorientation of lamellae. The reader is referred to the proper references footnoted which explain the parameters and their behavior.

The large increase in the transition width parameter, E, with strain seen in Table 16 cannot be readily explained on a molecular level since it is inconceivable that a 40% strain should produce a six-fold increase

in E. It has been shown in Appendix II, Parts A and B, that the unique separation of effects due to transition width and lamellar twisting is difficult. Since we do not have the capability at the ORNL facility as yet to calculate the true scattering invariant from these two point diagrams, we can calculate an approximate value from the four channels centered about the meridian and normalize to one channel invoking Equation (90) where the front factor becomes 2π, and Equations (107)-(110). It is not meant to be an invariant reflecting the nature of the system as a whole since there are intensity components which have not been properly considered; however, it does reflect the nature of the lamellae scattering into the meridian. The normalized results versus strain ratio are given in Table 18. The correction factor, $F(\psi)$, where $\psi = 90^{o}$ in this case, is calculated according to Equation (A-14). Since lamellae are initially detwisted, the possibility exists that upon deformation a twisting occurs due to inhomogeneous deformation of the amorphous regions at the molecular level. This conclusion was in fact reached by Ladizesky and Ward (126) in mechanical studies of parallel lamellar sheets. Therefore, the experimental relative intensity must be multiplied by F(90) as done in Table 18. We see that the correspondences are quite good suggesting that lamellar twisting may be indeed occurring during the deformation. Since stress will be relieved by this process, the mechanism of intralamellar c-axis slip or shear will be reduced. This has been found to be the case in Pope and Keller's work (124).

Several authors (12,43,124-129) have pointed out that the c-axis rotates toward the stretch direction in not only the parallel lamellae

sheets but in most semicrystalline polymers. This seems to be the case for the sample studied here also (Reference 123). The data, therefore, suggests that as the chain axes align the lamellae disorder, twist about the b-axis, and interleave to conserve overall volume while the amorphous interlayer material increases in thickness with the macroscopic strain.

Finally, the mechanical failure of the sample between 40% and 50% strain is probably due to the anisotropic nature of the system combined with built-up stress concentrations. Since the tie molecules transmit stress between lamellae, near the point of failure they must be fully extended. Further tensile strain probably produces failure in both the crystalline (mosaic blocks produced) and amorphous phases causing the final rupture of the sample. The more isotropic mechanical nature of the spherulite allows the transmission of stress by various relaxation mechanisms delaying the rupture of the sample and even allowing a new morphology to come into existence through yielding. No macroscopic yielding is observed in the parallel lamellar sheets deformed perpendicular to the lamellar planes.

Also, failure at 40% strain is consistent with the theoretically based predictions of Petraccone, et al. (130). This study will be described in greater detail in the next section.

2. Spherulitic Morphology.

The major findings of this work concerning the tensile deformation of spherulitic texture polyethylenes up to about 90% strain for

LDPE and 25% strain for HDPE are:

1. lamellae thicknesses remain constant despite their initial angular positions within the spherulites,
2. amorphous thickness changes can be predicted by the affine model up to 40% strain for lamellae perpendicular to strain and 90% for those parallel in LDPE. HDPE showed affineness up to 25% strain,
3. lamellae orient toward the stretch direction according to the affine prediction,
4. significant decreases in d/d_o and a/a_o are observed for LDPE at strains greater than 40%, and
5. the total scattered intensity remains relatively constant with strain.

Since the results in LDPE, SC for lamellae oriented perpendicular to strains are completely analogous to those of the parallel lamellar sheets up to 40% strain, we can envision a similar deformation mechanism as presented in Figure 50.

Kausch (131) has calculated the maximum stress which can be borne by a chain before it pulls through the crystal and has shown that for polyethylene it is less than the breaking strain. Rabinowitz and Brown (132) have shown that intralamellar c-axis chain slip (i.e. pulling through crystal) can occur at very low stresses so that these slip processes are expected to occur during early stages of deformation. Petraccone, et al. (130), developed a theory for amorphous orientation

in spherulite polymers based upon conformation changes in the tie chains, loops, cilia (one end attached) and unattached chains located between crystalline lamellae within a spherulitic superstructure assumed to undergo affine deformation. They found that for tie chains the orientation function, f, is negative at small interlamellar separation, ℓ, but becomes positive and increases at larger ℓ. It increases as the number of bonds between boundaries, N_B, decreases. The calculated responses are shown in Figure 13 of Reference 130. Loops, cilia, and unattached chains are of minor importance for this discussion. The major point here is that f approaches a value of 1 with strains and interlamellar separations similar to those found experimentally in this work. The rate of approach to the value 1 is governed by the lamellar twist parameter, n, the interlamellar thickness, and N_B, the details of which are described in the reference cited. Thus, it is not inconceivable that for the interlamellar spacings reported in this study (Tables 11, 12 16), a large fraction of the amorphous tie chains are fully extended at about 40% strain for LDPE and possibly 25% strain for HDPE. Further extension induces the mechanisms described by Kausch, Rabinowitz, and many other authors (43,112,114,128,133) of c-axis slip through the lamellae. With further stretching a continuous alteration of the lamellae by this mechanism occurs and the lamellae break up into smaller sections (mosaic blocks) while the c axes rotate toward the stretch direction. The result is a zig-zag lamellae pattern perpendicular to the stretch

direction. This type of pattern has been reported from deformation studies of polyoxymethylene (POM) by Geil (134) and qualitative photographic SAXS studies of the deformation of polyethylene by Tsvankin (135). Tsvankin, however, started with strains of 100%. He made no conjecture as to the smallest strains at which this phenomenon could be observed. Figure 51 gives his concept of the buckling mechanism which this author agrees with but with the addition of an interleaving mechanism (Figure 50) before and during the buckling. The similar mechanism of Petraccone, et al. (130), is given in Figure 52. It includes the arrangement of amorphous tie chains.

Finally in this regard, the work of Peterlin (136) on SAXS studies of deformed high density polyethylene at various temperatures suggests a rigid lattice at room temperature in which plastic deformation primarily proceeds in the interlamellar regions, along spherulite boundaries, and along the boundaries of stacks of parallel lamellae, lamellae, and mosaic crystalline blocks. At room temperature he concludes that the lamellae are brittle, show very little chain tilt and slip, and fracture at low values of strain in agreement with the results presented here. Figure 4 of Reference 136 shows that the long period along the meridian initially increases to $\lambda_s = 1.3$ then discontinuously drops to a value below the undeformed long period and remains constant with further strain. This is exactly the effect seen in Figure 37 and, therefore, we are quantifying here the onset of fiber formation, i.e. the transformation of the spherulitic structure into the fiber structure by the process of micronecking by

which every ribbon-like lamella of the original structure is fractured into smaller folded chain blocks and the blocks incorporated into the microfibrils with very nearly complete chain orientation. It should be emphasized that at this point in the deformation, macroscopic yielding is not visually evident! For the HDPE, SAXS results suggest that this transformation point has not yet been reached at 25% strain.

Studies very similar in nature to Peterlin's were performed by Kakudo and Kasai (33, p. 412; 137,138). They reported extensive WAXD and SAXS results for polyethylene drawn at room temperature. At low elongations elliptical SAXS patterns were presented very similar in shape to those in this report. No elliptical patterns were seen by Peterlin even at elongations as low as 10% for samples stretched at 120^{o}C but a four point pattern, typical of the final fiber structure, evolved immediately. The differences are obviously due to the drawing temperature. At 120^{o}C the sample is at a temperature far above that necessary to impart various loss mechanisms. Specifically, the α loss peaks, occurring at about 70^{o}C, have been associated with inter- and intracrystalline processes (i, p. 181; 139,140). Specifically, the lower temperature α_1 process involves a slipping of crystalline lamellae or their mosaic blocks past each other while the α_2 process involves rotation and translation of chains within crystals. Hence, at the higher drawing temperatures the spherulitic structures can more easily transform into the fiber morphologies.

Peterlin concludes that a lamellae thinning process occurs for those lamellae oriented parallel to the strain due to chain tilt. Within the accuracy of the experiments included in this report, no such thinning is observed for LDPE. Using the equation developed by Yoon (106) to describe the chain tilting process [Equation (3) of Reference 106], one can calculate the decrease in crystal thickness due to chain tilt. Since the initial crystal thickness, c_o, varies as $\sin\beta$ where β is the angle which the chains make with the spherulite radius (lamella plane) one can assume that the chain lengths remain constant within the crystal and calculate

$$\frac{c}{c_o} = \frac{\sin\beta}{\sin\beta_o}$$

If we also assume that the chains are aligned perpendicular to the radius along the polar axis then we can assume various values of the compliance parameter, K, and determine the expected decrease in the crystal thickness, c, with strain. For an elongation of 20%, assuming K = 1.2, the value determined by Yoon, the crystal thickness would be expected to decrease by about 30%. However, if K = 0.5, then the expected decrease is only 7%, well within the experimental error. Therefore, the ease of c axis tilt from SAXS disagrees with that

found by Yoon by a factor of about 2 suggesting that this process does not contribute as much as expected to the overall deformation process at least for strains up to 20%. At the higher strains studied, calculations similar to those above indicate the necessity for even lower values of K. This suggests that at these strains other mechanisms may predominate. Possibly inter- and intralamellar shear processes predominate in which lamellae slide past each other and crack at disordered regions such that the mosaic blocks enter into the microfibrillar structure in a similar manner as for those lamellae perpendicular to the strain. Others (124) have shown that the chain tilt mechanism cannot fully account for the increase in spherulite dimension along the pole during strain. More will be said concerning these mechanisms shortly.

A model for deformation of spherulites in terms of lamellae parallel to strain is embodied in Figures 51, 52 and 53. In Figure 53, the strain is along y and the dimensional changes are assumed to be taken up by the amorphous chains solely. Assuming the lamellar blocks cannot move from the imaginary edges confining the stack, a large area develops between separating but compressing lamellae. This would produce an increase in the scattered intensity. Concurrently, according to the dimensions involved in the figure, the adjacent lamellae would impinge on each other at $\lambda_s = 1.5$ according to the equation

$$d = a_o/\lambda_s + c \qquad (136)$$

assuming conservation of area ($\lambda_s\lambda_z = 1$). Since the intensity is not seen to increase dramatically (some increase is observed) the lamellae must be free to slide past each other while amorphous regions compress and elongate. Lamellae may crack along the c-axes as the chains rotate toward the strain direction thereby shortening along the lamellar axes and interleaving to a greater extent.

The slight intensity increase seen must be due, in part, to an increase in the number of lamellae scattering coherently in a given scattering volume due either to compression or to increased parallelness of lamellae with respect to each other. The relatively constant N in LDPE (Table 13a) suggests a similar average parallelness with strain while the increase seen for HDPE suggests greater alignment.

It is known that at low elongations (10-20%) crystal axis rotation occurs by twinning along the (110) diagonal (17,43,114,125,133) and phase transformation (43,125) from the orthorhombic to the monoclinic crystalline form. The relative contributions of these processes depend upon the orientation of the lamellae with respect to strain. Deformation experiments on solution grown linear polyethylene single crystals (114) showed that for draw directions parallel to the b axis or the (110) plane the phase transformation was dominant while drawing parallel to the a-axis resulted principally in twinning. Neither of these mechanisms could fully account for the total applied strain. c-axis slip and chain tilting were invoked, also. Both the twinning and martensitic (stress

induced) transformations in PE have been carefully studied and cataloged using WAXD (141-143). However, this study has dealt mainly with the macroscopic lamellar deformations and since twinning and phase transformations produce small changes in the overall thickness of lamellae, nothing definite can be inferred about these processes.

Direct observation of high density polyethylene spherulites by scanning electron microscopy (SEM) by the group at Maryland (144) has shown that the melt pressed samples exhibited deformation behavior very similar to that proposed here. The increase parallel to the strain axis in the spherulite was equivalent to the macroscopic strain and resulted in an increased separation of the twist bands. Perpendicular to the strain, a decrease in the twist period was observed. A shortening mechanism comprised of either buckling of the lamella or chain slip along the c-axis was proposed!

A valid concern in all of these SAXS experiments is that we are treating the real three dimensional system as a two dimensional cross-section.* Hence, twisting lamellae radiating from the spherulite center parallel to the incident x-ray beam are completely not accounted for in the model but in fact contribute to the overall scattering detected.

*Personal discussions with Dr. F. Khoury, National Bureau of Standards.

This problem is graphically demonstrated in Figure 54. A lamella whose axis is perfectly parallel to the incident beam will always scatter x-rays in contrast to one which is at right angles to it (see Appendix B). Also, due to the different deformation mechanisms lamellae may scatter into the same volume of reciprocal space due to their orientation but may have been subjected to different deformation mechanisms. Therefore, we must keep in mind the limitations of these interpretations and the fact that they reflect average properties. However, because of the internal consistency of the results and the support of the numerous investigations yielding or implying similar results, the concern, although real, may in fact by unfounded. Also, the task of composing a model taking into account all the possible orientations would be massive, expensive, and probably unnecessary in the long run.

3. Relationship to Mechanical Observations.

The deformation of spherulites in polyethylene has been studied by Wang (27) from a mechanical viewpoint based on linear elasticity and continuim micro-macroanalysis. The model consists of a spherical spherulite with the center of anisotropy at its geometrical center and a large homogeneous matrix with the overall isotropic properties of the bulk polymer. Dimensions of the spherulite boundaries deform as does the matrix, which consists of other spherulites, so as to preserve material continuity, i.e., voids do not form between spherulites. The stresses and strains are calculated from the center to the edge of the spherulites for radial and tangential elements parallel and perpendicular

to the polar axis (strain direction). Figures 1 and 2 of Reference 27b illustrate the responses showing generally the overall non-affine nature of the strains and the large stress concentration at the center of the spherulite. Strain in the stretching direction is much larger at the equator than at the poles. Also the tangential strain ε_θ (0^o) and the radial strain ε_r (90^o) are both negative indicating a compressive mode along the radii at the particular angles measured from the poles.

By assuming that the HDPE spherulite as a whole deforms affinely and from SAXS data of this report (Table 12), the strains necessary to calculate the appropriate stresses according to Equations (9) - (11) of Reference 27b are obtained. Table 19 lists the values. HDPE is considered because the elastic constants of the polyethylene spherulites are given in Table 1 of Reference 27b for the case of HDPE. We can see that the average stresses vary depending on their position within the spherulite. The largest stress magnitude calculated is for those lamellae perpendicular to the stretch direction along the equator of the spherulite. This has been observed by other authors from microscopy studies of strain distributions (10,12). Note that the experimental strain values are averages since the SAXS and SALS experiments lead to average values themselves.

4. Conclusions.

The picture of spherulite deformation which evolves from this study is one which is consistent with some other works in the field. Crystalline lamellae, however, do not vary in thickness dramatically as

had been thought previously but rather dimensional changes are reflected in the intercrystalline layers. Crystalline lamellae are very susceptible to internal ordering and disordering depending on their initial positions. Microvoid formation may not play as large a part in deformation mechanisms at these strains and temperatures. The onset of fiber formation (destruction of spherulite) has been uniquely characterized by application of a powerful model in SAXS. Also, the use of special morphology samples has facilitated our understanding of spherulite tensile deformations at the level of lamellae. Finally, such determinations will be useful in the accurate mechanical analysis of these structures by various mathematical models.

D. Future Experiments

The availability of the ORNL-10 meter spectrometer has generated a whole host of possible new experiments we can incorporate in the elucidation of lamella deformation. Some of these are mentioned below. Their order is not meant to specify their relative importance. Also, the availability of Thesis Contracts (T-Contract) from Oak Ridge Associated Universities (ORAU) for students involved in research similar to that described herein helps to defray the total expense of travel to and from the research facilities. ORNL personnel have details concerning this option. Due to the nature of the research agreement with ORNL, it is best if all possible experiments are run by the principal investigator. A complete set of blueprint copies concerning the spectrometer sample chamber is in our office or can be obtained from Dr. R. W. Hendricks.

1. Procurement of lower resolution data for LDPE in order to include the Porod's law region and determine the total integral properly. This would be important for the study of microvoid formation and to test the elliptically symmetric invariant derived here (Chapter 2, Section G). It would involve shortening the spectrometer by removal of tube sections in the beam path and realignment of the electronics and would be dependent upon the cooperative effort of the ORNL personnel and proper timing since this is no small task. An initial attempt to obtain this data failed because of spectrometer down time.

2. Swelling studies in the stretched state should be completed in order to confirm the results here concerning microvoid formation during deformation (see Reference 136). A sample holder for stretched and swollen samples was designed and built to fit directly into the sample chamber of the 10 meter spectrometer. Samples are elongated on the Instron or any appropriate stretching device then clamped in place by small, circular stainless steel clamps which fit directly into the aluminum holder. Solvent is introduced from a small set screw hole and is prevented from escaping by a thick teflon gasket and doubly thick mica windows epoxied in place.

Again, an unsuccessful attempt was made to use this equipment due to rupture at the mica windows caused by the high vacuum inside the spectrometer. The system was fully tested prior to shipment and we suspect that damage may have occurred during that time. Hence, this equipment should be "hand carried" to its destination.

Both HDPE and LDPE as well as the special texture samples should be analyzed in extension by this technique.

3. Because of discrepancies noted in Chapter 4, Section C2, concerning the variability in SAXS patterns and, therefore, mechanisms as a function of temperature of stretching, a study should be performed in this regard. A variable temperature cell including a stretching jig could be made similar to the one used with the Rigaku-Denki spectrometer in our laboratory. Possibly this same one could be modified and used. In the high resolution mode, the spectrometer is suited for complete analysis of HDPE patterns as implied in Chapter 4. Therefore, it may be necessary from an experimental viewpoint to concentrate effort on HDPE and its variations rather than LDPE.

4. We have seen that the onset of fiber morphology begins at a strain depending upon various factors including the crystal and amorphous thicknesses. A mechanism of deformation in which the lamellae fracture into mosaic blocks after the amorphous tie chains are fully extended has been suggested here. In order to test this more fully, use of samples of controlled molecular weight and narrow molecular weight distributions such as those prepared by Mandelkern (145-148) could be studied. Crystalline lamellae and amorphous interlamellae thicknesses could be discerned by application of the Hosemann SAXS model and the nature of the interlamellar tie chain could be characterized possibly by infrared or nuclear magnetic resonance studies. Its influence on the deformation characteristics could

then be discerned. Since there is already some experience gained in our laboratory with these samples, the interpretation of the findings would be simplified (123,149,150).

5. Another powerful advantage of the ORNL spectrometer is its ability to rapidly obtain data acquired either over one interval of time or in short bursts of the order of seconds. This suggests the possibility of following the time dependence of deformation either in relaxation experiments such as those of Stein and his associates (3,151-153) or in dynamic experiments where the electromagnetic response is compared to a mechanically oscillating input (see, e.g., 3,151-153).

The time dependence of spherulite deformation has been studied by Erhardt and Stein (154-156) using a high speed stretching apparatus whose speeds could be varied from 500 to 4000 in/min in conjunction with a high speed camera to record SALS pictures during the deformational process. They concluded that the velocity of spherulite deformation was of the same order of magnitude as that of the sample straining within the strain rates studied, i.e., no spherulite relaxation processes could be detected with regard to the spherulite as a whole. The rheo-optics of crystalline orientation in various polymeric systems has been studied as mentioned above. For the present work, results of Stein, et al. (152), and Fukui, et al. (157), are particularly interesting. Stein observed the temperature dependence of the orientations of the a, b and c axes of polyethylene from WAXD experiments. Replotting data of Figure 26 in Reference 152 to yield the time at which orientation is a maximum, one obtains the results given in Figure 55. A sharp increase in time for the

b-axis orientation is evident with decreasing temperature. Since the b-axis is aligned along the radius of the spherulite or parallel with the long axis of the lamella, the result suggests a similar dependence for lamella orientation. Fukui has shown a similar result and his Figure 2 is plotted in the same way as Figure 55 above (see Figure 56). His data was obtained using infrared measurements and the samples were annealed to a greater degree than in the Stein work. Relaxation times are much longer but a similar trend is observed. Relaxation times of the order of seconds are evident. The results suggest similar studies using the ORNL facility. Hence, the time dependent behavior of lamellae can be compared to crystallographic axes and suitable deformation mechanisms suggested and compared to existing ones. A variable temperature sample chamber would have to be designed and constructed for this purpose.

For dynamic experiments a variable temperature sample chamber equipped with stress and strain transducers capable of fitting into the evacuated sample chamber of the ORNL spectrometer would, again, have to be designed and constructed. This would require sophisticated, miniaturized mechanical and electrical components. Hendricks has suggested to us that he can control the detector to turn on and off at the very short times involved in sinusoidally straining the sample.

6. In the analysis of SAXS data a relatively new treatment of the direct analysis of curves has been presented by Strobl (119,158). Without the use of model calculations, parameters such as lamellar thickness, c,

and its distribution, the volume fraction of the two phases, the electron density defect per square unit of lamellar interface, and the boundary layer thickness distribution can be obtained. The mathematics is based on the assumption that the interference and structure factor curves can be separated uniquely since fluctuations in c are of the order of 1/c. The reader is referred to the appropriate references cited for details of the mathematics.

Results obtained for polyethylene are remarkably good, suggesting densities for crystalline and amorphous phases in HDPE in line with literature values, but for LDPE a lower crystalline density is reported (ρ_c' = 0.967 g/cm^3 versus 1.003 g/cm^3) and only a slightly different amorphous density (ρ_a' = 0.85 g/cm^3 versus 0.86 g/cm^3). This result suggests the defective nature of the crystalline phase in LDPE and its ramifications as to mechanistic differences in deforming LDPE and HDPE. The detailed mathematical procedure could be applied to the data for stretched samples and ρ_c' and ρ_a' obtained directly. The procedure must first be rigorously analyzed for application to deformed systems.

7. Finally, additional insight may be gained as to the deformation mechanisms of semi-crystalline polymers by the coupling of SALS and swelling experiments. Since the intensity of scattering (H_v mode) for the unswollen polymer, I_u, is proportional to $V_o^2 (\alpha_1 - \alpha_2)_o^2$ where V_o is the volume of a spherulite, swelling by an amount q_s with an appropriate solvent will change the scattered intensity I_s by

$$I_s = q_s^2 V_o^2 [(\alpha_1 - \alpha_s)_o^2 / q_s^2]$$

Thus, by cancellation of q_s terms we can see that there is no change in scattered intensity, a prediction which has only some preliminary verification (159), but needs further study. Also, since the volume goes as R^3 where R is the spherulite radius, swelling should change the R as $(q_s)^{1/3}$. If we allow the sample to swell by 10% or $q_s = 1.1$, then the radius will increase by about 3%. Photographic SAXS obviously does not contain the precision necessary for this determination. However, careful use of the optical multichannel analyzer (OMA) (see Reference 160) should increase the precision. Also, studies at higher temperatures where swelling would presumably increase would be beneficial.

The above simplified analysis has assumed that effects due to amorphous orientation and form birefringence effects are negligible. Deviations from the predictions noted above could be indicative of these effects. Form birefringence especially could be studied using solvents of differing refractive indicies at constant q_s. Constant q_s could be obtained for different solvents by either varying the time of swelling, varying the temperature or using mixed solvent pairs.

CAPTIONS FOR TABLES

1. Comparison of SAXS theories of Hosemann, Vonk and Tsvankin/Buchanan.
2. Physical characterization properties of samples studied.
3. Sample preparation conditions.
4. Geometry of Rigaku-Denki SAXS slit spectrometer.
5. Settings for DAC Model 200 spectrometer.
6. Weighting factors versus slit heights used in desmearing calculations.
7. Correlation function tables. Explanation and use described on page 90.
8. Analysis of LDPE,SC by Tsvankin/Buchanan theory.
9. Analysis of HDPE by Tsvankin/Buchanan theory.
10. Labarbe results for LDPE,SC.
11. Analysis of LDPE,SC by Hosemann theory. (a) $\psi = 0^{o}$, (b) $\psi = 90^{o}$.
12. Analysis of HDPE by Hosemann theory.
13. Crystallinities from densities and WAXD.
14. Invariant analysis for LDPE in swollen and unswollen LDPE. Calculated values included.
15. Invariant for HDPE from ORNL spectrometer. Calculated values included.
16. Analysis of parallel lamellar sheets via Hosemann scheme.

17. SAXS parameters and observations for the special morphology sample.

18. Effect of $F(\psi)$ on intensity parameters.

19. Results of HDPE applied to Wang calculations.

TABLE 1

	Hosemann	Vonk	Tsvankin/ Buchanan
Lattice Statistics	Second Order Paracrystal	First Order Paracrystal	Second Order Paracrystal
Lattice Size	Finite	Infinite	Infinite
Crystalline Distributions	Gaussian	Gaussian Log-Normal Square	Square
Amorphous Distributions	Gaussian	Gaussian Log-Normal Square	Exponential
Parameters	c,a,E g_a,g_c,N (curve fitting)	c,a,B_a,B_c (curve fitting)	Calibration Curves

TABLE 2

Physical Properties	MPE200/17942 (HDPE)	M8011 (LDPE)
Density (gm/cm^3)	0.9516	0.9254
Melt Flow (MI_{10})[1]	4.4	2.9
Elongation at Yield (%)	12.3	-
$CH_3/100$	0.29[2a]	~ 4.5[2b]
M_n[3]	15,500	15,000
M_w[3]	163,000	
M_w/M_n	10.5	11.5

1. ASTM-D-1238.
2a. By infrared.
2b. Estimate via density.
3. By gel permeation chromatography.

TABLE 3

	MPE200/ 17942	M8011 (541A,B, 542Q)
T_m (^oC)*	120-140	130-140
t_m (min)	15	15
T_p (^oC)*	145-150	145
t_p (min)	15	15
t_s (inches)+	0.050	0.092

*Subscripts m and p refer to melting (plates together with minimum pressure applied) and pressing (12000 psi added stepwise), respectively.

+Actual thicknesses used in calculations may vary somewhat due to sample variations. These are clearly noted.

TABLE 4

Target to	Slit Number 1	2	3	Sample	Slit Number 4	5	Detector
Distance in (mm)	-5.2	+190	245	265	535	575	580
Slit Widths (mm)	0.10	0.10	0.18	-	0.1	0.05	-

TABLE 5

DAC Model 200 Spectrometer Settings*

H_V = 1100 Volts

Baseline = 100 Volts

Window = 700 Volts

Time Constant = 0.5

Gain { Coarse 16 Volts
Fine 2 Volts

*Differential Mode of Operation

TABLE 6

Slit Length S_1, S_2, S_5	W(o)	p
10 mm	11.01	19.51
4 mm	27.52	48.78
2 mm	55.04	97.56

TABLE 7a

ϕ = 0.20, B_a(log), B_c(log)

$B_c \backslash B_a$	0.10	0.30	0.50	0.70
0.10		0.25 0.26 0.31	0.25 0.125 0.28	0.247 0.06 0.31
0.30	0.25 0.64 0.55	0.250 0.270 0.44	0.246 0.120 0.36	0.23 0.06 0.36
0.50	0.25 0.55 0.60	0.247 0.245 0.45	0.235 0.108 0.41	0.210 0.047 0.40
0.70	0.245 0.452 0.65	0.234 0.209 0.50	0.210 0.086 0.44	0.170 0.03 0.45
0.90	0.23 0.36 0.67	0.21 0.52	0.170 0.064 0.57	0.125 0.02 0.44

TABLE 7b

$\phi = 0.25\ B_a(\log),\ B_c(\log)$

$B_c \backslash B_a$	0.10	0.30	0.50	0.70
0.10		0.33 0.37 0.36	0.33 0.18 0.33	0.32 0.09 0.36
0.30	0.33 0.68 0.55	0.33 0.34 0.40	0.32 0.17 0.41	0.29 0.08 0.41
0.50	0.33 0.56 0.60	0.32 0.29 0.47	0.29 0.14 0.45	0.25 0.063 0.44
0.70	0.32 0.45 0.62	0.29 0.24 0.54	0.25 0.10 0.47	0.20 0.046 0.44
0.90	0.29 0.34 0.63	0.25 0.18 0.53	0.195 0.08 0.49	0.135 0.03 0.46

TABLE 7c

ϕ = 0.30, B_a(log), B_c(log)

$B_c \backslash B_a$	0.10	0.30	0.50	0.70
0.1		0.43 0.45 0.37	0.42 0.24 0.39	0.39 0.42
0.30	0.43 0.69 0.55	0.42 0.41 0.45	0.39 0.21 0.44	0.34 0.11 0.44
0.5	0.42 0.56 0.57	0.39 0.34 0.48	0.34 0.17 0.46	0.28 0.09 0.44
0.7	0.39 0.43 0.63	0.34 0.26 0.52	0.28 0.12 0.48	0.21 0.06 0.45
0.9	0.34 0.32 0.63	0.28 0.19 0.53	0.21 0.082 0.49	0.15 0.03 0.48

TABLE 7d

ϕ = 0.50, B_a(log), B_c(log)

$B_c \backslash B_a$	0.10	0.30	0.50	0.70
0.10	0.886 0.840 0.50	0.774 0.644 0.50	0.663 0.438 0.51	0.553 0.295 0.51
0.30	0.774 0.644 0.50	0.662 0.519 0.50	0.550 0.354 0.50	0.440 0.224 0.50
0.50	0.662 0.438 0.50	0.550 0.354 0.50	0.444 0.321 0.50	0.344 0.133 0.49
0.70	0.553 0.294 0.51	0.441 0.223 0.50	0.345 0.132 0.49	0.250 0.067 0.48
0.90	0.455 0.200 0.53	0.351 0.145 0.51	0.259 0.071 0.49	0.171 0.025 0.47

TABLE 7e

ϕ = 0.60, B_a(log), B_c(log)

$B_c \backslash B_a$	0.1	0.3	0.5	0.7
0.1	0.666 0.830 0.49	0.646 0.685 0.53	0.589 0.514 0.56	0.509 0.360 0.57
0.3	0.646 0.569 0.46	0.580 0.492 0.48	0.510 0.374 0.50	0.420 0.260 0.51
0.5	0.575 0.334 0.45	0.509 0.287 0.47	0.420 0.212 0.48	0.328 0.138 0.50
0.7	0.507 0.213 0.46	0.419 0.175 0.47	0.331 0.114 0.46	0.244 0.061 0.48
0.9	0.449 0.112 0.51	0.357 0.078 0.50	0.266 0.035 0.48	0.187 0.001 0.47

TABLE 7f

ϕ = 0.15; B_a, B_c (Gaussian)

$B_c \backslash B_a$	0.05	0.10	0.15	0.20	0.25	0.30
0.05	0.177 0.569 0.490	0.177 0.429 0.583	0.177 0.355 0.612	0.180 0.312 0.660	0.203 0.260 0.696	0.269 0.168 0.702
0.10	0.177 0.375 0.388	0.177 0.302 0.471	0.177 0.256 0.519	0.178 0.225 0.565	0.196 0.180 0.600	0.253 0.092 0.641
0.15	0.176 0.238 0.317	0.176 0.201 0.412	0.173 0.175 0.457	0.173 0.159 0.491	0.187 0.122 0.509	0.235 0.037 0.537
0.20	0.175 0.096 0.284	0.172 0.131 0.373	0.166 0.114 0.406	0.162 0.108 0.435	0.174 0.073 0.486	
0.25	0.171 0.096 0.263	0.164 0.085 0.349	0.155 0.080 0.393	0.150 0.071 0.413	0.159 0.038 0.444	
0.30	0.163 0.061 0.257	0.153 0.058 0.332	0.143 0.054 0.373	0.136 0.046 0.381	0.144 0.013 0.429	

TABLE 7g

ϕ = 0.20; B_a, B_c (Gaussian)

$B_c \backslash B_a$	0.05	0.10	0.15	0.20	0.25	0.30
0.05	0.25	0.25 0.46 0.43	0.25 0.31 0.35	0.25 0.20 0.32	0.24 0.13 0.29	0.22 0.08 0.28
0.10	0.25 0.50 0.57	0.25 0.37 0.49	0.25 0.26 0.44	0.24 0.17 0.40	0.22 0.11 0.37	
0.15	0.25 0.39 0.59	0.25 0.31 0.53	0.24 0.22 0.48	0.23 0.15 0.45	0.21 0.10 0.40	
0.20	0.25 0.34 0.65	0.24 0.26 0.55	0.23 0.19 0.49	0.21 0.14 0.37	0.19 0.09 0.43	
0.25	0.25 0.30 0.65	0.24 0.23 0.57	0.22 0.18 0.52	0.20 0.125 0.48	0.18 0.08 0.45	

TABLE 7h

ϕ = 0.25; B_a, B_c (Gaussian)

$B_c \backslash B_a$	0.05	0.10	0.15	0.20	0.25	0.30
0.05	0.333 0.679 0.500	0.333 0.543 0.559	0.331 0.426 0.608	0.327 0.351 0.618	0.320 0.302 0.618	0.311 0.269 0.625
0.10	0.333 0.530 0.416	0.331 0.432 0.485	0.324 0.347 0.519	0.312 0.289 0.548	0.300 0.246 0.558	0.289 0.221 0.558
0.15	0.331 0.368 0.373	0.323 0.311 0.442	0.308 0.254 0.479	0.289 0.213 0.500	0.274 0.189 0.519	0.260 0.169 0.538
0.20	0.322 0.245 0.349	0.303 0.211 0.407	0.282 0.176 0.443	0.263 0.156 0.463	0.243 0.138 0.477	
0.25	0.305 0.159 0.337	0.281 0.138 0.391	0.257 0.124 0.426	0.235 0.109 0.450	0.216 0.097 0.460	
0.30	0.282 0.103 0.324	0.256 0.094 0.373	0.230 0.085 0.405	0.208 0.015 0.424	0.192 0.065 0.443	

TABLE 7i

ϕ = 0.30; B_a, B_c (Gaussian)

$B_c \backslash B_a$	0.05	0.10	0.15	0.20	0.25	0.30
0.05	0.429 0.731 0.500	0.428 0.582 0.554	0.421 0.452 0.569	0.407 0.363 0.598	0.385 0.302 0.602	0.371 0.260 0.009
0.10	0.428 0.577 0.431	0.421 0.477 0.490	0.403 0.380 0.515	0.380 0.307 0.546	0.355 0.255 0.558	0.337 0.219 0.558
0.15	0.420 0.416 0.402	0.401 0.354 0.444	0.374 0.286 0.490	0.344 0.231 0.510	0.320 0.195 0.512	0.298 0.170 0.528
0.20	0.400 0.284 0.379	0.371 0.245 0.414	0.337 0.199 0.457	0.308 0.171 0.484	0.280 0.147 0.491	
0.25	0.370 0.187 0.358	0.334 0.163 0.407	0.301 0.142 0.443	0.272 0.123 0.461	0.245 0.105 0.464	
0.30	0.343 0.122 0.354	0.303 0.111 0.393	0.264 0.100 0.423	0.241 0.086 0.434	0.216 0.073 0.455	

TABLE 7j

ϕ = 0.65; B_a, B_c (Gaussian)

$B_c \backslash B_a$	0.05	0.10	0.15	0.20	0.25	0.30
0.05	0.538 0.752 0.500	0.533 0.610 0.535	0.510 0.474 0.559	0.484 0.371 0.563	0.455 0.299 0.573	0.428 0.248 0.573
0.10	0.533 0.608 0.460	0.513 0.510 0.495	0.476 0.404 0.515	0.442 0.318 0.524	0.407 0.256 0.534	0.376 0.211 0.548
0.15	0.509 0.453 0.426	0.474 0.387 0.456	0.435 0.311 0.500	0.390 0.245 0.505	0.357 0.197 0.512	0.329 0.165 0.519
0.20	0.477 0.315 0.412	0.433 0.274 0.442	0.386 0.221 0.469	0.345 0.183 0.481	0.310 0.153 0.491	
0.25	0.437 0.212 0.398	0.388 0.185 0.421	0.340 0.158 0.453	0.303 0.134 0.468	0.270 0.112 0.473	
0.30	0.398 0.140 0.389	0.346 0.125 0.408	0.300 0.112 0.440	0.267 0.095 0.460	0.238 0.077 0.465	

TABLE 7k

ϕ = 0.40; B_a, B_c (Gaussian)

$B_c \backslash B_a$	0.05	0.10	0.15	0.20	0.25	0.30
0.05	0.603 0.765 0.500	0.637 0.629 0.525	0.598 0.489 0.535	0.549 0.375 0.549	0.502 0.292 0.559	0.463 0.233 0.563
0.10	0.637 0.628 0.470	0.597 0.532 0.490	0.539 0.421 0.510	0.488 0.325 0.515	0.444 0.252 0.522	0.406 0.199 0.524
0.15	0.597 0.478 0.455	0.537 0.412 0.466	0.483 0.330 0.495	0.427 0.255 0.500	0.383 0.197 0.505	0.348 0.159 0.505
0.20	0.542 0.340 0.431	0.480 0.296 0.452	0.425 0.239 0.471	0.373 0.191 0.491	0.331 0.156 0.498	
0.25	0.487 0.233 0.418	0.427 0.204 0.440	0.373 0.171 0.455	0.326 0.144 0.486	0.289 0.116 0.487	
0.30	0.438 0.157 0.409	0.381 0.138 0.433	0.330 0.124 0.441	0.287 0.104 0.482	0.254 0.085 0.483	

TABLE 71

ϕ = 0.45; B_a, B_c (Gaussian)

$B_c \backslash B_a$	0.05	0.10	0.15	0.20	0.25	0.30
0.05	0.784 0.772 0.500	0.721 0.460 0.520	0.648 0.498 0.522	0.585 0.375 0.525	0.530 0.281 0.525	0.484 0.214 0.525
0.10	0.721 0.639 0.485	0.658 0.545 0.594	0.586 0.431 0.510	0.517 0.326 0.512	0.460 0.244 0.512	0.415 0.185 0.510
0.15	0.467 0.493 0.471	0.585 0.426 0.480	0.515 0.341 0.495	0.451 0.259 0.500	0.397 0.193 0.500	0.357 0.151 0.500
0.20	0.581 0.357 0.461	0.515 0.312 0.466	0.450 0.251 0.486	0.391 0.197 0.491	0.343 0.157 0.495	
0.25	0.522 0.251 0.456	0.455 0.220 0.562	0.314 0.181 0.469	0.340 0.150 0.481	0.300 0.119 0.482	
0.30	0.471 0.174 0.452	0.405 0.153 0.459	0.349 0.134 0.465	0.300 0.111 0.477	0.265 0.088 0.478	

TABLE 7m

ϕ = 0.50; B_a, B_c (Gaussian)

$B_c \backslash B_a$	0.05	0.10	0.15	0.20	0.25	0.30
0.05						
0.10		0.680 0.549 0.50	0.600 0.432 0.50	0.530 0.321 0.49	0.470 0.233 0.48	0.420 0.169 0.48
0.15		0.602 0.432 0.50	0.530 0.345 0.49	0.459 0.258 0.49	0.403 0.188 0.50	0.357 0.143 0.48
0.20		0.530 0.322 0.49	0.459 0.258 0.49	0.397 0.198 0.50	0.346 0.155 0.49	0.308 0.117 0.48
0.25		0.470 0.233 0.49	0.403 0.188 0.50	0.345 0.155 0.48	0.304 0.120 0.48	0.270 0.091 0.48
0.30		0.420 0.169 0.48	0.357 0.143 0.48	0.308 0.117 0.48	0.269 0.91 0.48	0.238 0.074 0.47

TABLE 8

LDPE, SC

Strain	$\psi(p)$	ϕ_c ($\pm$ 0.02)	X_m	d (Å)	$X_m d$ (Å)	c (Å)	a (Å)
1.0	0.43	0.475	1.21	123	149	71	78
$\psi = 90^o$							
1.1	0.37	0.51	1.21	130	157	80	77
1.2	0.38	0.50	1.21	134	162	81	81
1.3	0.45	0.46	1.21	140	169	78	91
1.4	0.41	0.48	1.21	147	179	85	94
1.5	0.53	0.43	1.21	143	173	74	99
1.6	0.50	0.44	1.21	140	169	74	95
1.87	0.42	0.48	1.21	140	169	81	88
$\psi = 0^o$							
1.1	0.40	0.49	1.21	106	128	63	65
1.2	0.42	0.48	1.21	103	125	60	65
1.3	0.41	0.48	1.21	96.4	117	56	61
1.4	0.41	0.48	1.21	94.6	114	55	59
1.5	0.41	0.48	1.21	90.7	110	53	47
1.6	0.38	0.50	1.21	88.1	107	53	54
1.87	0.40	0.49	1.21	81.1	98	48	50

TABLE 9

HDPE, SC

Strain	$\psi(p)$	ϕ_c ($\pm$ 0.02)	X_m	d (Å)	X_md (A)	c (Å)	a (Å)
1.0	0.39	0.49	1.21	270	327	160	167
$\psi = 90^o$							
1.25	0.41	0.48	1.21	285	345	166	179
$\psi = 0^o$							
1.25	0.37	0.51	1.21	257	311	158	153

TABLE 10

LDPE, SC

(From Labarbe, et al.)

Strain	$\psi(p)$	ϕ_c ($\pm$ 0.02)	X_m	d (Å)	X_md (Å)	c (Å)	a (Å)
1.0		0.45	1.18	132.5	157	71	86
$\psi = 90^o$							
1.1		0.47	1.18	147	174	82	92
1.2		0.46	1.19	155	184	85	99
1.3		0.44	1.19	166	197	86	111
1.4		0.44	1.25	183	229	101	128
1.5		0.44	1.19	212	252	112	140
1.6		0.46	1.19	221	262	120	142
$\psi = 0^o$							
1.1		0.46	1.18	132.5	157	72	85
1.2		0.47	1.18	132.5	157	74	83
1.3		0.46	1.18	131	155	71	84
1.4		0.46	1.19	110	131	60	71
1.5		0.46	1.19	102	121	55	66
1.6		0.45	1.19	102	121	55	66

TABLE 11a

LDPE, SC; $\psi = 0^{o}$

Strain Ratio	c (Å) (± 2)	a (Å) (± 2)	ϕ_c	g_c	g_a	N (± 0.1)	E (Å)	± Δ
1.0	54	61	0.47	0.3 ± 0.2	0.2 ± 0.2	1.6	10 ± 10	0.08
1.1	54	61	0.47	0.1 ± 0.1	0.1 ± 0.1	1.5	10 ± 10	0.09
1.2	54	55	0.50	0.1 ± 0.1	0.1 ± 0.1	1.4	10 ± 10	0.03
1.3	50	60	0.46	0.1 ± 0.1	0.1 ± 0.1	1.4	0	0.05
1.4	50	50	0.50	0.1 ± 0.1	0.1 ± 0.1	1.4	0	0.10
1.5	50	45	0.52	0.1 ± 0.1	0.1 ± 0.1	1.5	0	0.10
1.6	48	42	0.53	0.2 ± 0.1	0.2 ± 0.1	1.5	0	0.05
1.87	50	42	0.54	0.1 ± 0.1	0.1 ± 0.1	1.5	0	0.18

TABLE 11b

LDPE, SC; $\psi = 90^{o}$

Strain Ratio	c (Å) (± 2)	a (Å)	ϕ_c	g_c	g_a	N (± 0.1)	E (Å)	± Δ
1.0	54	61 ± 2	0.47	0.3 ± 0.2	0.2 ± 0.2	1.6	10 ± 10	0.08
1.1	54	79 ± 3	0.41	0.1 ± 0.1	0.1 ± 0.1	1.4	10 ± 10	0.03
1.2	54	85 ± 3	0.39	0.1 ± 0.1	0.1 ± 0.1	1.4	10 ± 10	0.04
1.3	49	90 ± 3	0.35	0.1 ± 0.1	0.1 ± 0.1	1.3	10 ± 10	0.01
1.4	50	97 ± 4	0.34	0.1 ± 0.1	0.1 ± 0.1	1.3	0	0.03
1.5	50	85 ± 3	0.37	0.1 ± 0.1	0.1 ± 0.1	1.3	0	0.09
1.6	45	70 ± 3	0.39	0.1 ± 0.1	0.1 ± 0.1	1.2	10 ± 10	0.05
1.87	50	53 ± 2	0.48	0.1 ± 0.1	0.1 ± 0.1	1.4	20 ± 10	0.10

TABLE 12

HDPE

Strain Ratio	c (Å) (± 5)	a (Å) (± 2)	ϕ_c	g_c	g_a	N (± 1.0)	E (Å)	± Δ
1.0	190	37	0.84	0.32 ± 0.03	0.30	8	30	0.05
($\psi = 0^o$)								
1.25	190	33	0.85	0.3 ± 0.05	0.3	10	40	0.08
($\psi = 90^o$)								
1.25	190	56	0.80	0.35 ± 0.05	0.10	5	30	0.07

TABLE 13

Sample	ρ' (gm/cm^3)	ϕ_c* (ρ_c = 1.00, ρ_a = 0.86)	ϕ_c+ (ρ_c = 0.96, ρ_a = 0.86)	ϕ_c (DSC)	ϕ_c (WAXD)
LDPE:					
S241A (Slowly Cooled)	0.927 ± 0.001	0.48 ± 0.01	0.66 ± 0.01	0.42 ± 0.02	0.49 ± 0.05
S42Q				0.41 ± 0.03	
S39Q	0.92 ± 0.01	0.44 ± 0.1	0.61 ± 0.01		
Keller Sp. Text. (Prep. from S39Q)	0.918	0.41	0.58		

* ρ_c and ρ_a values from Reference 59

\+ ρ_c and ρ_a values from Reference 119

TABLE 14

LDPE, SC

Sample	Sample State	$\langle \Delta\eta^2 \rangle \times 10^4$ (eu/Å^3)^2				
		No Voids (Eqns. 42, 58)	Voids (Eqns. 50, 64) $\phi_v = 0.02$	Voids (Eqns. 50, 64) $\phi_v = 0.04$	Transition Zone (E = 10Å, Eqns. 71, 72)	Experimental
S40	Unswollen (u)	5.28	25.2	45.1	4.76	3.2 ± 0.3
$\phi_v = 0.48$	Swollen (s)	5.86	5.83	8.12	5.58	4.4 ± 0.4
	Ratio (s/u)	1.11	0.23	0.18	1.17	1.4 ± 0.1
S41B	Unswollen (u)	5.27	25.6	45.0	4.66	6.6 ± 0.6
$\phi_v = 0.47$	Swollen (s)	5.41	4.74	5.82	5.41	5.8 ± 0.5
	Ratio (s/u)	1.03	0.18	0.13	1.16	0.9 ± 0.1

TABLE 15

HDPE, SC

Strain	Azimuthal Angle	$\langle \Delta n^2 \rangle \times 10^4$ (eu/Å^3)^2 Experimental	Calculated (Eqn. 71, Table 14)
0%	-	1.5 ± 0.2	1.91
25%	0^o	1.8 ± 0.2	-
25%	90^o	1.7 ± 0.2	-

TABLE 16

Special Texture Polyethylene

Strain Ratio	d_B (Å)	c (Å) (± 3)	a (Å)	E (Å)	ϕ_c	N (± 0.1)	g_c	g_a (± 0.1)	Δ
1.0	188	72	98 ± 3	0	0.42	2.5	0.15 ± 0.1	0.3	0.02
1.1	195	72	107 ± 2	10 ± 10	0.40	2.5	0.3 ± 0.2	0.28	0.08
1.25	220	75	125 ± 2	60 ± 5	0.38	2.1	0.2 ± 0.4	0.3	0.08
1.4	257	72	145 ± 3	65 ± 5	0.33	1.7	0.2 ± 0.15	0.3	0.12

TABLE 17

Parameter	Fewer Lamellae	Lamellar Fracture	Disorientation	Observation
$\Sigma I(X,Y)^a$	Decrease*	Constant*	Constant*	Slight Decrease**
$I(\psi = 0^o)^b$	Decrease	Constant	Decrease	Decrease
Meridional Spread[c]	No Spread	Spread	Spread	Spread
$\langle N \rangle_{Hosemann}$[d]	Constant	Constant	Decrease	Decrease

**Slight decrease accounted for on basis of change in linear crystallinity; therefore, for this argument, essentially constant.

*An increase would be predicted if microvoid formation were included.

[a]Chapter 4, Section A5; [b,c]Chapter 2; [c]Reference 31, p. 334.

TABLE 18

λ_s	$\langle\Delta\eta^2\rangle_{rel}$	$F\ (90^o)$	$\langle\Delta\eta^2\rangle \times F$
1.0	1.0	1.0	1.0
1.1	0.86	1.6	1.38
1.25	0.66	2.2	1.45
1.4	0.46	2.55	1.17

TABLE 19

Orientations	Strains		Stresses $\times 10^{10}$ dynes/cm^2	
	ε_r		σ_r	σ_θ
0^o	0.25*	-0.02*	0.96	-0.6
90^o	-0.02*	0.04$^+$	-0.28	1.05

*From SALS

$^+$From SAXS, Table 12

CAPTIONS FOR FIGURES

1. Lamellae for which stress is (a) perpendicular, (b) parallel, and (c) at an angle to the lamellae planes.
2. SAXS photograph from LDPE stretched to elongation ratios, λ_s, given. Stretch direction, S.D., as shown.
3. Graphic representation of the distribution of points in a linear paracrystalline lattice. From Reference 33.
4. Random arrangement of lamellar "clusters".
5. Electron density profile including finite transition thickness, E. ρ_c and ρ_a are electron densities of the crystalline and amorphous regions, respectively.
6. Intensity versus number of parallel rods for finite number of parallel rods (——) and for 50 rods with random angular disorder (●). Values of random number limits are shown.
7. Stack of four lamellae, one of which is angularly disordered.
8. Geometry of Rigaku-Denki SAXS spectrometer. Slit mode.
9. Weighting function, W(u) versus u at various slit heights.
10. Schematic of ORNL 10-Meter SAXS spectrometer.
11. Tsvankin/Buchanan calibration curves.
12. Computer generated two-dimensional SAXS contour plots of LDPE,SC at various stages of strain λ_s. For plots a-h, λ_s = 1.0-1.6, 1.87, respectively. S.D. horizontal.

13. SAXS contour plot of LDPE,SC before sensitivity, background, and sample transmission corrections.

14. SAXS contour plots for LDPE,Q. For plots a-d, λ = 1.0, 1.1, 1.25, 1.50, respectively.

15. Ratios of long spacings perpendicular and parallel to strain versus stretch ratios. Affine prediction $(M_1/M_2)_a$ also included (solid line).

16. Lamella orientation function, f_ℓ, versus strain ratio, λ_s, for LDPE. Affine prediction, solid line, as well as that including lamellar twisting, η, given.

17. H_V SALS of deformed LDPE,SC. Strain ratio and direction as shown.

18. Spherulite, λ_3, versus sample, λ_s, extension for LDPE,SC from H_V SALS.

19. SAXS contour plots for HDPE. For plots a and b, λ_s = 1.0 and 1.25, respectively.

20. Background and Lorentz correction effects on unstretched LDPE. Data obtained with ORNL facility. No sensitivity correction applied.

21. SAXS intensity (corrected) versus scattering angle for LDPE,SC. Experimental points are omitted for simplicity. (a) Lamellae perpendicular to strain; (b) lamellae parallel to strain. Stretch ratios: 1.0 ——, 1.1 —— – ——, 1.2 – – –, 1.3 — 0 ——, 1.4 – 0 – 0 –, 1.5 — 0 ——, 1.6 – 0 – 0 – 0 –.

22. SAXS intensity (corrected) versus scattering angle for LDPE,Q. (a) Lamellae perpendicular to strain. (b) Lamellae parallel to strain. Elongation ratios as shown.

23. SAXS intensity (corrected) versus scattering angle for HDPE. 0^{o} and 90^{o} designate lamellae parallel and perpendicular to strain at $\lambda_s = 1.25$. 0% is unstretched sample.

24. Reduced long spacing, d/d_o, versus strain ration, L/L_o, for samples studied.

25. SAXS intensity versus scattering angle at various azimuthal angles for LDPE,SC at 30% strain. Azimuthal angles, 0^{o} ——, 10^{o} ●●●, 20^{o} — – —, 30^{o} — ● —, 40^{o} – ● – ● – ●, 50^{o} — ● – ● —, 60^{o} – – – –, 70^{o} —— 0 ——, 80^{o} – 0 – 0 – 0, 90^{o} — 0 – 0 —.

26. Lorentz corrected curves of Figure 25a.

27. Background subtracted, Lorentz corrected SAXS curves for 30% stretched LDPE,SC. Curves a-d represent azimuthal angles of 0, 30, 60 and 90 degrees, respectively. Slit heights: 10 mm ——, 4 mm – – –, 2 mm — – —.

28. Observed Bragg spacing versus slit height at various azimuthal angles.

29. Comparison of corrected intensity versus scattering angle for unstretched LDPE,SC from slit desmeared and joint-like geometry.

30. Same as Figure 29 except 60% strain. (a) 0^{o} azimuthal angle, (b) 90^{o} azimuthal angle.

31. Comparison of Tsvankin/Buchanan fit (points) of corrected intensity versus scattering angle for LDPE,SC unstretched (line). ORNL spectrometer.

32. Same as Figure 31 but for HDPE.

33. Experimental (line) and calculated (points) correlation function of LDPE,SC.

34. Corrected SAXS intensity versus angle for LDPE,SC. Experimental (——), calculated (●) via Hosemann analysis.

35. (a) Same as 35 but for HDPE. (b) $\lambda_s = 1.25$, $\psi = 0^o$. (c) $\lambda_s = 1.25$, $\psi = 90^o$.

36. Linear crystallinity versus elongation ratio for LDPE,SC. From application of Hosemann analysis.

37. Reduced long periods, d/d_o, and amorphous thicknesses, a/a_o, versus strain ratio, λ_s, for LDPE,SC from Hosemann calculations.

38. Hosemann N versus elongation ratio for LDPE,SC.

39. Corrected SAXS intensity versus scattering angle for swollen and unswollen LDPE.

40. Porod's law plot of HDPE.

41. Total intensity versus strain for LDPE. From ORNL spectrometer.

42. Density versus elongatio ratio of LDPE,SC. From hydrostatic weighing.

43. Geometry of parallel lamellar sheets.

44. SAXS three-dimensional perspective plot of parallel lamellar sheet.

45. SAXS contour plot for H29, parallel lamellar morphology.

46. SAXS contour plots for S39 parallel lamellar morphology. Stretch direction perpendicular to lamellar planes. Curves a-d represent $\lambda_s = 1.0, 1.1, 1.25, 1.40$, respectively.

47. f_{ℓ} versus % strain for parallel lamellar morphology. Strain perpendicular to lamellar planes.

48. Intensity versus scattering angle for S39 at various strain ratios. λ_s = 1.0 ——, 1.1 – – –, 1.25 — – —, 1.4 — – – —.

49. Reduced long periods, d/d_o, and amorphous thicknesses, a/a_o, versus strain ratios for parallel lamellar sheets. Affine prediction shown (– – –).

50. Proposed deformation mechanism. Stretch direction perpendicular to lamellar planes (along z).

51. Tsvankin (135) deformation mechanism.

52. Petraccone (130) deformation mechanism.

53. Proposed deformation mechanism. Stretch direction parallel to lamellar planes (along y).

54. Effect on SAXS from lamellae lying parallel to incident x-rays, I_o, and twisting about the spherulite radius. Tensile, F_t, and compressive, F_c, forces are shown as well as crystallographic axes.

55. Temperature versus time at which orientation is maximized. From data of Stein, et al. (152).

56. Temperature versus time at which orientation is maximized. From data of Fukui, et al. (157).

57. Intensities at first (——) and second (– – –) order maxima versus disorder angle for 50 rods.

58. $F(\psi)$ versus ψ for various elongation ratios, λ_s.

59. Optical diffraction mask. 1.5X magnification of original (10 cm).

60. Computer generated calcomp plot of Figure 59.

61. Optical diffraction apparatus.

62. Optical diffraction analogs (interference) from corresponding masks.

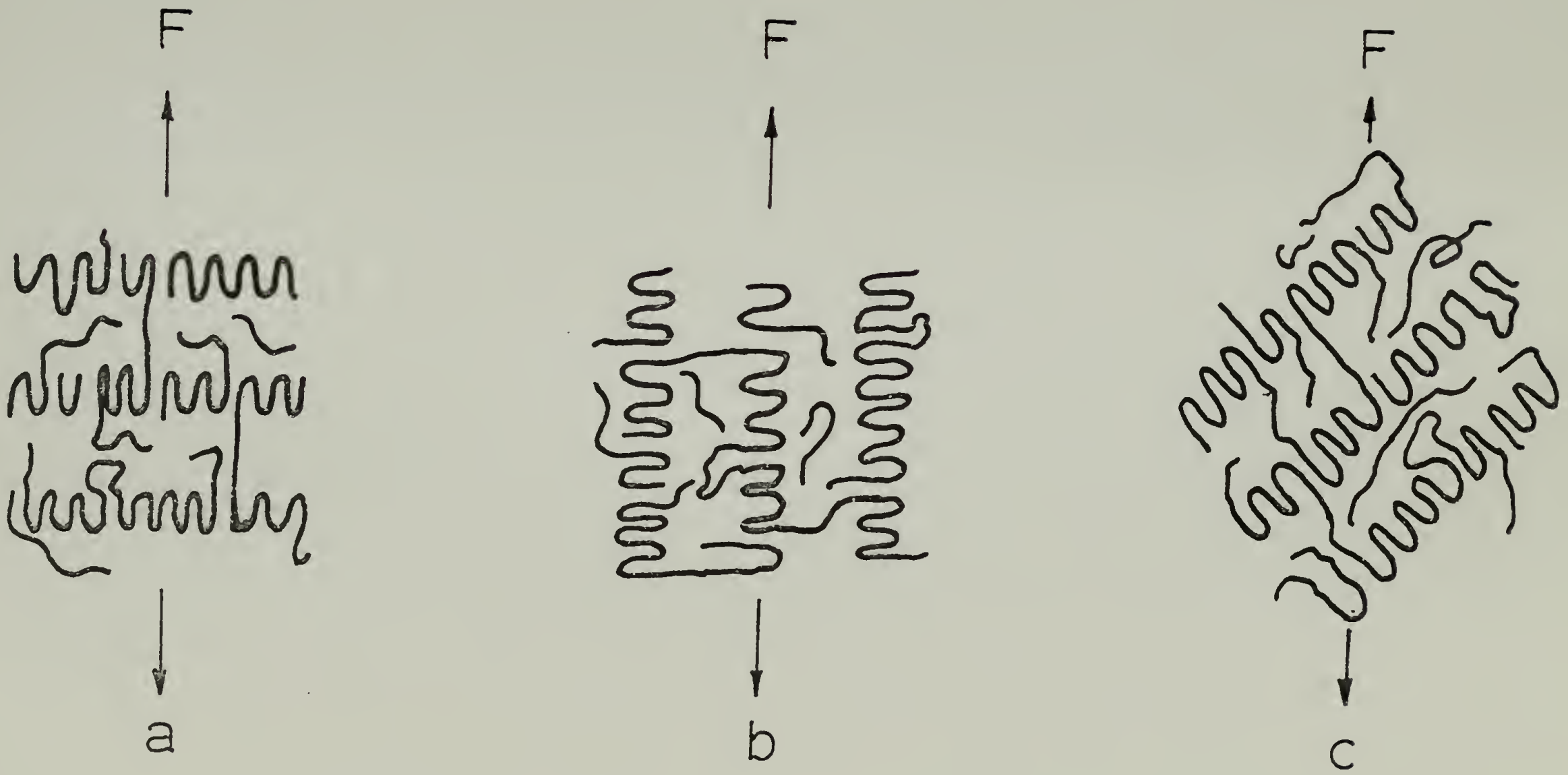

Figure 1

SAXS OF DEFORMED LDPE

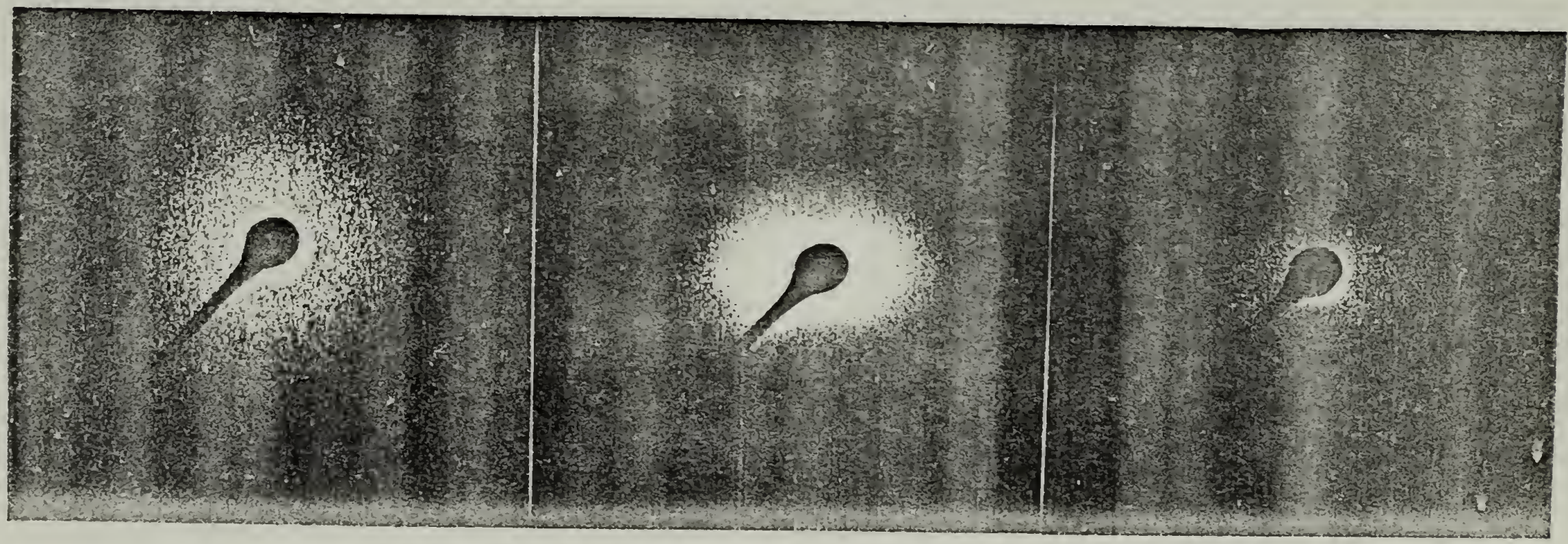

Figure 2

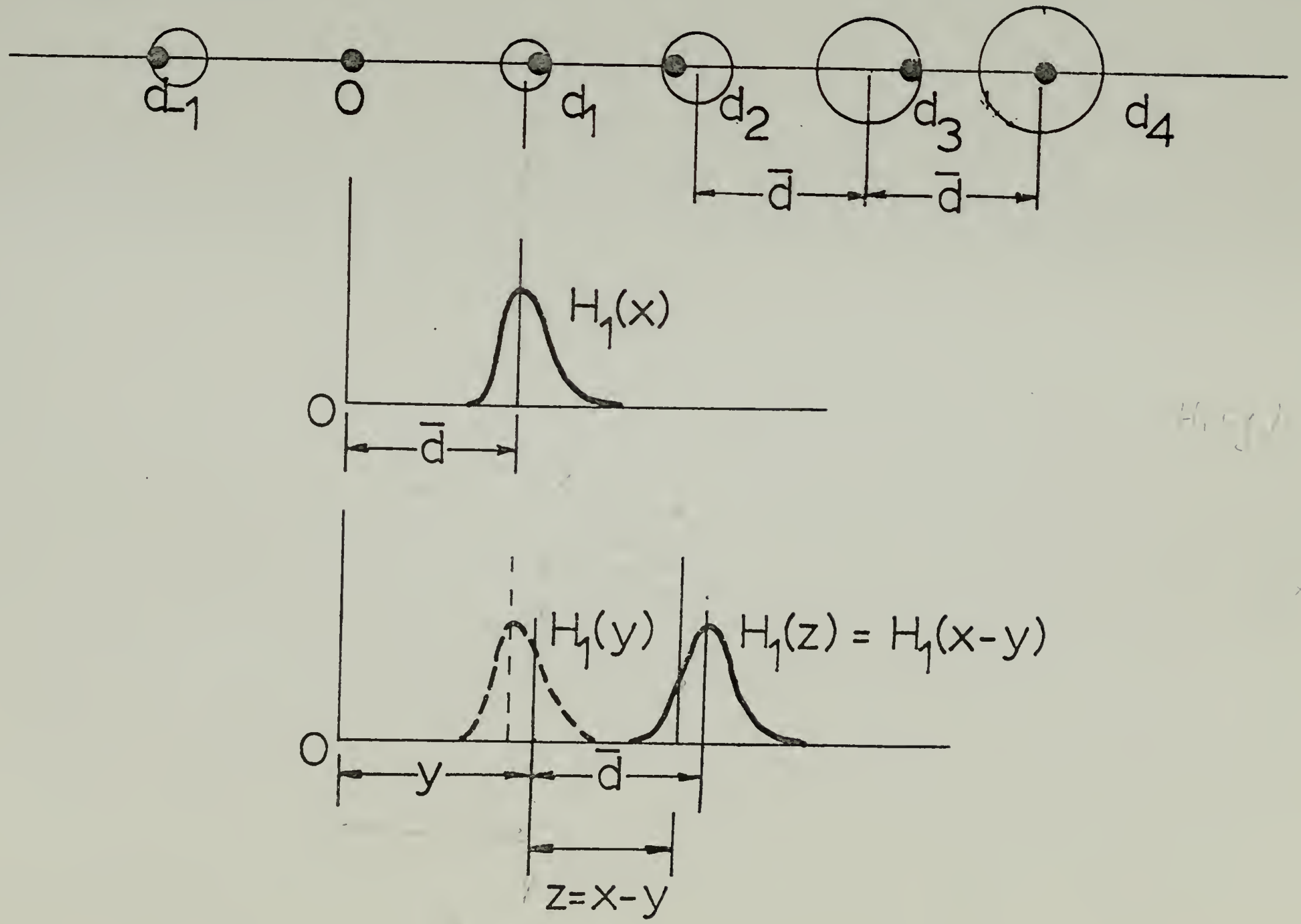

Figure 3

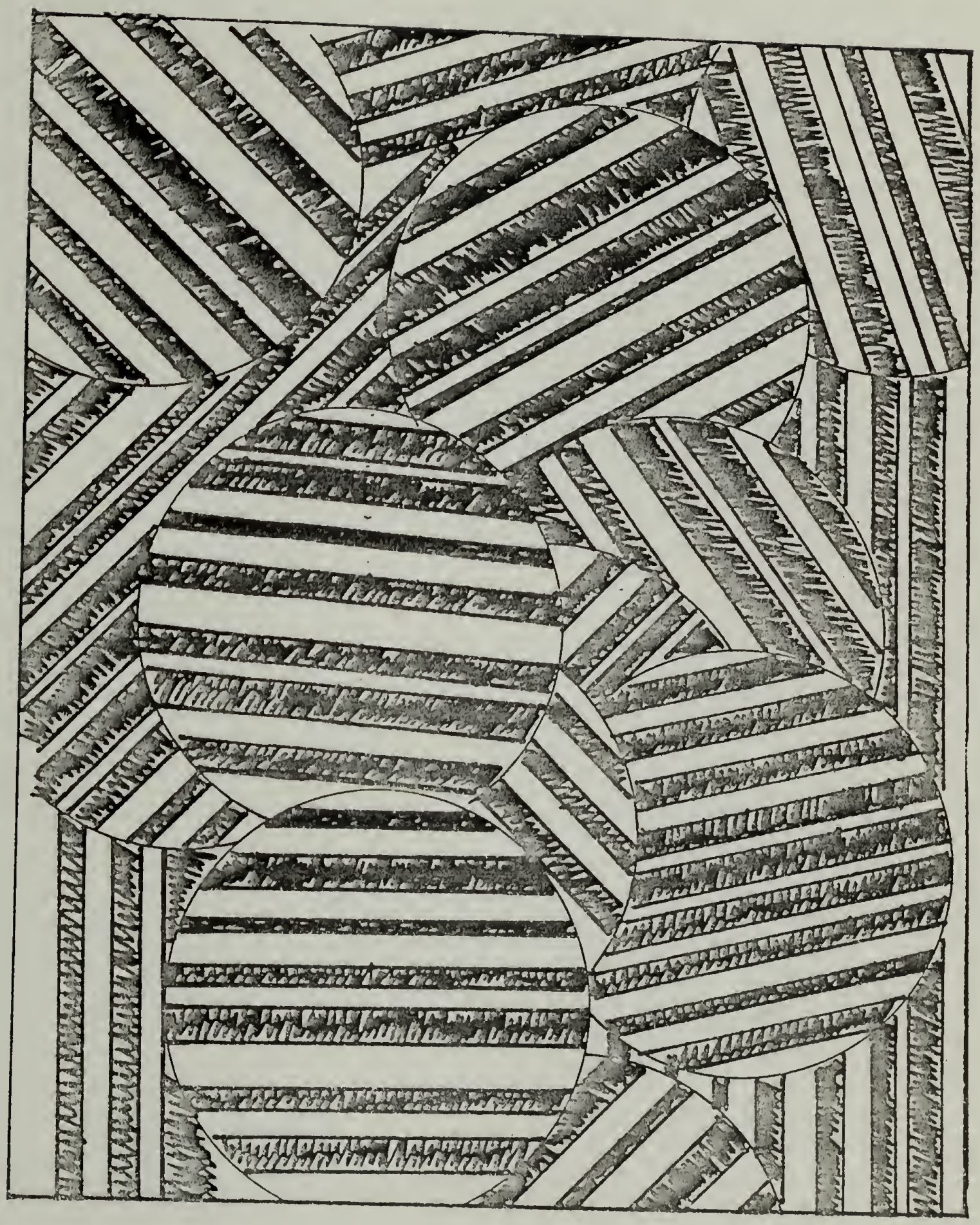

Figure 4

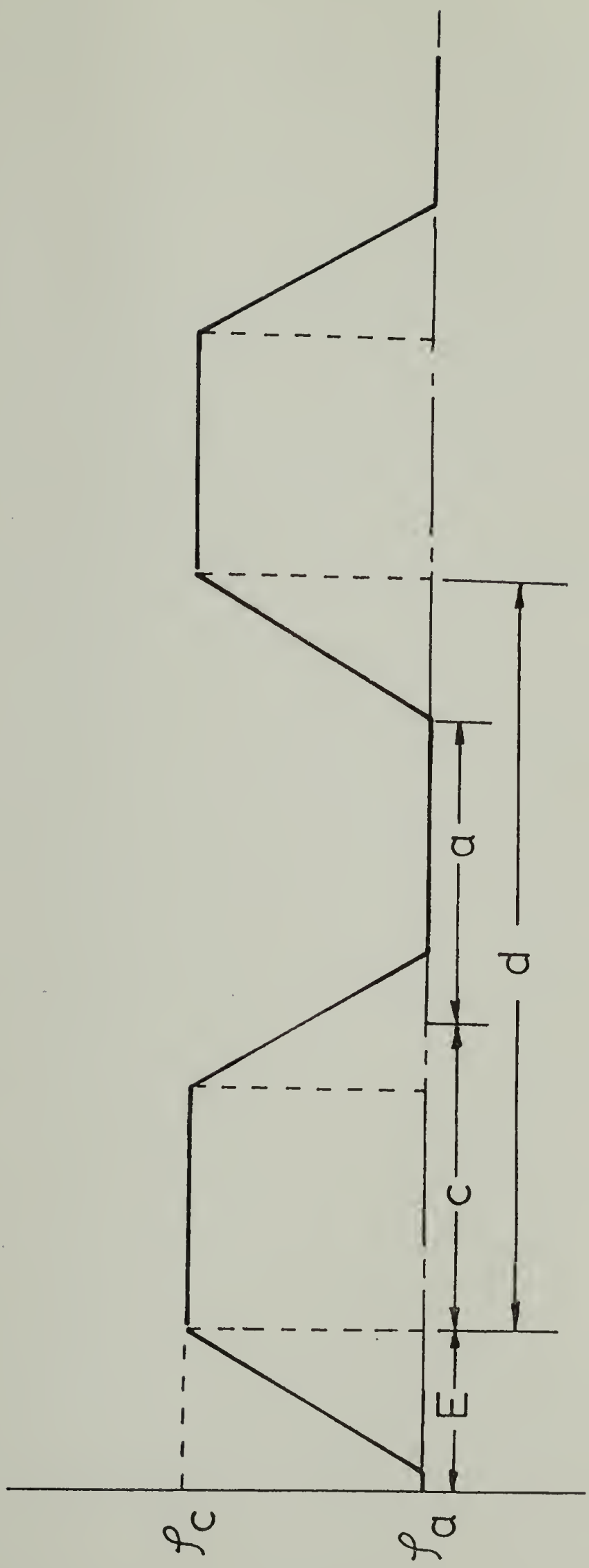

Figure 5

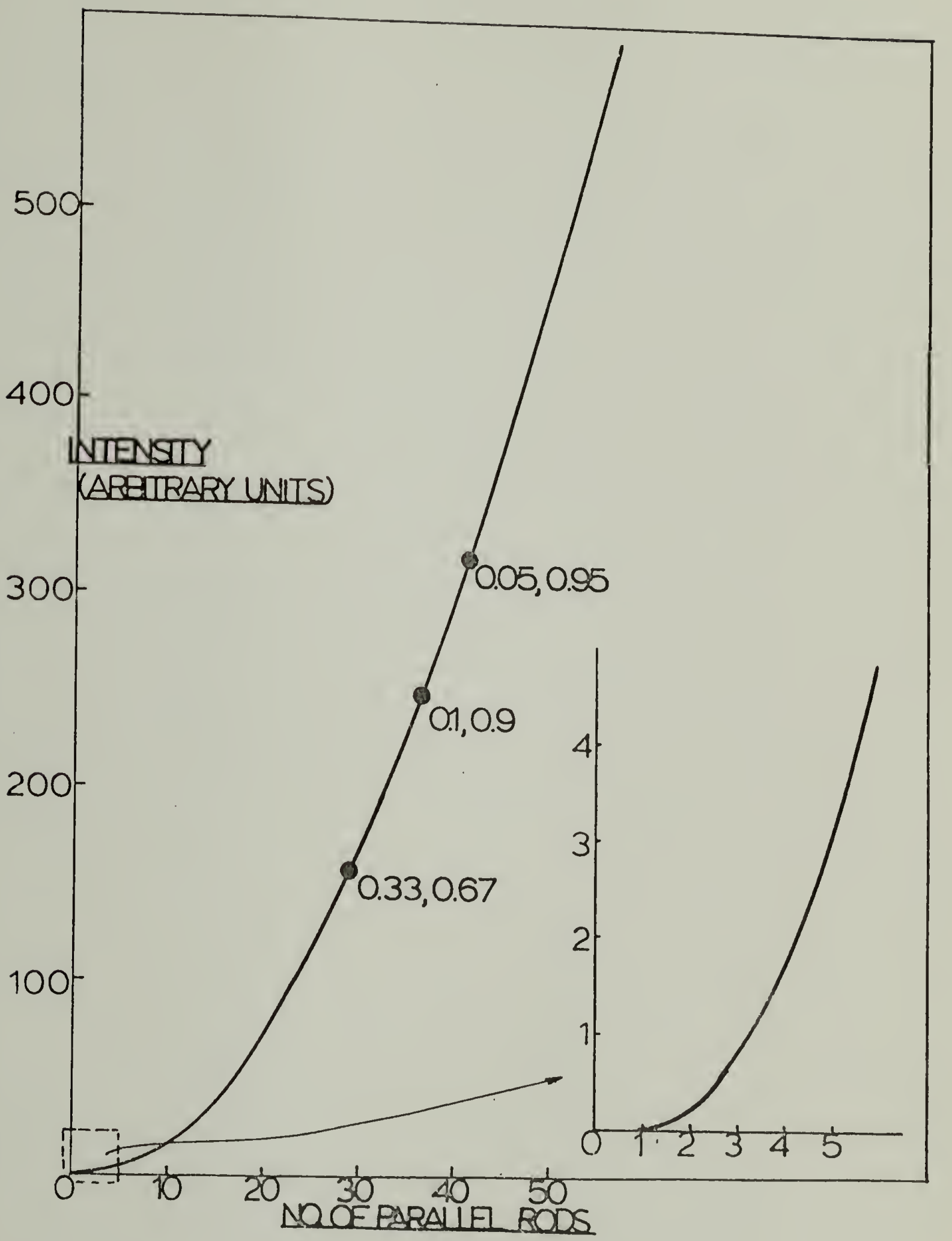
500
400
300
200
100
INTENSITY
(ARBITRARY UNITS)
0.05, 0.95
0.1, 0.9
0.33, 0.67
0
10
20
30
40
50
NO. OF PARALLEL RODS
4
3
2
1
0
1
2
3
4
5

Figure 6

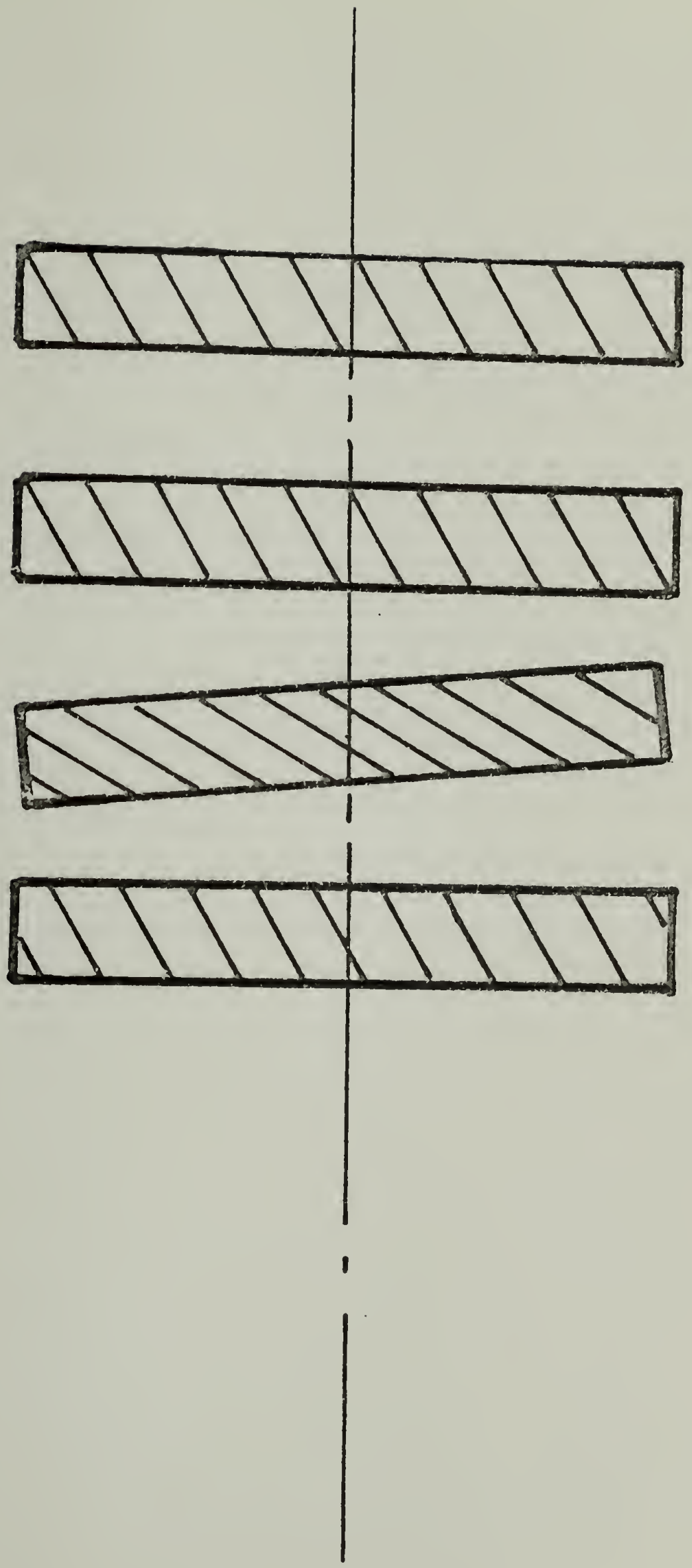

Figure 7

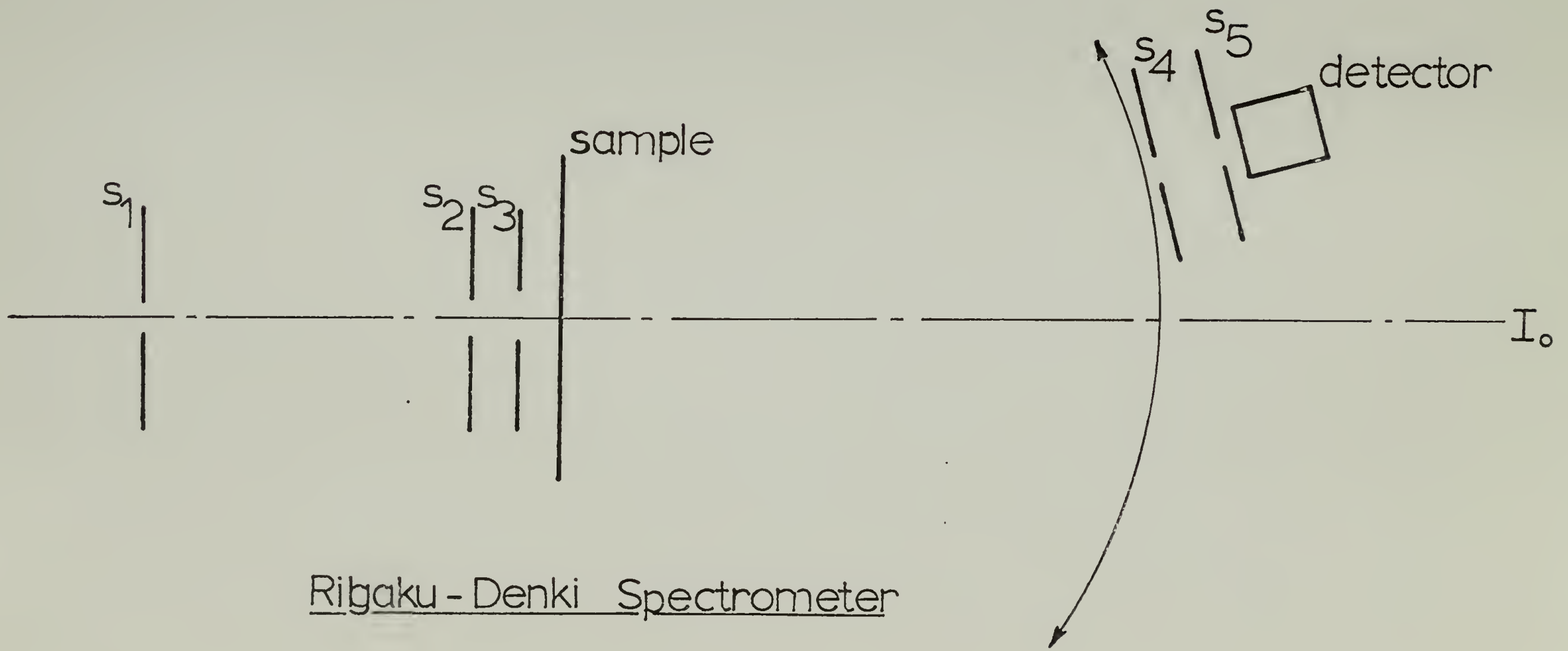

Rigaku-Denki Spectrometer

Figure 8

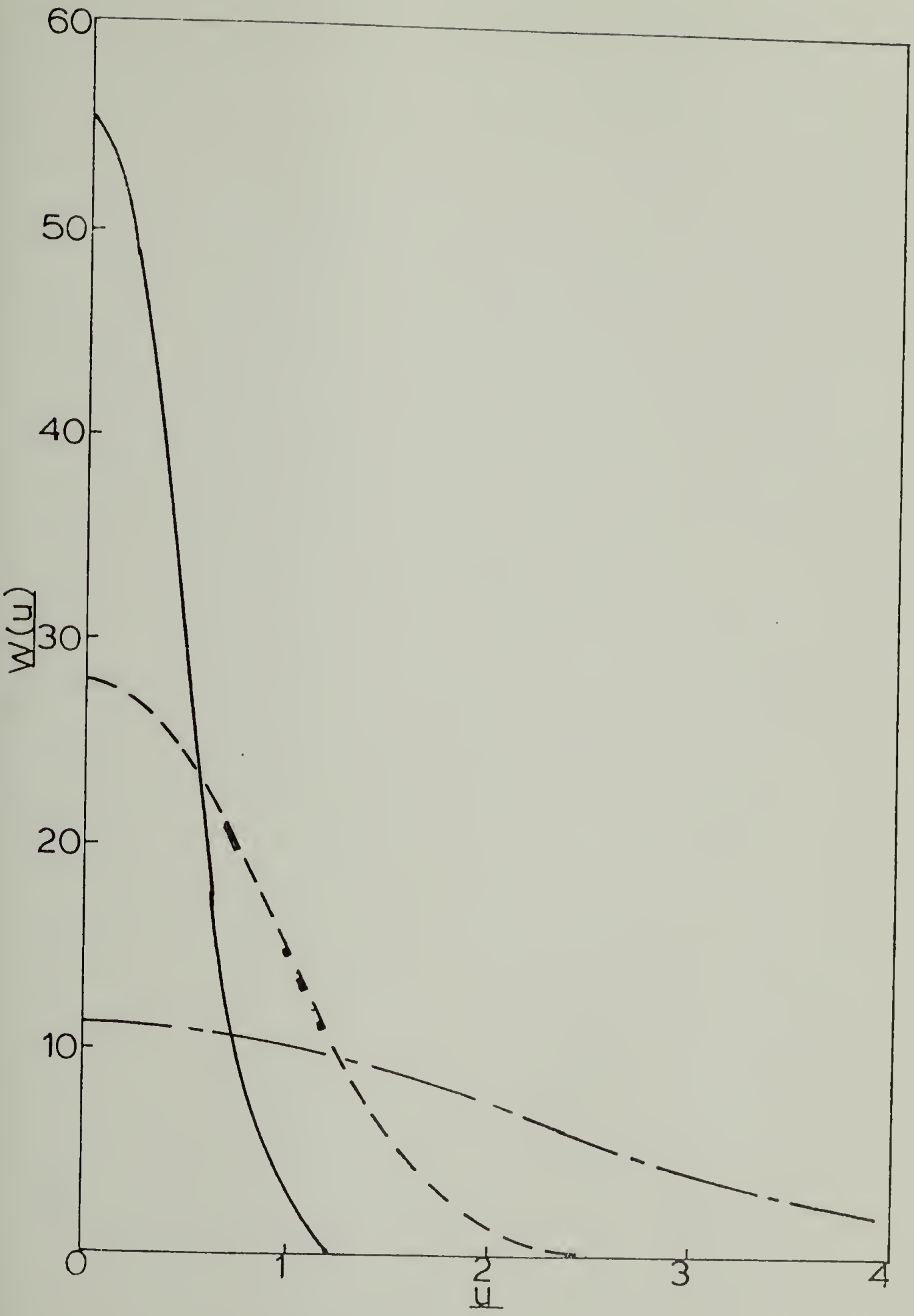

Figure 9

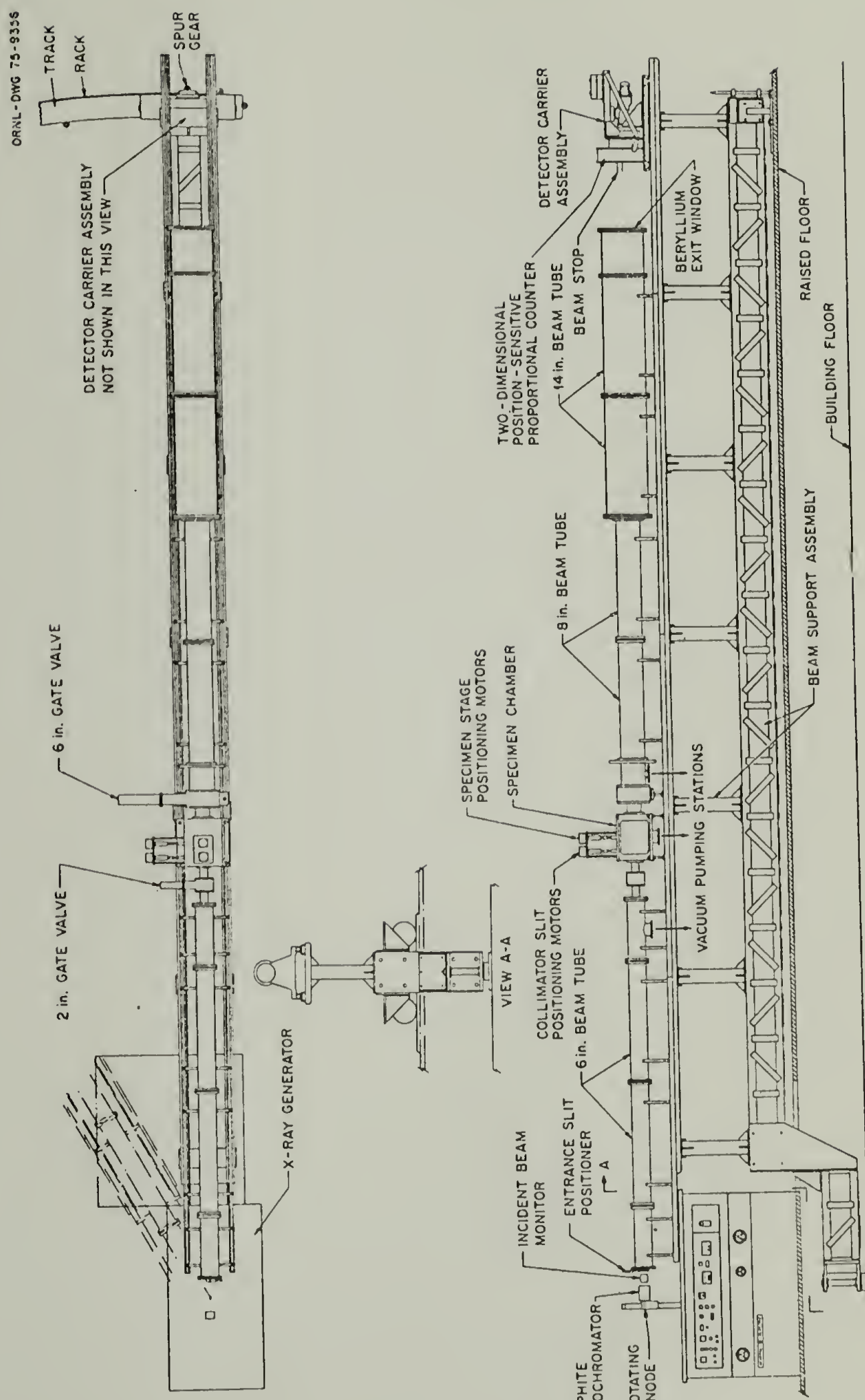
ORNL-DWG 73-9336
TRACK
RACK
SPUR GEAR
DETECTOR CARRIER ASSEMBLY NOT SHOWN IN THIS VIEW
6 in. GATE VALVE
2 in. GATE VALVE
X-RAY GENERATOR
VIEW A-A
SPECIMEN STAGE POSITIONING MOTORS
SPECIMEN CHAMBER
COLLIMATOR SLIT POSITIONING MOTORS
6 in. BEAM TUBE
VACUUM PUMPING STATIONS
INCIDENT BEAM MONITOR
ENTRANCE SLIT POSITIONER
A
GRAPHITE MONOCHROMATOR
ROTATING ANODE
TWO-DIMENSIONAL POSITION-SENSITIVE PROPORTIONAL COUNTER
14 in. BEAM TUBE
BEAM STOP
DETECTOR CARRIER ASSEMBLY
BERYLLIUM EXIT WINDOW
RAISED FLOOR
BUILDING FLOOR
BEAM SUPPORT ASSEMBLY
A

Figure 10

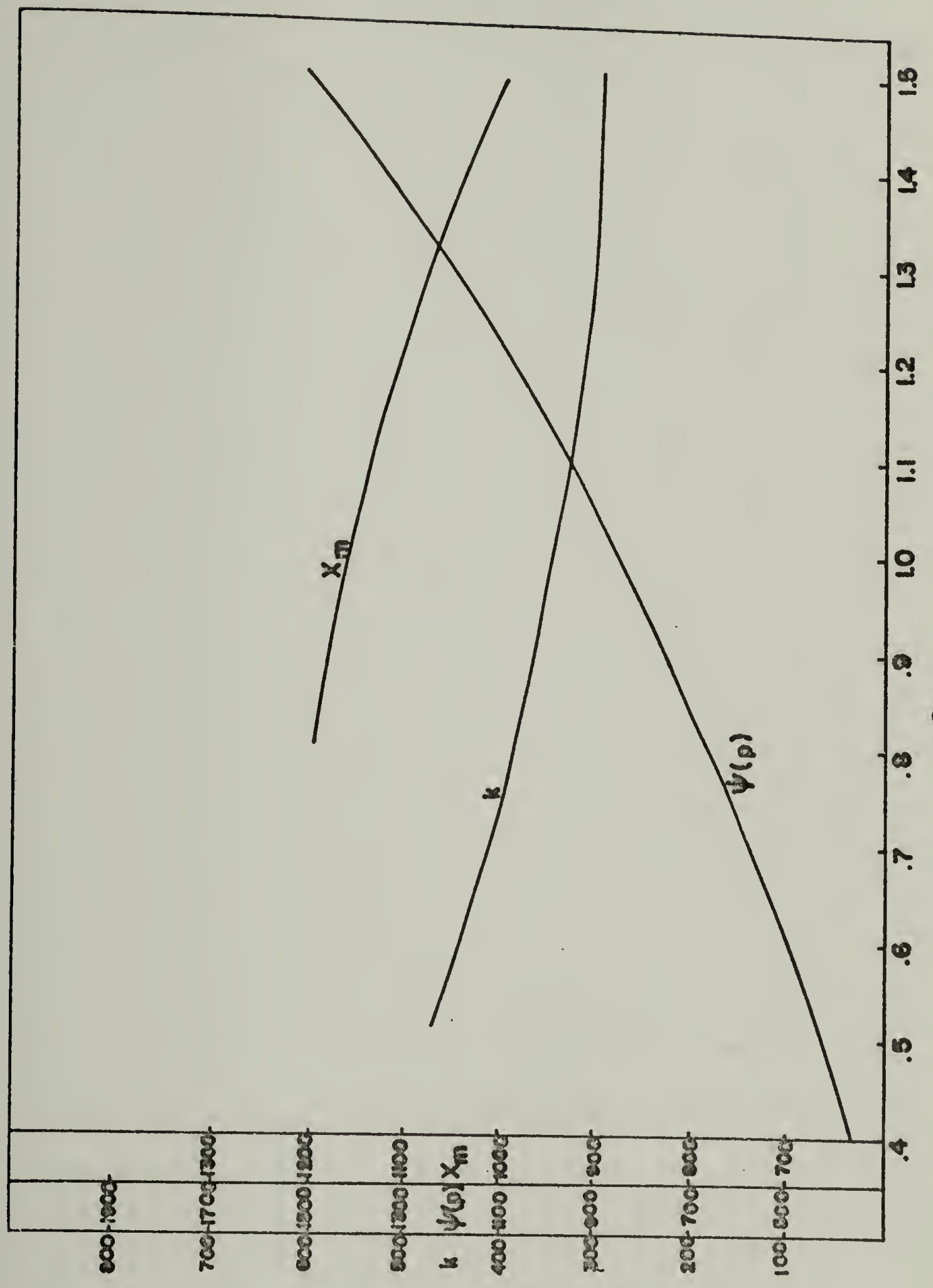
X_m
k
$\psi(\rho)$
k $\psi(\rho)$ X_m
800 1900
700 1700 1300
600 1500 1200
500 1300 1100
400 1100 1000
300 900 900
200 700 800
100 500 700
.4 .5 .6 .7 .8 .9 1.0 1.1 1.2 1.3 1.4 1.5
ρ

Figure 11

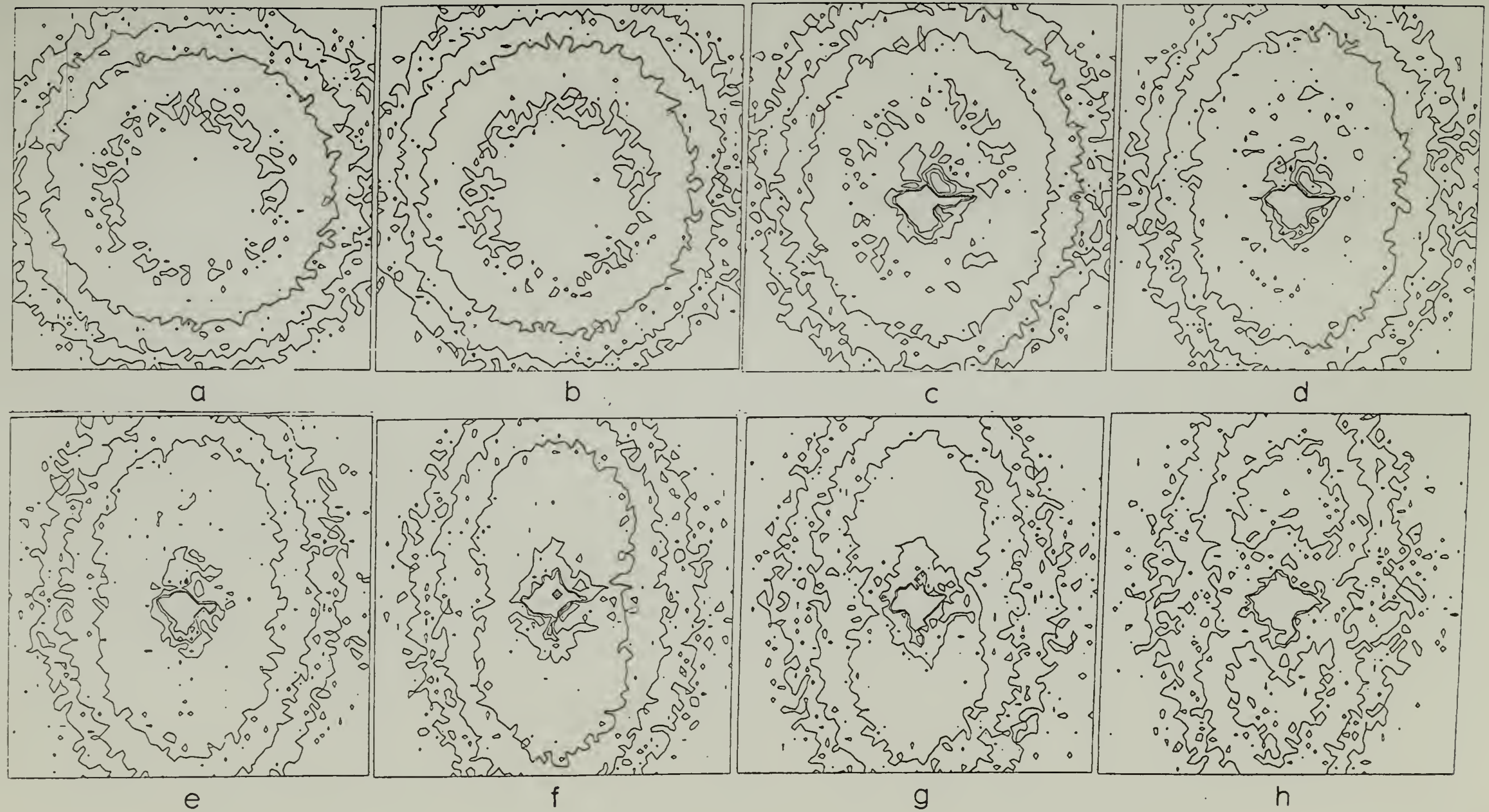

Figure 12

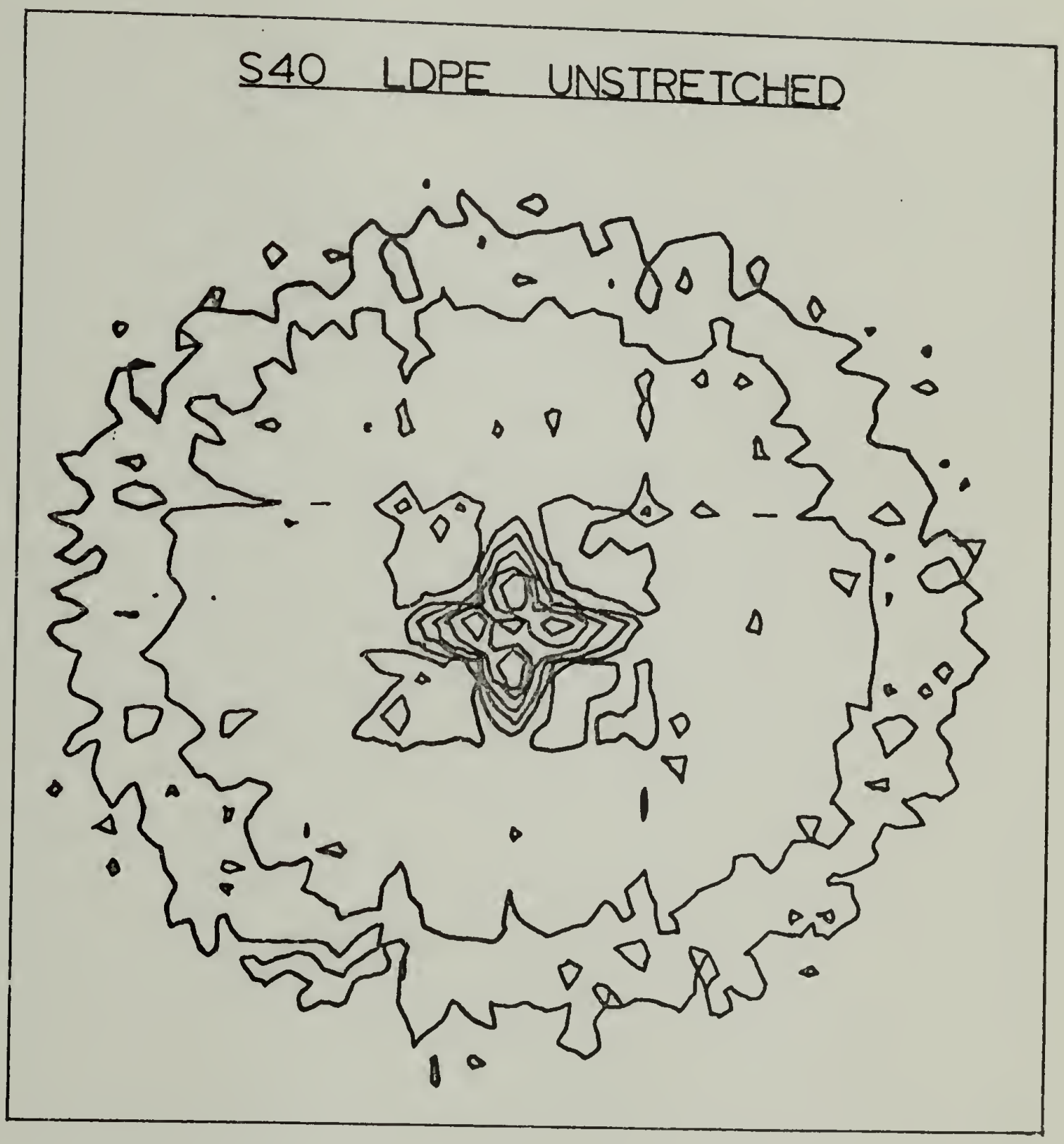

Figure 13

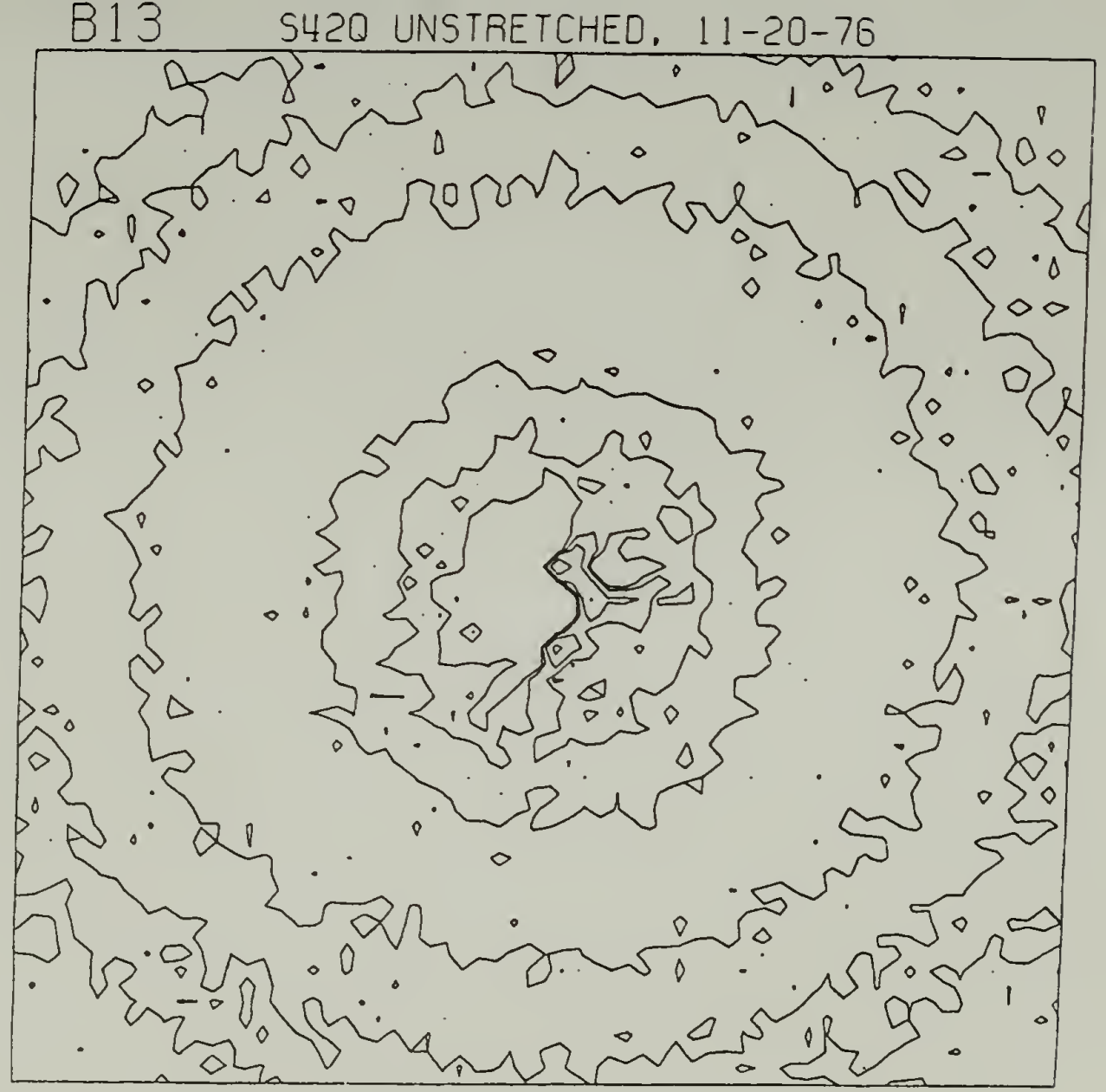

Figure 14a

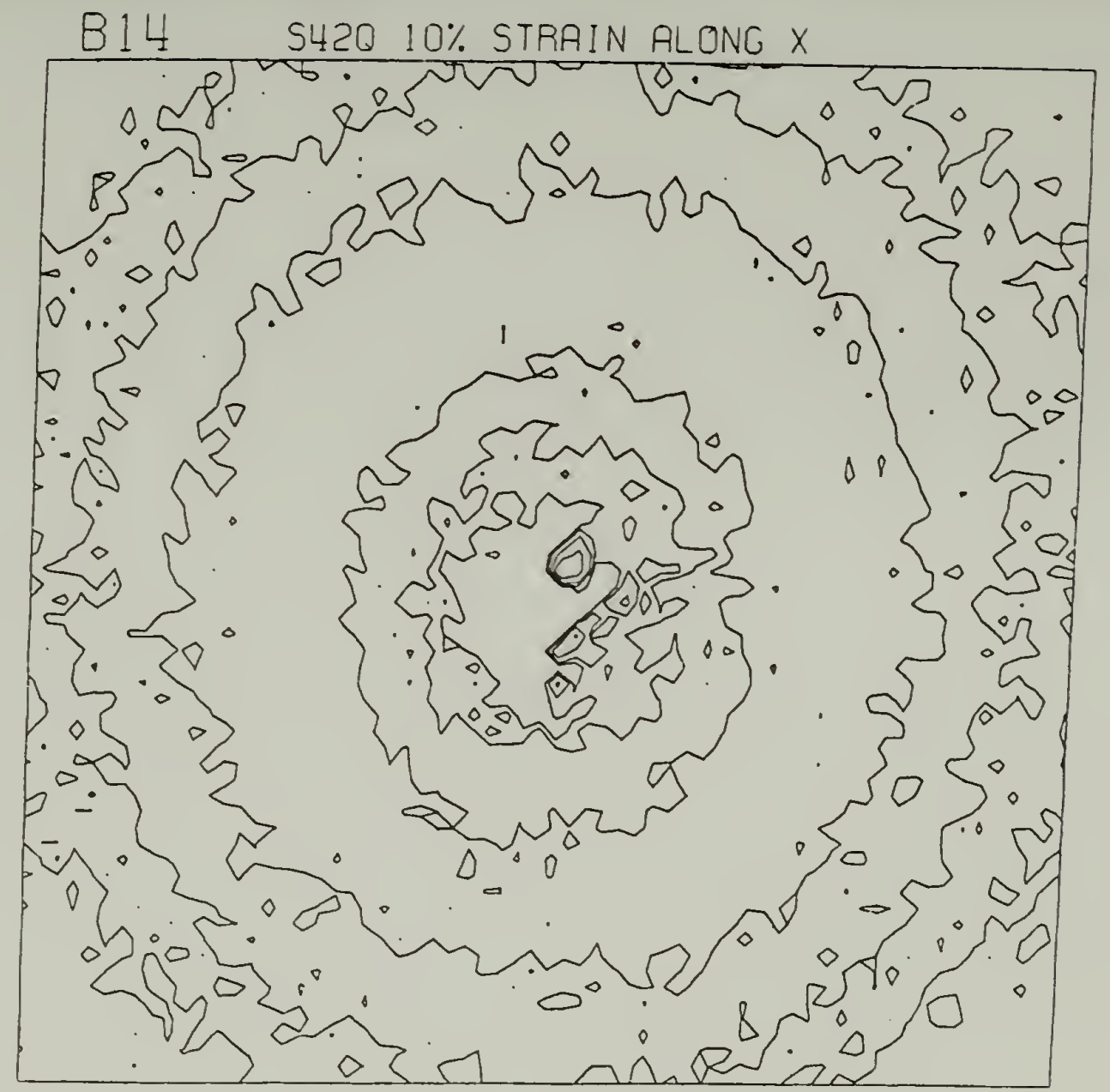

Figure 14b

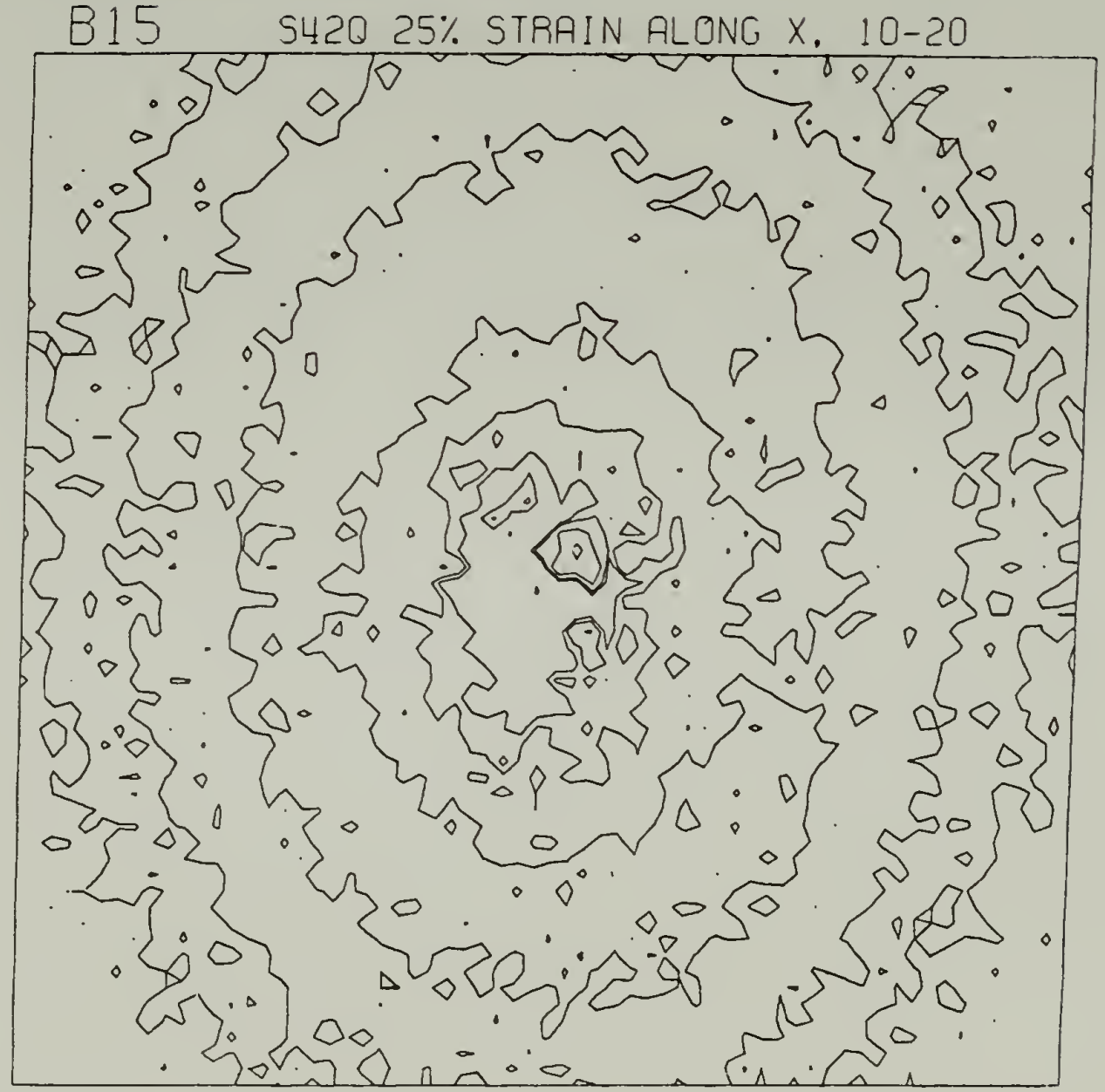

Figure 14c

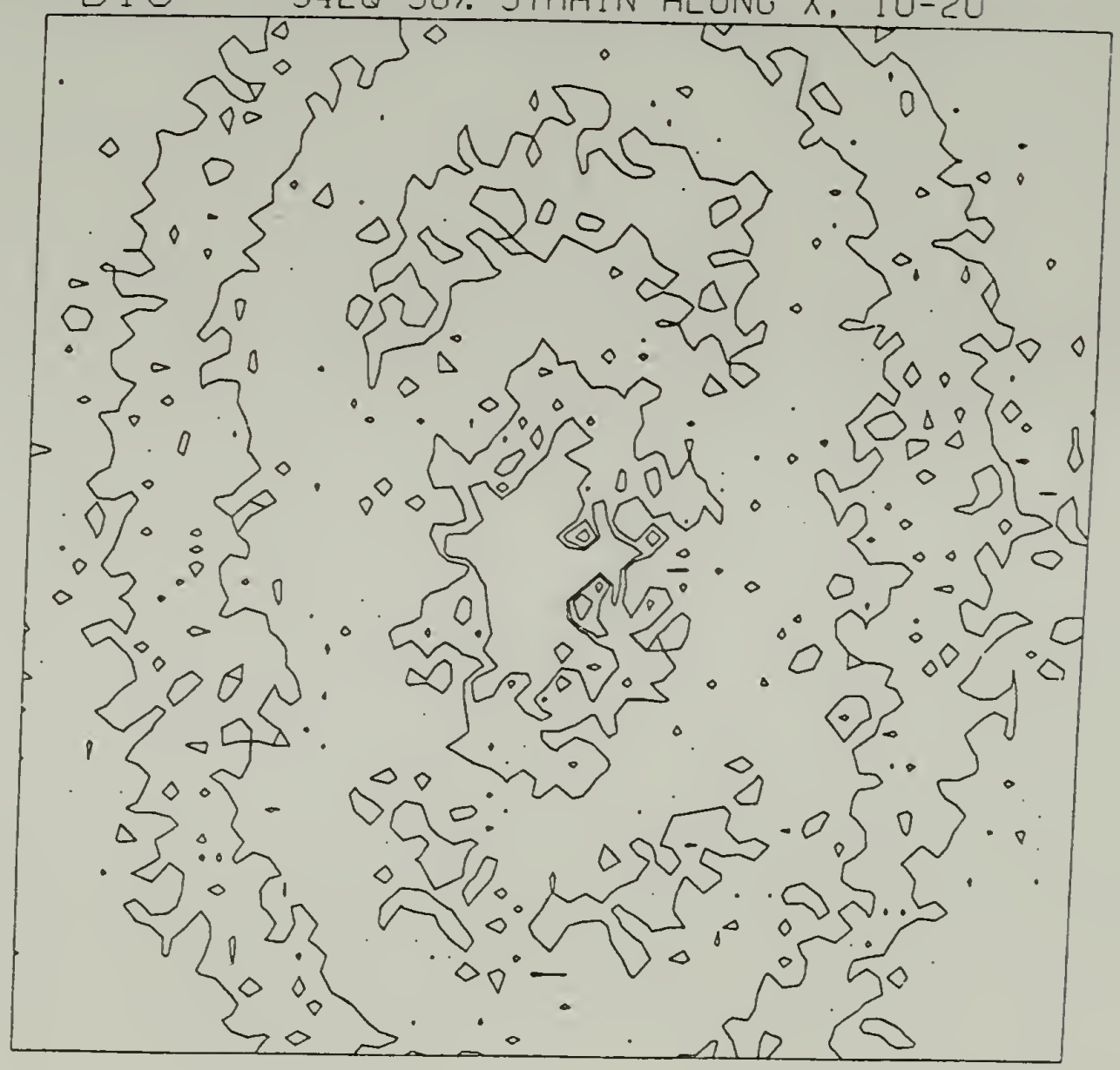

Figure 14d

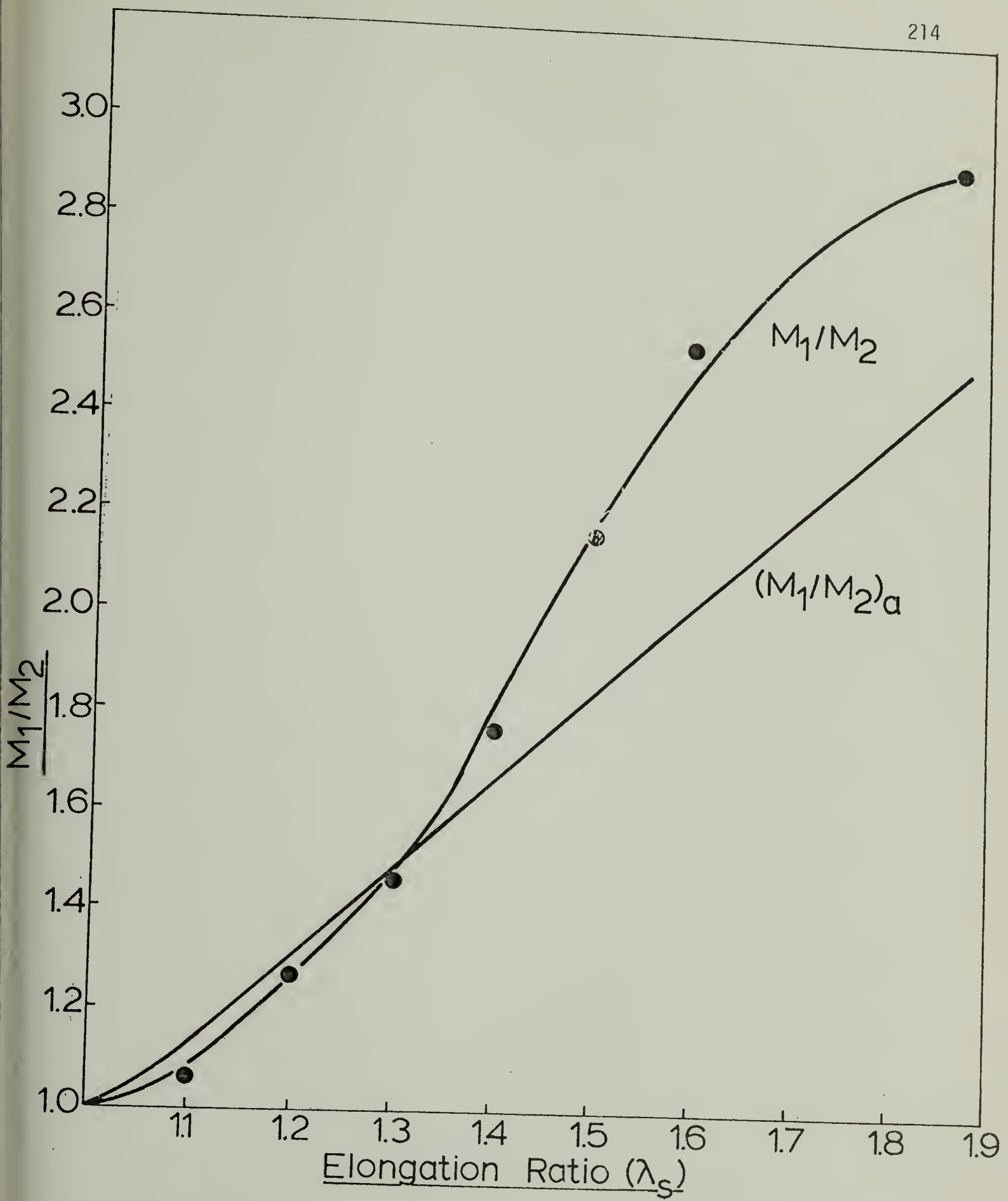
3.0
2.8
2.6
2.4
2.2
2.0
1.8
1.6
1.4
1.2
1.0
M1/M2
M1/M2
(M1/M2)a
1.1
1.2
1.3
1.4
1.5
1.6
1.7
1.8
1.9
Elongation Ratio (λs)

Figure 15

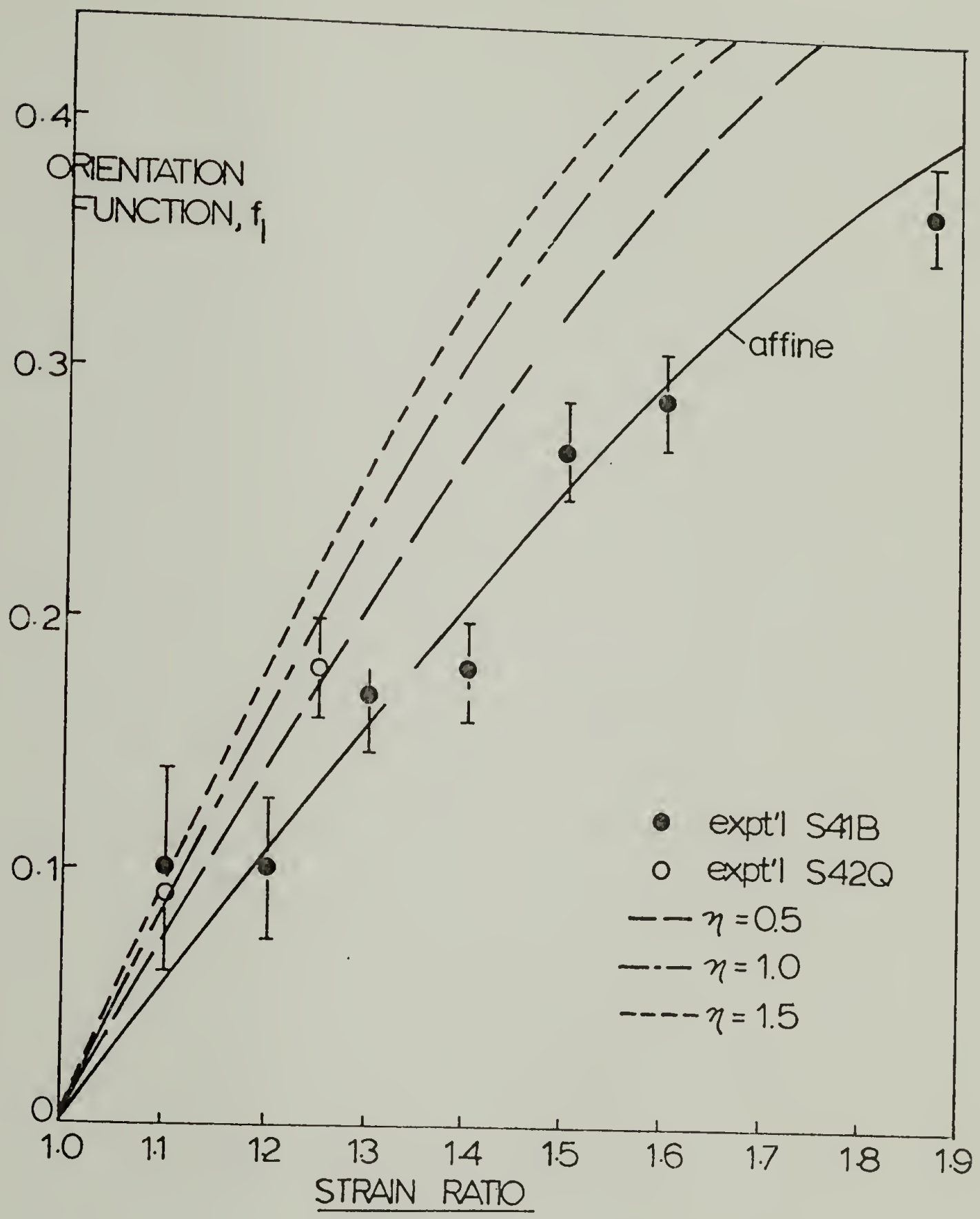
0·4
ORIENTATION
FUNCTION, f_1
0·3
0·2
0·1
0
affine
expt'l S41B
expt'l S42Q
$\eta = 0.5$
$\eta = 1.0$
$\eta = 1.5$
1·0
1·1
1·2
1·3
1·4
1·5
1·6
1·7
1·8
1·9
STRAIN RATIO

Figure 16

SALS OF DEFORMED LDPE

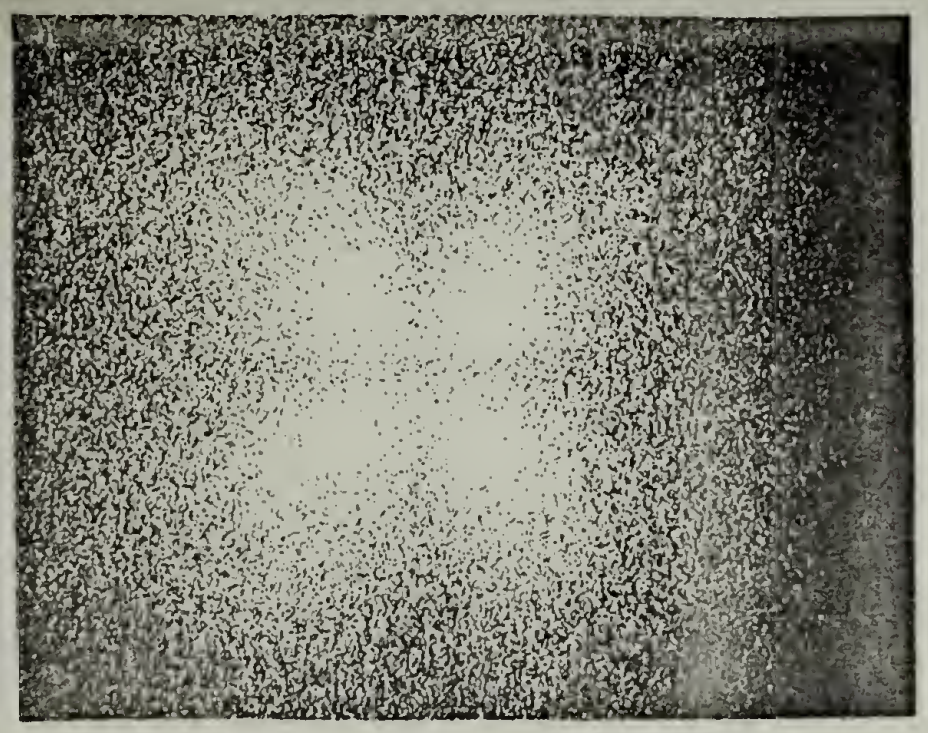

λ = 1.0

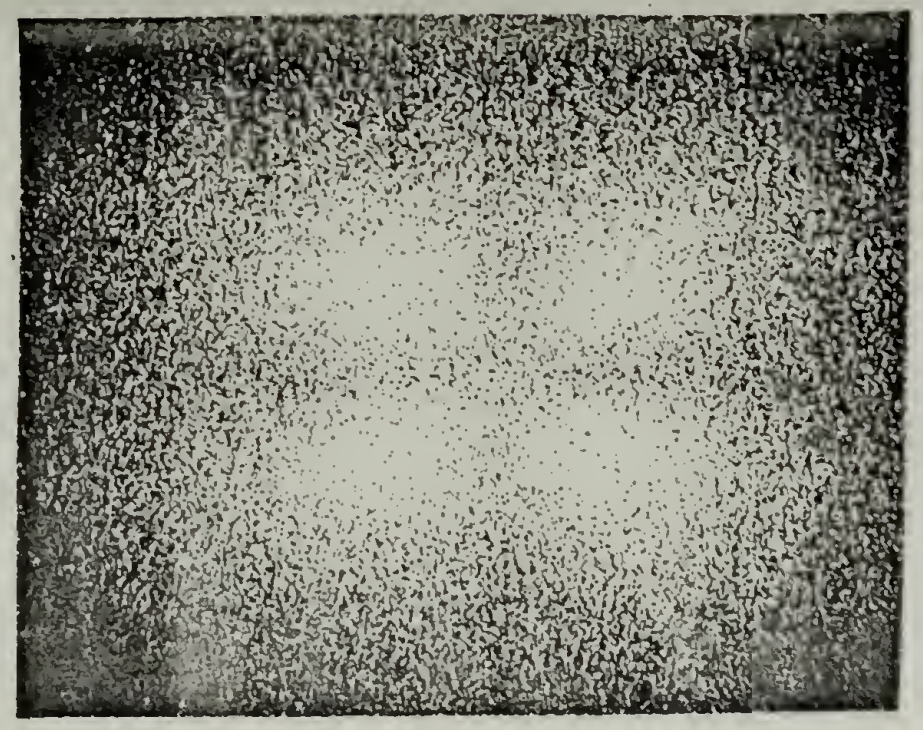

1.1

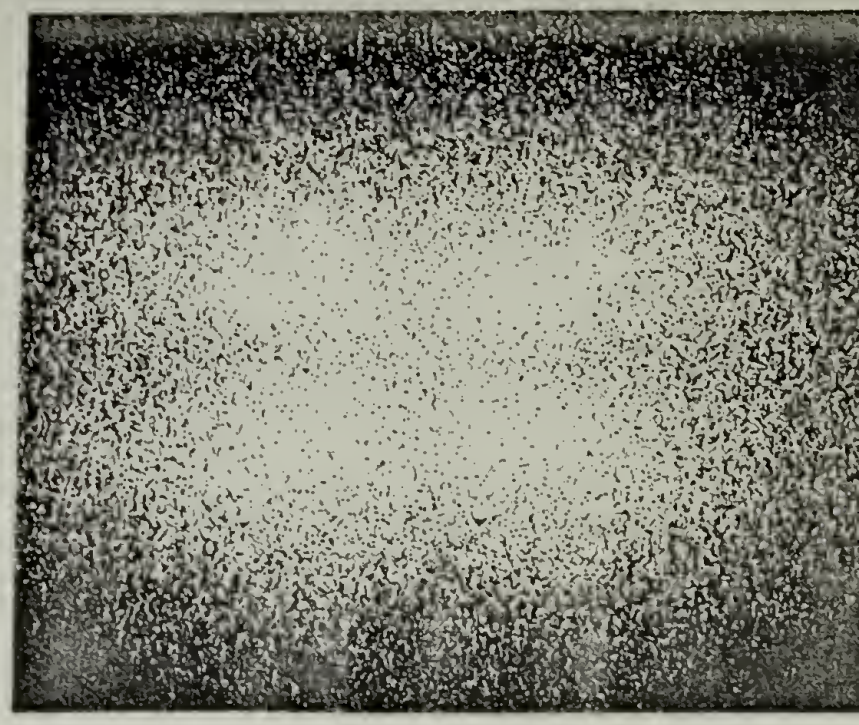

1.2

S.D.

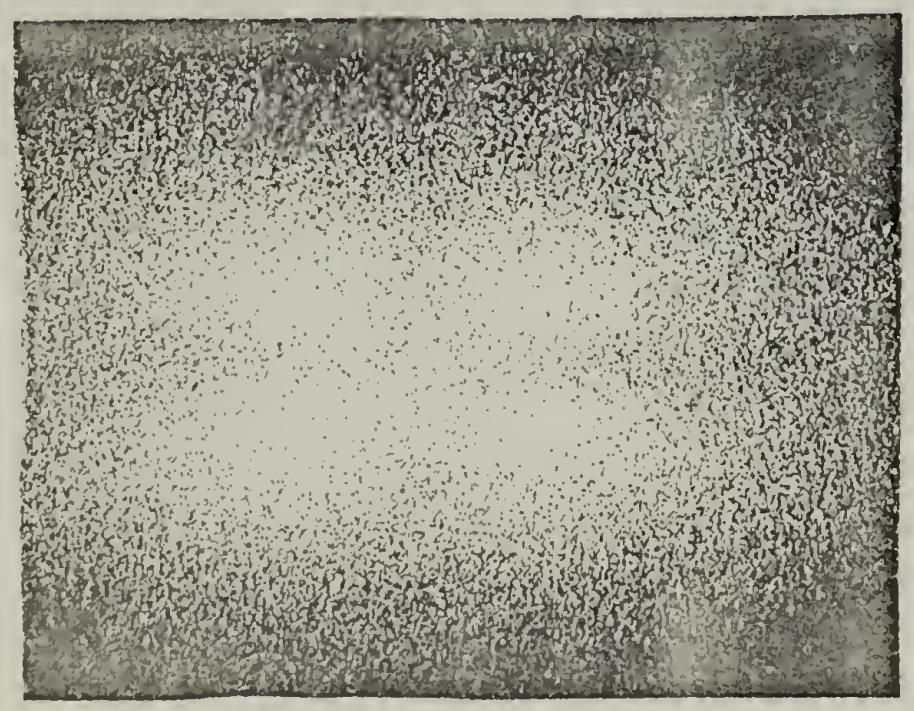

1.3

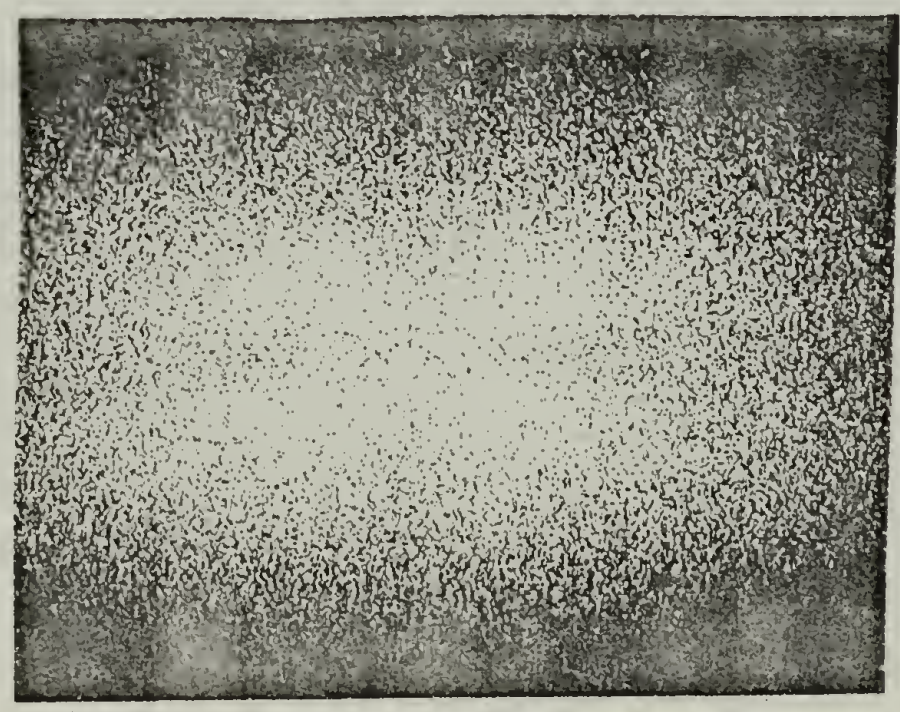

1.4

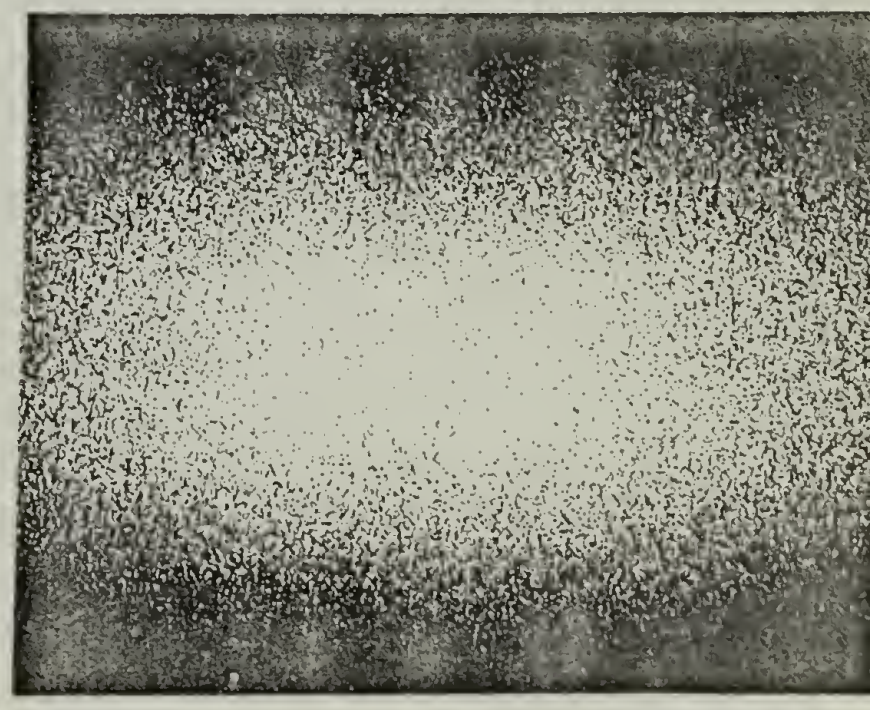

1.5

SPHERULITE vs. SAMPLE EXTENSION

For LDPE

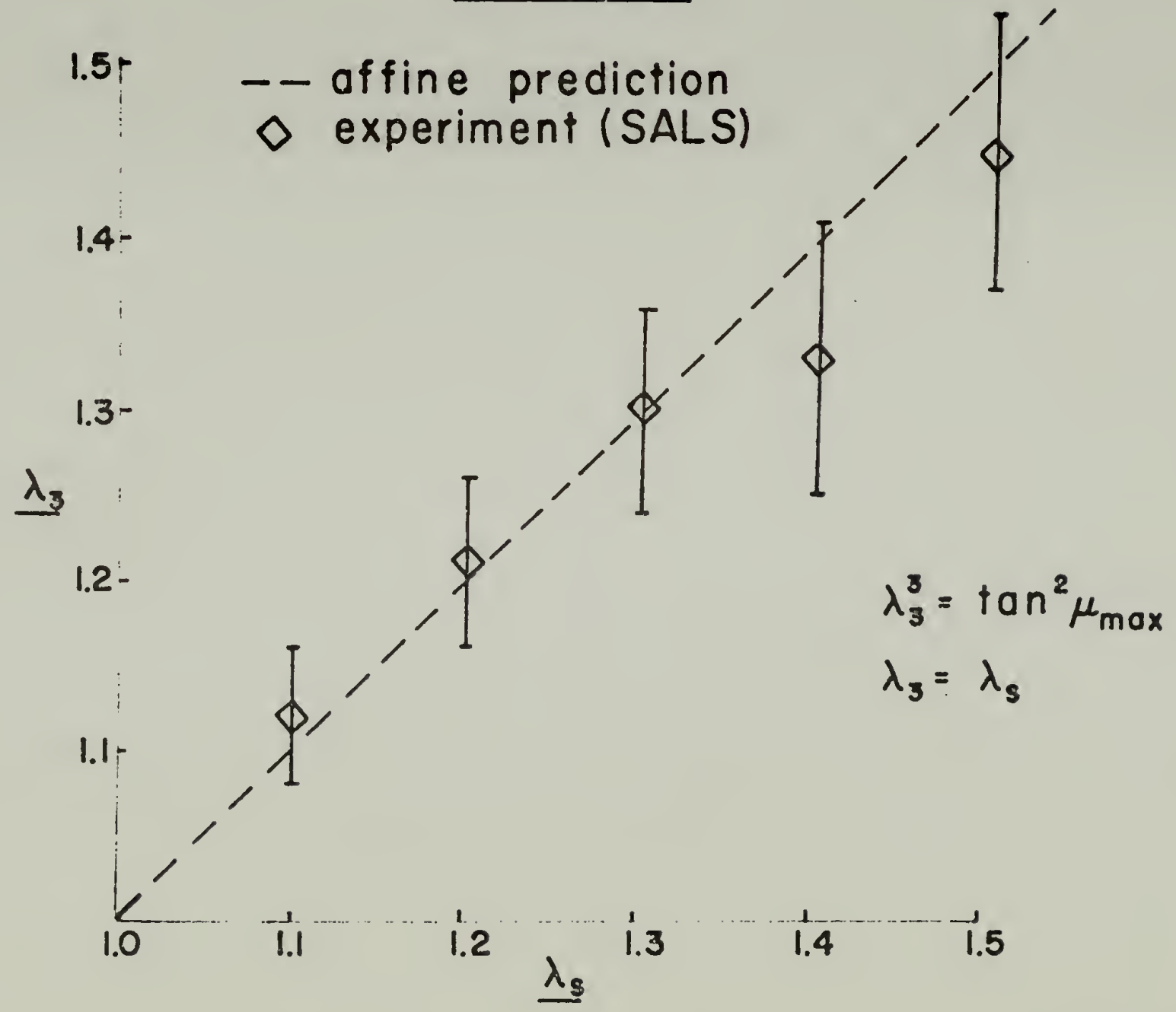

Figure 18

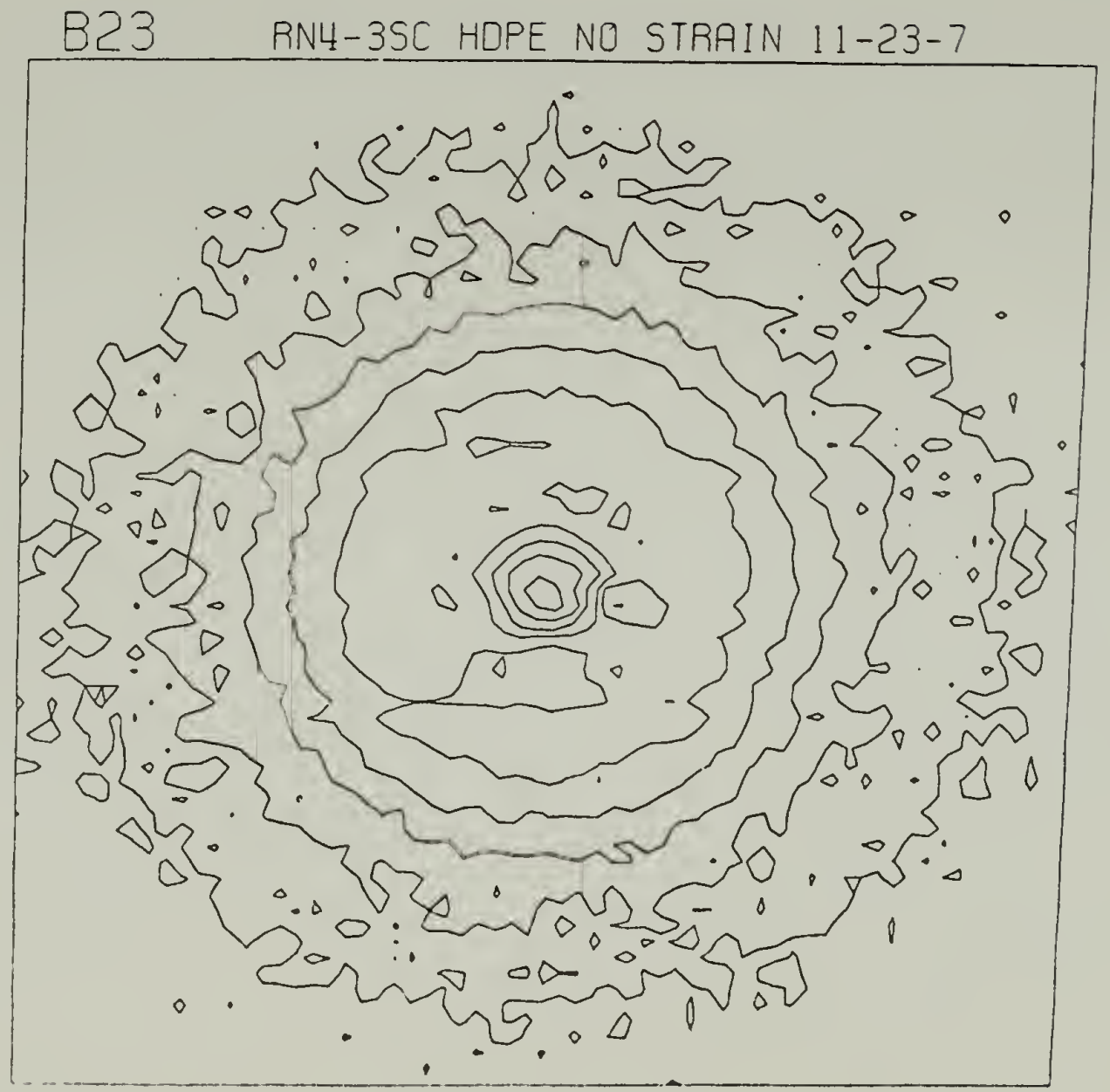

Figure 19a

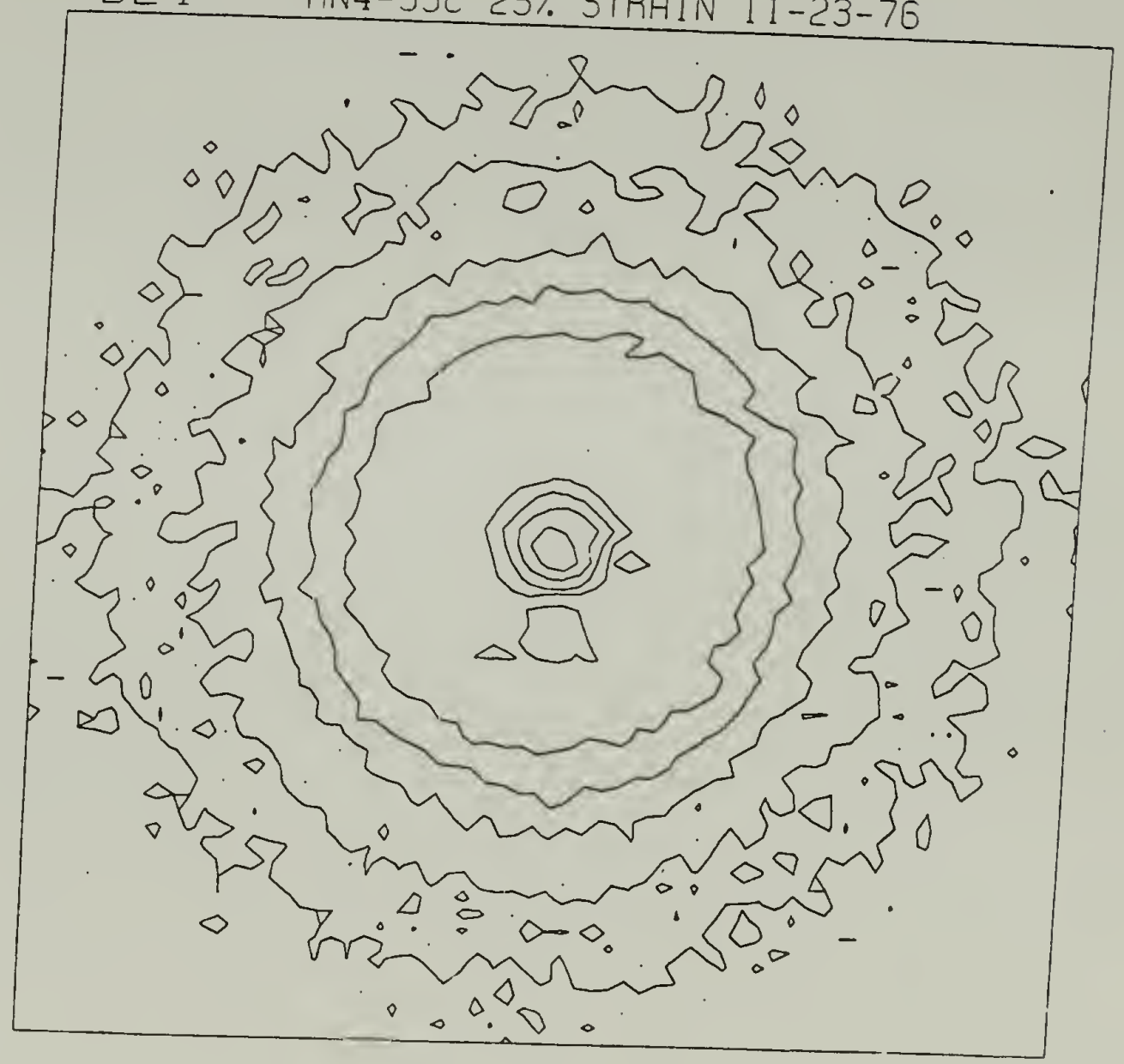

Figure 19b

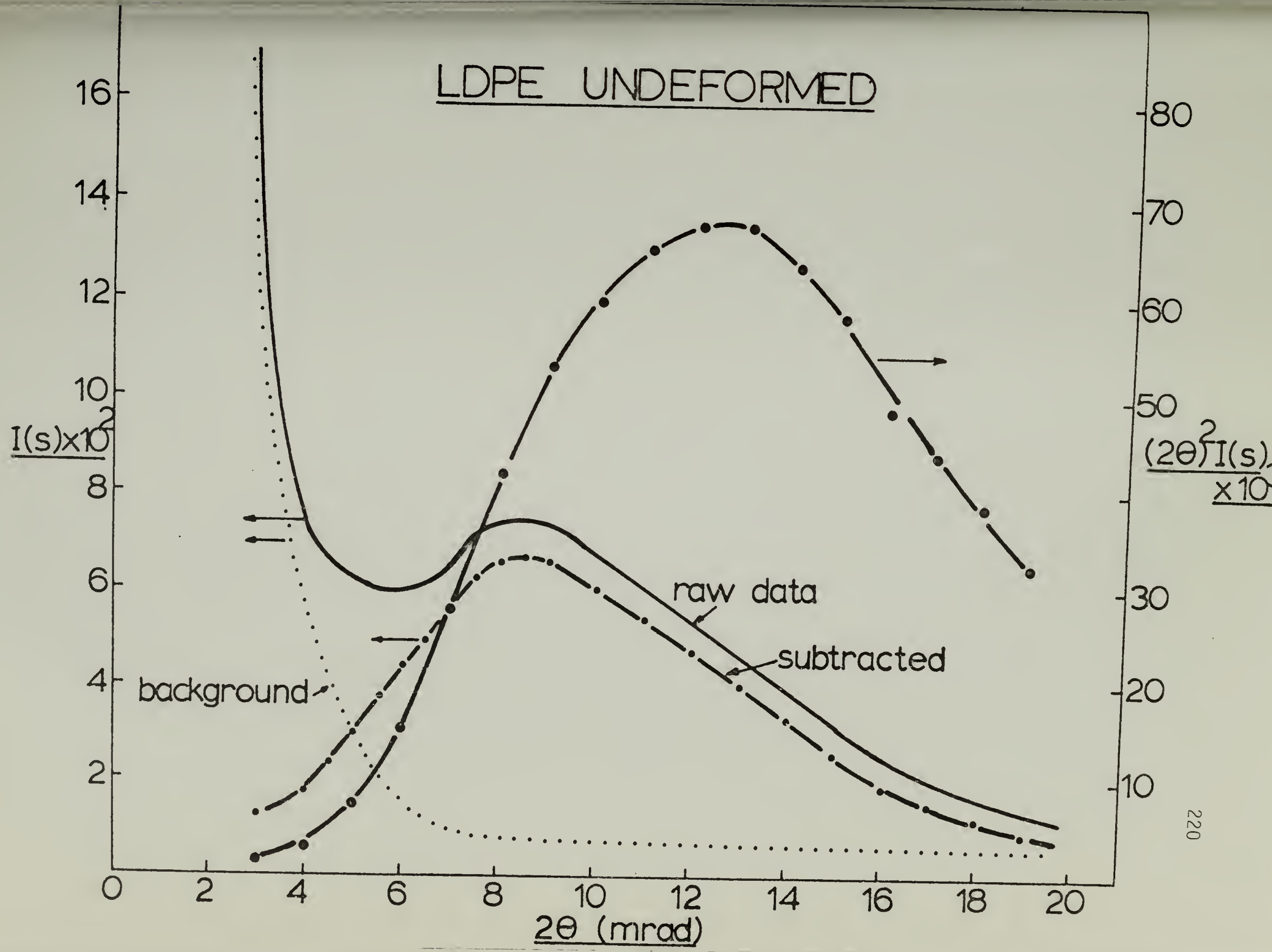
LDPE UNDEFORMED
I(s)x10²
(2θ)²I(s) x10³
raw data
subtracted
background
2θ (mrad)
0
2
4
6
8
10
12
14
16
18
20
10
20
30
50
60
70
80

Figure 20

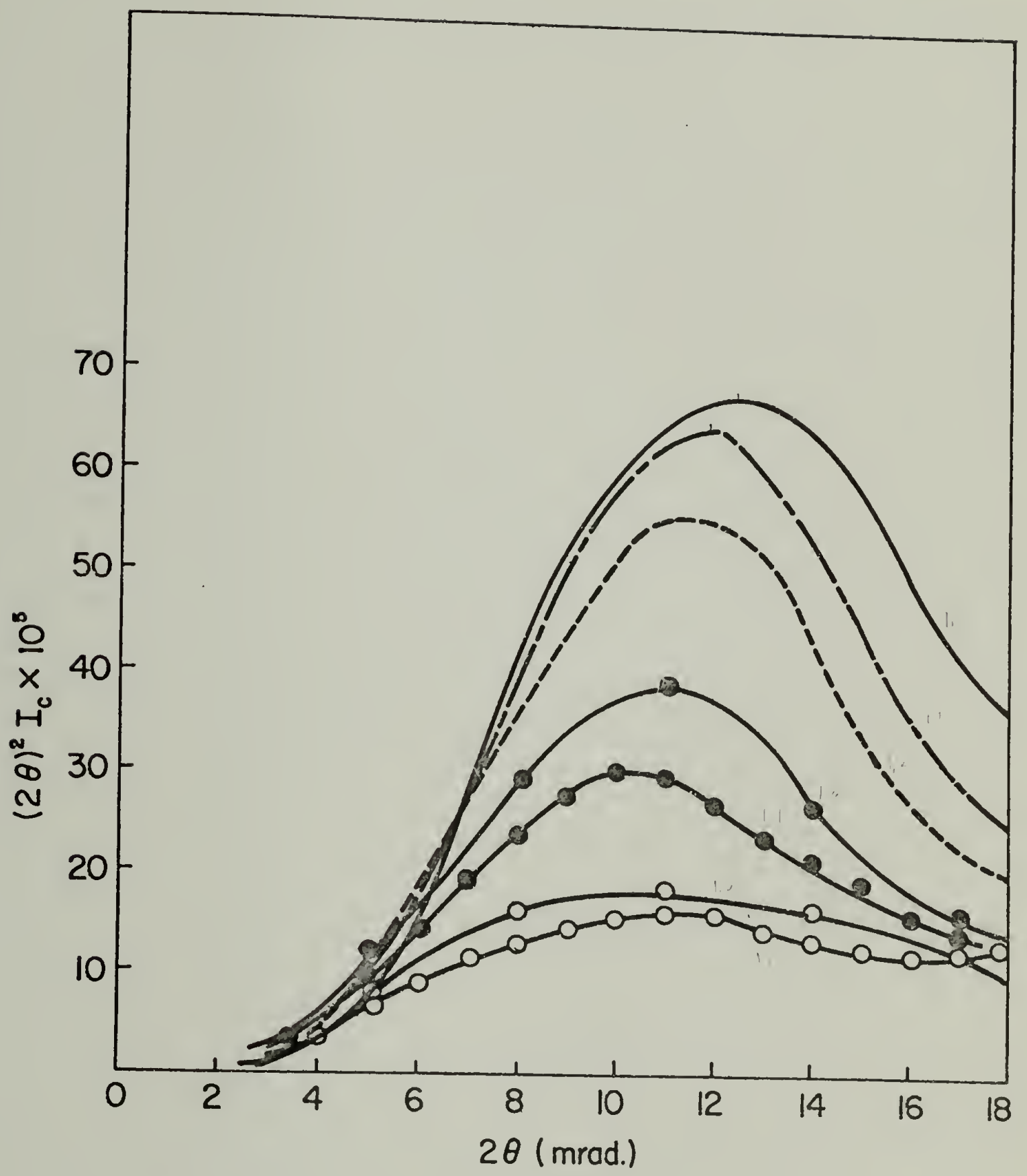
70
60
50
40
30
20
10
$(2\theta)^2 I_c \times 10^5$
0
2
4
6
8
10
12
14
16
18
2θ (mrad.)

Figure 21a

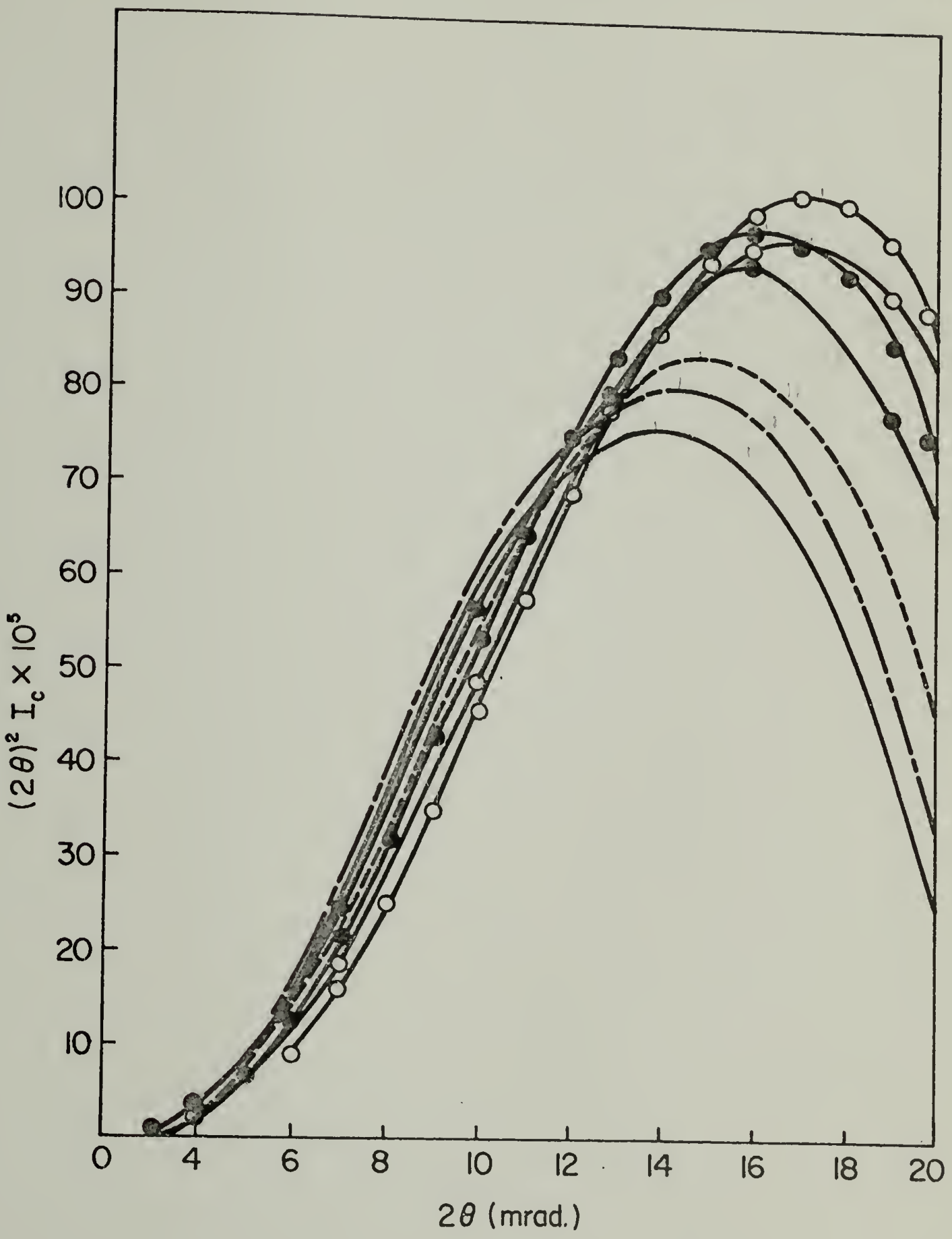
100
90
80
70
60
50
40
30
20
10
$(2\theta)^2 I_c \times 10^5$
0
4
6
8
10
12
14
16
18
20
2θ (mrad.)

Figure 21b

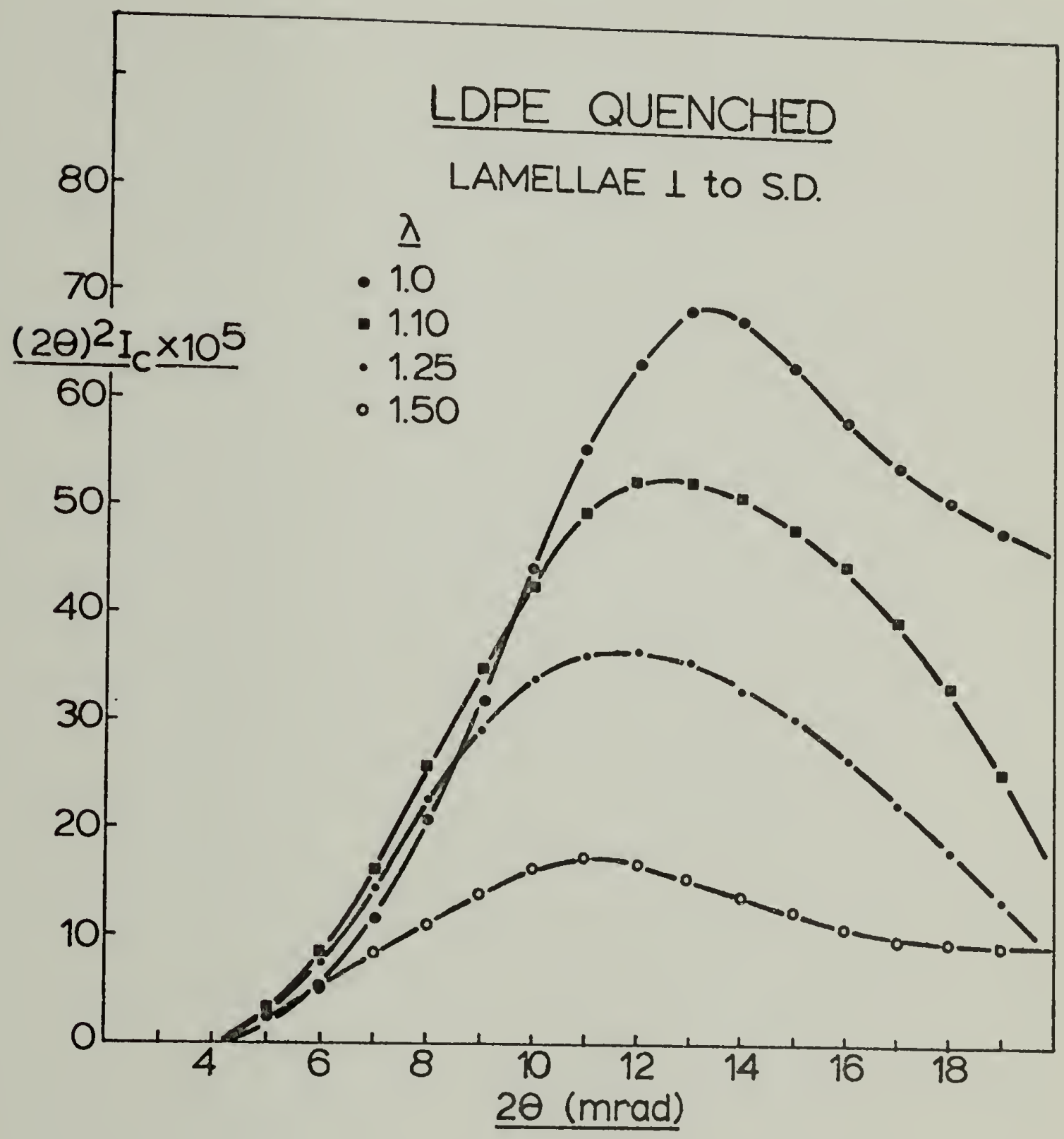
LDPE QUENCHED
LAMELLAE ⊥ to S.D.
λ
• 1.0
▪ 1.10
• 1.25
◦ 1.50
(2θ)²I_c x10⁵
80
70
60
50
40
30
20
10
0
4
6
8
10
12
14
16
18
2θ (mrad)

Figure 22a

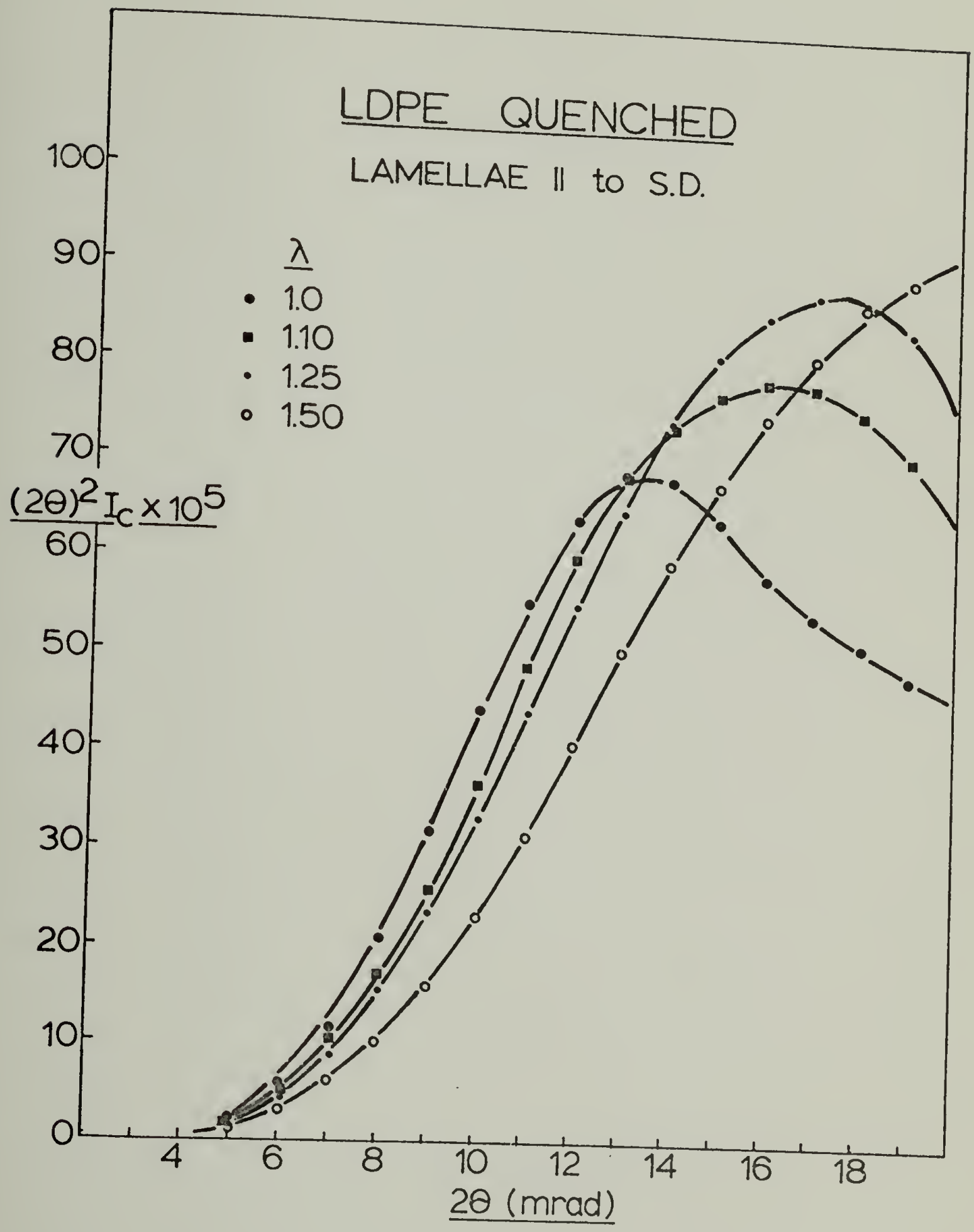
LDPE QUENCHED
LAMELLAE ⊥ to S.D.
λ
1.0
1.10
1.25
1.50
(2θ)² I_c x 10⁵
100
90
80
70
60
50
40
30
20
10
0
4
6
8
10
12
14
16
18
2θ (mrad)

Figure 22b

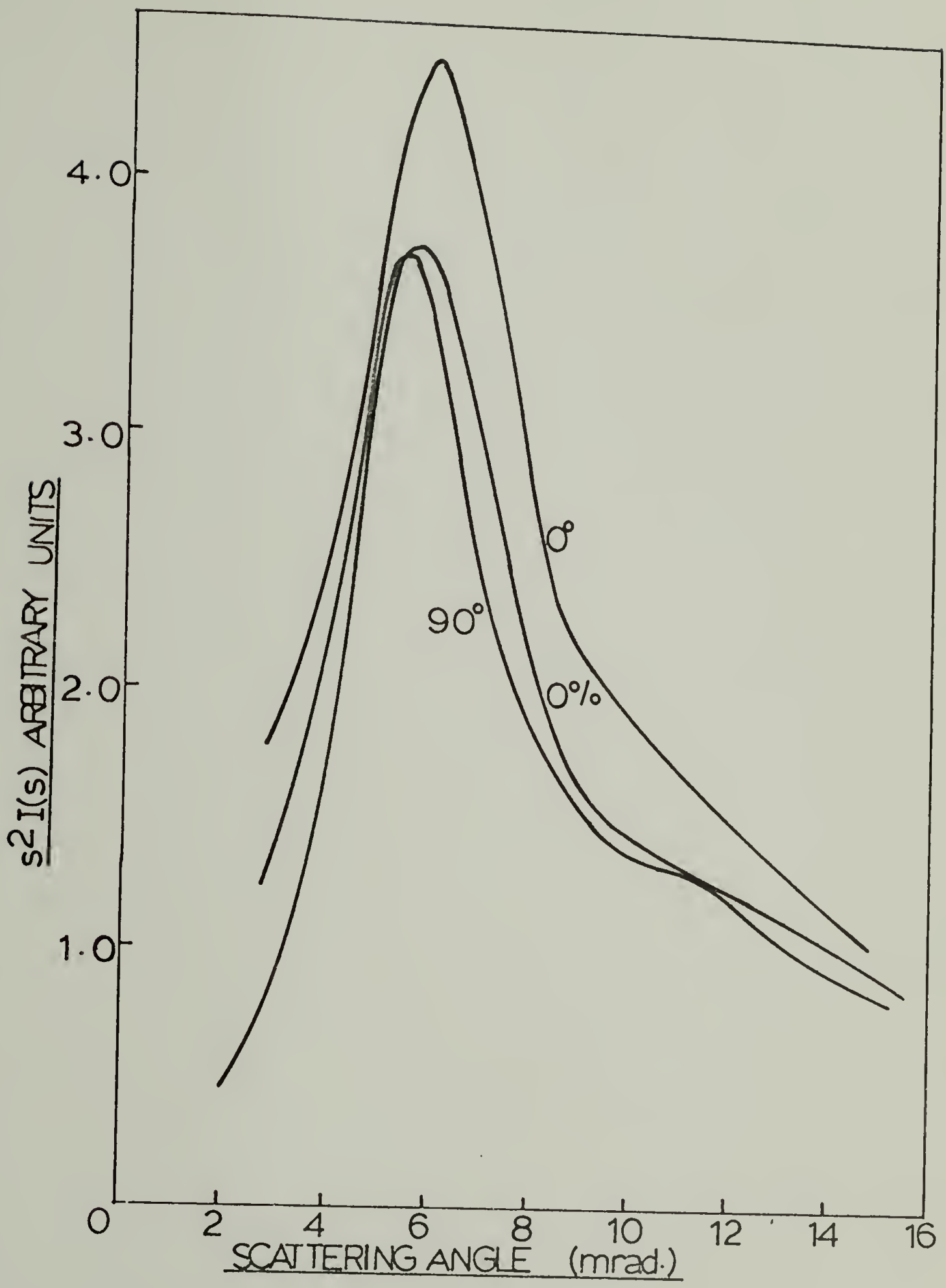
4.0
3.0
2.0
1.0
0
2
4
6
8
10
12
14
16
$s^2 I(s)$ ARBITRARY UNITS
SCATTERING ANGLE (mrad.)
0°
90°
0%

Figure 23

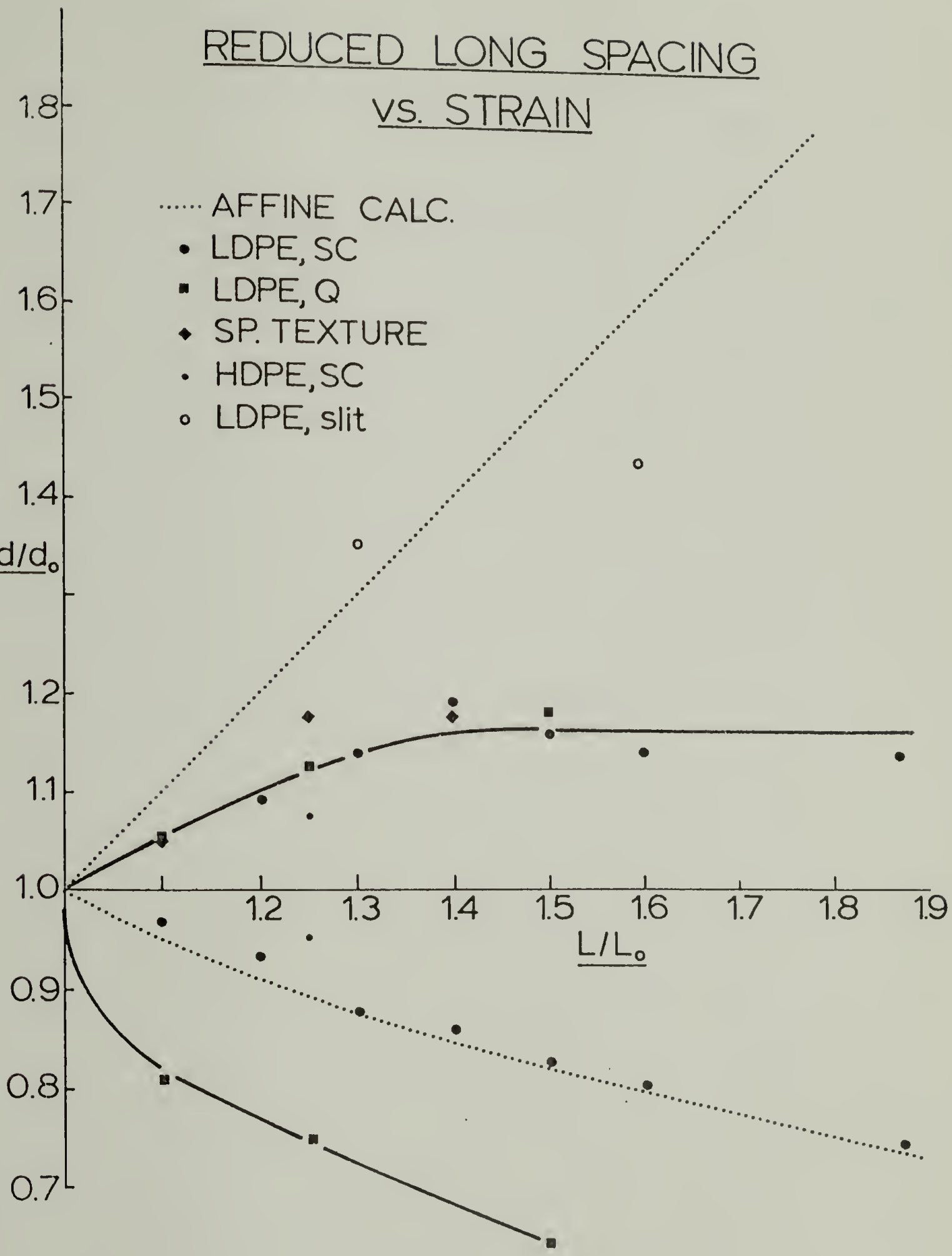
REDUCED LONG SPACING
VS. STRAIN
..... AFFINE CALC.
• LDPE, SC
▪ LDPE, Q
◆ SP. TEXTURE
• HDPE, SC
o LDPE, slit
d/d₀
L/L₀
1.8
1.7
1.6
1.5
1.4
1.2
1.1
1.0
0.9
0.8
0.7
1.2
1.3
1.4
1.5
1.6
1.7
1.8
1.9

Figure 24

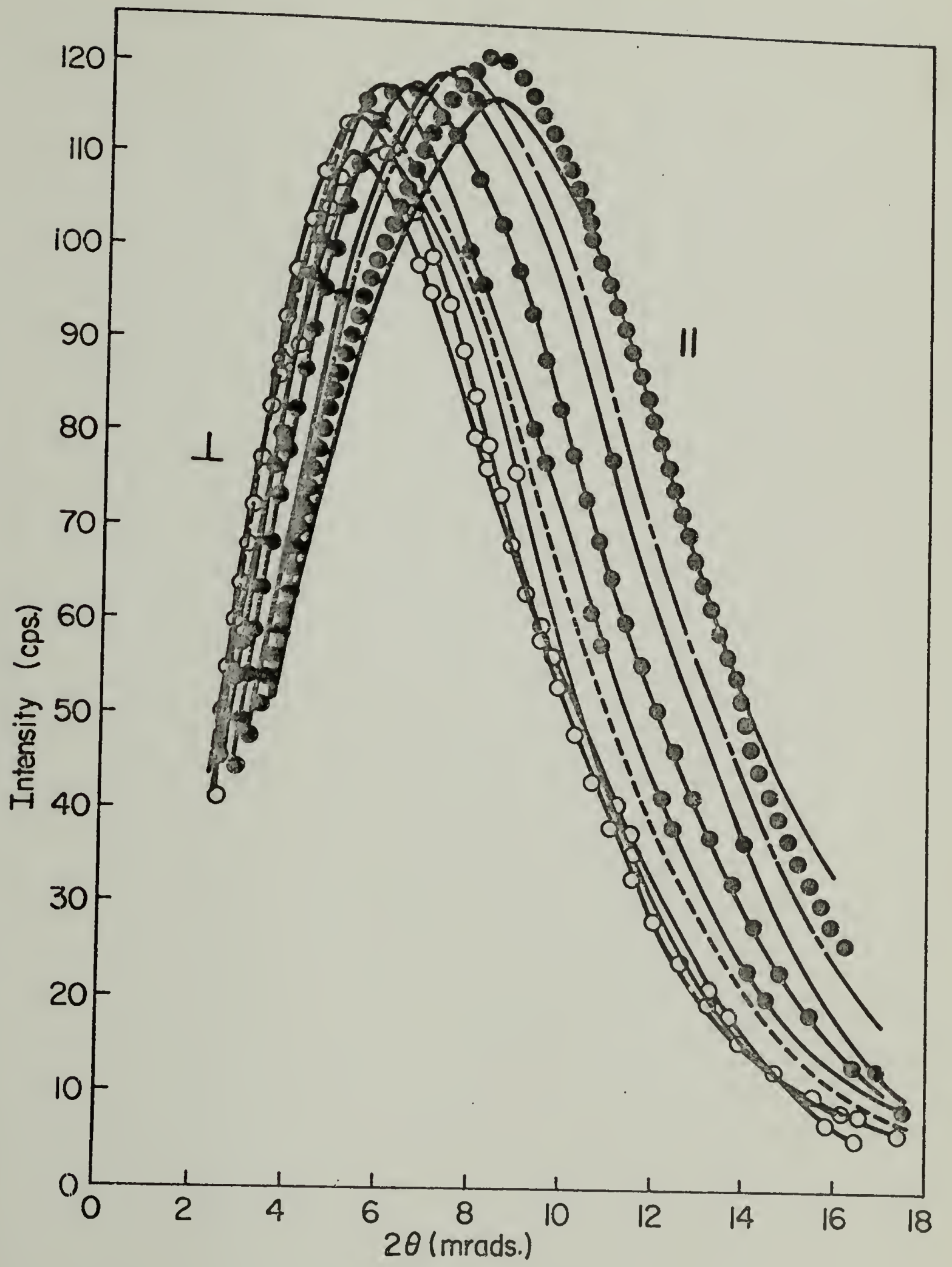
120
110
100
90
80
70
60
50
40
30
20
10
0
Intensity (cps.)
0
2
4
6
8
10
12
14
16
18
2θ (mrads.)
⊥
II

Figure 25

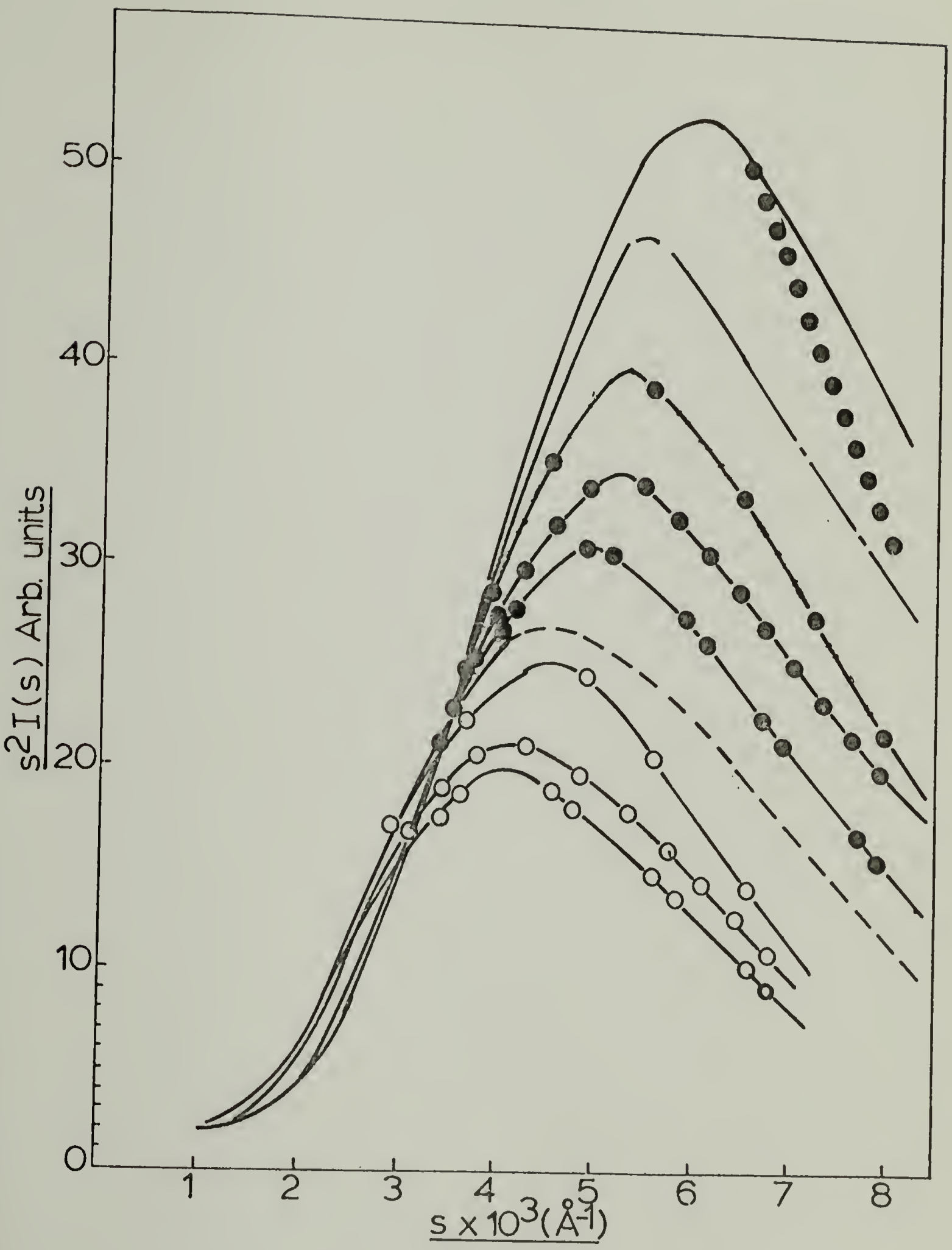

Figure 26

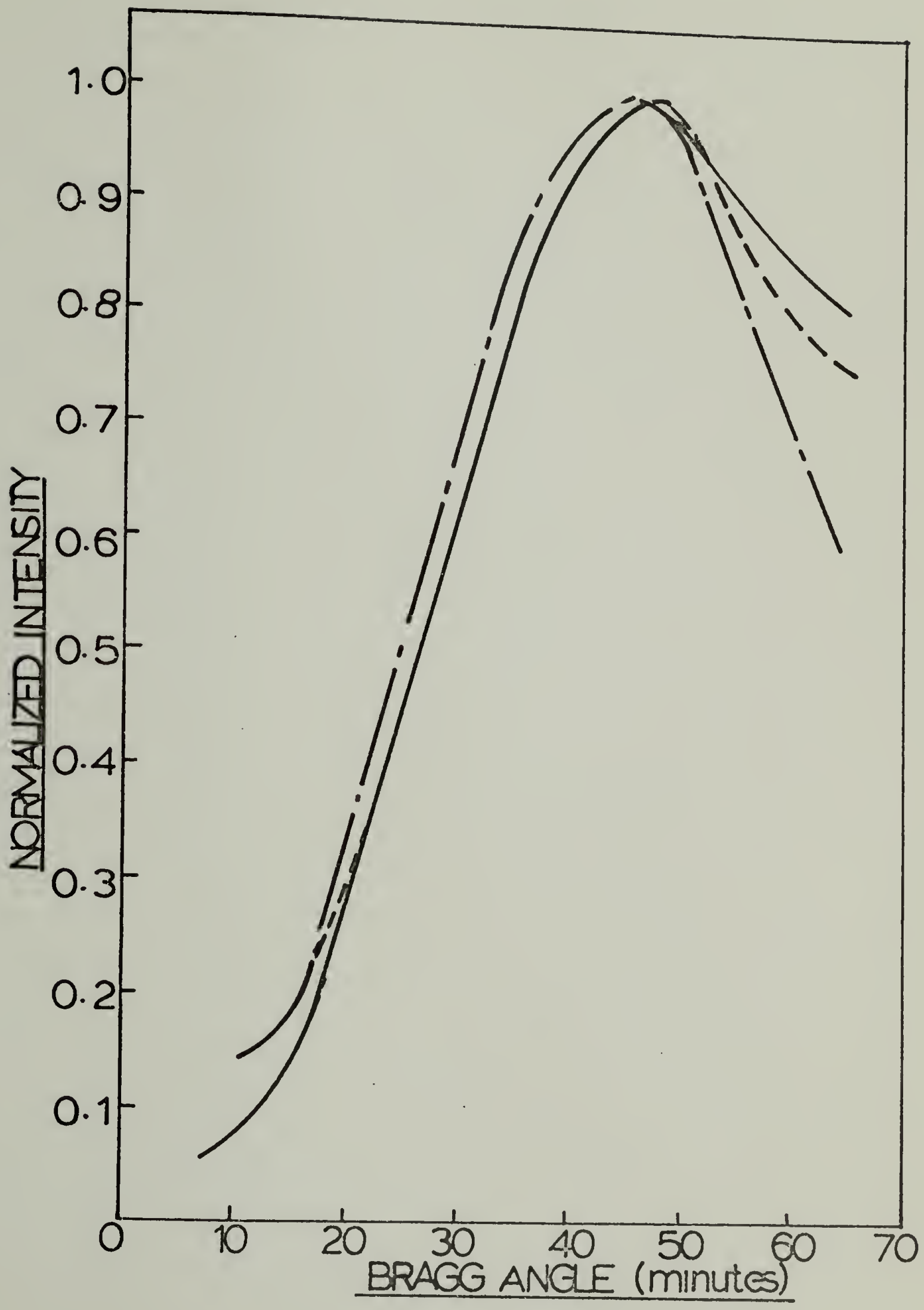
NORMALIZED INTENSITY
1.0
0.9
0.8
0.7
0.6
0.5
0.4
0.3
0.2
0.1
0
10
20
30
40
50
60
70
BRAGG ANGLE (minutes)

Figure 27a

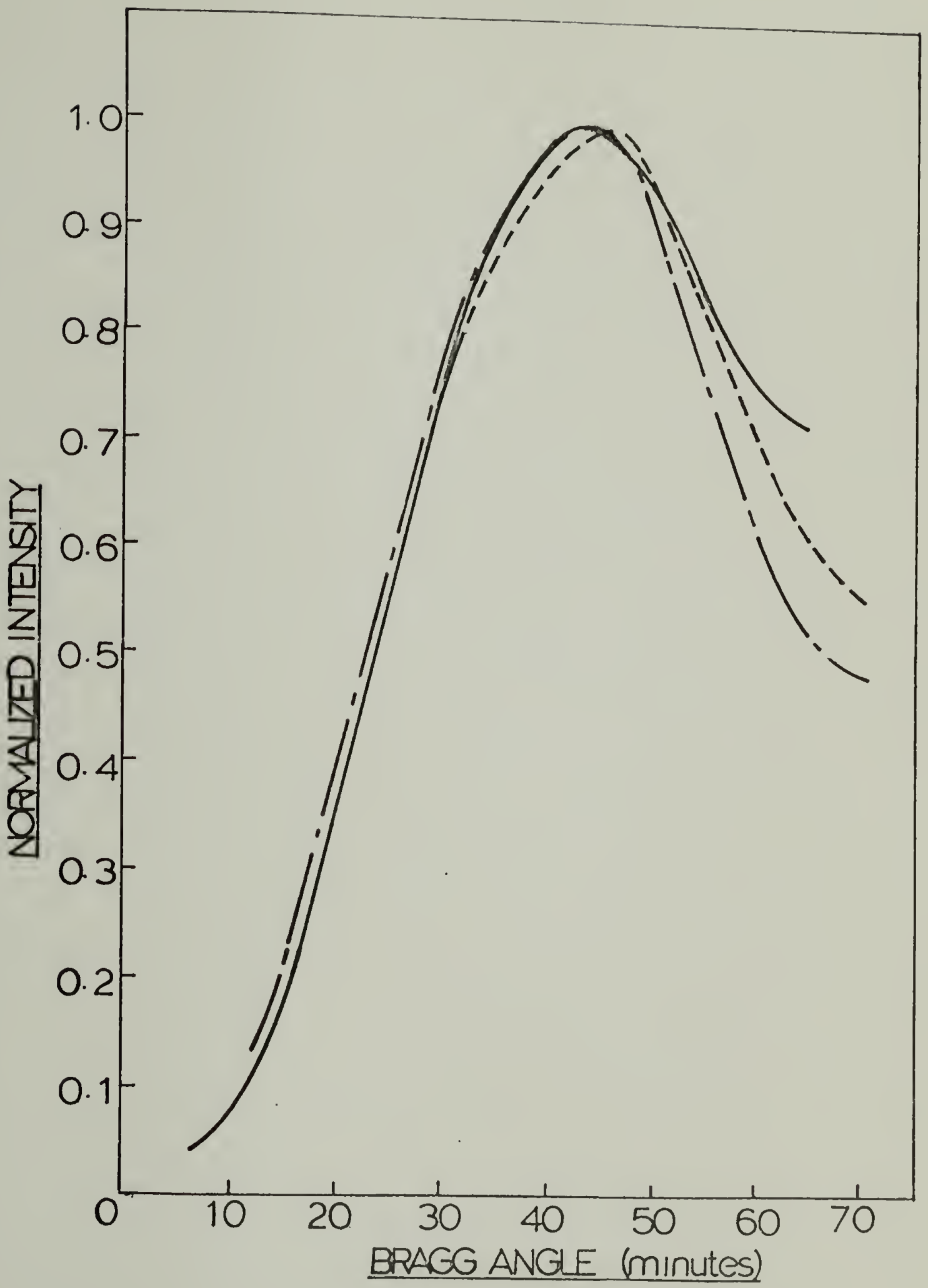
NORMALIZED INTENSITY
1.0
0.9
0.8
0.7
0.6
0.5
0.4
0.3
0.2
0.1
0
10
20
30
40
50
60
70
BRAGG ANGLE (minutes)

Figure 27b

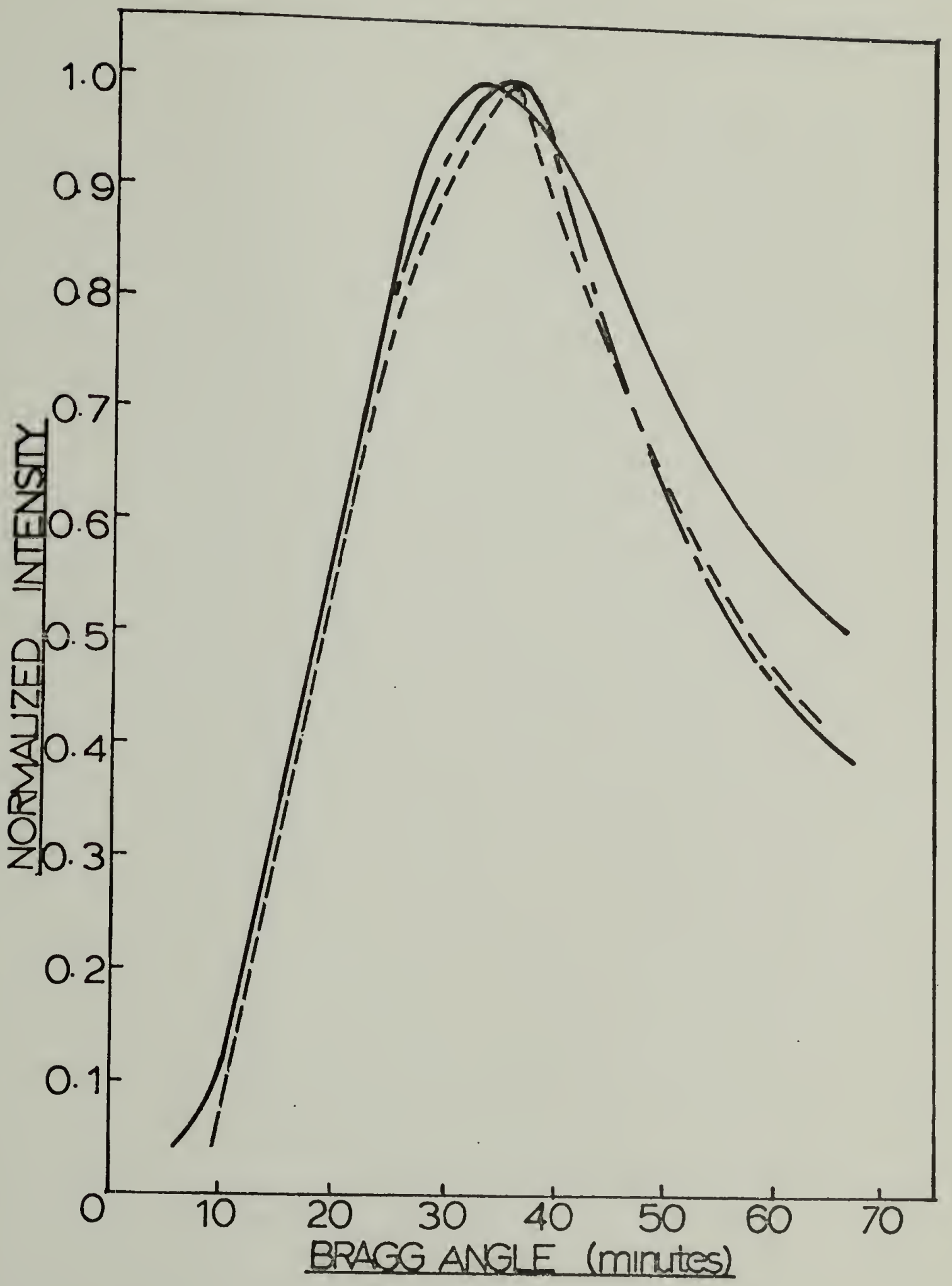
NORMALIZED INTENSITY
1.0
0.9
0.8
0.7
0.6
0.5
0.4
0.3
0.2
0.1
0
10
20
30
40
50
60
70
BRAGG ANGLE (minutes)

Figure 27c

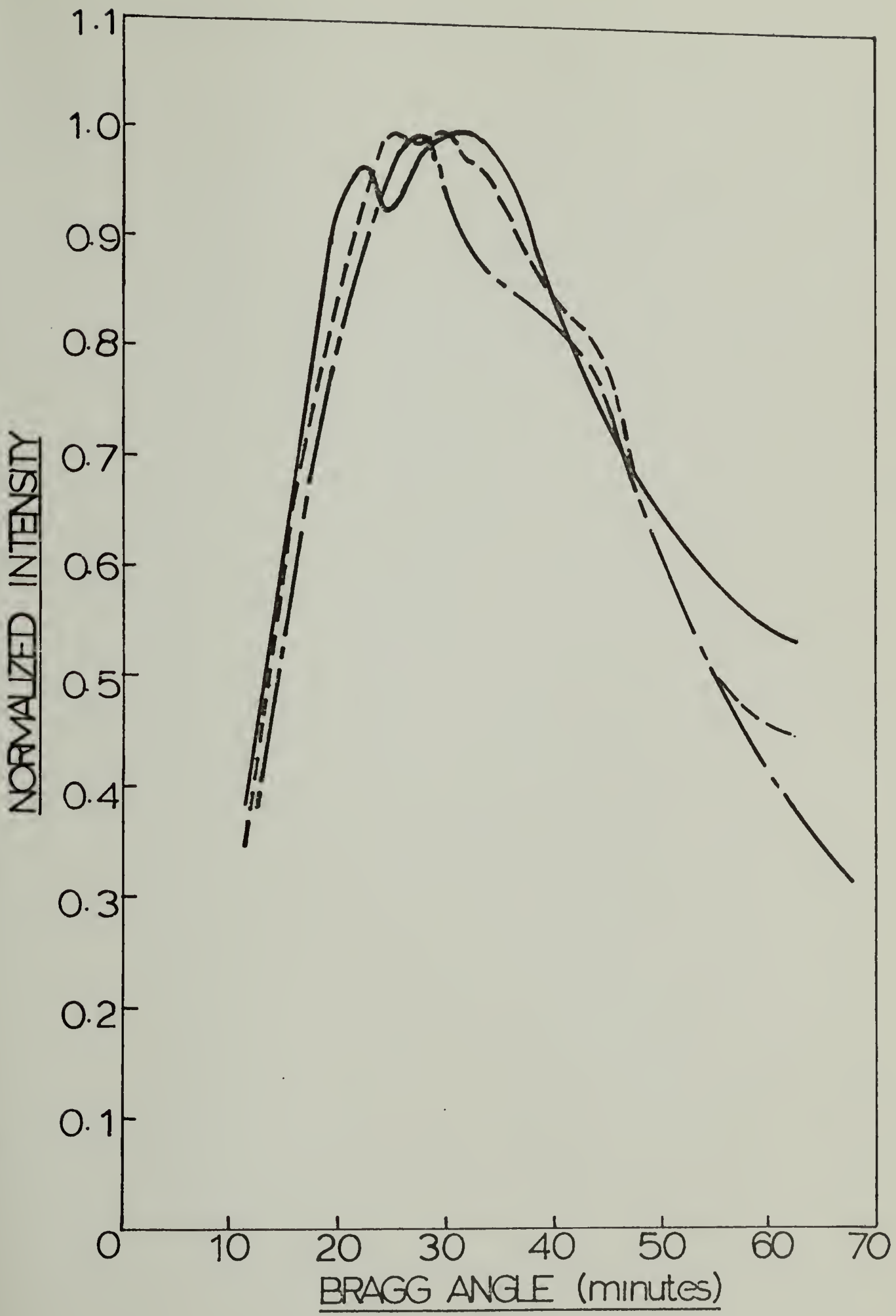
1.1
1.0
0.9
0.8
0.7
0.6
0.5
0.4
0.3
0.2
0.1
0
NORMALIZED INTENSITY
10
20
30
40
50
60
70
BRAGG ANGLE (minutes)

Figure 27d

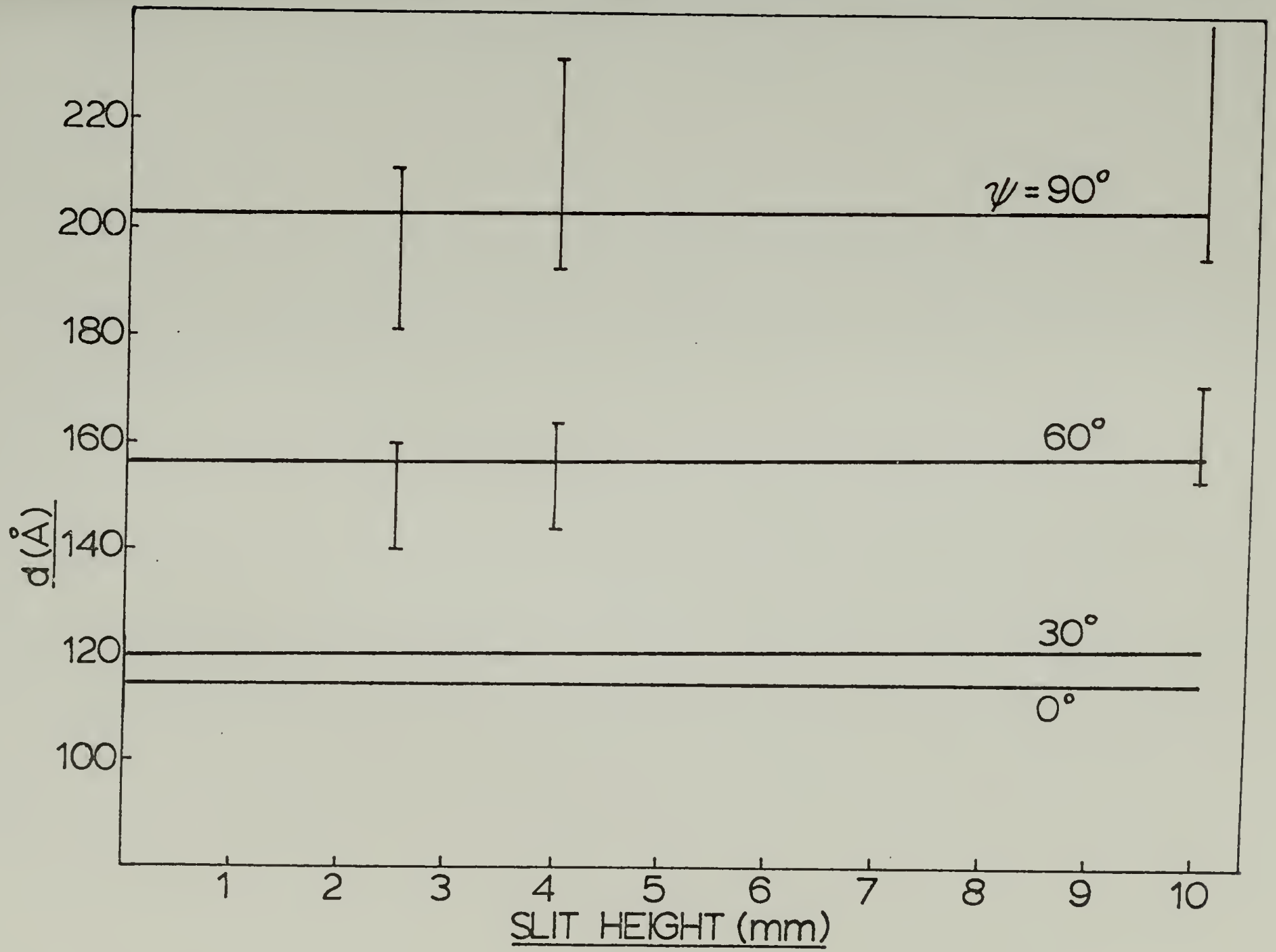
220
200
180
160
140
120
100
d(Å)
ψ = 90°
60°
30°
0°
1
2
3
4
5
6
7
8
9
10
SLIT HEIGHT (mm)

Figure 28

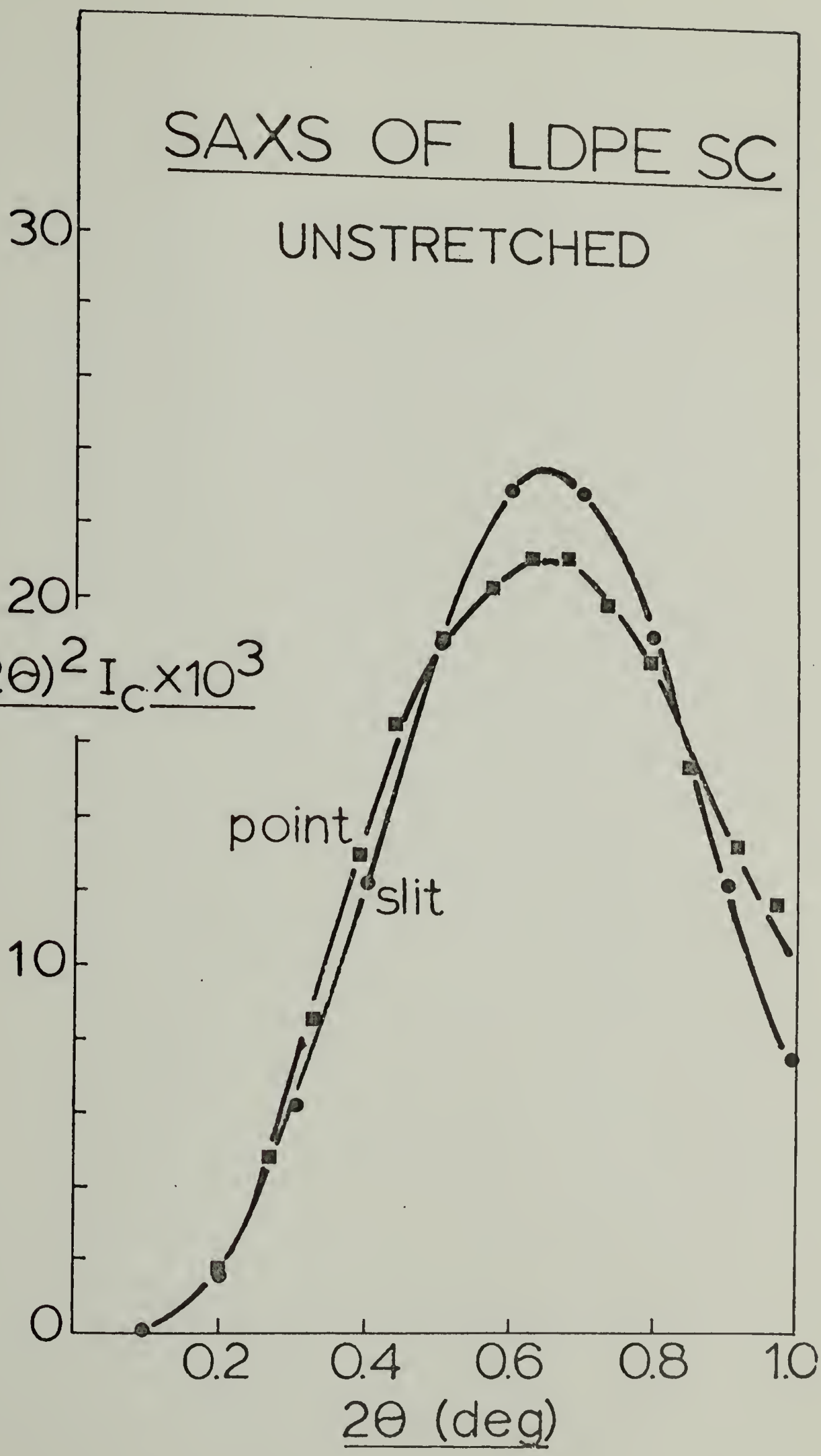
SAXS OF LDPE SC
UNSTRETCHED
30
20
10
0
(2θ)² I_c x10³
point
slit
0.2
0.4
0.6
0.8
1.0
2θ (deg)

Figure 29

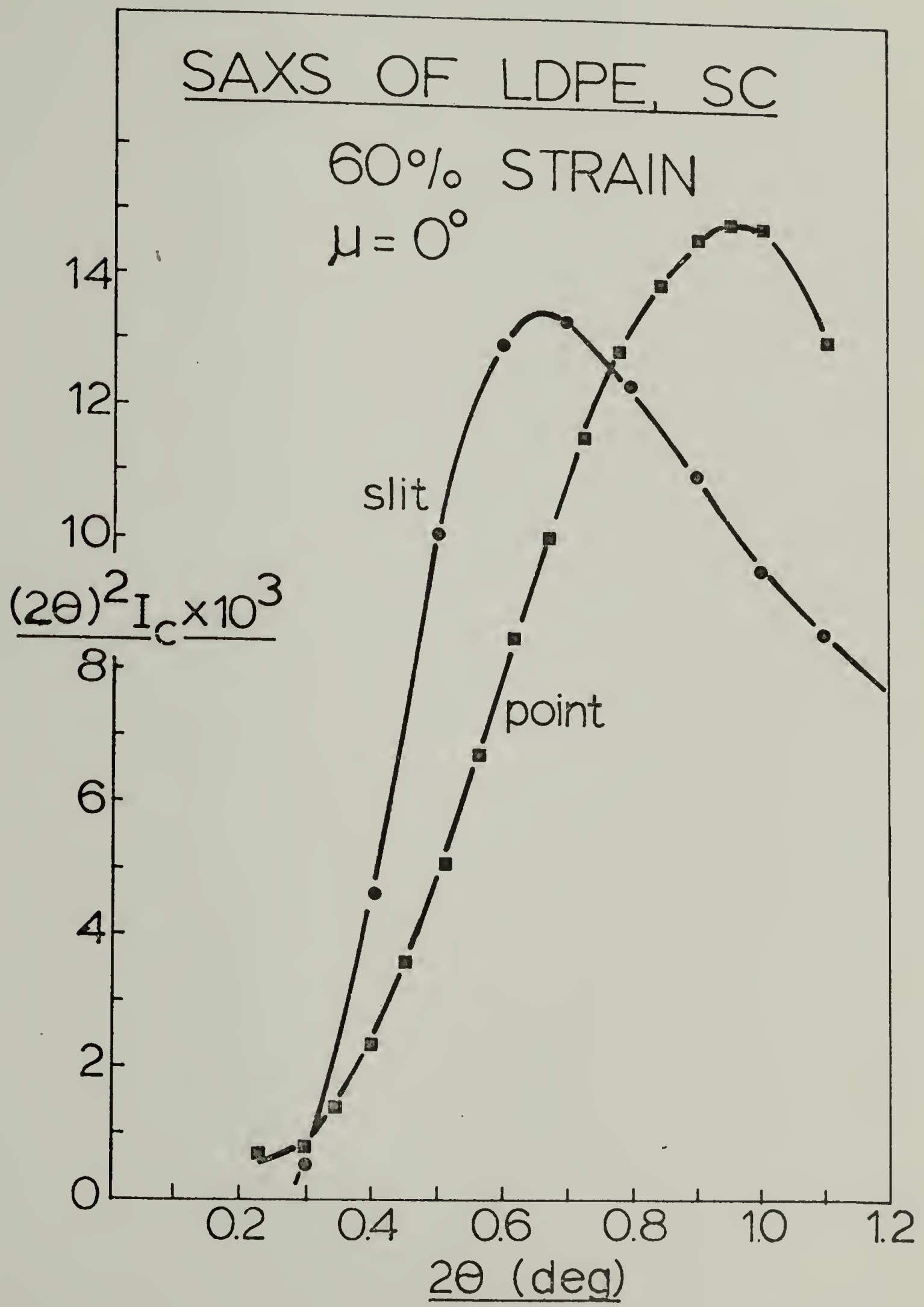
SAXS OF LDPE, SC
60% STRAIN
μ = 0°
slit
point
(2θ)²I_c x10³
14
12
10
8
6
4
2
0
0.2
0.4
0.6
0.8
1.0
1.2
2θ (deg)

Figure 30a

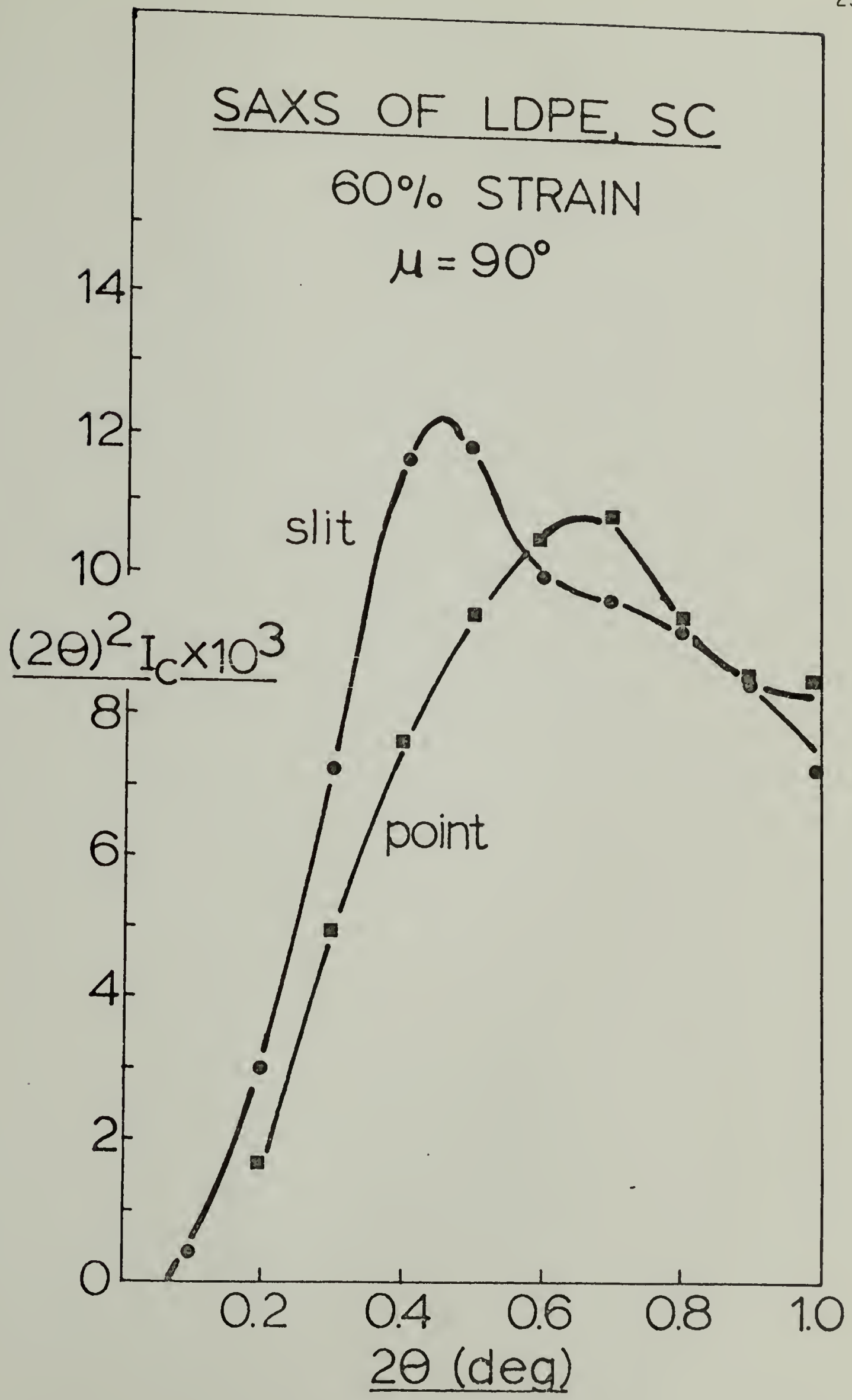
SAXS OF LDPE, SC
60% STRAIN
μ = 90°
slit
point
(2θ)² I_c x 10³
14
12
10
8
6
4
2
0
0.2
0.4
0.6
0.8
1.0
2θ (deg)

Figure 30b

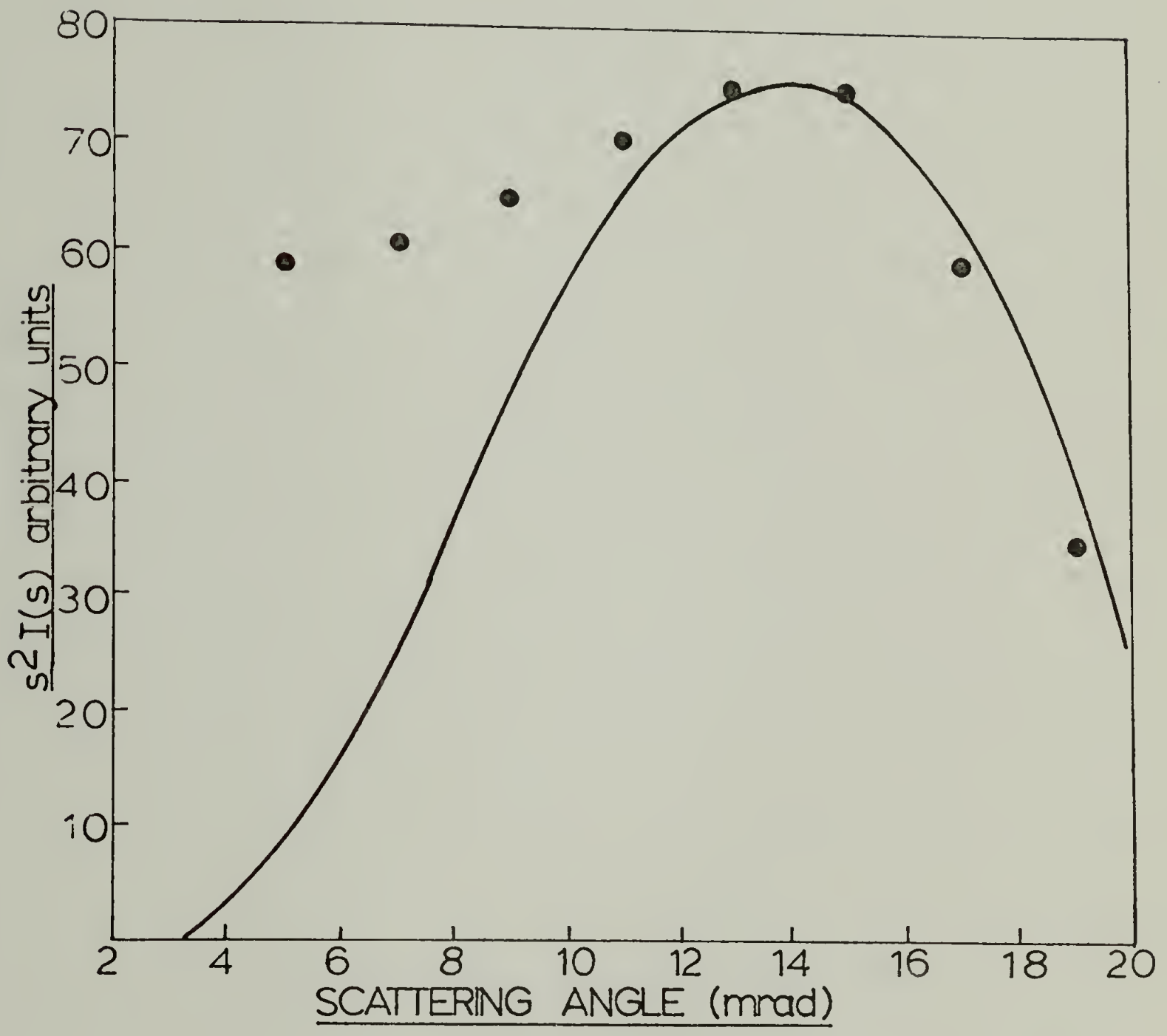
80
70
60
50
40
30
20
10
$s^2 I(s)$ arbitrary units
2
4
6
8
10
12
14
16
18
20
SCATTERING ANGLE (mrad)

Figure 31

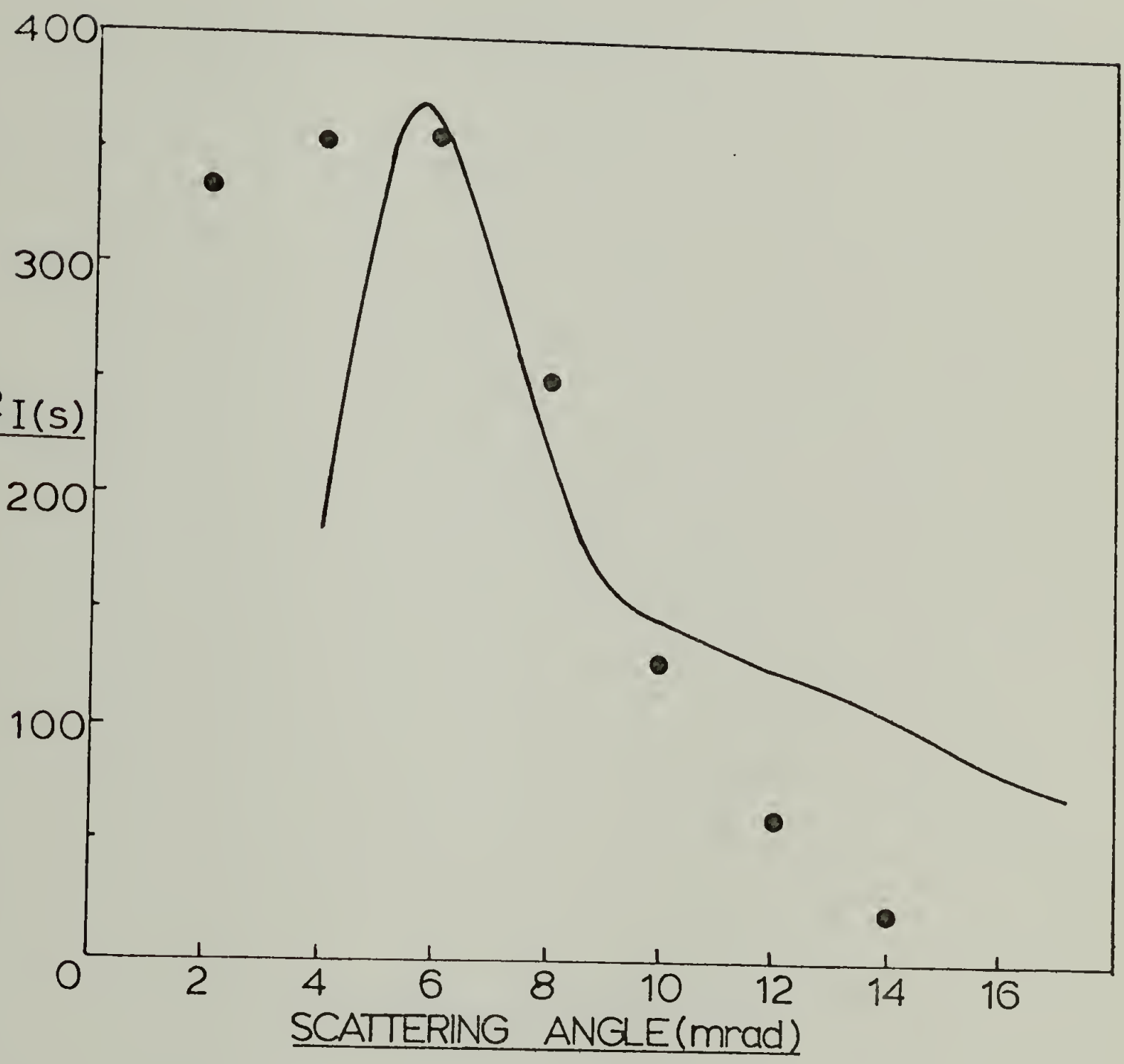

Figure 32

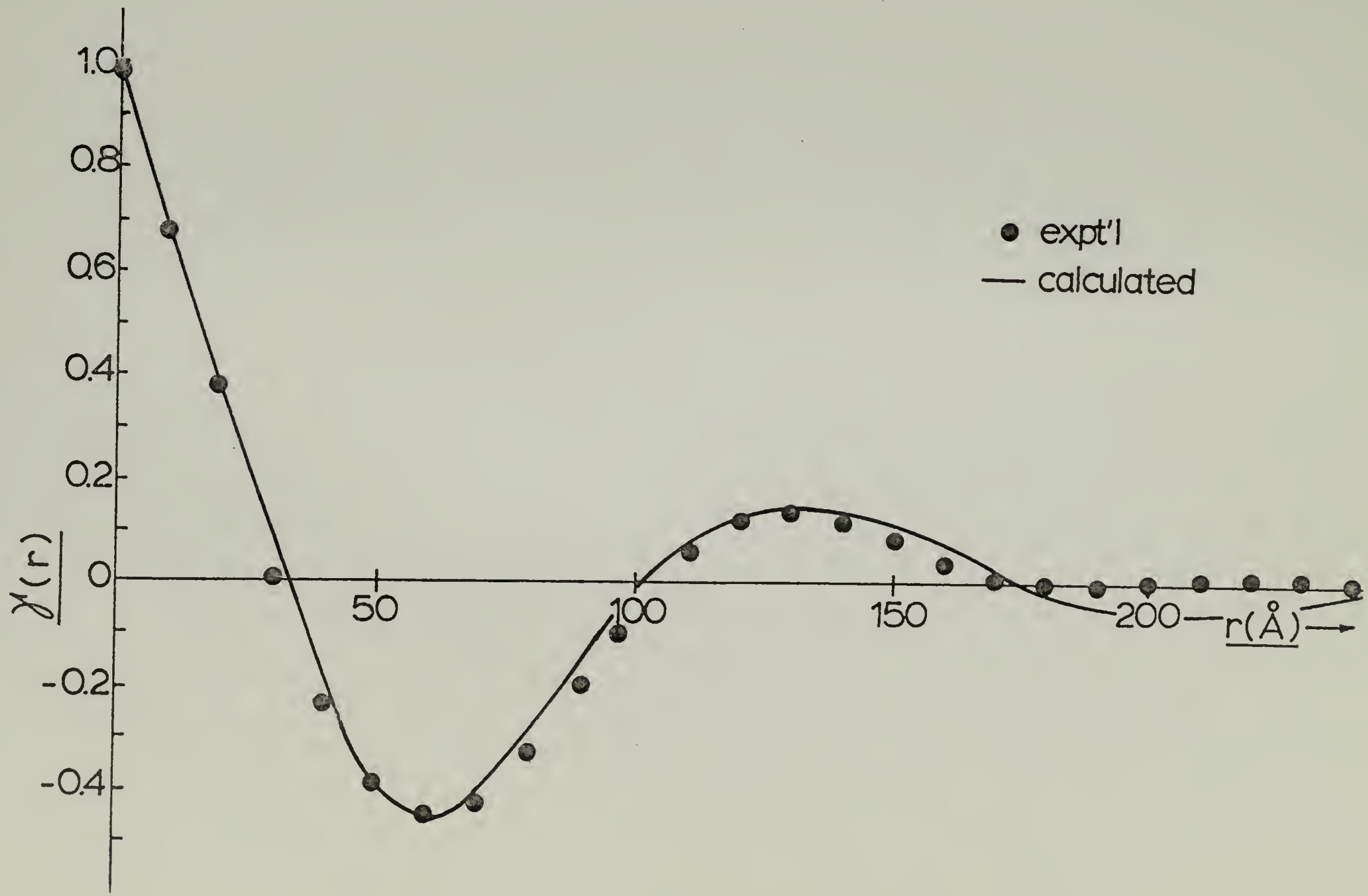

Figure 33

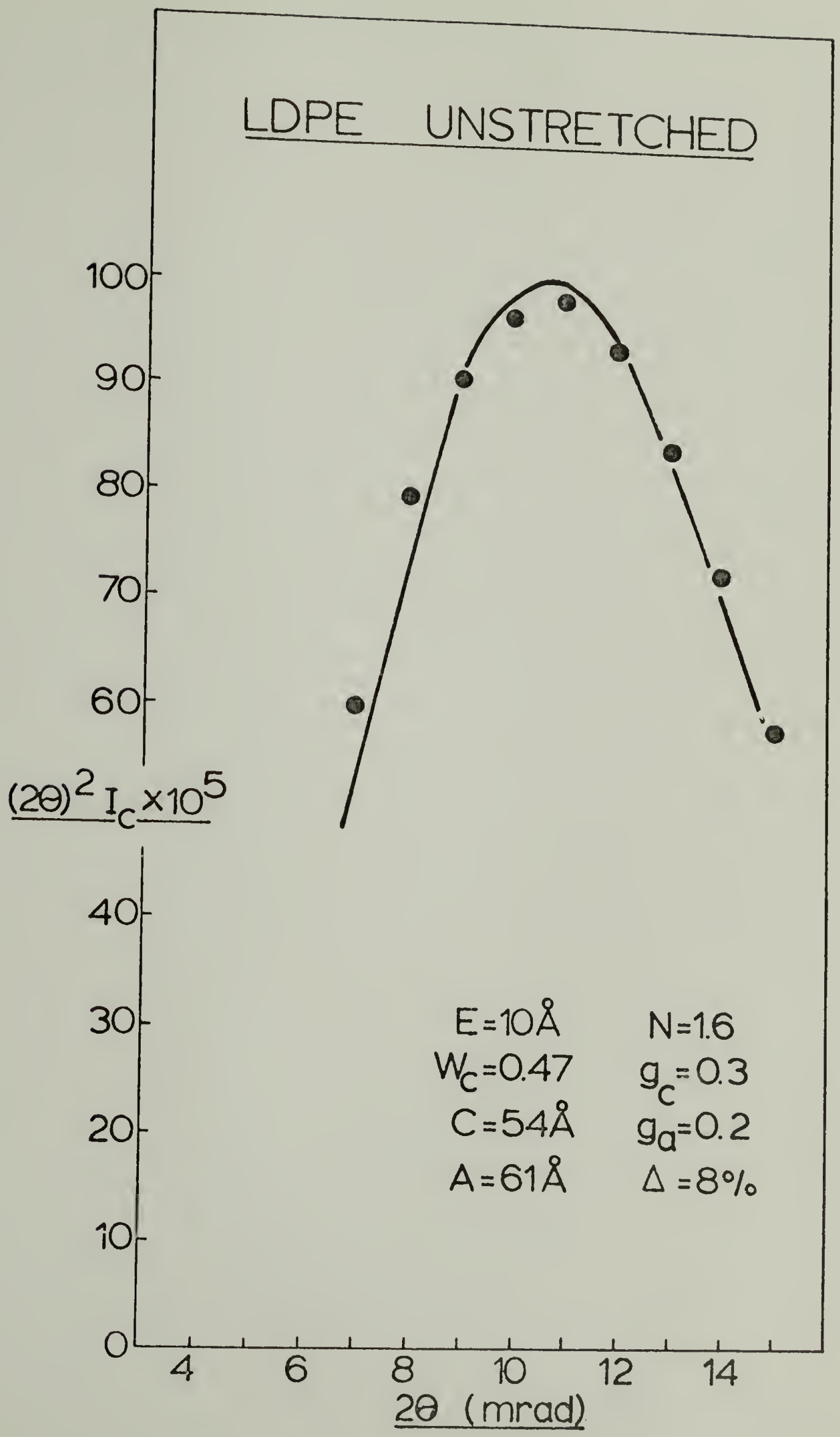
LDPE UNSTRETCHED
100
90
80
70
60
40
30
20
10
0
$(2\theta)^2 I_c \times 10^5$
4
6
8
10
12
14
2θ (mrad)
E=10Å
N=1.6
W_c=0.47
g_c=0.3
C=54Å
g_a=0.2
A=61Å
Δ=8%

Figure 34

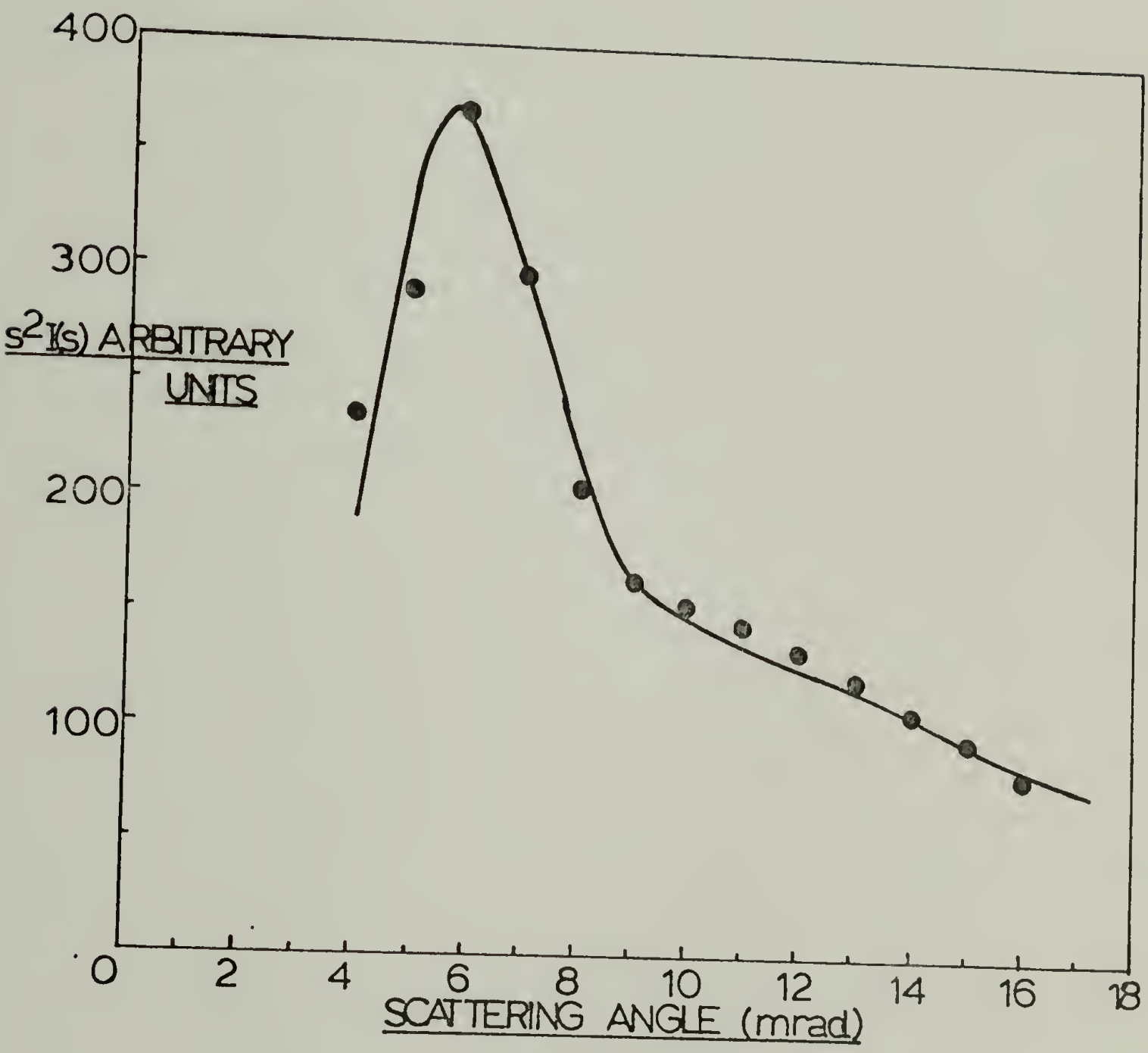
400
300
200
100
$s^2I(s)$ ARBITRARY UNITS
0
2
4
6
8
10
12
14
16
18
SCATTERING ANGLE (mrad)

Figure 35a

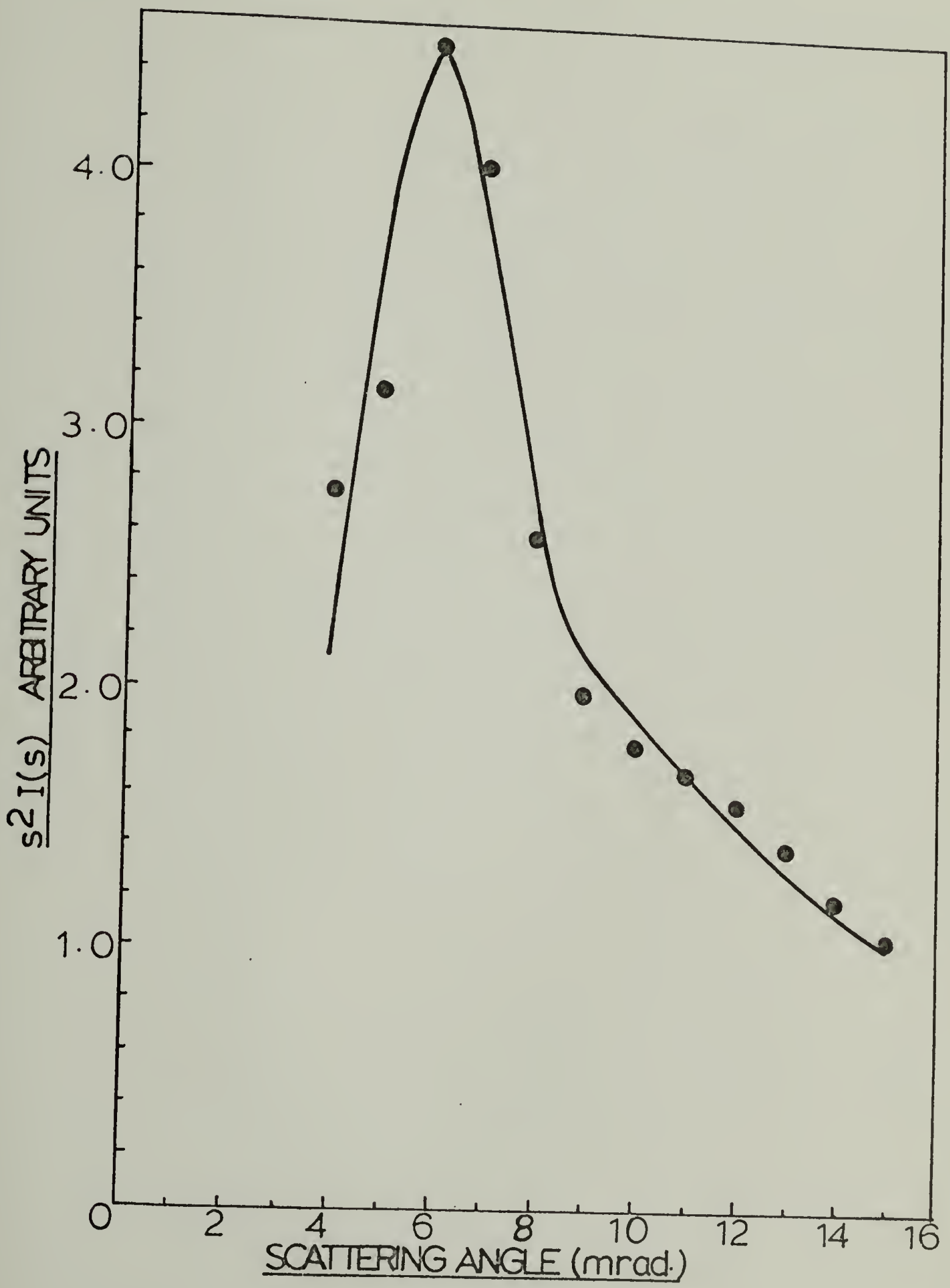
4.0
3.0
2.0
1.0
0
$s^2 I(s)$ ARBITRARY UNITS
2
4
6
8
10
12
14
16
SCATTERING ANGLE (mrad.)

Figure 35b

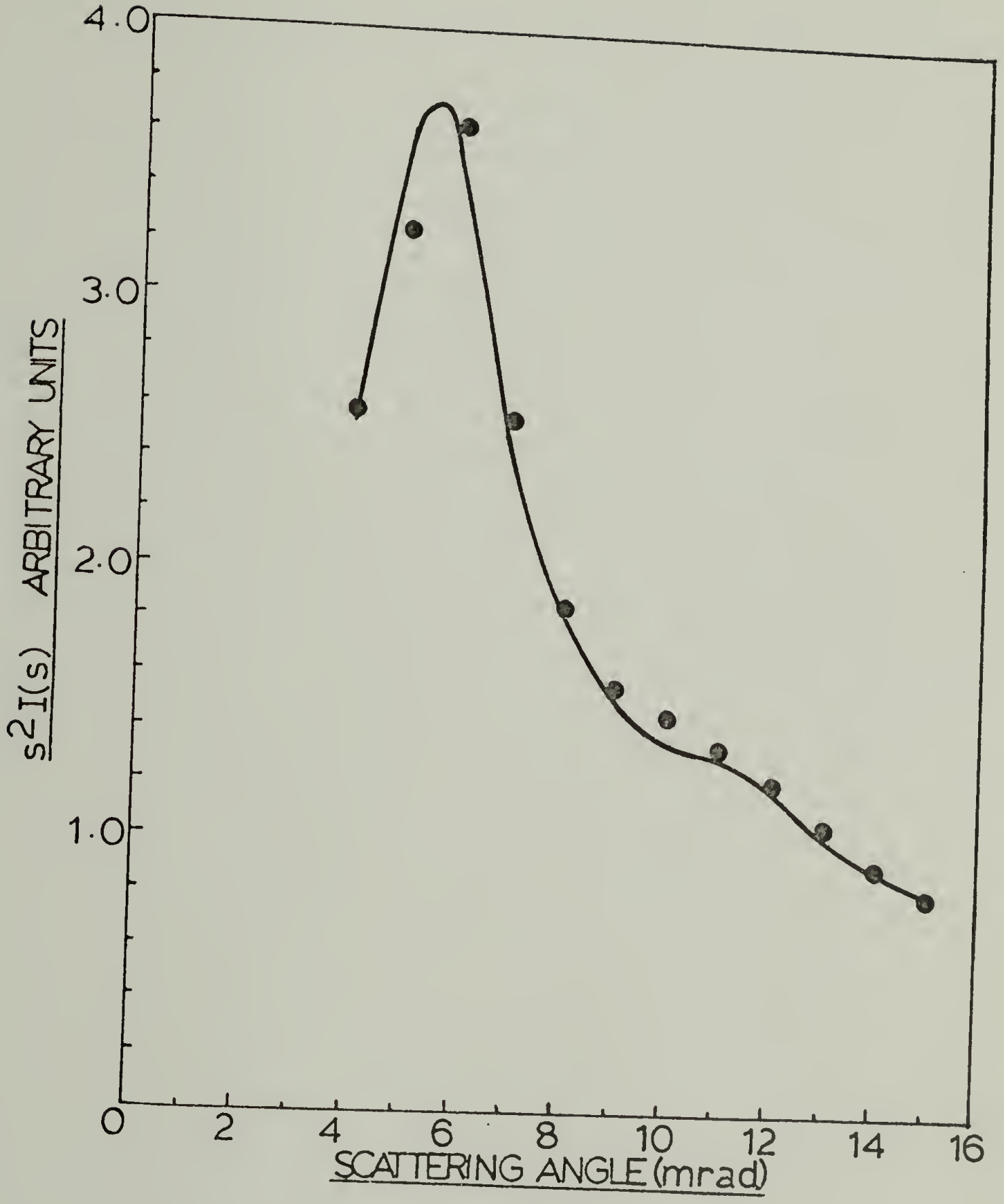
4.0
3.0
2.0
1.0
0
2
4
6
8
10
12
14
16
ARBITRARY UNITS
s²I(s)
SCATTERING ANGLE (mrad)

Figure 35c

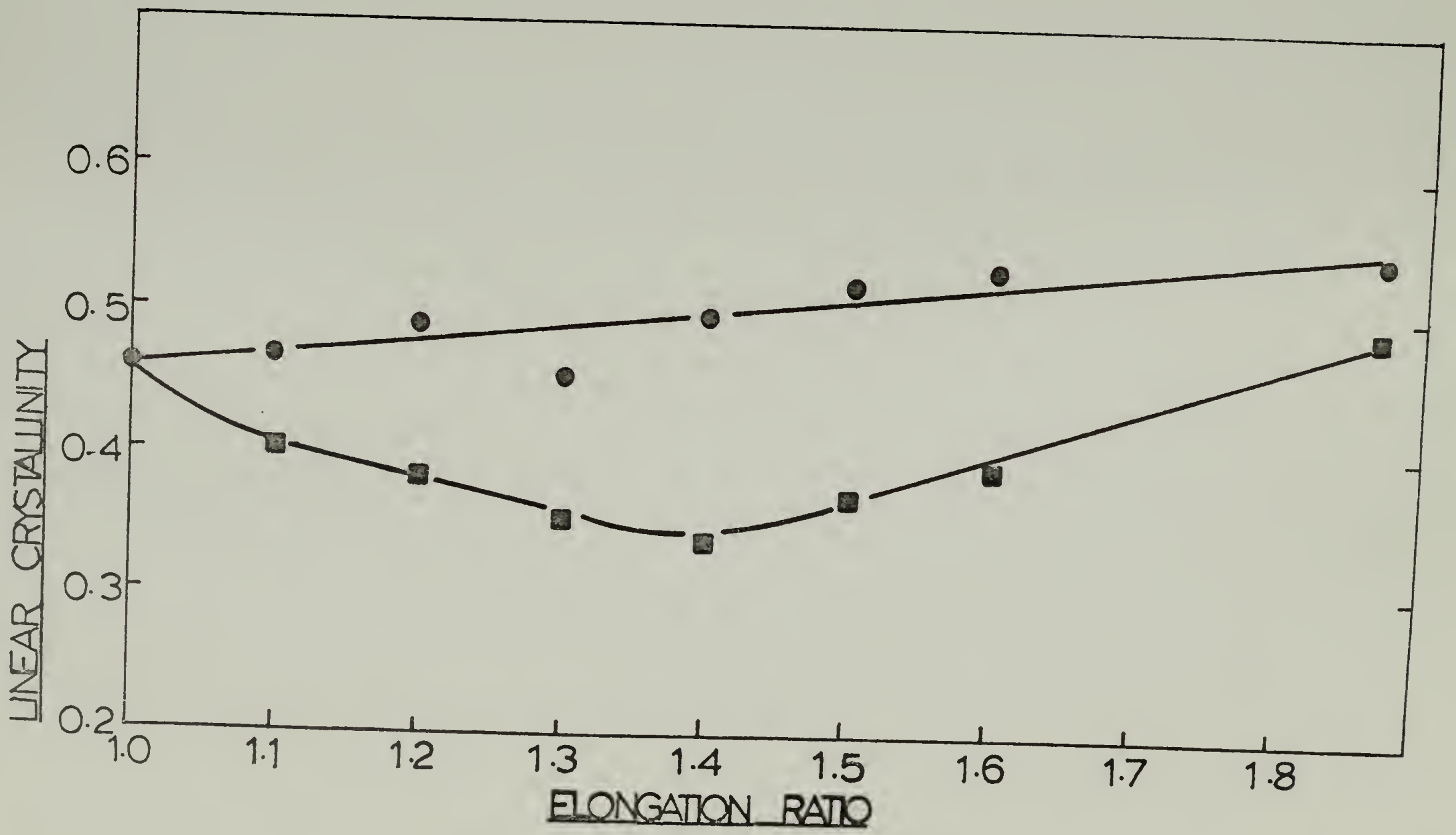
LINEAR CRYSTALLINITY
0.6
0.5
0.4
0.3
0.2
1.0
1.1
1.2
1.3
1.4
1.5
1.6
1.7
1.8
ELONGATION RATIO

Figure 36

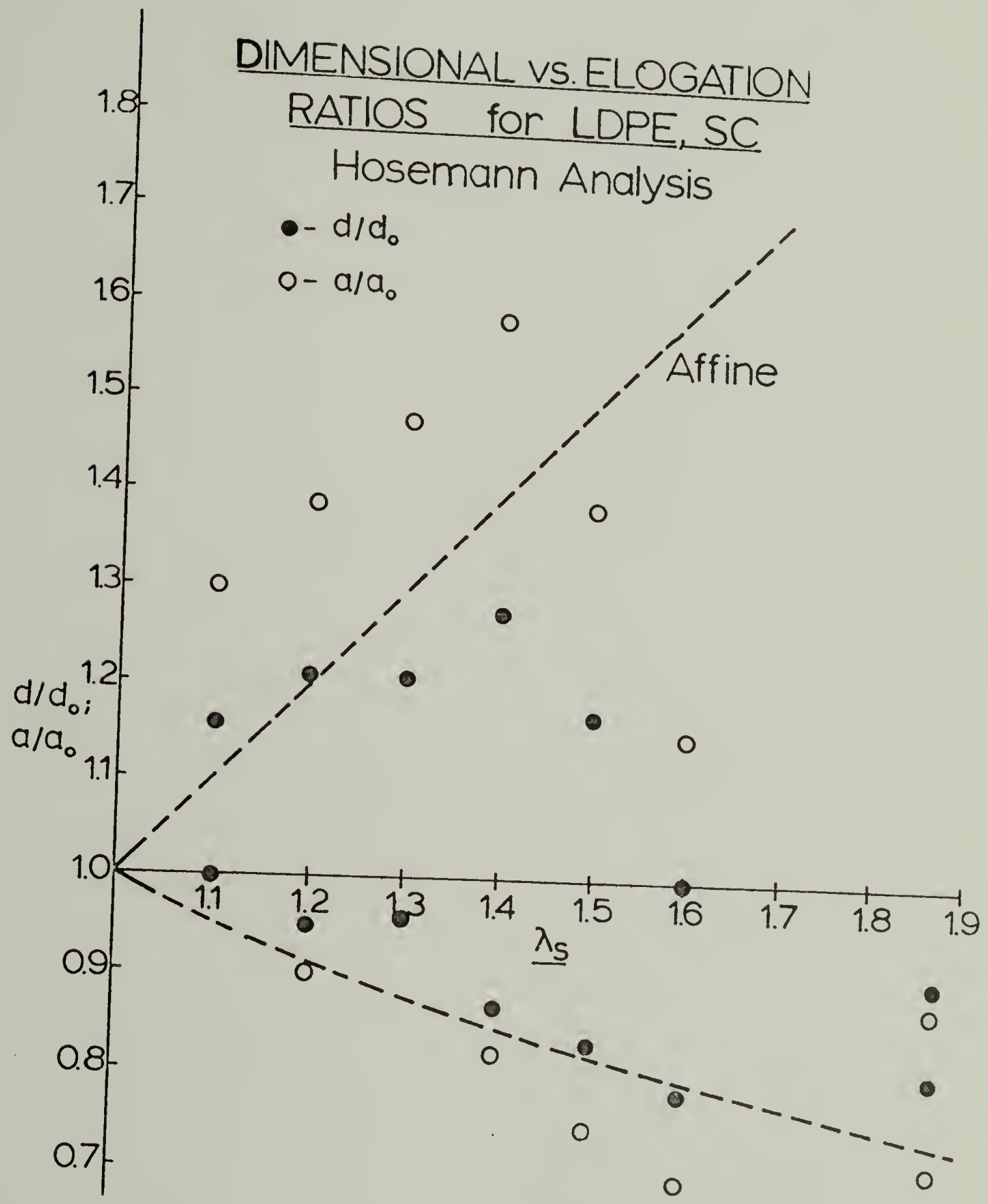
DIMENSIONAL vs. ELOGATION RATIOS for LDPE, SC
Hosemann Analysis
● - d/d₀
○ - a/a₀
Affine
d/d₀; a/a₀
λs
1.8
1.7
1.6
1.5
1.4
1.3
1.2
1.1
1.0
0.9
0.8
0.7
1.1
1.2
1.3
1.4
1.5
1.6
1.7
1.8
1.9

Figure 37

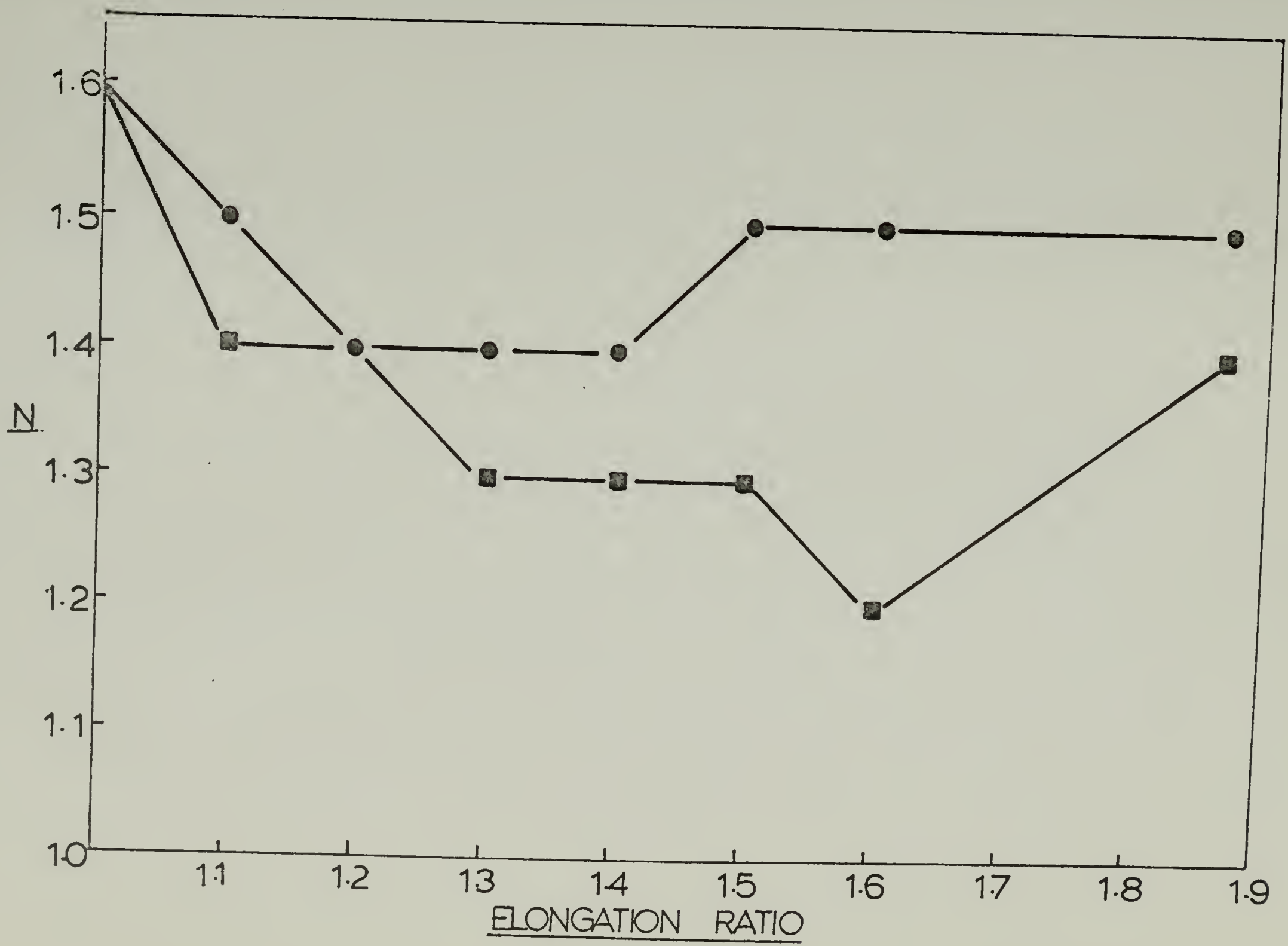

Figure 38

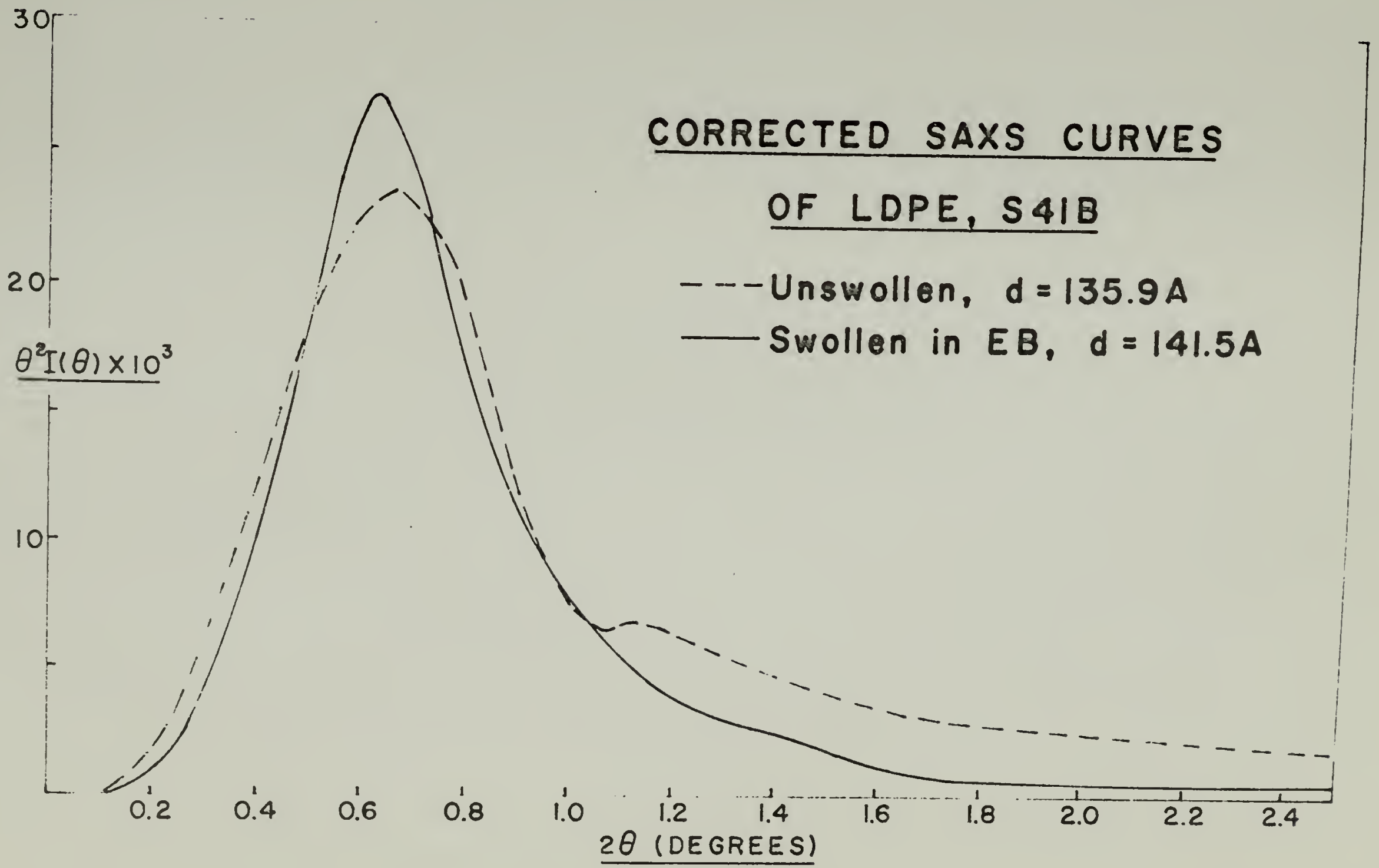
CORRECTED SAXS CURVES
OF LDPE, S41B
---Unswollen, d = 135.9A
——Swollen in EB, d = 141.5A
30
20
10
θ²I(θ) x 10³
0.2
0.4
0.6
0.8
1.0
1.2
1.4
1.6
1.8
2.0
2.2
2.4
2θ (DEGREES)

Figure 39

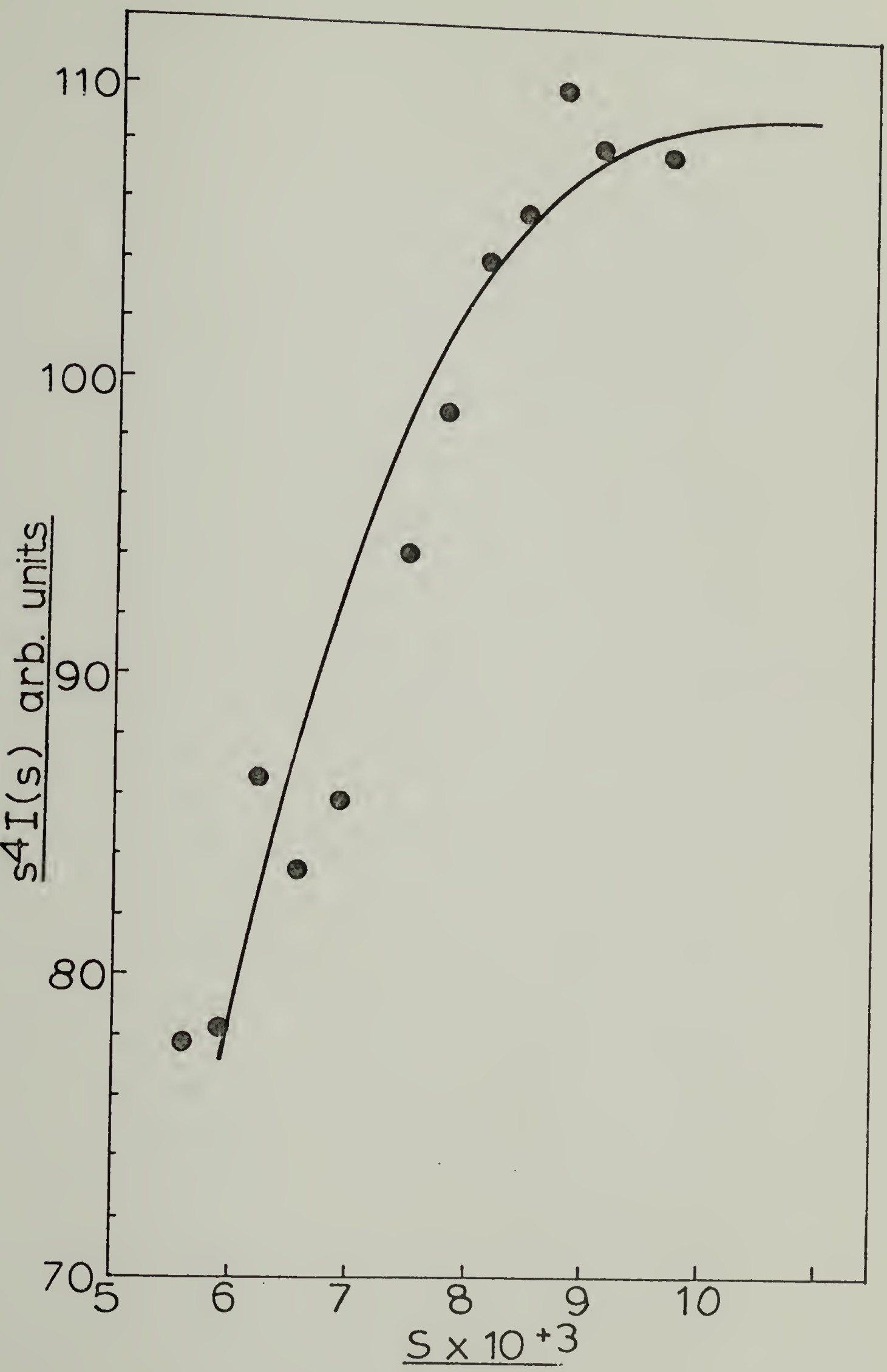

Figure 40

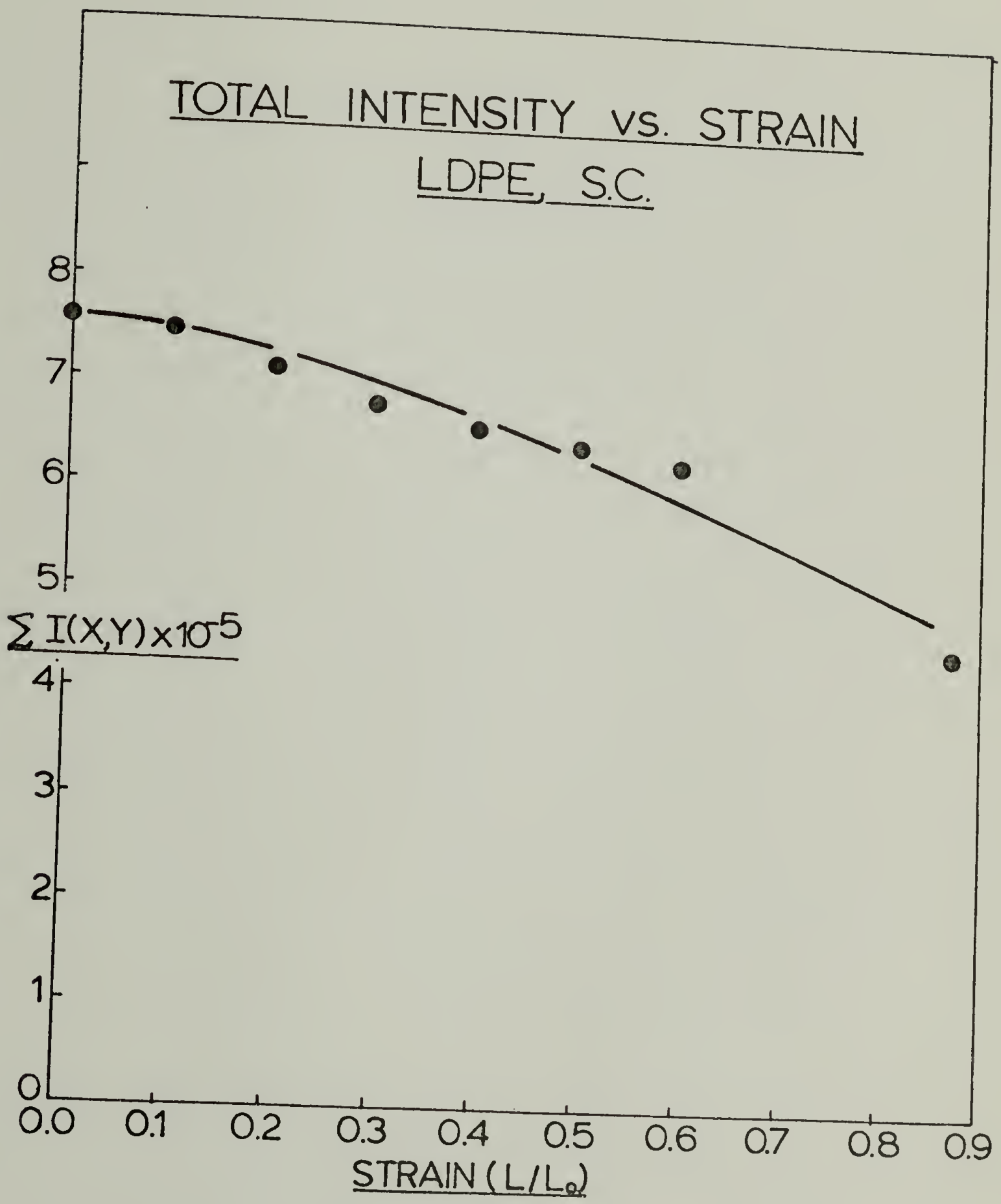
TOTAL INTENSITY VS. STRAIN
LDPE, S.C.
8
7
6
5
$\sum I(X,Y) \times 10^{-5}$
4
3
2
1
0
0.0
0.1
0.2
0.3
0.4
0.5
0.6
0.7
0.8
0.9
STRAIN (L/L_o)

Figure 41

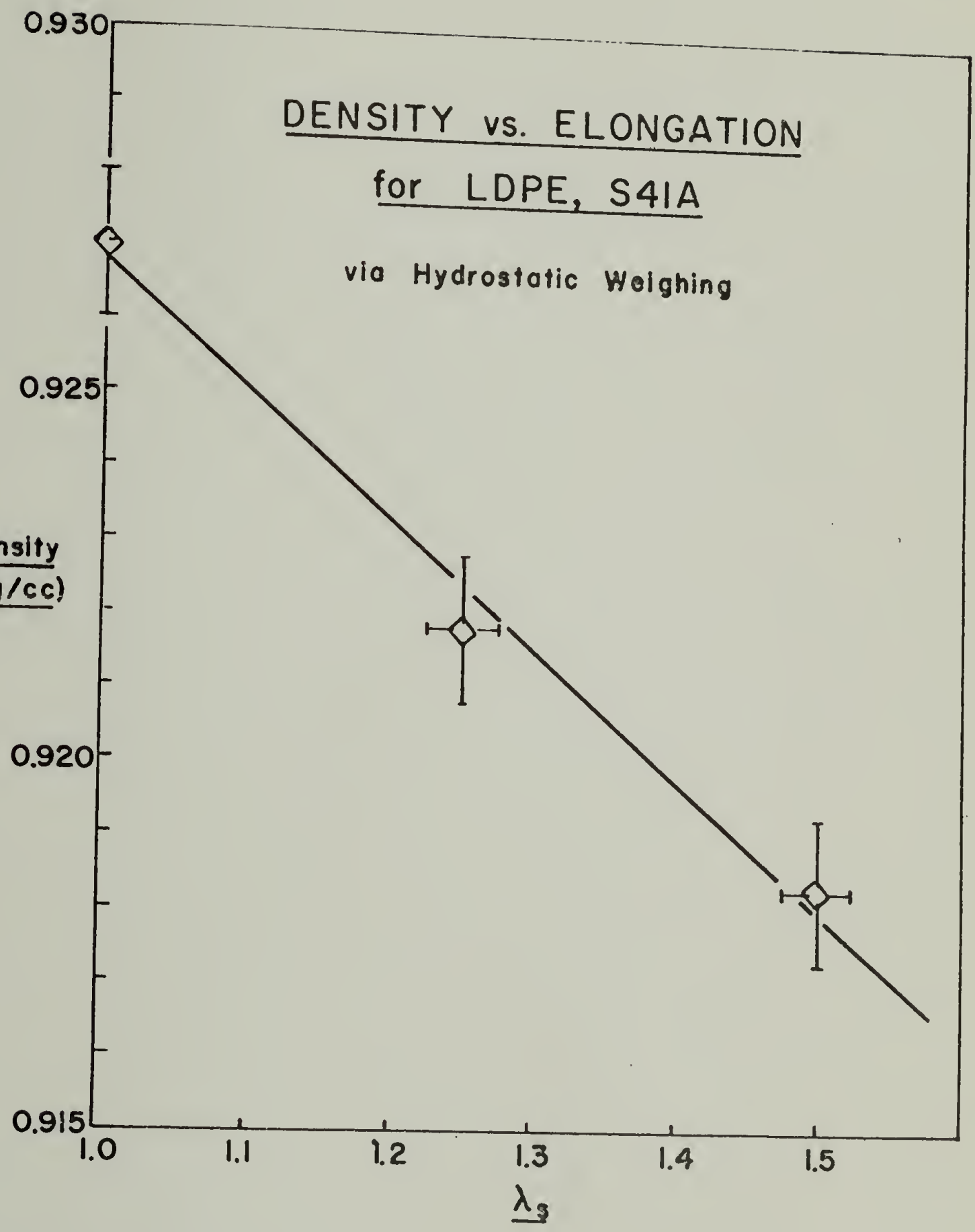
DENSITY vs. ELONGATION
for LDPE, S41A
via Hydrostatic Weighing
0.930
0.925
0.920
0.915
Density (g/cc)
1.0
1.1
1.2
1.3
1.4
1.5
λ3

Figure 42

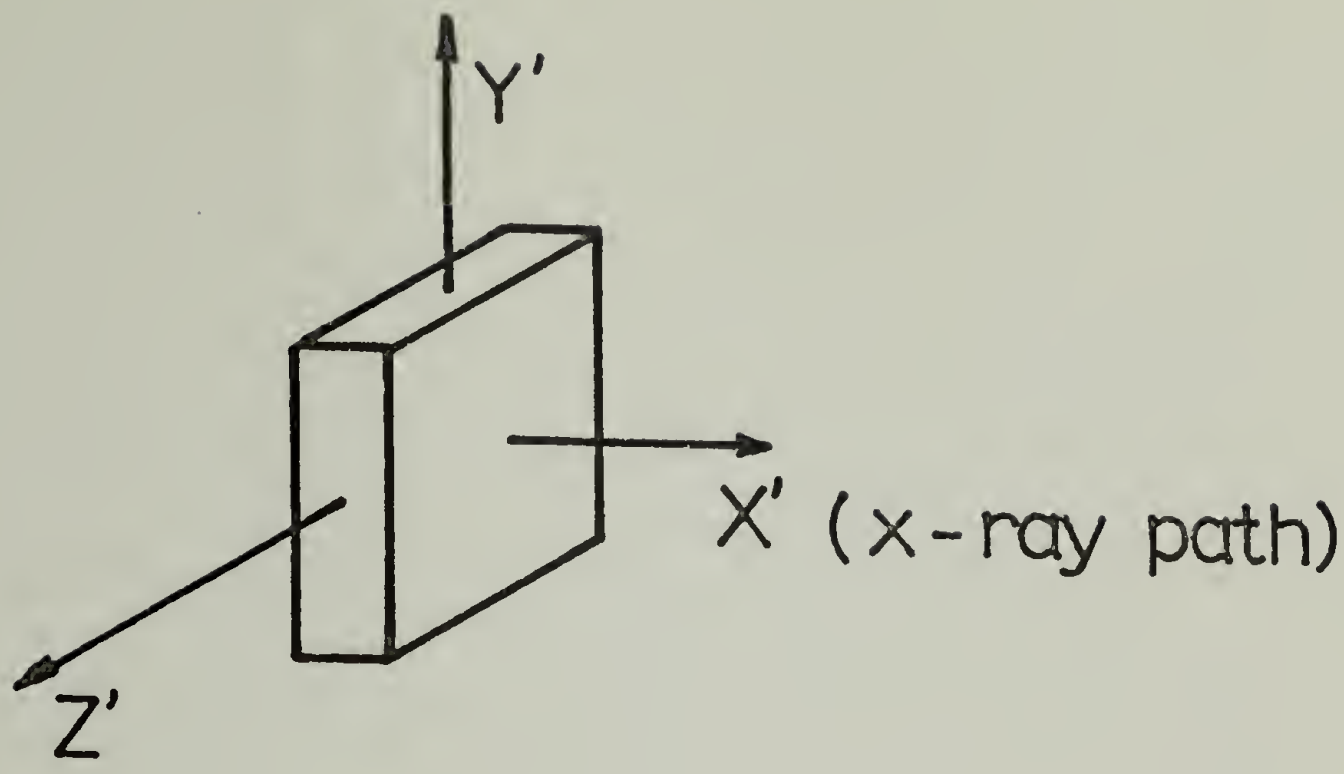

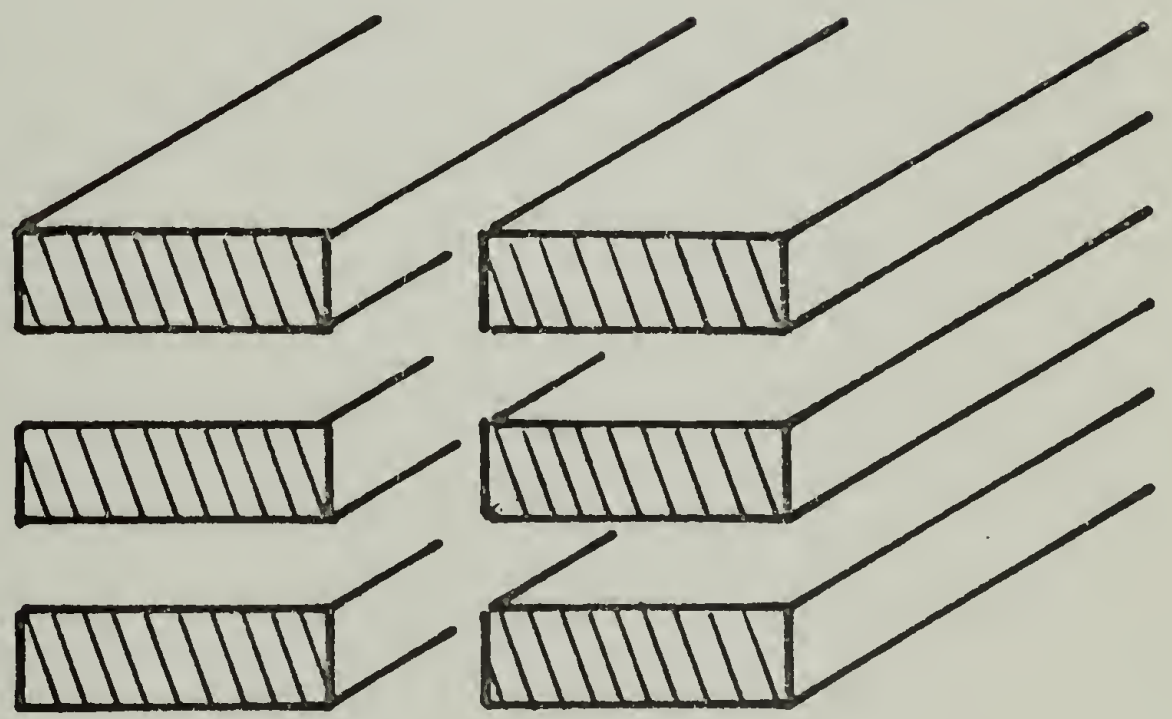

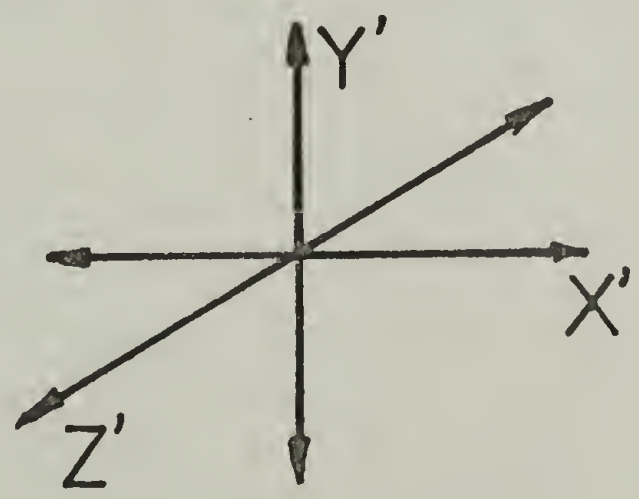

Figure 43

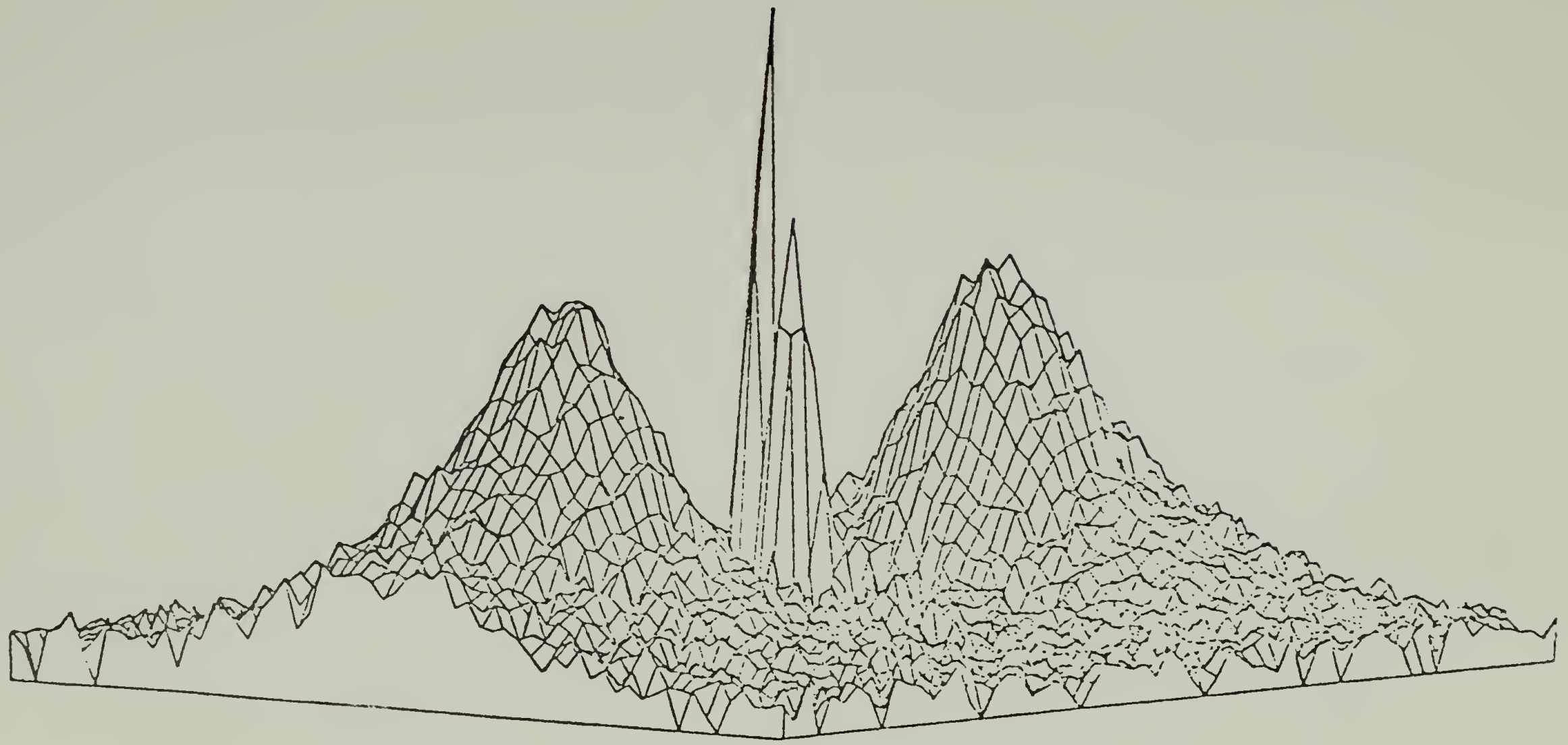

Figure 44

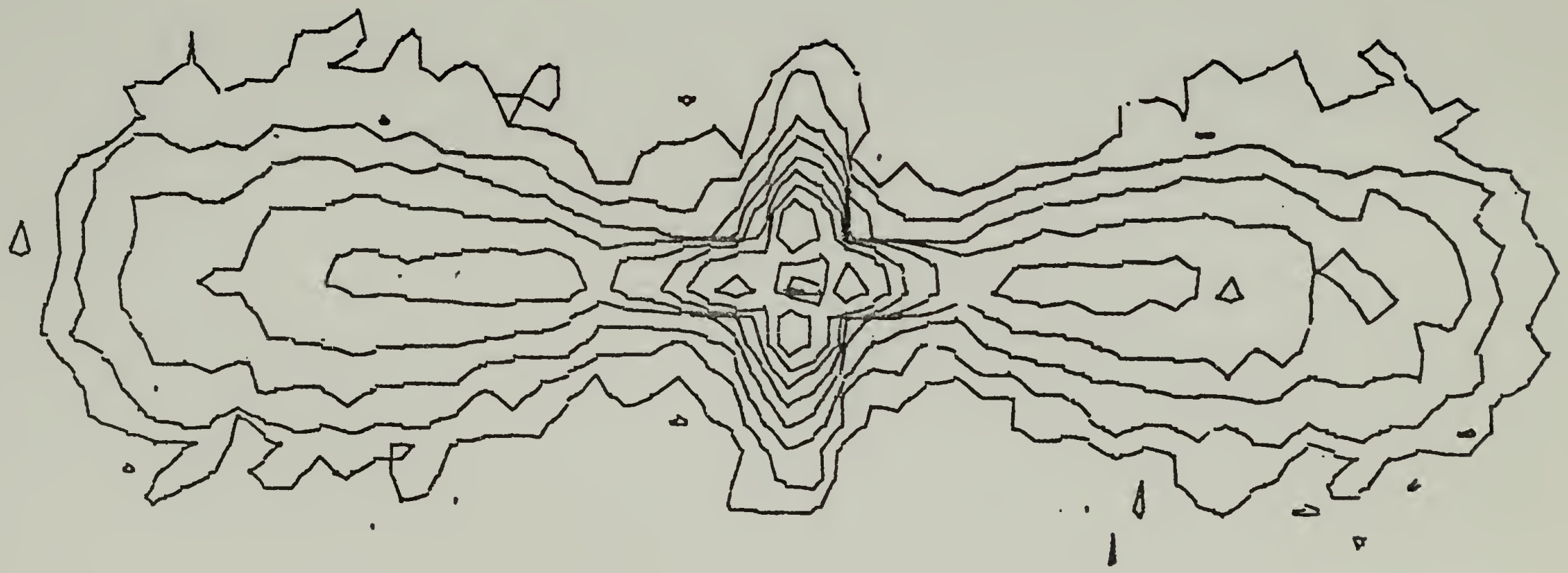

Figure 45

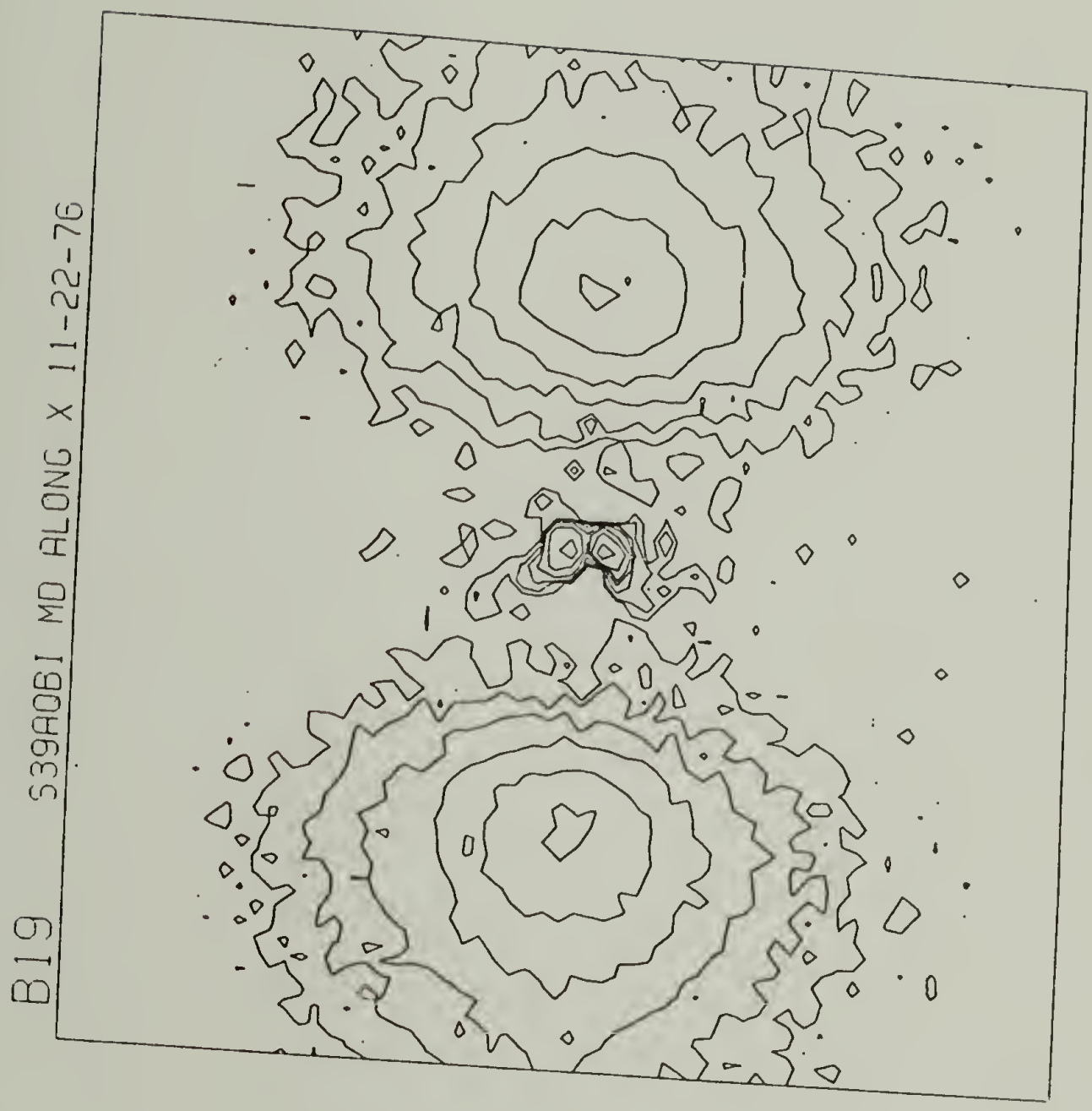

Figure 46a

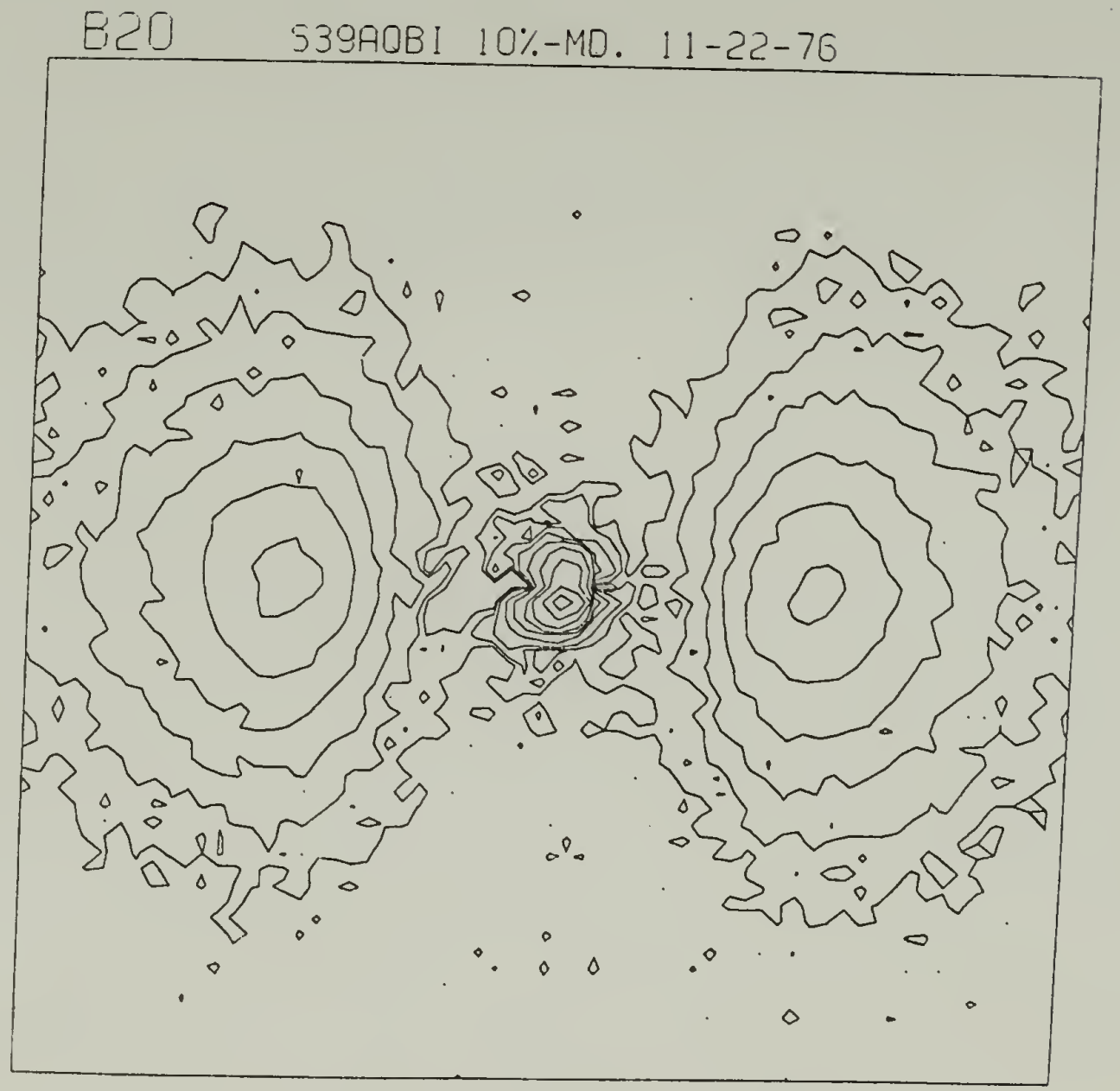

Figure 46b

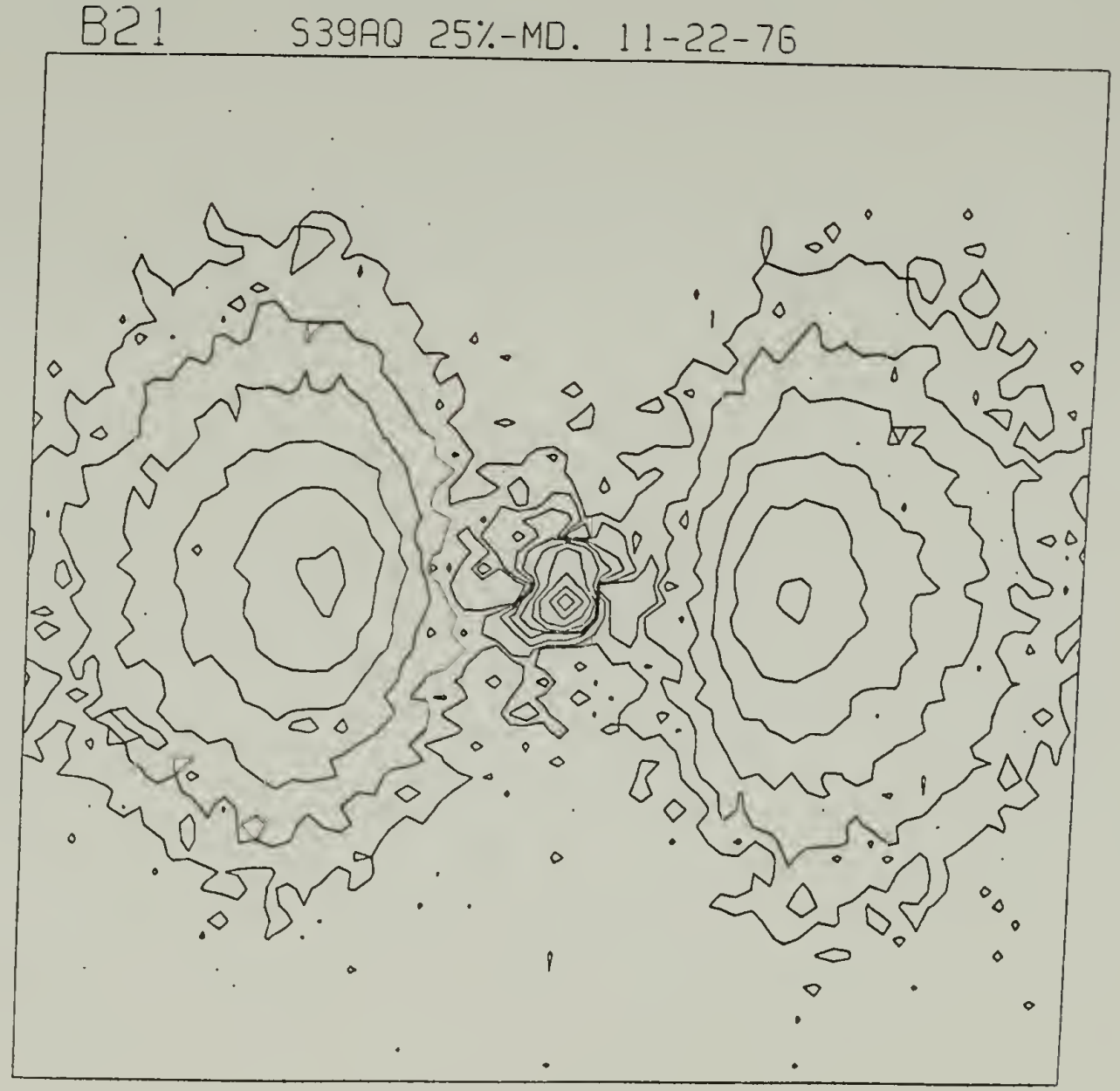

Figure 46c

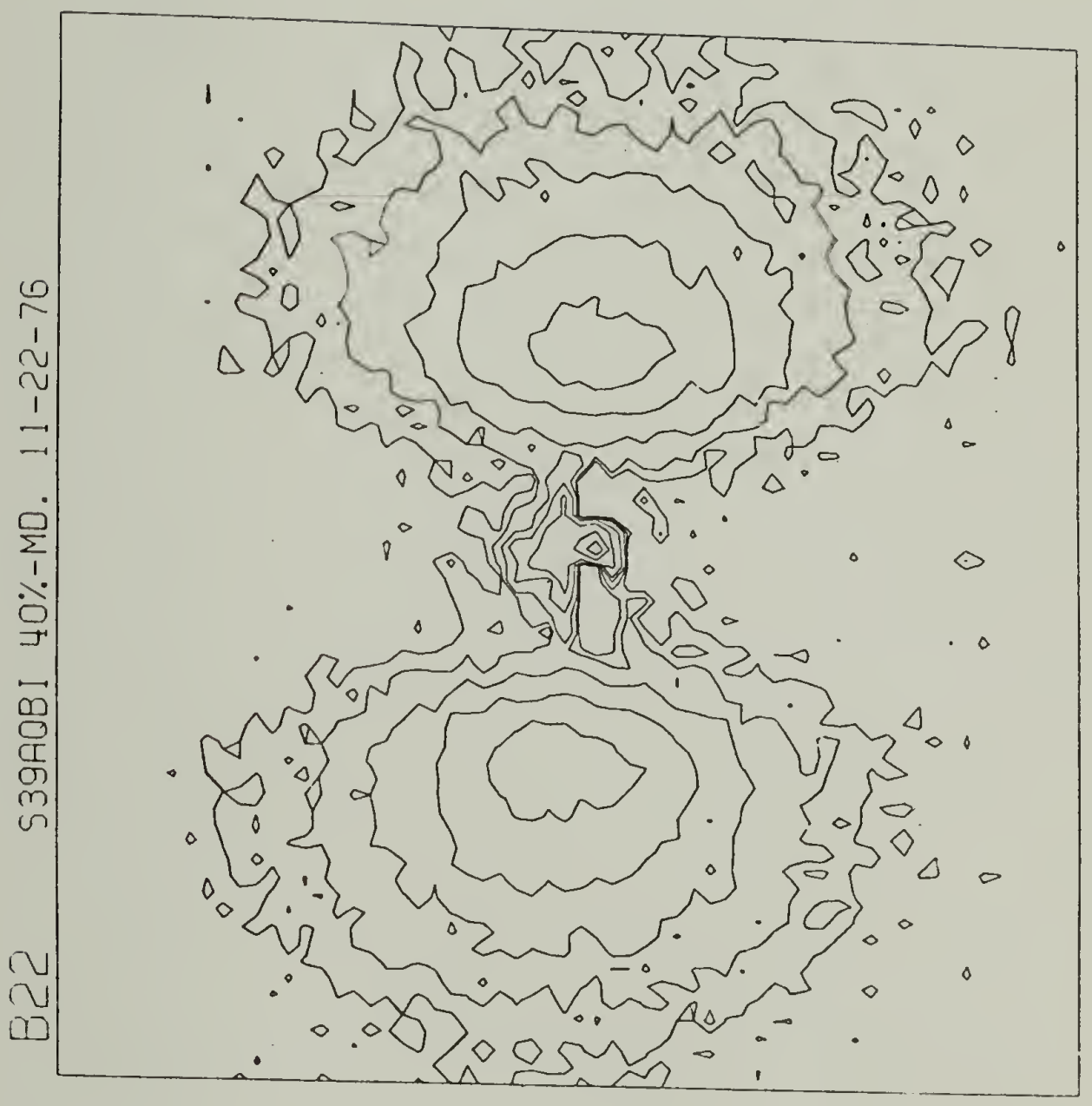
B22 S39A0BI 40%-MD. 11-22-76

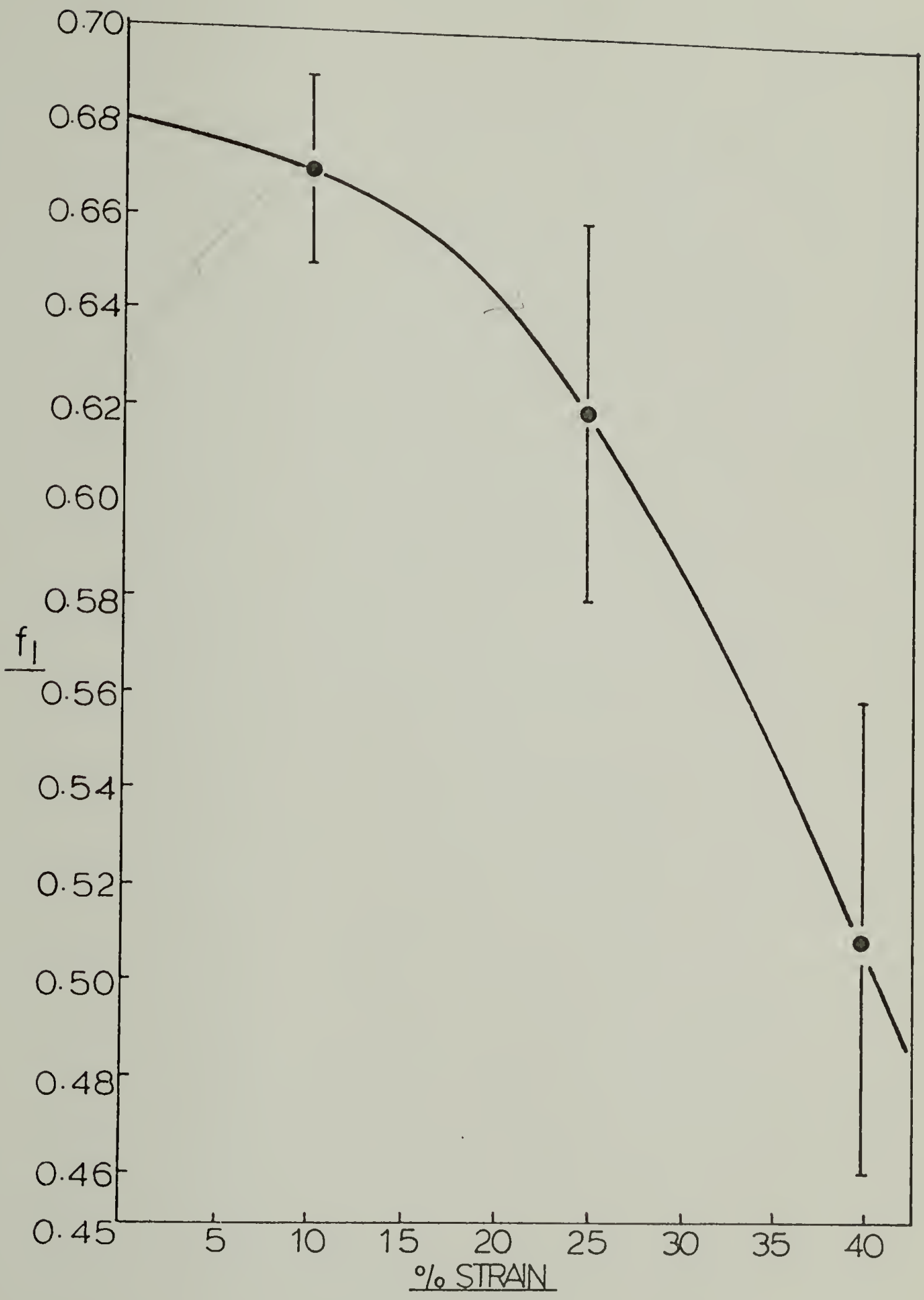
0.70
0.68
0.66
0.64
0.62
0.60
0.58
f1
0.56
0.54
0.52
0.50
0.48
0.46
0.45
5
10
15
20
25
30
35
40
% STRAIN

Figure 47

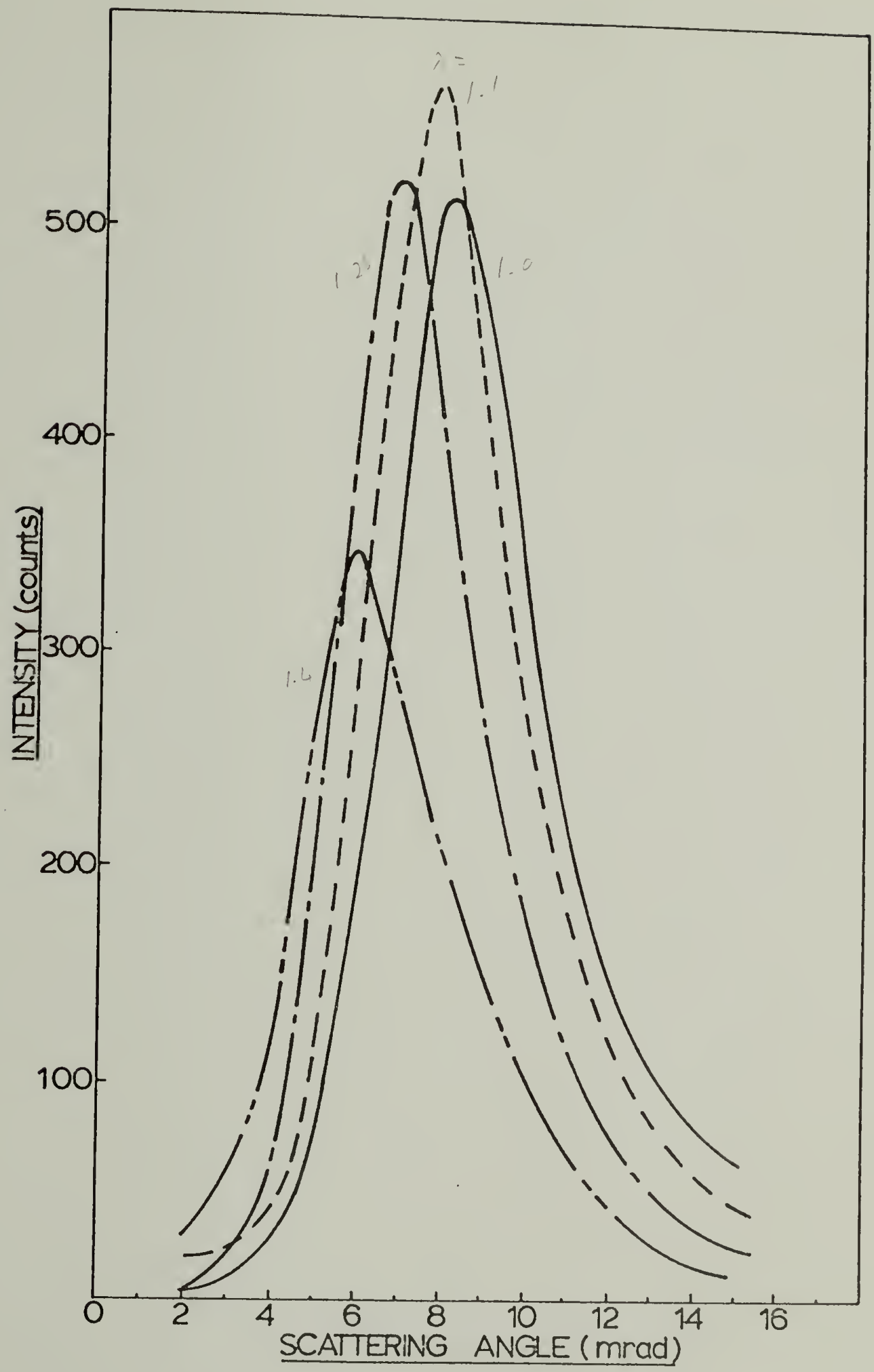
λ =
1.1
1.2
1.0
1.4
500
400
300
200
100
INTENSITY (counts)
0
2
4
6
8
10
12
14
16
SCATTERING ANGLE (mrad)

Figure 48

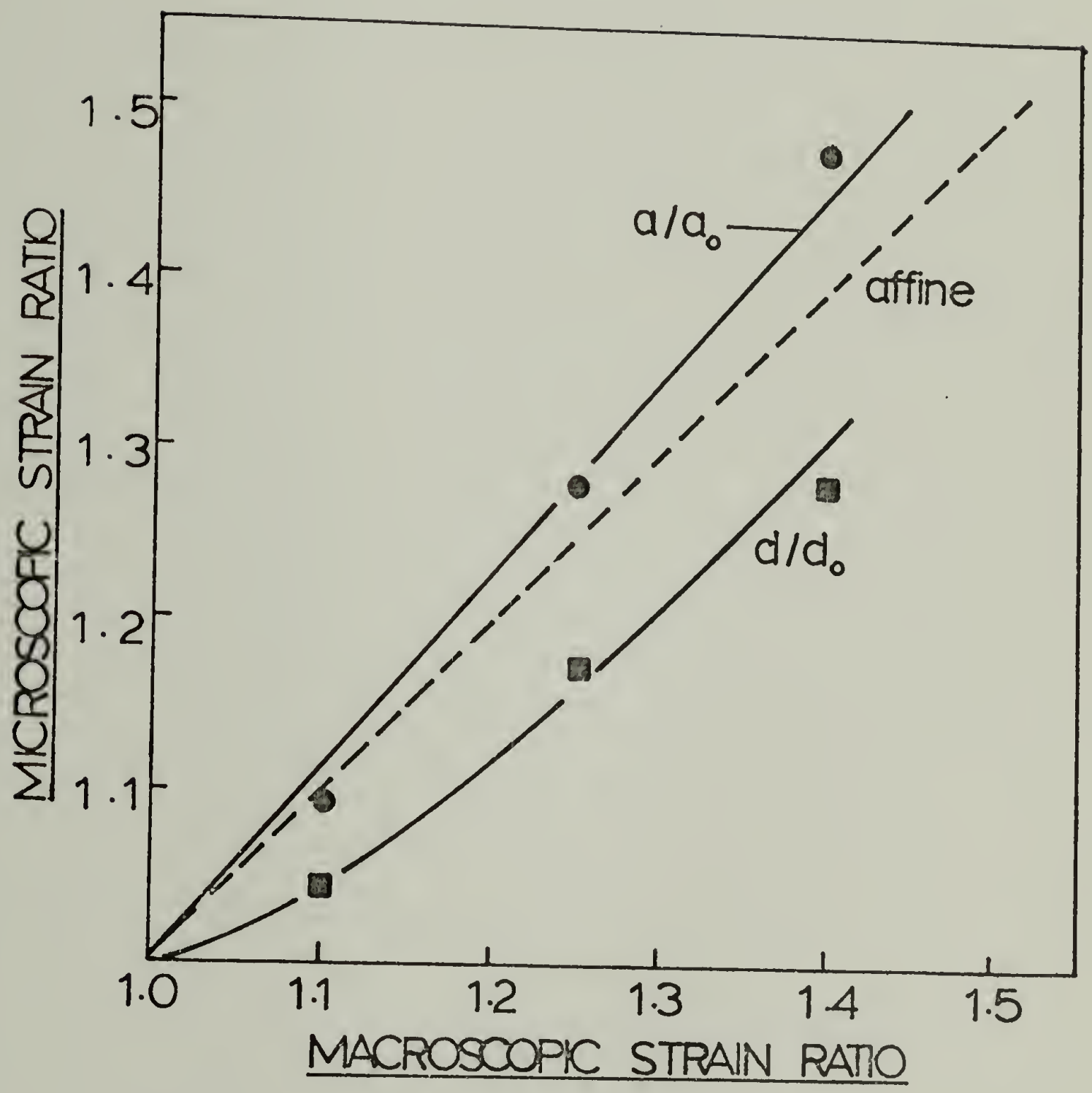
MICROSCOPIC STRAIN RATIO
1.5
1.4
1.3
1.2
1.1
1.0
1.1
1.2
1.3
1.4
1.5
MACROSCOPIC STRAIN RATIO
a/a₀
affine
d/d₀

Figure 49

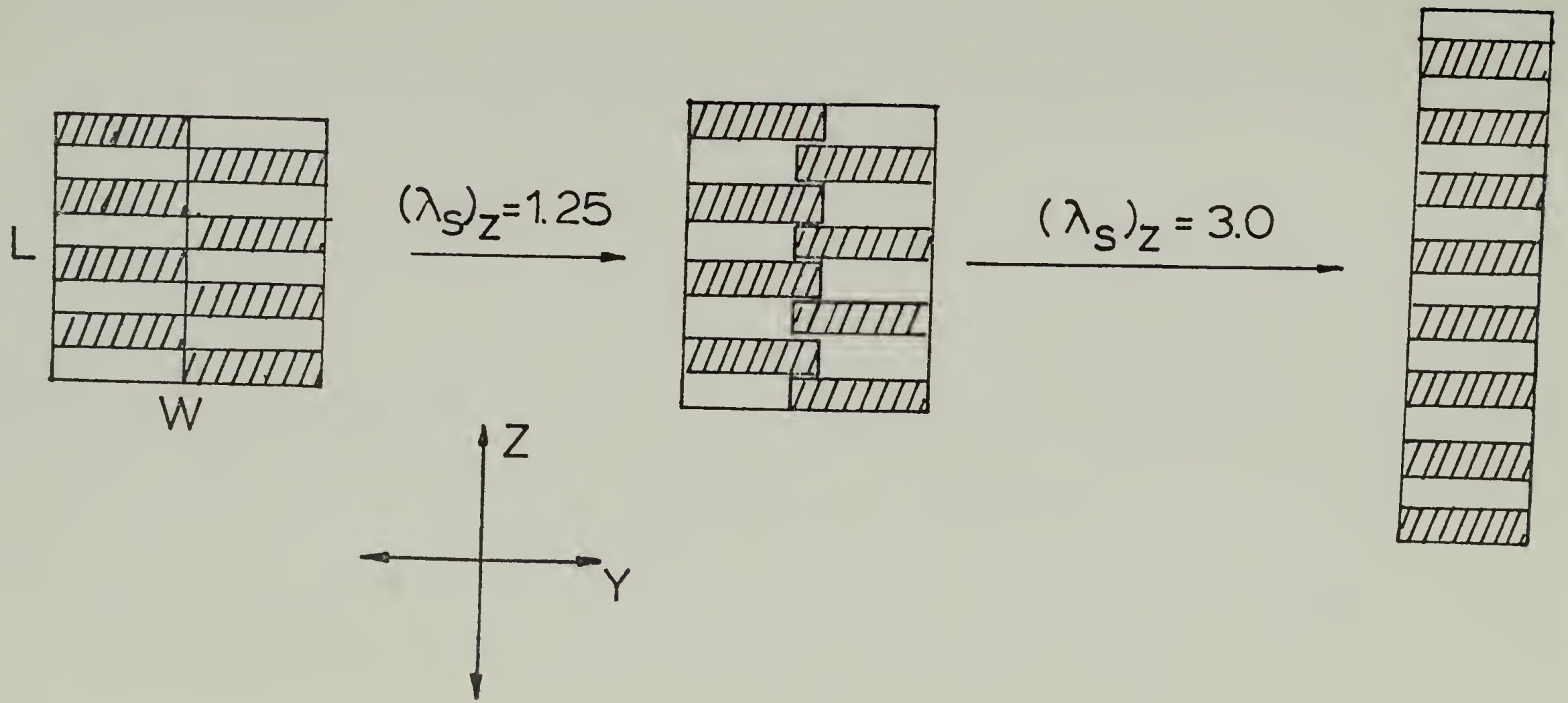

Figure 50

TSVANKIN DEFORMATION MECHANISM 1974

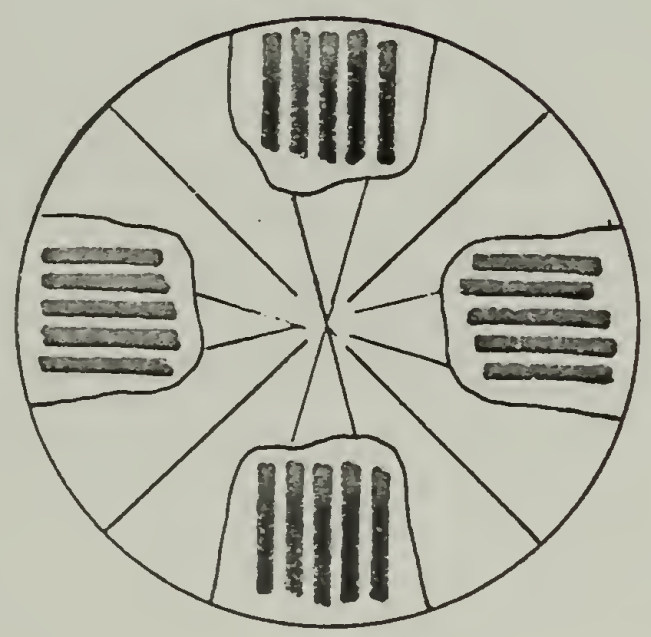

Undeformed

60% strain

Figure 51

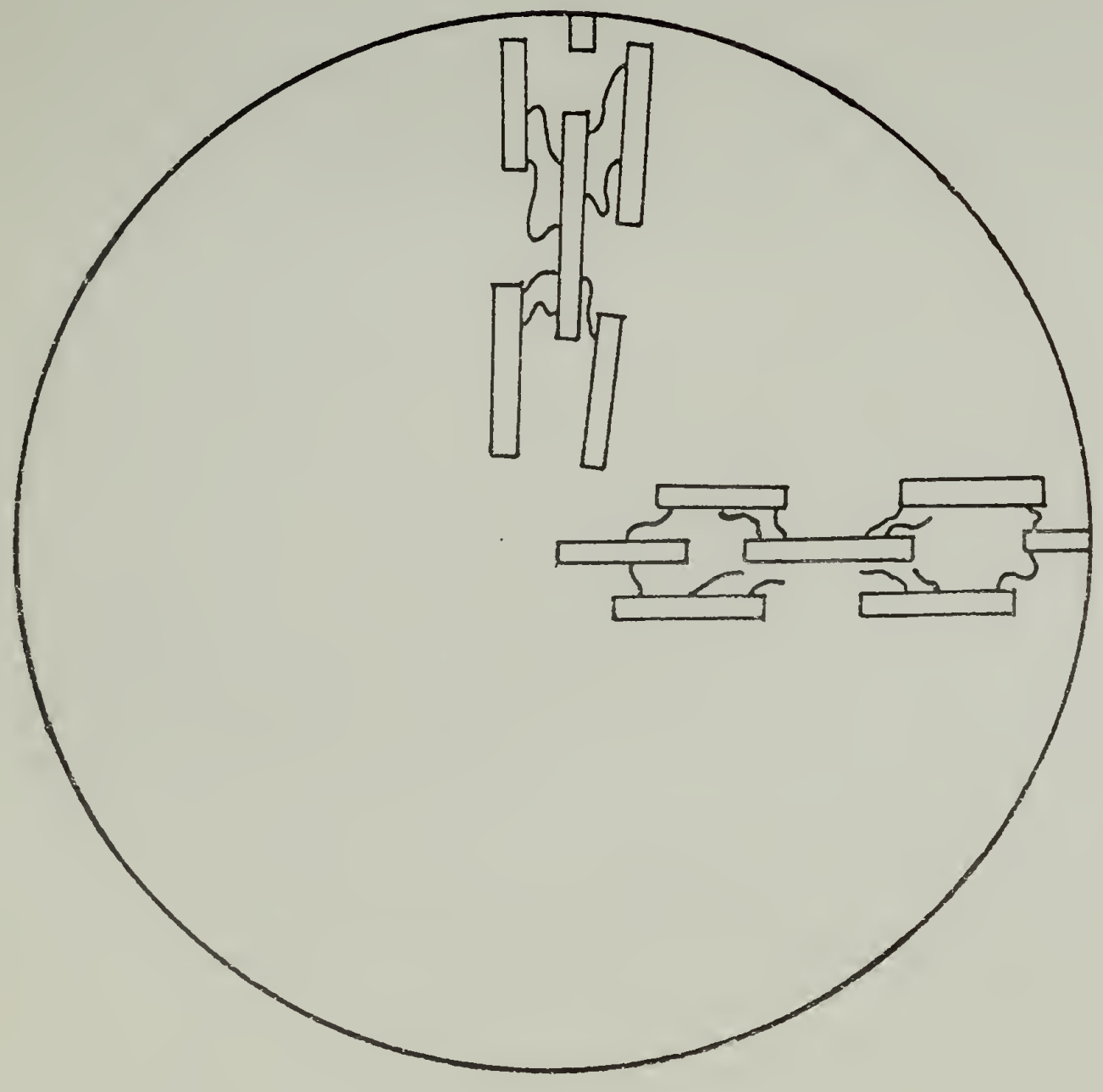

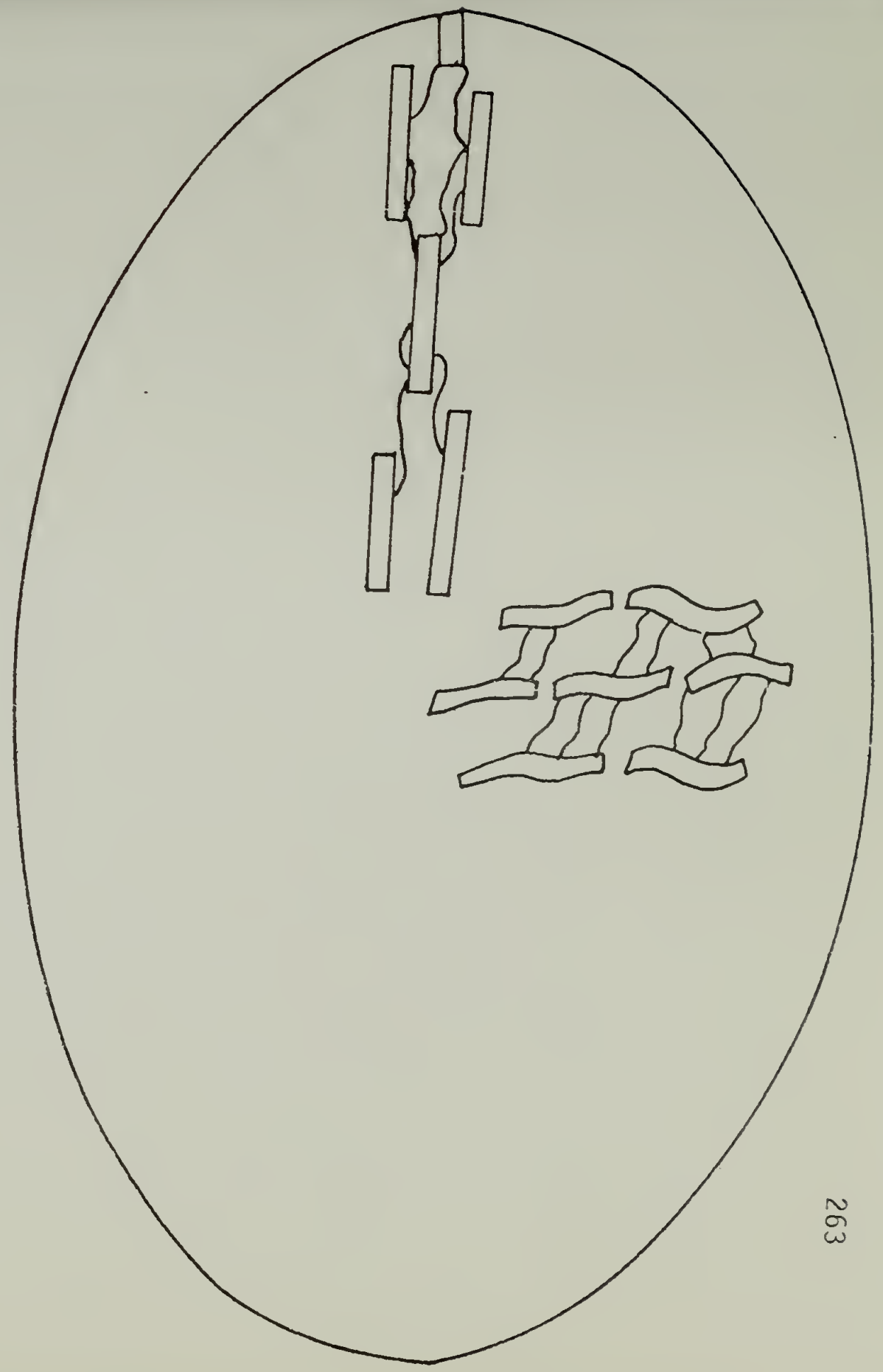

Figure 52

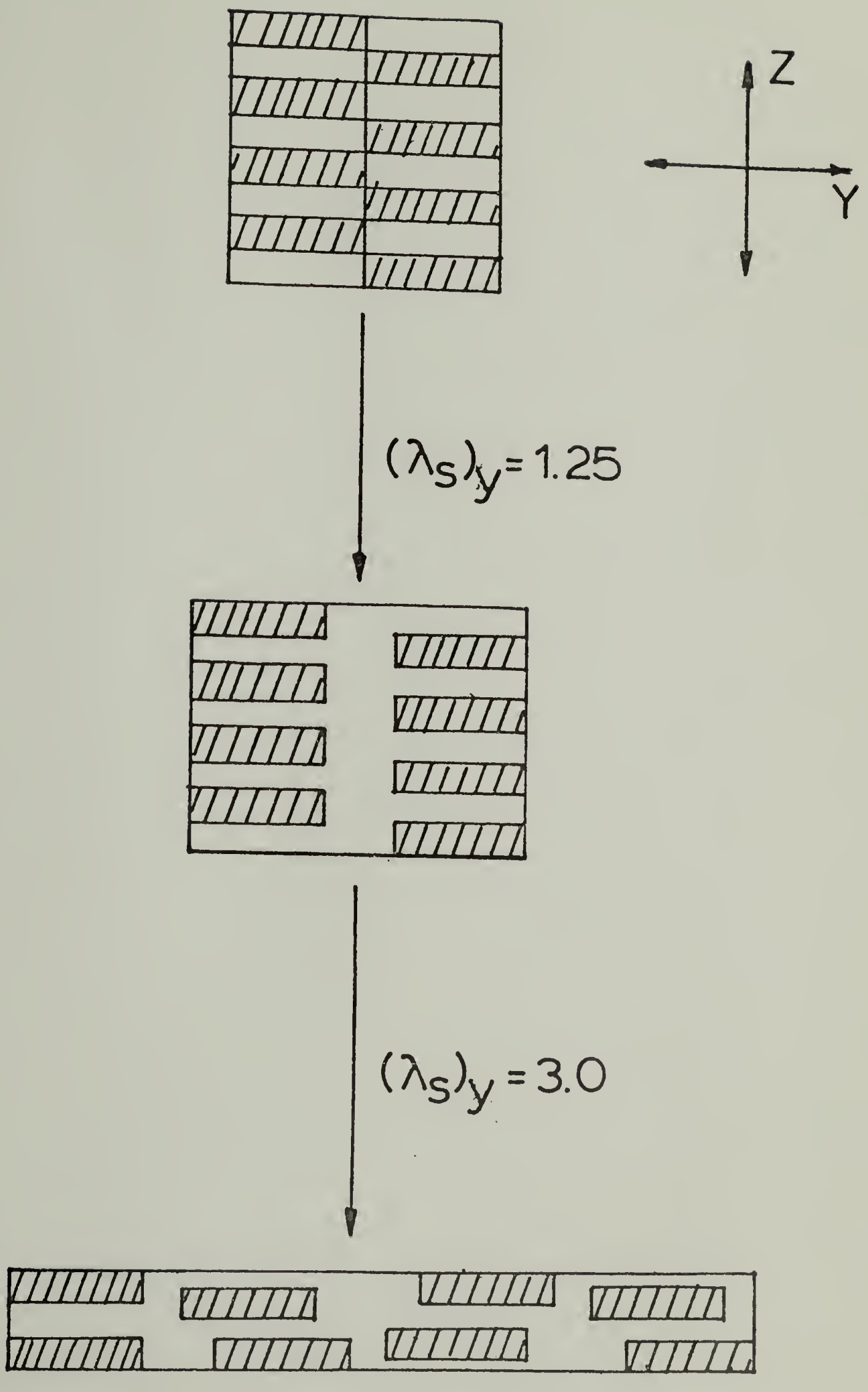

Figure 53

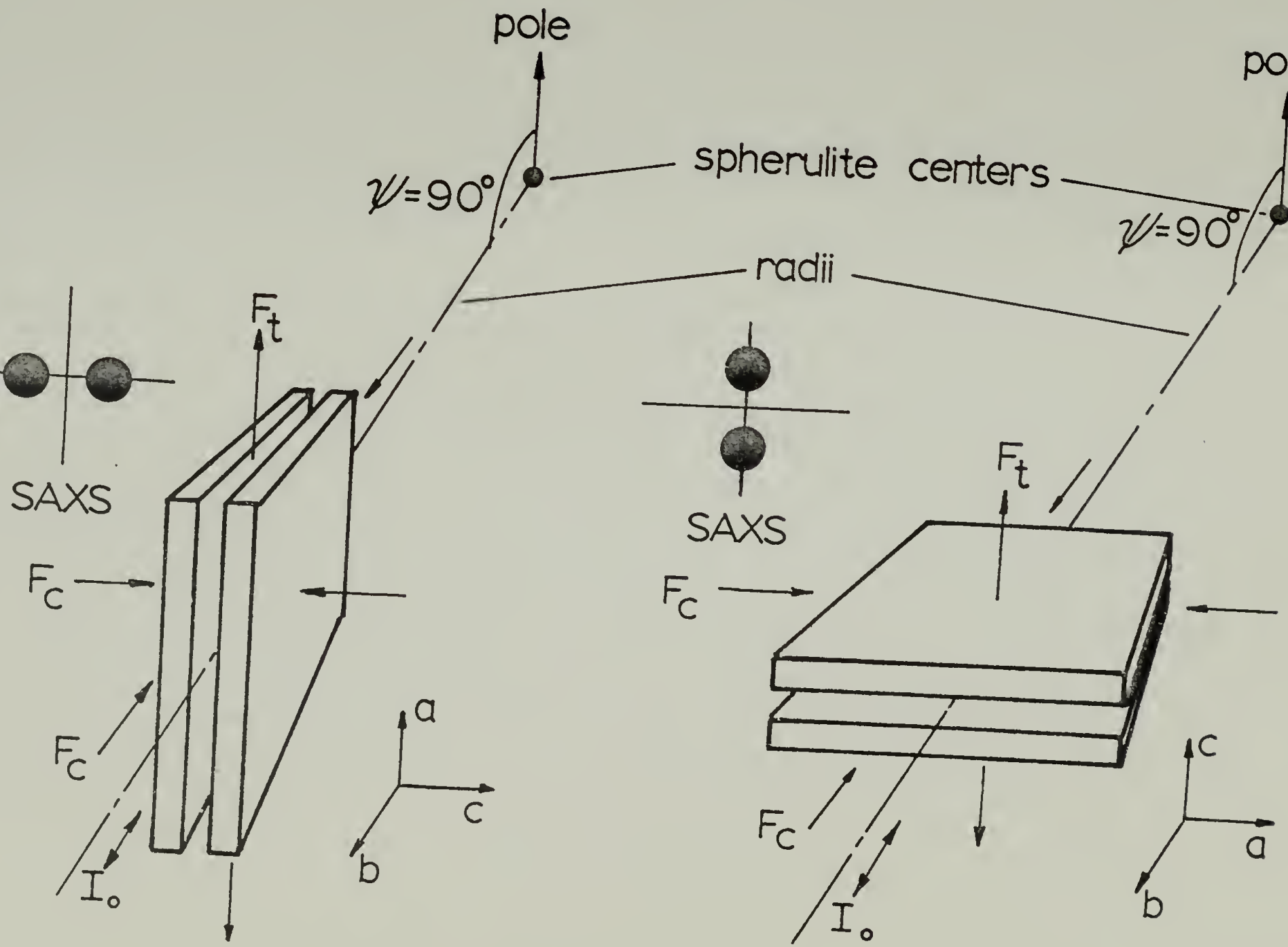
pole
ψ=90°
spherulite centers
radii
pole
ψ=90°
F_t
SAXS
F_c
F_c
I_o
a
c
b
SAXS
F_t
F_c
F_c
I_o
c
a
b

Figure 54

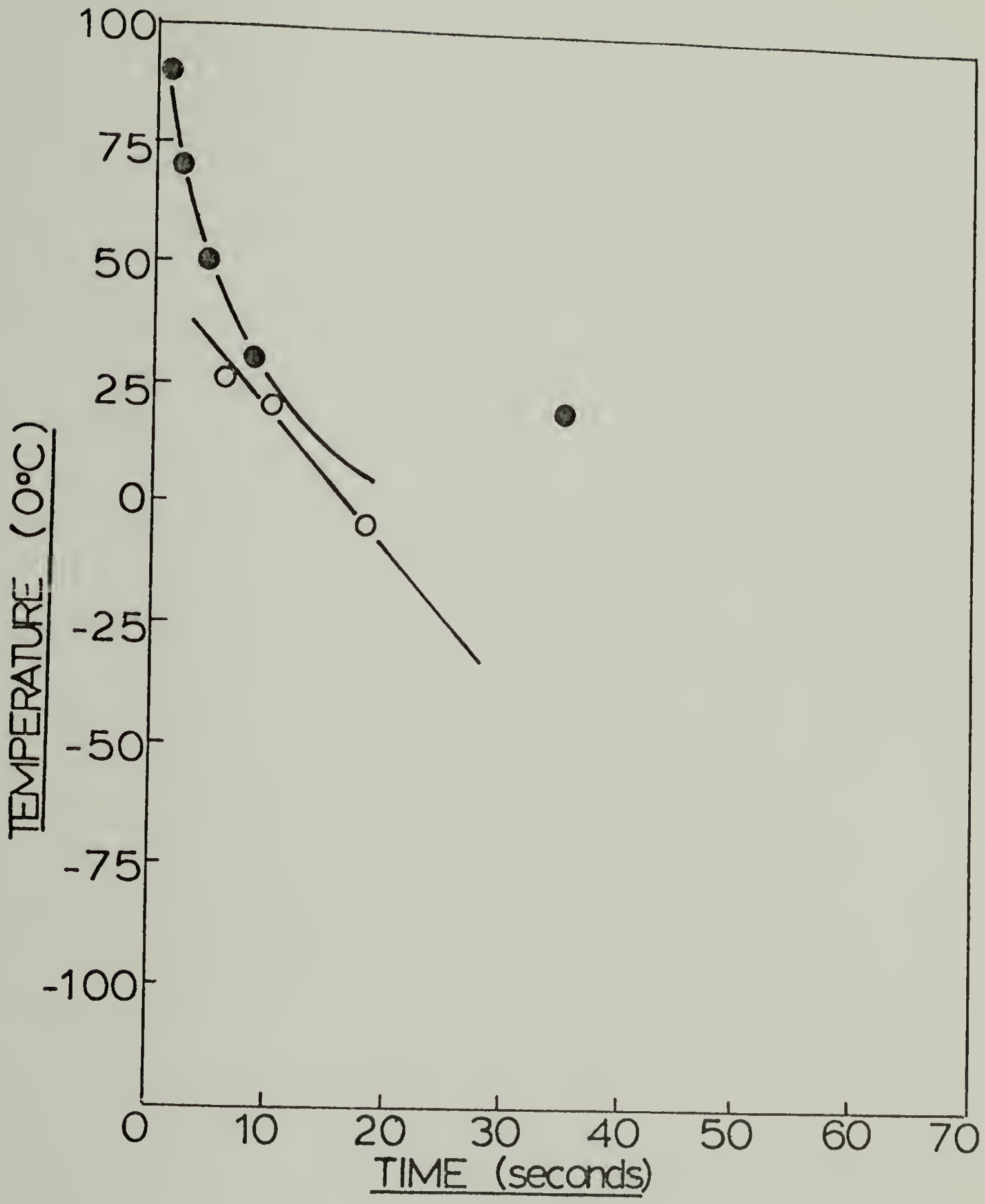
100
75
50
25
0
-25
-50
-75
-100
TEMPERATURE (0°C)
0
10
20
30
40
50
60
70
TIME (seconds)

Figure 55

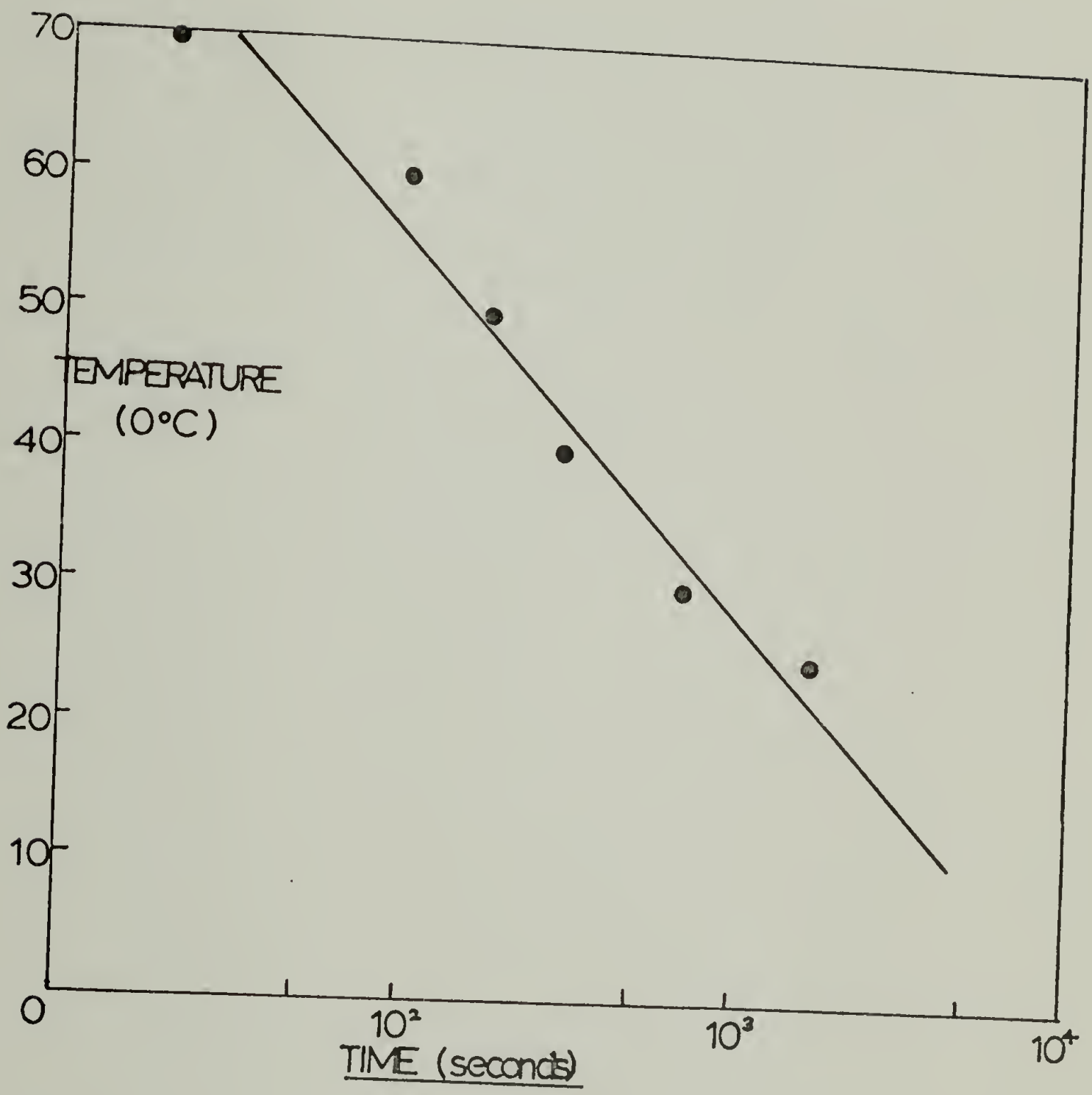

Figure 56

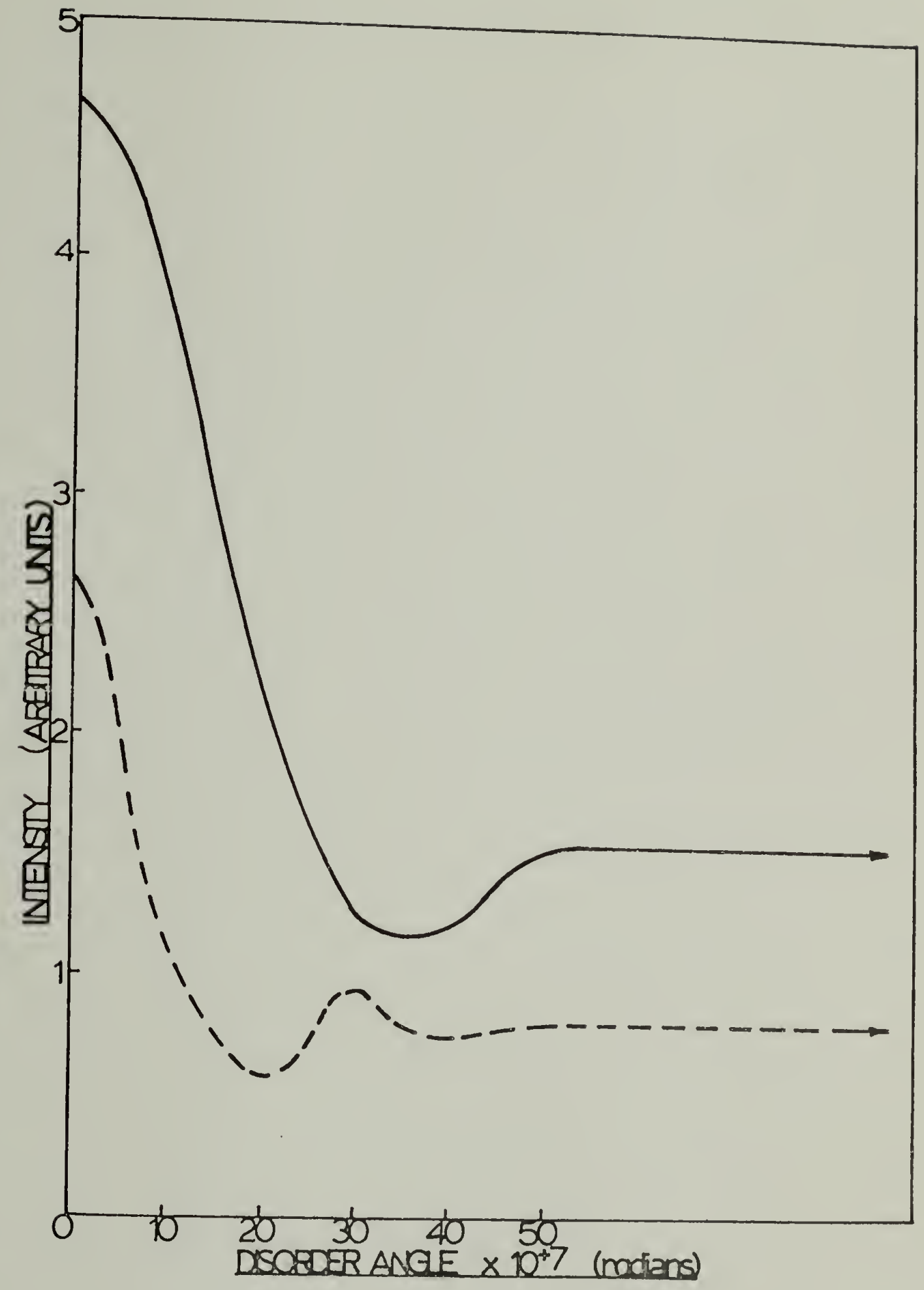
5
4
3
2
1
0
INTENSITY (ARBITRARY UNITS)
10
20
30
40
50
DISORDER ANGLE x 10+7 (radians)

Figure 57

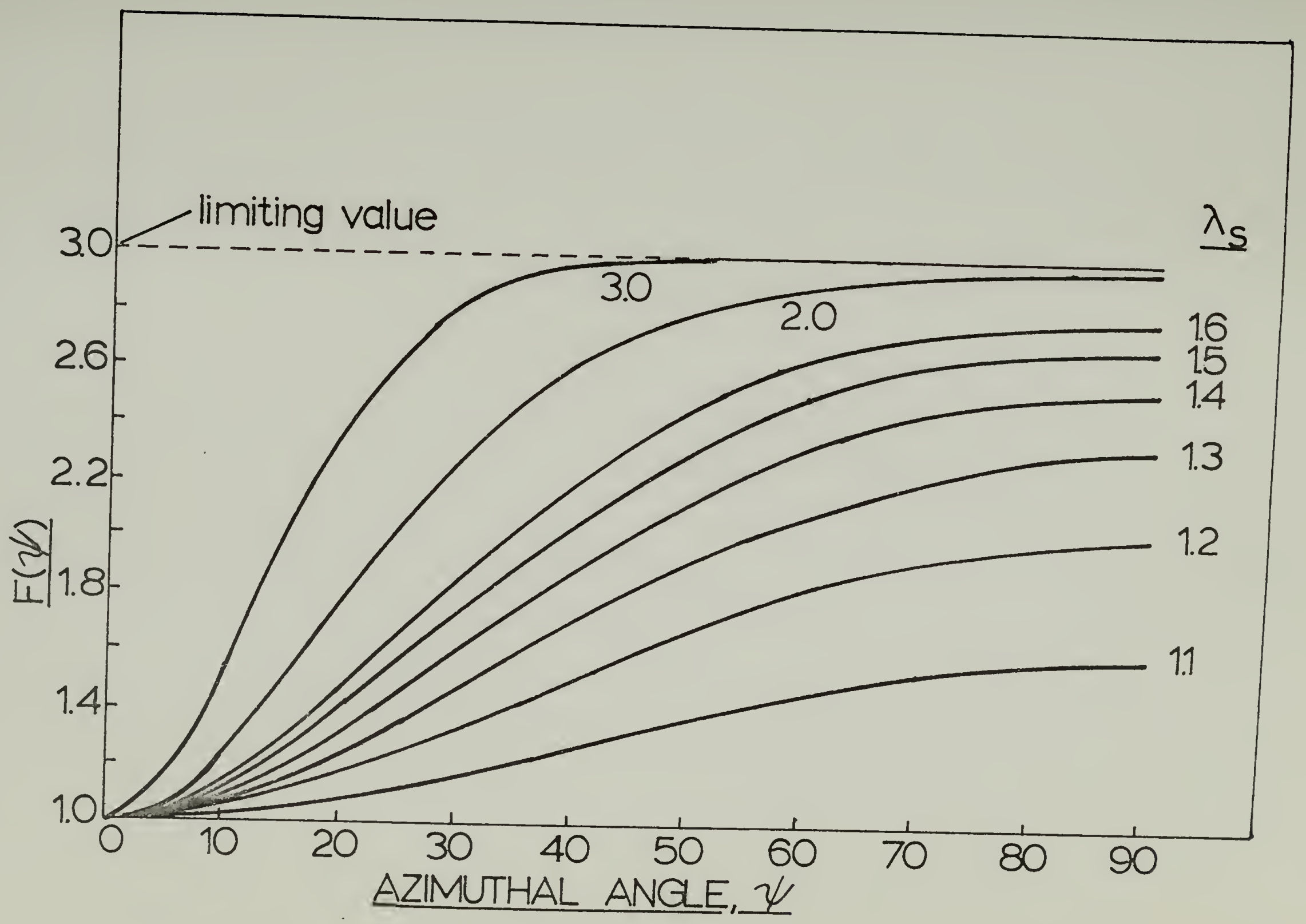
limiting value
3.0
2.6
2.2
1.8
1.4
1.0
F(ψ)
0
10
20
30
40
50
60
70
80
90
AZIMUTHAL ANGLE, ψ
λs
3.0
2.0
1.6
1.5
1.4
1.3
1.2
1.1

Figure 58

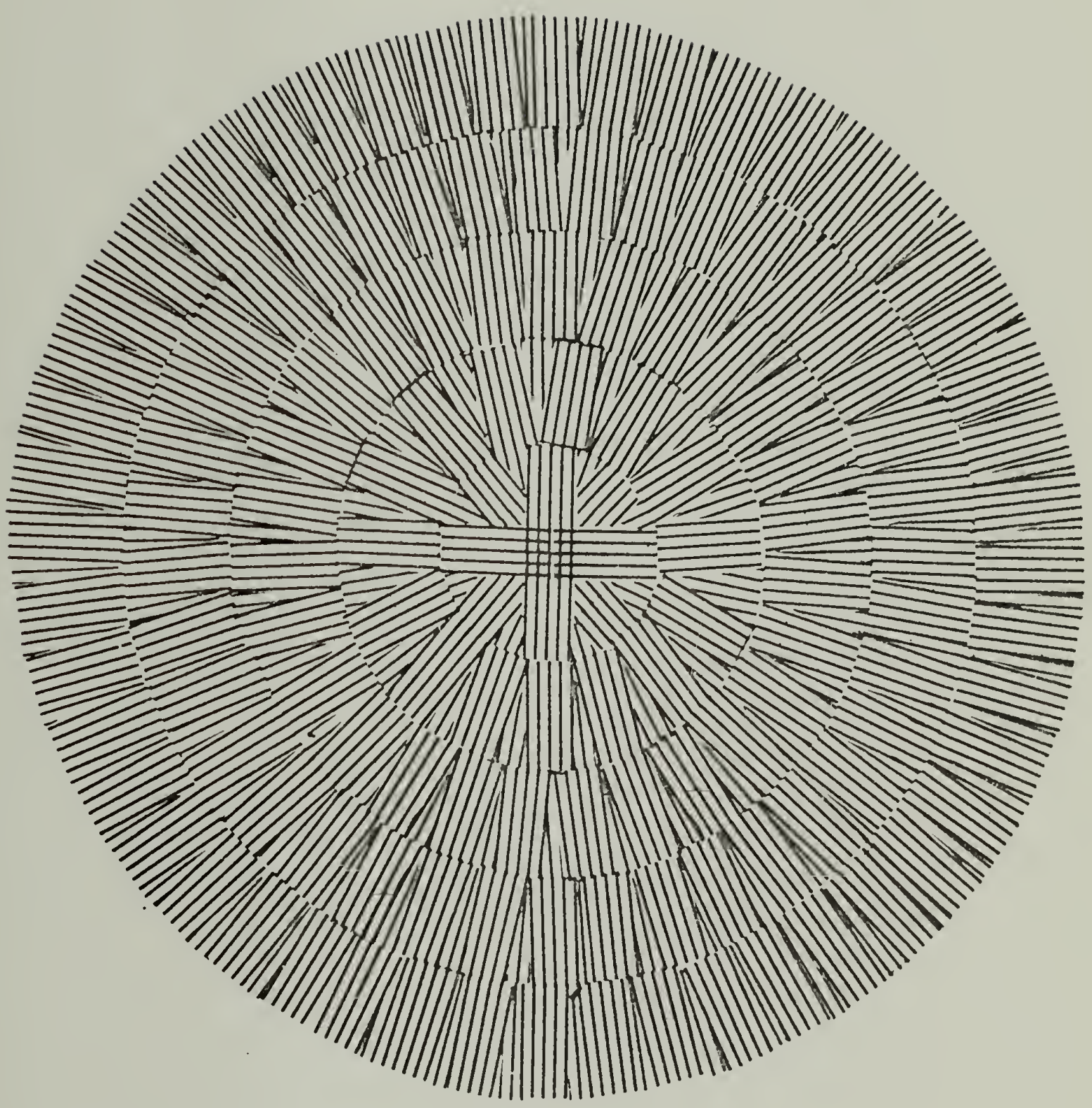

Figure 59

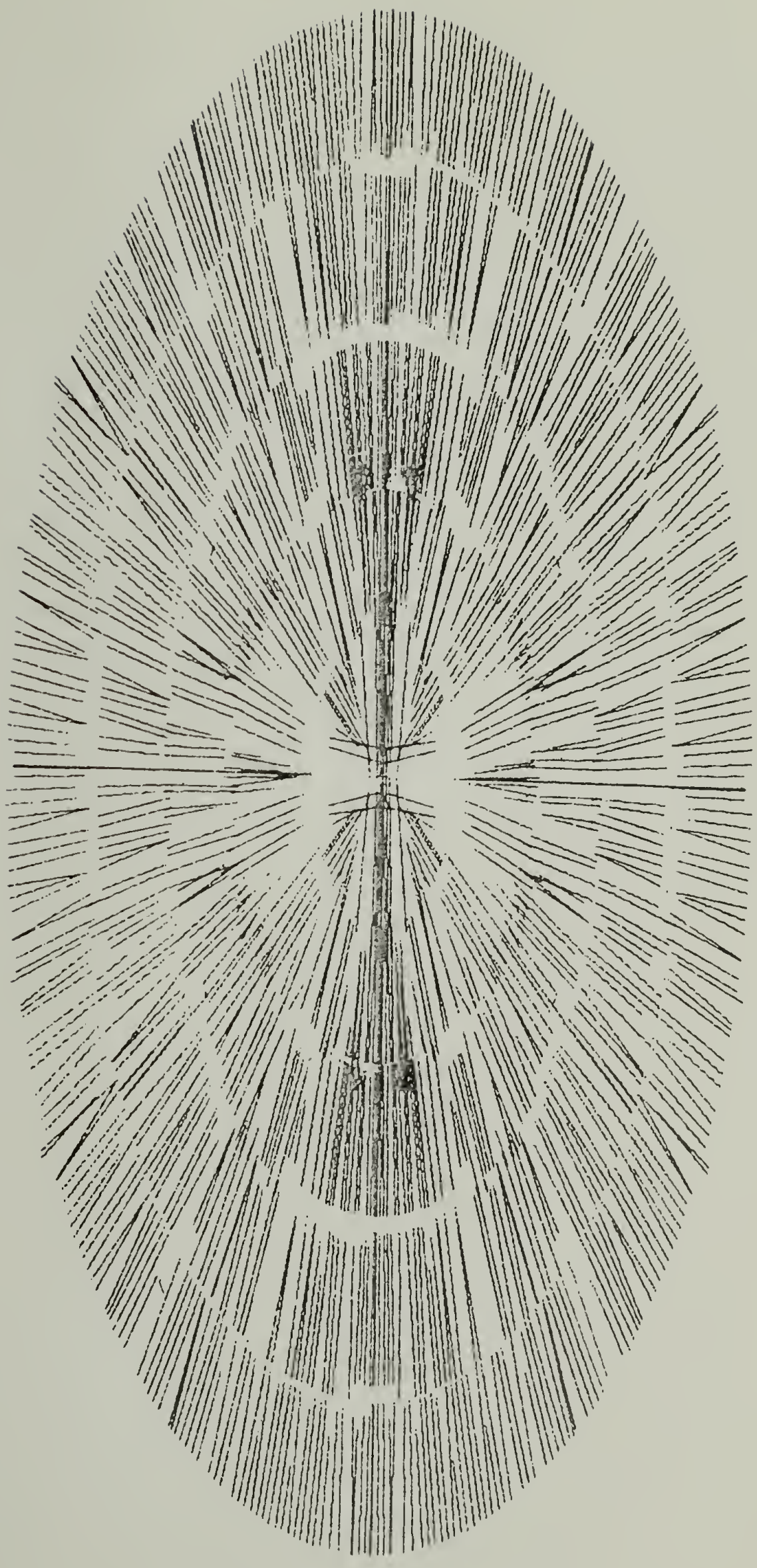

Figure 60

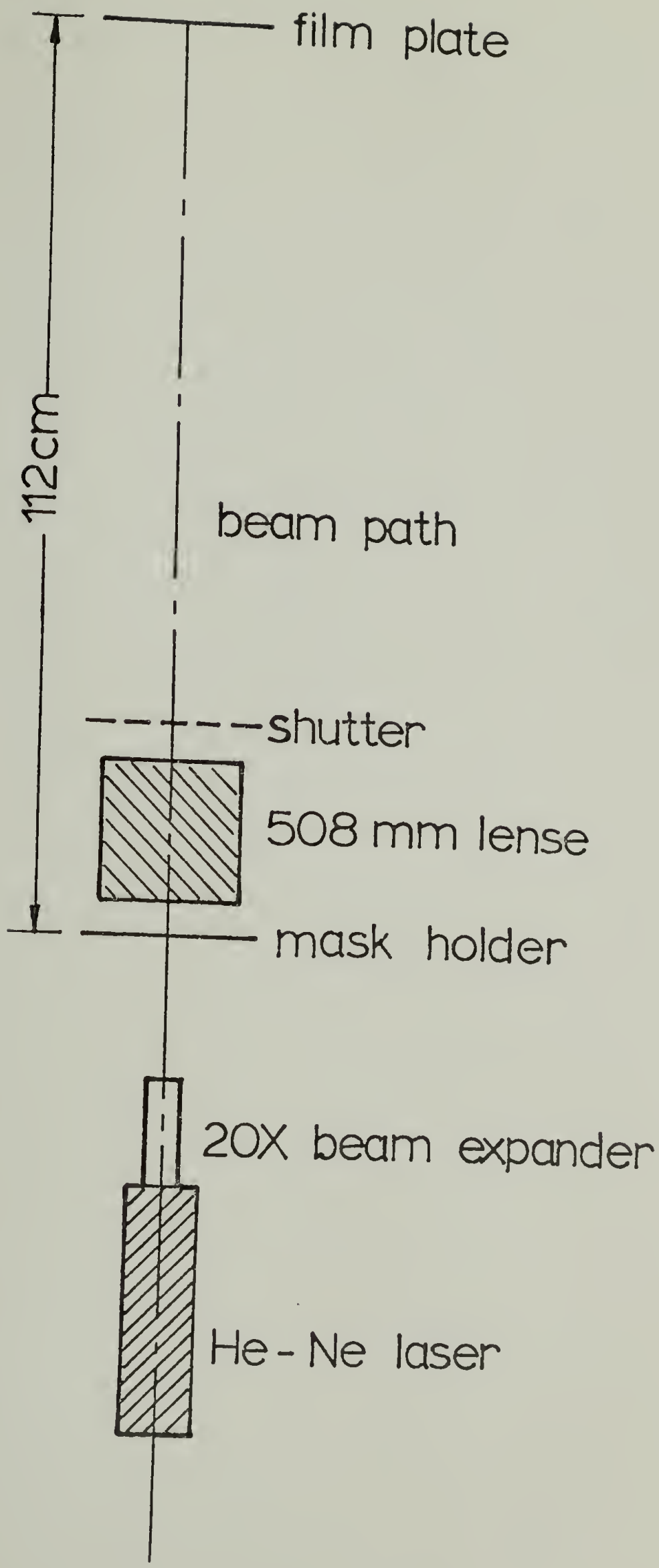
film plate
112cm
beam path
shutter
508 mm lense
mask holder
20X beam expander
He - Ne laser

Figure 61

STRAIN

0%

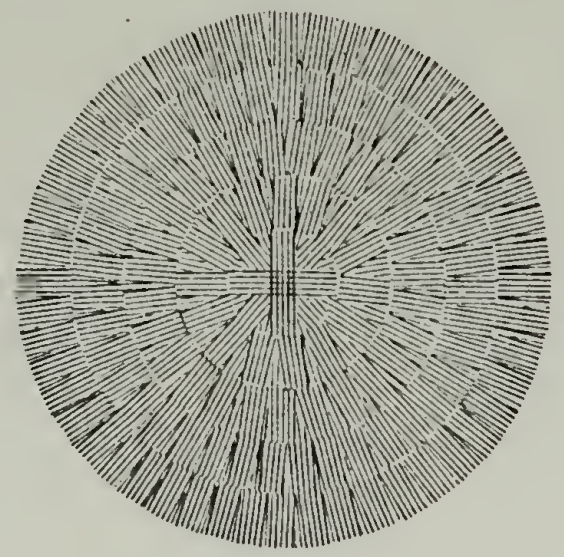

MASKS 8X

60%

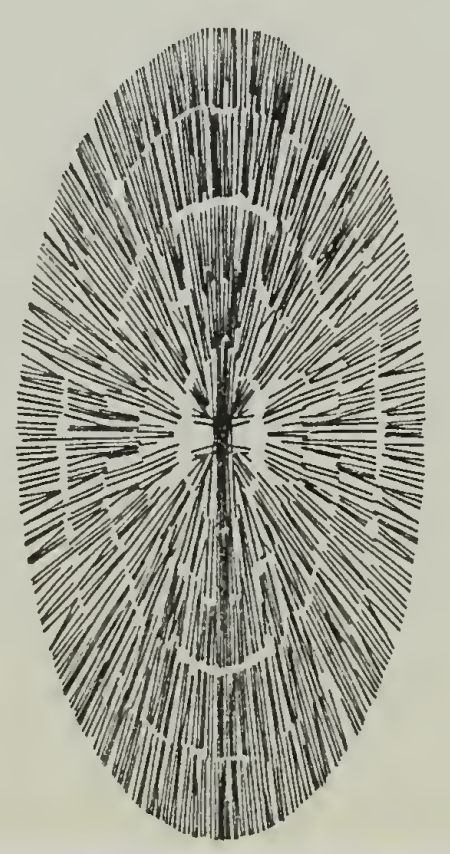

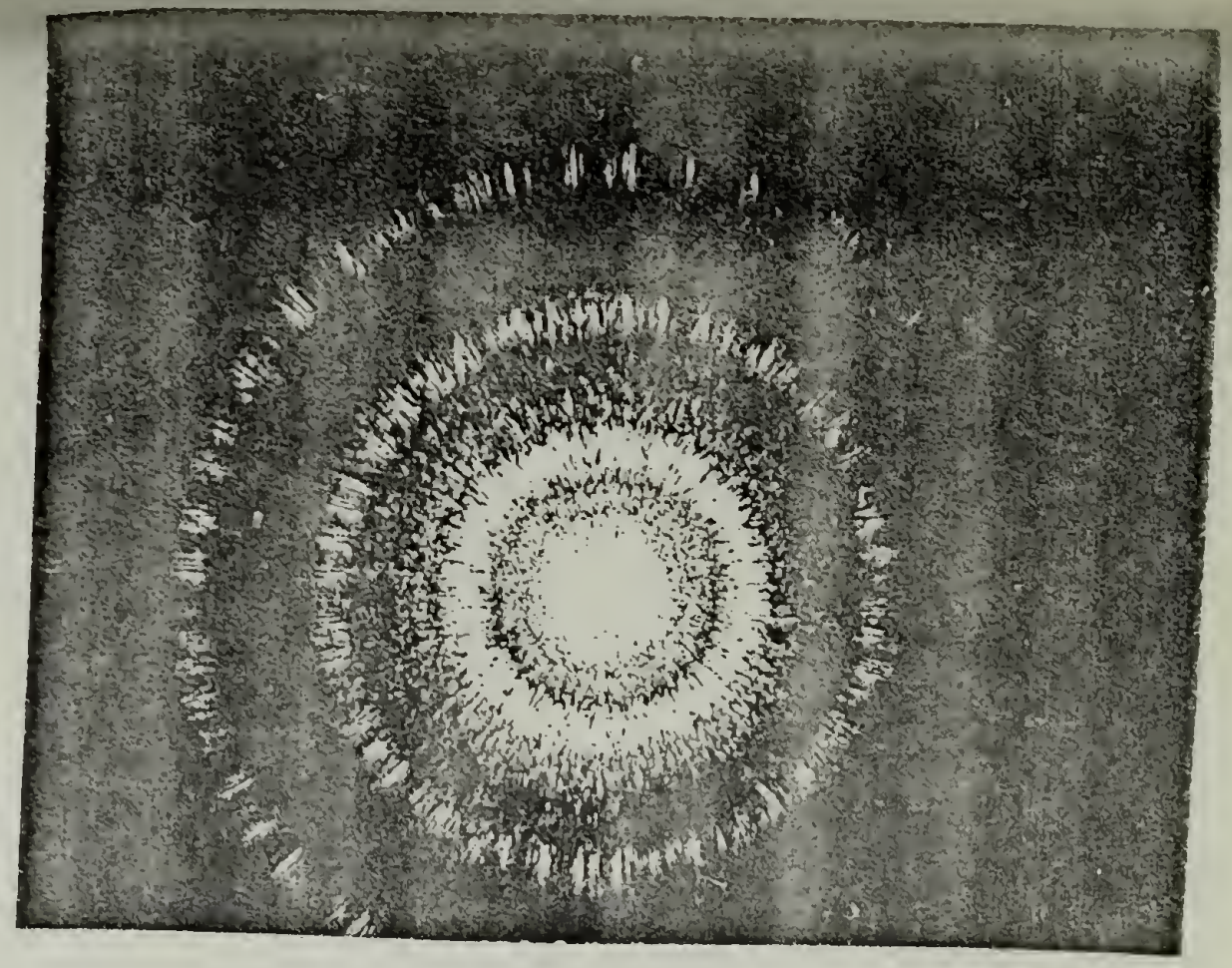

INTERFERENCE

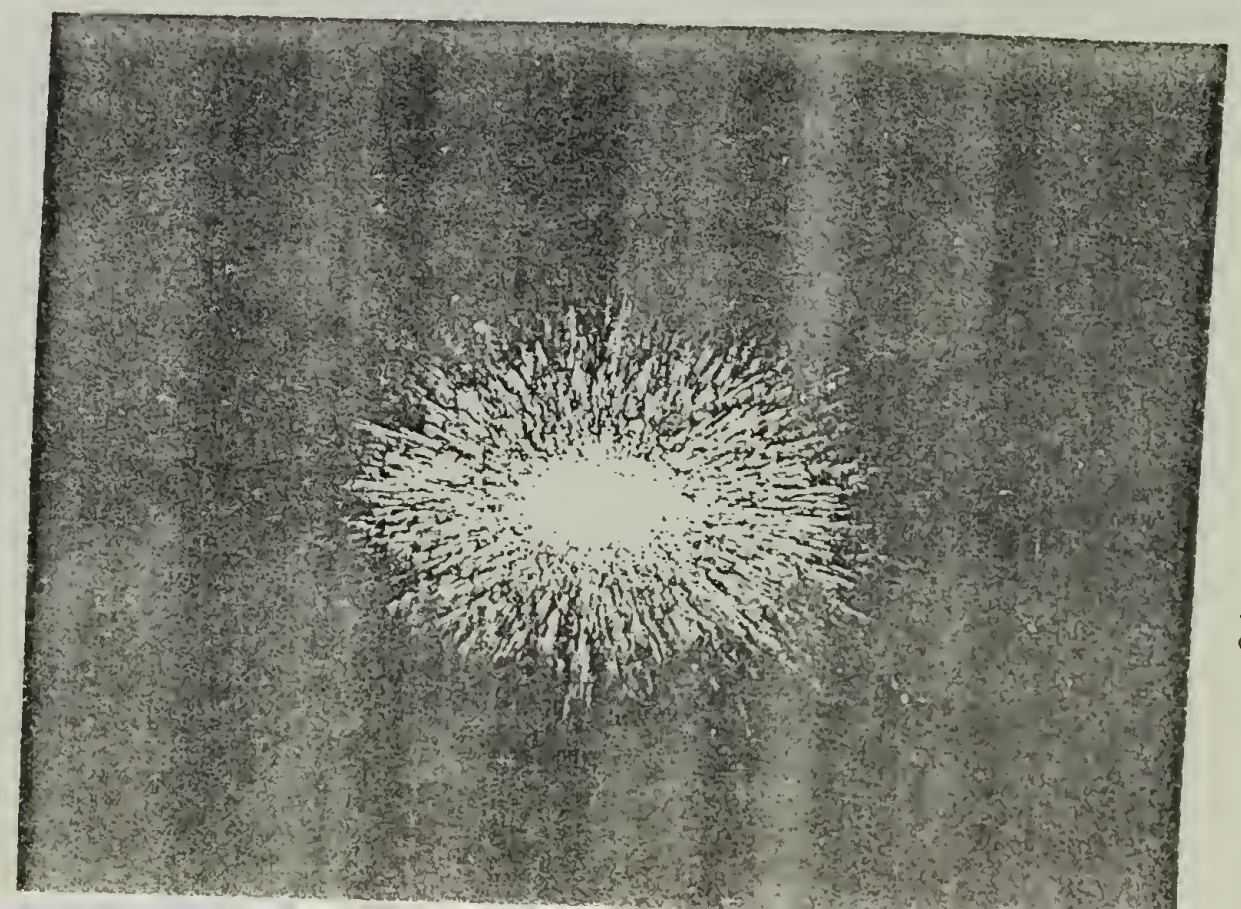

GLOSSARY OF SAXS TERMS

This Work	Hosemann	Vonk	T/B	Meaning
$\bar{x}_d$, d	z_n, $\bar{x}_d$	D	c	Long spacing
$\bar{x}_c$, c	x_n, $\bar{x}_y$	C	a	Crystal thickness
x_a, a	y_n, x_z	A	ℓ	Amorphous thickness
$\bar{x}_E$, E	$\bar{x}_E$	E	ε	Transition thickness
λ	λ	λ	λ	X-ray wavelength
θ	θ	θ	θ	Scattering half angle
$\underset{\sim}{s}$, $\underset{\sim}{s}_T$	$\underset{\sim}{b}$, $\underset{\sim}{h}$ $\frac{2\pi}{\lambda}\sin\theta$	$\underset{\sim}{s}$ $\frac{2\pi}{\lambda}\sin\theta$	$\underset{\sim}{s}$ $\frac{4\pi}{\lambda}\sin\theta$	Scattering vector
ρ_α	ρ_α	ρ_α	ρ_α	Electron density of phase, α
ρ_α'	-	-	-	Mass density of phase, α
I, $\bar{I}$	$\bar{I}$, ISN	i	I	Scattered intensity
F_α	F_α, f_α	-	F, A	Structure factors
H_α, P_α	H_α^2	P_a, P_c^2	-	Thickness distribution functions

g_α, B_α	g_α	β_α	-	Thickness distribution parameters
$\overline{(\Delta x_i)^2}$	Δ^2_α	-	-	Mean squared electron density fluctuations
ϕ	-	ϕ	k	Linear crystallinity
ϕ_c, Φ	-	-	-	Volume crystallinity
W_c	-	-	-	Weight average crystallinity

[1] s_T used for T/B notation in text.

[2] p_a and p_c denote general functional forms.
H_α refers to specific Gaussian types.

REFERENCES

1. L. R. G. Treloar, "The Physics of Rubber Elasticity," Second Edition, Oxford Press, London, 1958.
2. I. M. Ward, "Mechanical Properties of Solid Polymers," Wiley-Interscience, New York, 1971.
3. R. S. Stein, Acc. Chem. Res. 5, 121 (1972).
4. F. Bueche, J. Polym. Sci. 22, 113 (1956).
5. J. M. Schultz, "Polymeric Materials Science," Prentice-Hall, New Jersey, 1974, Chapters 2, 4, 11.
6. R. Hosemann, Polymer 3, 349 (1962).
7. R. S. Stein, 'Studies of the Deformation of Crystalline Polymers' in "Rheology," Vol. 5, F. R. Eirich, Ed., Academic Press, New York, 1969.
8. I. M. Ward, "Mechanical Properties of Solid Polymers," Wiley-Interscience, New York, 1971, Chapter 10.
9. K. Sasaguri, M. B. Rhodes and R. S. Stein, J. Polym. Sci. B1, 571 (1963).
10. R. Yang and R. S. Stein, J. Polym. Sci. 5, 939 (1967).
11. R. Samuels, Nat. Meeting Am. Chem. Soc., 152nd, New York, September, 1966; Polymer Preprints 7, 870 (1966).
12. I. L. Hay and A. Keller, Kolloid-Z. 204, 43 (1965).
13. W. Kuhn and F. Grun, Kolloid-Z. 101, 248 (1942).
14. O. Kratky, Kolloid-Z. 84, 149 (1938).
15. K. Sasaguri, S. Hoshino and R. S. Stein, J. Appl. Phys. 35, 3188 (1964).

16. K. Sasaguri, R. Yamada and R. S. Stein, J. Appl. Phys. 35, 3188 (1964).

17. Z. W. Wilchinsky, Polymer 5, 271 (1964).

18. S. Clough, J. J. Van Aartsen and R. S. Stein, J. Appl. Phys. 36, 3072 (1965).

19. J. J. Van Aartsen and R. S. Stein, J. Polym. Sci. A-2, 9, 295 (1971).

20. P. Labarbe, S. Baczek, R. J. Gaylord and R. S. Stein, Polym. Preprints 15, 471 (1974).

21. R. Yang and R. S. Stein, J. Polym. Sci. A-2, 5, 939 (1967).

22. R. G. Crystal and D. Hansen, J. Polym. Sci. A-2, 6, 981 (1968).

23. M. Takayanagi, K. Imada and T. Kajiyama, J. Polym. Sci. C-15, 263 (1966).

24. J. C. Halpin and J. L. Kardos, J. Appl. Phys. 43, 2235 (1972).

25. D. Yoon, Ph.D. Thesis, University of Massachusetts, 1973.

26. J. Patel and P. J. Phillips, Polymer Letters 11, 771 (1973).

27. T. T. Wang, J. Appl. Phys. 44, 2218 (1973); J. Polym. Sci., Polym. Phys. Ed. 12, 145 (1974).

28. T. Kawaguchi, ONR Tech. Rep. No. 88, Project NR 056-378, Contract NONR 3357(01), Polymer Research Institute, University of Massachusetts, 1966

29. T. Pakula and M. Kryszewski, J. Polym. Sci. C38, 87 (1972).

30. T. Pakula, A. G. Galeski and M. Kryszewski, J. Polym. Sci., Symp. No. 42, 753 (1973).

31. L. E. Alexander, "X-Ray Diffraction Methods in Polymer Science," Wiley-Interscience, New York, 1969, Chapter 1.

32. A. Guinier, "X-Ray Diffraction," W. H. Freeman and Company, San Francisco, 1963, Chapter 2.

33. M. Kakudo and N. Kasai, "X-Ray Diffraction by Polymers," Kodansha Ltd., Tokyo, and Elsevier Publishing Company, Amsterdam, New York, 1972.

34. D. Ya. Tsvankin, Polym. Sci. USSR 6, 2304 (1964).

35. D. R. Buchanan, J. Polym. Sci. A-2, 9, 645 (1971).

36. D. Ya. Tsvankin, Polym. Sci. USSR 6, 2310 (1964).

37. W. E. Kaufman and J. M. Schultz, J. Mat. Sci. 8, 41 (1973).

38. S. Kavesh and J. M. Schultz, J. Polym. Sci. A-2, 9, 85 (1971).

39. P. W. Schmidt, Acta Cryst. 19, 938 (1965).

40. A. Guinier, G. Fournet, C. B. Walker and K. L. Yudowitch, "Small Angle Scattering of X-Rays," John Wiley, New York, 1955, Chapter 3.

41. R. W. Hendricks, in press.

42. S. K. Baczek, R. S. Stein, R. W. Hendricks and D. Carlson, in press.

43. P. H. Geil, "Polymer Single Crystals," Interscience, New York, 1962.

44. P. H. Geil in "Small Angle Scattering from Fibrous and Partially Oriented Systems" (J. Polym. Sci. C13), R. H. Marchessault, Ed., Interscience, New York, 1966, p. 149.

45. W. O. Statton, J. Polym. Sci. 41, 143 (1959).

46. G. Meinel, N. Morosoff and A. Peterlin, J. Polym. Sci. A-2, 8, 1723 (1970).

47. B. Crist, J. Polym. Sci., Polym. Phys. Ed. 11, 635 (1973); 11, 1023 (1973).

48. F. Zernicke and J. A. Prins, Z. Phys. 41, 184 (1927).

49. J. J. Hermans, Recueil. Trav. Chim. Pays.-Bas. 63, 5 (1944).

50. R. Hosemann and S. Bagchi, "Direct Analysis of Diffraction by Matter," North Holland, Amsterdam, 1962, p. 408.

51. B. K. Vainshtein, "Diffraction of X-Rays by Chain Molecules," Elsevier Publishing Company, Amsterdam and New York, 1966.

52. R. Bramer, Ph.D. Thesis, University of Ulm, 1973.

53. W. Wenig, Ph.D. Thesis, University of Ulm, 1974.

54. W. Wenig, F. E. Karasz and W. J. MacKnight, J. Appl. Phys. 46, 4194 (1975).

55. F. P. Warner, W. J. MacKnight and R. S. Stein, in press.

56. P. Debye and A. M. Bueche, J. Appl. Phys. 20, 518 (1949).

57. P. Debye, H. R. Anderson and H. Brumberger, J. Appl. Phys. 28, 679 (1957).

58. G. Porod, Kolloid-Z. 124, 83 (1957); 125, 51 (1952); 125, 109 (1952).

59. C. G. Vonk and G. Kortleve, Kolloid-Z. 220, 19 (1967); 225, 124 (1968).

60. G. C. Vonk, J. Appl. Cryst. 6, 81 (1973).

61. K. U. Fulcher, D. S. Brown and R. E. Wetton, J. Polym. Sci. C38, 315 (1972).

62. F. P. Warner, D. W. Brown and R. E. Wetton, J. Chem. Soc., Faraday Trans. I, 72, 1064 (1976).

63. F. P. Warner, Ph.D. Thesis, Loughborough University of Technology, 1975.

64. D. S. Brown, K. U. Fulcher and R. E. Wetton, Polymer 14, 379 (1973).

65. T. Russell, University of Massachusetts, private communication.

66. V. Luzzati, Acta Cryst. 13, 939 (1960).

67. W. Ruland, J. Appl. Cryst. 4, 70 (1971).

68. O. Kratky, Makromol. Chem. 35A, 12 (1960).

69. O. Kratky, J. Pilz and P. J. Schmitz, J. Colloid Interface Sci. 21, 24 (1966).

70. H. Janeschitz-Kriegl, Ph.D. Thesis, University of Graz, 1951.

71. T. Sakai, K. Miyasaka and K. Ishikawa, J. Polym. Sci. A-2, 10, 253 (1972).

72. M. B. Rhodes and R. S. Stein, J. Appl. Phys. 32, 2344 (1961).

73. D. A. Blackadder and J. S. Kenirg, J. Appl. Polym. Sci. 16, 1261 (1972).

74. D. A. Blackadder and P. I. Vincent, Polymer 15, 2 (1974).

75. D. Heikens, J. Polym. Sci. 35, 139 (1959).

76. P. H. Hermans, D. Heikens and E. Weidinger, J. Polym. Sci. 35, 145 (1959).

77. D. J. Blundell, Acta Cryst. A26, 472 (1970).

78. F. Khambatta, Ph.D. Thesis, University of Massachusetts, 1974.

79. R. W. Hendricks, private communication.

80. R. W. Hendricks, D. Carlson, S. K. Baczek and R. S. Stein, in press.

81. R. S. Stein and T. Hashimoto, J. Polym. Sci. A-2, 9, 517 (1971).

82. R. J. Samuels, "Structured Polymer Properties," Wiley, New York, 1974.

83. R. S. Moore and C. Gieniewski, J. Appl. Phys. 36, 10 (1965).

84. I. L. Hay and A. Keller, J. Mat. Sci. 1, 41 (1966); 2, 538 (1967).

85. D. P. Pope and A. Keller, J. Mat. Sci. 9, 920 (1974).

86. W. Parrish and T. R. Kohler, Rev. Sci. Instr. 27, 795 (1956).

87. P. W. Schmidt, Acta. Cryst. 19, 938 (1965).

88. P. W. Schmidt, J. Appl. Cryst. 3, 137 (1970).

89. O. Kratky, G. Porod and L. Kahovec, Z. Electrochem. 55, 53 (1951).

90. R. W. Hendricks and P. W. Schmidt, Acta Physica Austriaca 26, 97 (1967).

91. O. Kratky, G. Porod and Z. Skala, Acta Physica Austriaca 13, 76 (1960)

92. K. Kranjc, Acta Cryst. 7, 709 (1954).

93. V. Synecek, Acta Cryst. 15, 642 (1962).

94. G. Kortleve, C. A. F. Tuijnman and C. G. Vonk, J. Polym. Sci. A-2, 10, 123 (1972).

95. C. J. Borkowski and M. Kopp, IEEE Trans. Nucl. Sci. NS-17, 340 (1970); NS-19, 161 (1972).

96. J. Schelten and R. W. Hendricks, J. Appl. Cryst. 8, 421 (1975).

97. L. B. Schaeffer and R. W. Hendricks, J. Appl. Cryst. 7, 159 (1974).

98. T. Hashimoto, A. Todo, H. Itoi and H. Kawai, Macromolecules 10, 377 (1977).

99. W. Ruland, Acta Cryst. 14, 1180 (1961).

100. W. Ruland, Polymer 5, 89 (1964).

101. F. W. Billmeyer, Jr., J. Appl. Phys. 28, 1114 (1957).

102. M. Dole, J. Chem. Phys. 20, 781 (1952).

103. F. H. Muller, Kolloid-Z. 95, 172, 307 (1941).

104. P. H. Hermans and P. Platzek, Kolloid-Z. 88, 68 (1939).

105. S. Hoshino, J. Powers, D. G. Legrand, H. Kawai and R. S. Stein, J. Polym. Sci. 58, 185 (1962).

106. D. Y. Yoon, C. Chang and R. S. Stein, J. Polym. Sci., Polym. Phys. Ed. 12, 2091 (1974).

107. T. Oda, S. Nomura and H. Kawai, J. Polym. Sci., Part A, 3, 1993 (1965).

108. S. Nomura, A. Asanuma, S. Suehiro and H. Kawai, J. Polym. Sci. A2, 9, 1991 (1971).

109. S. Nomura, M. Matsuo and H. Kawai, J. Polym. Sci., Polym. Phys. Ed. 10, 2489 (1972).

110. I. L. Hay and A. Keller, J. Mat. Sci. 1, 41 (1966).

111. A. Peterlin, J. Mat. Sci. 6, 490 (1971).

112. A. Peterlin, J. Polym. Sci. C15, 427 (1966); C18, 123 (1967).

113. A. Peterlin, Kolloid-Z. 233, 857 (1969).

114. H. Kiho, A. Peterlin and P. H. Geil, J. Appl. Phys. 35, 1599 (1964); J. Polym. Sci. A-3, 157 (1965).

115. R. Hosemann, J. Loboda-Cackovic and H. Loboda-Cackovic, Zeit. fur Naturforch. 27a, 478 (1972).

116. G. S. Y. Yeh, R. Hosemann, J. Loboda-Cackovic and H. Cackovic, Polymer 17, 309 (1976).

117. B. Crist and N. Morosoff, J. Polym. Sci., Polym. Phys. Ed. 11, 1023 (1973).

118. R. S. Stein, F. P. Warner, S. K. Baczek, T. P. Russell and W. J. MacKnight, Bull. Am. Phys. Soc. 22 (3), 258 (1977).

119. G. R. Strobl and N. Muller, J. Polym. Sci., Polym. Phys. Ed. 11, 1219 (1973).

120. F. A. Bettelheim and R. S. Stein, J. Polym. Sci. 27, 567 (1958).

121. D. Peiffer, S. D. Hong and R. S. Stein, J. Polym. Sci., Polym. Phys. Ed. 13, 1945 (1975).

122. M. W. Darlington and D. W. Saunders, J. Macromol. Sci. B5, 207 (1971).

123. D. Peiffer, Ph.D. Thesis, University of Massachusetts, 1976.

124. D. P. Pope and A. Keller, J. Mat. Sci. 6, 453 (1971); J. Polym. Sci., Polym. Phys. Ed. 13, 533 (1975).

125. A. Goffin, M. Dosiere, J. J. Point and M. Gilliot, J. Polym. Sci. C38, 135 (1972).

126. N. H. Ladizesky and I. M. Ward, J. Macromol. Sci.-Phys. B9, 565 (1974).

127. P. Ingram and A. Peterlin, J. Polym. Sci. B2, 739 (1964).

128. J. A. Sauer, G. C. Richardson and D. R. Morrow in "Rev. of Macromol. Chem.", Vol. 10, G. B. Butler, K. F. O'Driscoll and M. Shen, Ed., Dekker, New York, 1975.

129. I. L. Hay and A. Keller, J. Mat. Sci. 2, 538 (1967).

130. V. Petraccone, I. C. Sanchez and R. S. Stein, J. Polym. Sci., Polym. Phys. Ed. 13, 1991 (1975).

131. H. H. Kausch, "Advances in Polymer Science and Engineering," K. A. Pae, Ed., Plenum Press, New York, 1972, p. 207.

132. S. Rabinowitz and N. Brown, J. Polym. Sci., A-2, 5, 143 (1967).

133. P. H. Geil, J. Polym. Sci. A-2, 3813, 3835 (1964).

134. K. O'Leary and P. H. Geil, J. Macromol. Sci.-Phys. B2 (2), 261 (1968).

135. V. I. Gerasimov, Ya. V. Genin and D. Ya. Tsvankin, J. Polym. Sci., Polym. Phys. Ed. 12, 2035 (1974).

136. A. Peterlin and G. Meinel, Makromol. Chemie 142, 227 (1971).

137. N. Kasai and M. Kakudo, Rept. Progr. Polym. Phys. Japan 6, 319 (1963); 9, 243 (1966).

138. N. Kasai and M. Kakudo, J. Polym. Sci. A2, 1955 (1964).

139. A. Tanaka, E. P. Chang, B. Delf, I. Kimura and R. S. Stein, J. Polym. Sci., Polym. Phys. Ed. 11, 1891 (1973).

140. R. S. Stein, J. Macromol. Sci.-Phys. B8, 29 (1973).

141. M. Bevis and A. G. Crocker, Proc. Royal Soc. 304, 123 (1968); 313, 509 (1959).

142. M. Bevis and E. B. Crellin, Polymer 12, 666 (1971).

143. P. Allen, E. B. Crellin and M. Bevis, Phil. Mag. 27, 127 (1973).

144. J. E. Breedon, J. F. Jackson, M. J. Marcinkowski and M. E. Taylor Tung, J. Mat. Sci. 8, 1071 (1973).

145. L. Mandelkern, J. Polym. Sci. C15, 129 (1966).

146. L. Mandelkern, Polym. Eng. and Sci. 7, 232 (1967); 9, 255 (1969).

147. E. Ergoz, J. G. Fatou and L. Mandelkern, Macromolecules 5, 147 (1972).

148. F. Kloos, S. Go and L. Mandelkern, J. Polym. Sci. 12, 1145 (1974).

149. R. Prud'homme, Ph.D. Dissertation, University of Massachusetts, 1973.

150. S. Go. L. Mandelkern, R. Prud'homme and R. S. Stein, J. Polym. Sci. 12, 1485 (1974).

151. R. S. Stein, A. Tanaka and R. S. Finkelstein, J. Appl. Polym. Sci., Appl. Polym. Symp. 20, 335 (1973).

152. R. S. Stein, R. S. Finkelstein, D. Y. Yoon and C. Chang, J. Polym. Sci., Symp. No. 46, 15 (1974).

153. R. S. Stein, S. Onogo, K. Sasaguri and D. A. Keedy, J. Appl. Phys. 34, 80 (1963).

154. P. F. Erhardt, K. Sasaguri and R. S. Stein, Rheo-Optics of Polymers (J. Polym. Sci. C5), R. S. Stein, Ed., Interscience, New York, 1964, p. 179.

155. P. F. Erhardt and R. S. Stein, Appl. Polym. Symp. 5, 113 (1967).

156. P. F. Erhardt and R. S. Stein, J. Appl. Phys. 39, 4898 (1968).

157. Y. Fukui, T. Asada and S. Onogi, Polym. J. 3, 100 (1972).

158. G. R. Strobl, J. Appl. Cryst. 6, 635 (1973).

159. R. S. Stein in "Growth and Perfection of Crystals," R. H. Doremus, B. W. Roberts and D. Turnbull, Eds., Wiley, New York, 1958, p. 549.

160. A. Wasiak, D. Peiffer and R. S. Stein, Polym. Letters 14, 381 (1976).

161. C. A. Taylor and N. Lipson, "Optical Transforms," Cornell University Press, Ithaca, New York, 1965.

162. P. Predecki and W. O. Statton in "Small Angle X-Ray Scattering," H. Brumberger, Ed., Gordon and Breach, New York, 1967, p. 131.

163. C. A. Taylor, J. Polym. Sci., Part C, 20, 19 (1967).

164. R. Bonart, Z. Krist. 109, 296 (1957).

165. D. Kratky, Kolloid Z. 84, 149 (1938).

APPENDIX

I. SCATTERING FROM ANGULARLY-DISORDERED RODS

Consider a system of N_r rectangular rods whose centers are arranged along a lattice line whose long axes (termed "axes" or "axis") lie perpendicular to the line as shown below.

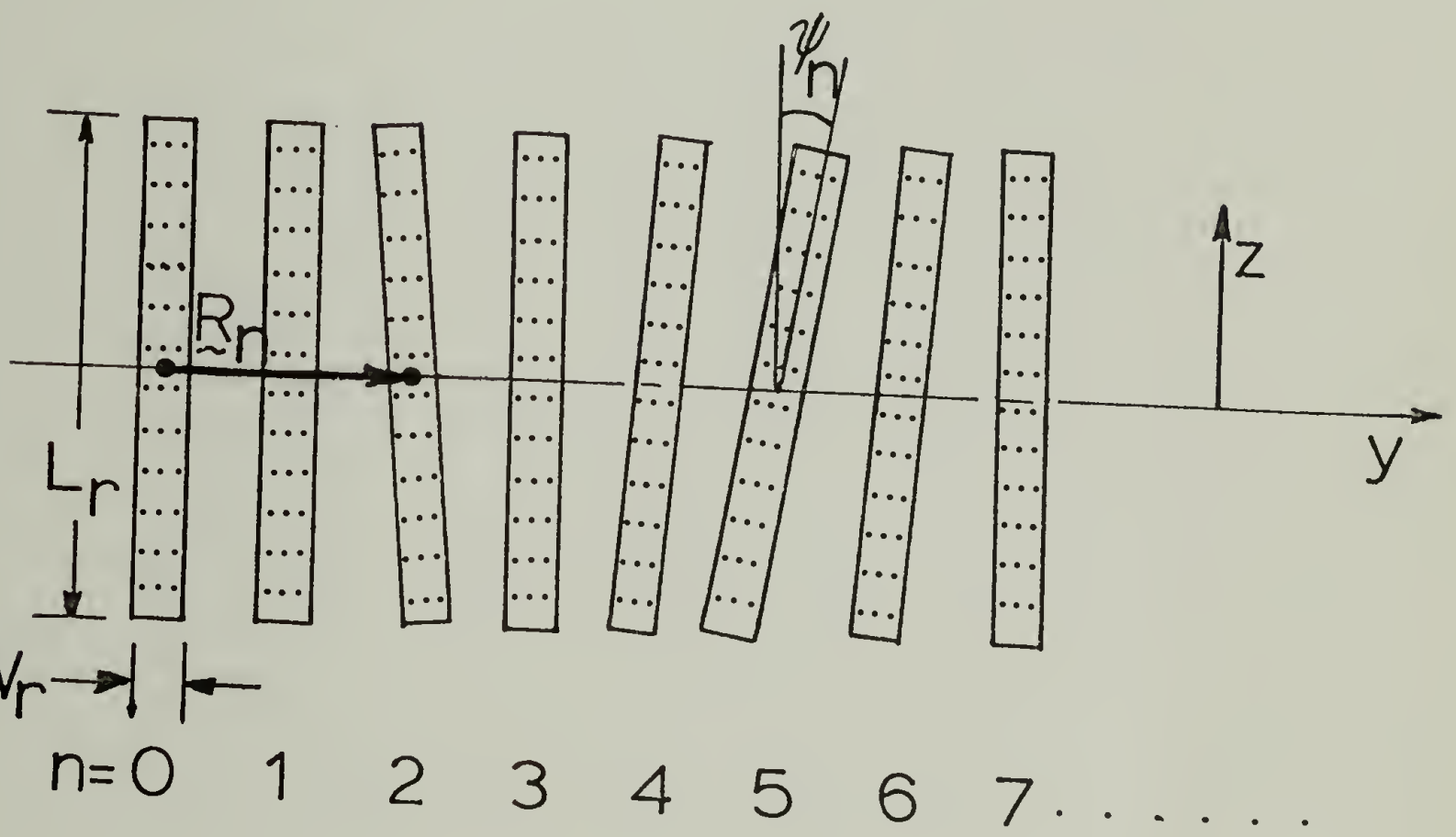

The length and width of a rod are given by L_r and W_r, respectively, and each rod is identical. We now allow a certain probability that a given rod axis may deviate from the lattice line normal by an angular amount $\pm \psi_n$.

The scattering amplitude from a given rod, E_n, may be calculated from Equation (A-1).

$$E_n = K\, W_r\, L_r \left[\frac{\sin\left(\frac{a_n W_r}{2}\right)}{\left(\frac{a_n W}{2}\right)} \right] \left[\frac{\sin\left(\frac{b_n L_r}{2}\right)}{\left(\frac{b_n L_r}{2}\right)} \right] \qquad \text{(A-1)}$$

and K is a constant, and

$$a_n = \left(\frac{2\pi}{\lambda}\right) \sin\theta \sin\left[\psi_n - \mu\right]$$

$$b_n = \left(\frac{2\pi}{\lambda}\right) \sin\theta \cos\left[\psi_n - \mu\right] \qquad \text{(A-2)}$$

where μ is the azimuthal angle of observation of the scattered rays and λ is the wavelength of the incident monochromatic radiation.

For an array of N lamellae, the scattering amplitude, E_N, may be represented by

$$E_N = \sum_{n=1}^{N} E_n \exp\left[-ik\left(\underset{\sim}{R}_n \cdot \underset{\sim}{s}\right)\right] \qquad \text{(A-3)}$$

where $\underset{\sim}{R}_n$ is shown in the above figure and is given by

$$\underset{\sim}{R}_n = n\ d\ \underset{\sim}{j} \tag{A-4}$$

d is the distance between adjacent rod centers, or the long spacing, $k = (2\pi/\lambda)$, and $i = \sqrt{-1}$.

The scattering vector, $\underset{\sim}{s}$, is given by

$$\underset{\sim}{s} = (1 - \cos\theta)\ \underset{\sim}{i} - \sin\theta\ \sin\mu\ \underset{\sim}{j} - \sin\theta\ \cos\mu\ \underset{\sim}{k} \tag{A-5}$$

where $\underset{\sim}{i}$, $\underset{\sim}{j}$ and $\underset{\sim}{k}$ are the unit vectors along the three orthogonal axes, x, y, and z.

Performing the dot product and substitution into (A-2) yields

$$E_N = \sum_{i=1}^{N} E_n \exp\left[i\ k\ n\ d\ \sin\theta\ \sin\mu\right] \tag{A-6}$$

According to (A-1) and (A-2), E_n depends on ψ_n where $\psi_n = \psi_{n-1} + m\delta$. δ is the angular disorder which is specified in a given calculation.

m can be either + 1, 0, or -1 for a given rod. It is determined by defining limits (lower Z1, upper Z2 as in "DRODS") such that for random numbers falling between Z1 and Z2 m = 0 while below Z1 and above Z2 m = $\pm$ 1, respectively.

The effect of angular deviations may be cumulative since deviations with the same integer m are simply added; the total angular deviation of a given rod is dependent on that of the previous one.

The final intensity of scattering from the array, I_N, is given by

$$I_N = K_1 E_N E_N^* \qquad \text{(A-7)}$$

where K_1 is a constant, and E_N^* is the complex conjugate of the amplitude of the array. E_N and E_N^* are calculated individually then multiplied in the program "DRODS" given at the end of this section.

This calculation has been performed assuming values of $W_r = 80\mathring{A}$, $L_r = 1{,}000\mathring{A}$ and $d = 200\mathring{A}$. No distribution parameters have been included. Also, the scattered intensity has been observed at $\mu = 90^o$ throughout; i.e., along a line parallel to the lattice line axis in reciprocal space. Finally, in all cases where angular disorder was varied, N = 50 was chosen as a reasonable value to study since larger values gave very similar results and because of computing costs. Also,

N was systematically decreased in one instance with $\delta = 0$ to study its effects on the intensity scattered from a perfect array.

Figure 57 shows the effects of varying the angle of disorder, δ, on the scattered intensity of the first and second order maxima. In this calculation, m was allowed an equal probability of being + 1, 0, -1. A rapid decrease in intensity is observed in going from perfectly-ordered rods ($\delta = 0$) to $\delta = 3 \times 10^{-4}$ degrees between adjacent rods. The intensity reaches an asymptotic limit and remains there at subsequently higher values of δ. The ratios of the intensities of the first and second order peaks (at 200Å and 100Å, respectively) remain relatively constant throughout the decreasing portion of the curves. The minimum in I_1 at 3.5×10^{-7} radians and the strange shape of the I_2 curve in this region remain unexplained at this time. However, we feel they are insignificant relative to the major trends seen.

Thus, the total scattered intensity decreases but does not disappear in a set of N rods containing a certain amount of angular disorder with respect to each other. In a real system of lamellae, the disorder would probably vary by an amount greater than the 3×10^{-4} degrees observed here if disorder were to occur at all. Therefore, the controlling factor in determining the observed intensity may not be the value of δ but rather the number of disordered rods relative to the size of the stack. Figure 6 shows the intensity, I_1, as a function of the number of parallel rods in a perfect stack where N is systematically varied from 0 to 50. The relationship is given by the solid line.

Superimposed on this curve are points obtained from calculations where N = 50, the value of δ in the local region of Figure 57 and only the probabilities of the amounts of m = + 1, 0, -1 are varied. For instance, taking the uppermost point on the curve obtained with a probability that 10% of the rods would angularly deviate, or every sixth rod would deviate, yields an intensity of scattering which would be comparable to the case of scattering from an array of approximately 41 perfectly-aligned rods. Yet, on the average only five rods will be perfectly aligned at any given position throughout the stack of 50 rods. Another example is the case where the rods have an equal probability of orienting in the + 1, 0, -1 orientations. Here the average number of parallel rods along any position in the stack of 50 approaches a value of about one since it is expected that only every third rod may, in fact, be normal to the lattice line. Other examples are shown in Figure 6 and calculation of the average numbers of parallel rods is straightforward and left to the reader's enjoyment. A check on these average values was done by outputing the results of the random number generator and the limits set to allow either m = + 1, 0, or -1. An average of ten calculations of Equation (A-7) was performed to ensure a statistically average intensity. The average numbers of parallel rods were determined by actually counting those bundles of rods parallel to each other and perpendicular to the lattice line and the numbers of rods within a bundle, and averaging the results over all 500 rods (50 rods calculated 10 times). Results were as expected. Thus the average N values quoted above are accurate.

The computer printout of the Fortran IV program, "DRODS", is given on the next page, followed by a sample output of the intensity data.

```
      PROGRAM DRODS(INPUT,OUTPUT,TAPE10=INPUT,TAPE11=OUTPUT)
C THIS PROGRAM CALCULATES THE SCATTERED INTENSITY OF A SERIES OF
C ANGULARLY DISORDERED RODS AT ANY DESIRED AZIMUTHAL ANGLE. S. K.
C BACZEK, 1976
C N1 = 100.*STARTING ANGLE IN TERMS OF J1/D
C N2 = 100.0*STOPPING ANGLE IN TERMS OF J2/D
C NN=100.*STEP SIZE IN TERMS OF (J1+NN)/D..ETC.
C I2 = NO. RODS IN BUNDLE
C AZMU=AZIMUTHAL ANGLE IN DEG., DELTA=DISORDER PARAMETER IN RADIANS
C W = ROD WIDTH IN ANGSTRMS, XL = ROD LENGTH IN ANGSTRMS
C D = LONG PERIOD IN ANGSTRMS, Z1 AND Z2 ARE LOWER AND UPPER LIMITS O
C THE RANDOM NUMBERS AND ARE USED TO SET  N AVG.
      DIMENSION PSI(200),EN(200),E(200),EC(200),P(200),SCATI(200)
      TYPE COMPLEX EX,EXC, E, EC
      A= 2.0*3.1416/1.5416
    1 READ(10,*) N1,N2,NN
      IF(EOF(10)) 80,3
    3 READ(10,*) AZMU,DELTA,W,XL,D,Z1,Z2,I2
      WRITE(11,6) N1,N2,NN,I2
    6 FORMAT(4I5)
      WRITE(11,7) AZMU,DELTA,W,XL,D,Z1,Z2
    7 FORMAT(2F10.6,3F7.0,2F5.2)
      WRITE(11,5)
    5 FORMAT(/7X,*  S  *,14X,*D*,9X,*INTESITY*,5X,*LN(INT)*
     1 ,4X,*LOG(INT)*)
      AZMU = AZMU/57.29578
      DO 70 J=N1,N2,NN
      SCAT = 0.0
      SCATI(I) =0.0
      TA=J/100.0
      TA=TA/D
      THETA = TA
      SINTA = 1.5412*TA
      S = 1.0/TA
      DO 65 N=1,10
      P(K)=0.0
      X=RTIME(0)
      X = RANF(X)
      DO 250 K=1,I2
      R(K) = RANF(0)
      IF(R(K).LT.Z1) 200,210
  200 P(K)=-1.0
      GO TO 250
  210 IF(P(K).GE.Z1.AND.R(K).LE.Z2) 220,230
  220 R(K)=0.0
      GO TO 250
  230 P(K)= 1.0
  250 CONTINUE
      PSI(I) =0.0
      PSI(1) = 0.0
      DO 40 I=2,I2
      K=I
      M=I-1
      IF(P(M).EQ.R(K)) 260,270
  260 PSI(I) =0.0
      GO TO  280
  270 PSI(I) = PSI(M) + P(K) *DELTA
```

```
280 CONTINUE
    PSI(1) =0.0
    AW = A*W*XL*SINTA
    PA = PSI(I)-AZMU
    AN = AW*SIN(PA)
    BN = AW*COS(PA)
    ANN = AN*W/2.0
    BNN = BN*XL/2.0
    IF(ANN.EQ.0.0) 100,110
100 SA=1.0
    GO TO 120
110 SA = (SIN(ANN))/ANN
120 IF(BNN.EQ.0.0) 130,140
130 SB = 1.0
    GO TO 150
140 SB = (SIN(BNN))/BNN
150 CONTINUE
    EN(M) = W*XL*SIN(SA)*SIN(SB)
    XN = I-1
    PNS = A*XN*D*SINTA*SIN(AZMU)
    EX = COS(PNS) + (0.0,1.0) *SIN(PNS)
    EXC = COS(PNS) - (0.0,1.0)*SIN(PNS)
    E(M) = EN(M)*EX
    EC(M) = EN(M)*EXC
 40 CONTINUE
    SUM = 0.0
    SUMC = 0.0
    DO 50 I=1,I2
    SUM = SUM + E(I)
    SUMC = SUMC +EC(I)
 50 CONTINUE
    SCATI(N)=SUM*SUMC
 65 CONTINUE
    DO 500 N=1,10
    SCAT = SCAT + SCATI(N)/10.0
500 CONTINUE
    G = ALOG((SCAT))
    GL = G/2.303
    WRITE(11,60) THETA,S,SCAT,G,GL
 60 FORMAT(1X,F12.6,5X,F12.6,5X,F12.2,5X,F5.2,5X,F5.2)
 70 CONTINUE
    GO TO 1
 80 CONTINUE
    STOP
    END
```

```
     PROGRAM LENGTH                          35513    1887
      BUFFER LENGTH                         -1068    2118
   20   600    20    50
-90.000000   .000005      80.   1000.    200.   .33   .67

        S              D          INTENSITY      LN(INT)      LOG(INT)
     .001000    1000.000000          23.22         3.15          1.37
     .002000     500.000000           9.25         2.23           .97

     .003000     333.333333            .39         -.95          -.41
     .004000     250.000000           4.95         1.60           .69
     .005000     200.000000         155.39         5.05          2.19
     .006000     166.666667            .26        -1.33          -.58
     .007000     142.857143           1.53          .43           .18
     .008000     125.000000            .46         -.77          -.34
     .009000     111.111111            .17        -1.77          -.77
     .010000     100.000000          79.54         4.38          1.90
     .011000      90.909091            .06        -2.78         -1.21
     .012000      83.333333            .22        -1.53          -.66
     .013000      76.923077            .51         -.69          -.29
     .014000      71.428571            .11        -4.97         -2.16
     .015000      66.666667          25.20         3.23          1.40
     .016000      62.500000            .22        -1.52          -.66
     .017000      58.823529            .00        -7.23         -3.14
     .018000      55.555556            .36        -1.01          -.44
     .019000      52.631579            .09        -2.45         -1.06
     .020000      50.000000           1.34          .43           .19
     .021000      47.619048            .16        -1.84          -.80
     .022000      45.454545            .02        -3.85         -1.68
     .023000      43.478261            .02        -3.90         -1.70
     .024000      41.666667            .15        -1.92          -.83
     .025000      40.000000           2.66          .98           .42
     .026000      38.461538            .03        -3.57         -1.54
     .027000      37.037037            .07        -2.67         -1.16
     .028000      35.714286            .00        -5.94         -2.58
     .029000      34.482759            .07        -3.15         -1.35
     .030000      33.333333           6.50         1.87           .81
```

II. EFFECT OF LAMELLAR TWISTING ON SAXS ("THE VENETIAN BLIND PROBLEM")

A. The concept of twisting in lamellar structures has much experimental verification (7,43,144). The question then arises as to the influence of the twisting on the nature of the SAXS patterns and their subsequent interpretation. An approach to illuminating this problem was undertaken by Dr. F. P. Warner* and myself by considering the geometry involved in cooperative rotation of lamellae about a given axis within them perpendicular to the incident x-rays and the influence on the resulting projection of electron density.

As viewed from the axis of the incident x-rays, this geometry parallels that encountered in opening and closing a Venetian blind and has been referred to as the "Venetian Blind Problem". The geometry is given below.

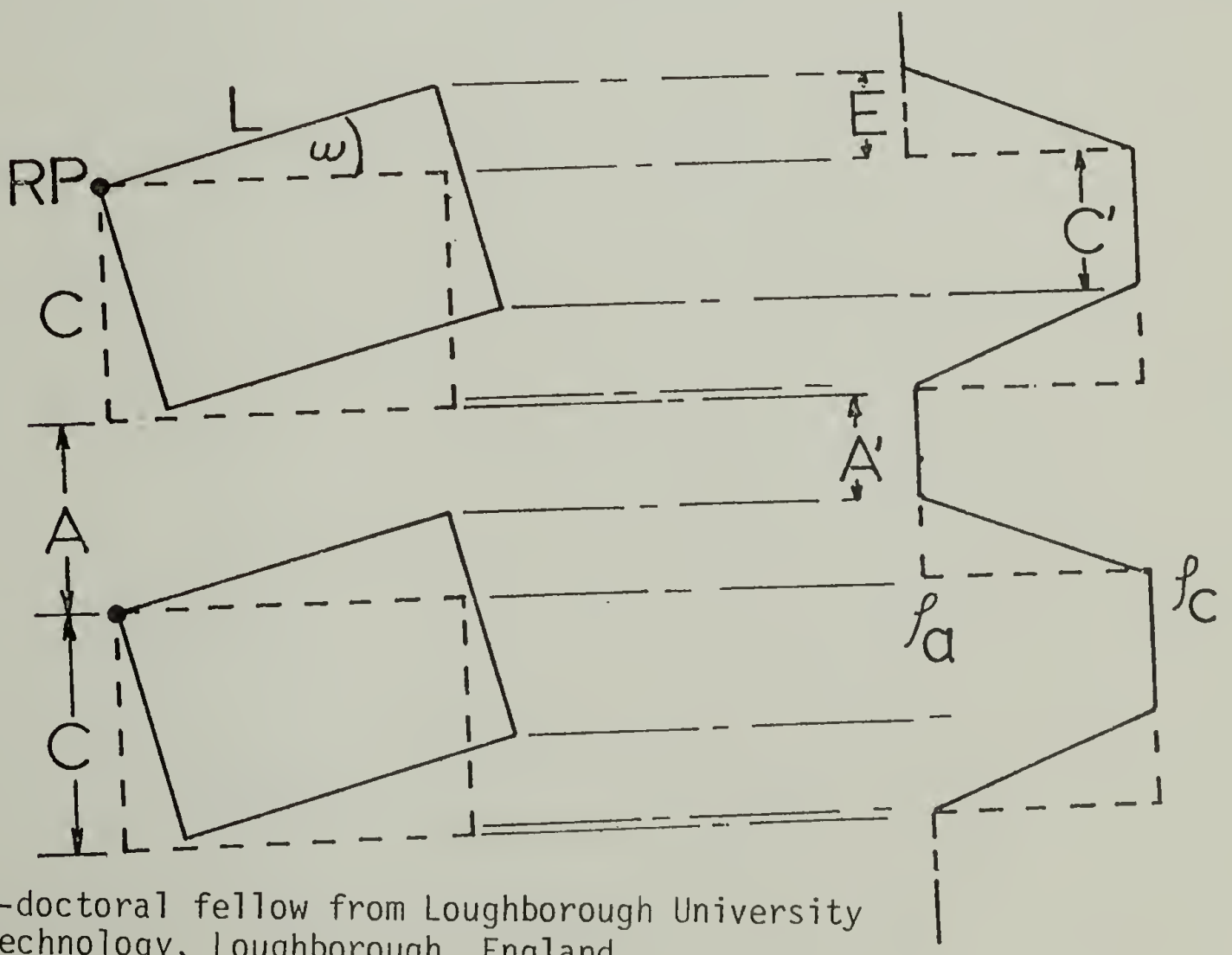

*Post-doctoral fellow from Loughborough University of Technology, Loughborough, England.

The position of the rotation axis will not affect the final results to any great extent since it will primarily shift the electron density profile along the vertical. The rotation point, RP, as shown was chosen for ease of geometric calculations. C and A are the dimensions of the crystalline and amorphous thicknesses, and L is the length of the crystal along the axis of the incident x-rays prior to rotation. Two limiting cases of rotation are defined strictly for ease of computer calculations. In the first, $\tan \omega < \frac{C}{L}$, such that the projection of the edges of adjacent crystals do not coincide while in the second case, $\tan \omega \geq \frac{C}{L}$ and the opposite is true. ω is the angle by which the lamellae have rotated about RP relative to the direction of incident x-rays. When $\omega = 0$, the transition boundary width, E, is also zero.

Thus, for Case I, the new dimensions at a given rotation angle are given by

$$C' = C \cos \omega + L \sin^3 \omega$$

$$A' = A + c - C \cos \omega + L \sin^3 \omega$$

$$E' = L \sin \omega \qquad \text{(A-8)}$$

while for the case of $\omega > \tan^{-1}\left(\frac{C}{L}\right)$, Case II,

$$C' = C + A - C \cos \omega$$

$$A' = C \cos \omega$$

$$E' = C + A - L \sin \omega \qquad \text{(A-9)}$$

These equations were incorporated into the Hosemann program calculation (TTSC) to determine the variations of C', A', and E' with ω and to calculate the appropriate scattering curves. The program is included at the end of this section. Initial dimensions were specified such that C = 120Å, A = 80Å, and L = 500Å. The Gaussian width parameters, g_a and g_c, were set to the nominal values of 0.15, and the average number of lamellae in a stack was set equal to 100. It should be emphasized that the "cases" studied are arbitrary and only distinguished for convenience in performing the computer calculations. Rotational angles were varied from 0 to 20 degrees in increments of 4 degrees; 20 degrees being the angle at which the crystals physically tough for these dimensions.

Rotation, or twisting by an angular amount, ω, did not change the crystalline and amorphous thicknesses to any great extent. However, the transition width, E, varied from 0 to 56Å as shown in the subsequent table. This had the predictable effect of lowering the calculated

intensities in the tail of the scattering curve. The computer printout and program are given in this appendix.

A relative mean squared electron density difference may be calculated using Equation (71) in the Theoretical Section. Values of E are obtained directly from the computer program or from Equations (A-8) and (A-9). The mean squared electron density difference between the crystalline and amorphous zones may be estimated by

$$\left(\frac{L - L \text{ (in amorphous region)}}{L}\right)^2 \qquad \text{(A-10)}$$

for angles greater than 12^{o}; the approximate angle at which adjacent crystal edges may intersect along the line parallel to the incident x-rays. Here, $\tan \omega > \frac{C}{L}$. The following table gives the expected results.

ω	E(Å)	$(\rho_c - \rho_a)^2$ [Eqn. (A-10)]	$(\phi_c\phi_a - \frac{E}{3D})$	$\langle\Delta n^2\rangle_{rel}$
0	0	1.0	0.24	0.24
4	34.9	1.0	0.18	0.18
8	69.6	1.0	0.12	0.12
12	96.	0.59	0.08	0.05
16	62.	0.34	0.14	0.05
20	29.	0.22	0.19	0.04

One can see that for the dimensions chosen, the relative mean squared electron density fluctuation decreased by a factor of five at a twist angle of 12 degrees. Since real lamellae systems probably have larger lateral dimensions than those studied here, the intensity drop is likely to occur at even smaller twist angles.

It is evident, then, that the twisting of lamellae can be discussed in terms of its effects on the apparent transition zone thicknesses and, therefore, characterization of the twisting of lamellae in various regions of the spherulite on deformation cannot be uniquely described by this particular model approach. Conversely, changes in the apparent transition zone thickness on stretching, as observed in the Keller-type samples, cannot be ascribed strictly to molecular interpretations of changes in electron densities, but must also include the possibility of

lamellae twisting. External evidence must be incorporated to sort out the problem. This has been done in the Discussion section of this work.

```
      PROGRAM ITSC (INPUT,OUTPUT,TAPE1=INPUT,TAPE2=OUTPUT)
      DIMENSION SIB(300),SIC(300),SI(300)
      DIMENSION T(300),IDENT(5)
      DIMENSION F(300),ZS(300)
      TYPE COMPLEX FC2,FC,FA2,FA,SIC1,SIC2,SIC3,SIC4,SICO
      TYPE COMPLEX CEA,CEB
C     THIS PROGRAM COMPUTES SAXS CURVES VIA THE HOSEMANN TREATMENT
C     AND COMPARES THEM TO THE EXPERIMENTALLY DETERMINED ONE,
C     THE EQUATIONS USED WITHIN THIS PROGRAM MAY BE FOUND IN W, WENIG,
C  THE PROGRAM WAS INITIATED BY F.P.WARNER AND COMPLETED BY S,K,BACZEK
C     ET,AL., J, APPL, PHYS, VOL,46 NO,10; 4194 (U9MK);
C     ON 10-14-76)   IT CALCULATES A CURVE AT ANY NUMBER OF SCATTERING
C     POINTS DETERMINED BY THE DIMENSION STATEMENTS AT THE BEGINNING
C     OF THE PROGRAM,  THE NUMBER OF CURVES ONE COMPARES DEPENDS ON THE
C     LIMITS ONE SETS FOR THE GXC, GXA, AND RN VALUES.  THE NOTATION
C     HAS REMAINED VERY CLOSE TO THAT USED IN THE HOSEMANN PAPER
C     REFERRED TO ABOVE AND IT, THEREFORE, SHOULD BE OBVIOUS AS TO
C     MEANING.  A DEVIATION IS CALCULATED FROM NORMALIZED DATA AND
C     THIS NUMBER SHOULD BE MINIMIZED TO HAVE ANY CONFIDENCE IN A FIT.
C     THIS IS DONE BY SYSTEMATICALLY VARYING THE PARAMETERS
C     A SET OF DATA, PROGRAM TEST DATA, IS INCLUDED.
C
C                  GOOD LUCK...
C
    2 READ(1,110) (IDENT(I),I=1,5)
  110 FORMAT(5A10)
      IF(EOF(1)) 300,3
    3 WRITE(2,115) (IDENT(I), I=1,5)
  115 FORMAT(1H1,1X,5A10)
      READ (1,*) SMIN,SS,SMAX
      READ(1,*) XL,DTI,DTF,DTS
      NDT=(DTF-DTI)/DTS+1
      READ(1,*) XC1,XA1
      READ(1,*) GXC1,GXCM,DGXC
      READ(1,*) GXA1,GXAM,DGXA
      READ(1,*) RN1,RNM,DRN
      MN=(SMAX-SMIN+SS)/SS
      DT=DTI
      DO 250 N=1,NDT
      SINDT=SIN(3,142*DT/180,0)
      COSDT=COS(3,142*DT/180,0)
      ZZ=XC1+XA1**2,0*XL*SINDT-XC1*COSDT*XL*SINDT*COSDT*COSDT
      IF (ZZ,LT,0,0) GO TO 321
      XC=XC1*COSDT*XL*(SINDT**3)
      XA=XC1*XA1*(XC1*COSDT)*XL*(SINDT**3,0)
      XB=XL*SINDT
      GO TO 322
  321 XC=XC1+XA1*(XC1*COSDT)
      XA=XC1*COSDT
      XB=XC1+XA1*XL*SINDT
  322 CONTINUE
      WRITE(2,6) XB
    6 FORMAT(2X,*TRANSITION BOUNDARY = *F6,1,*A*)
```

```
      PRINT*,MN
30    PI=3.14159
      PI2=PI*PI
      WC=XC/(XC+XA)
      IGC = 1 + (GXCM-GXC1)/DGXC
      IGA = 1+ (GXAM - GXA1)/DGXA
      IRN = 1 + (RNM - RN1)/DRN
      GXC = GXC1
      DO 200 IGX = 1, IGC
      DXC = GXC*GXC*XC*XC
      GXA = GXA1
      DO 210 IGY =  1,IGA
      DXA = GXA*GXA*XA*XA
      RN = RN1
      DO 220 IRNX = 1, IRN
      SD = 0.0
      SIT = 0.0
      S = SMIN
      DO 5 M=1,MN
      T(M) = S
      FC1=EXP(-2.0*PI2*S*S*DXC)
      FC2=COS(2.0*PI*S*XC)-(0.0,1.0)*SIN(2.0*PI*S*XC)
      FC=FC1*FC2
      FA1=EXP(-2.0*PI2*S*S*DXA)
      FA2=COS(2.0*PI*S*XA)-(0.0,1.0)*SIN(2.0*PI*S*XA)
      FA=FA1*FA2
      SIB1=(1.0-FC)*(1.0-FA)/(1.0-FC*FA)
      SIB(M)=SIB1/(2.0*PI2*S*S)
      SIC0=(1.0-FC)/(1.0-FC*FA)
      SIC1=SIC0*SIC0
      SIC3=FA*FC
      SIC3=RN*CLOG(SIC3)
      SIC4=CEXP(SIC3)
      SIC2=FA*(1.0-SIC4)
      SIC(M)=(SIC1*SIC2)/(2.0*PI2*S*S)
      SI(M)=(SIC(M)/RN)*SIB(M)
      IF(XB.EQ.0.0) GO TO 320
      FF = -1.0/(4.0*PI2*S*S*XB)
      CEA = COS(2.0*PI*S*XB) + (0.0,1.0)*SIN(2.0*PI*S*XB)
      CEB = COS(2.0*PI*S*XB) + (0.0,1.0)*SIN(2.0*PI*S*XB)
      CE1 = (1.0-CEA)*(1.0-CEB)
      ZS(M) = FF*CE1
      GO TO 330
320   ZS(M) = 1.0
330   CONTINUE
      SI(M) = SI(M)*ZS(M)
      SIT = SIT + SI(M)
      S = S + SS
    5 CONTINUE
      WRITE(2,70) XL,DT
   70 FORMAT(/,5X,'CRYSTAL LENGTH =',F6.1,'A',5X,'ROTATION ANGLE =',F4.
     1,'DEGREES')
      WRITE (2,60) WC,RN,XC,GXC,XA,GXA
```

```
 60 FORMAT(/,10X,5HWC = ,F5.4,7X,4HN = ,F5.1,/,10X,5HXC = ,F5.1,7X
   16HGXC = ,F7.2,/,10X,5HXA = ,F5.1,7X,6HGXA = ,F7.3)
    DO 410 M = 1, MN
    I = M
    SI(M)=(SI(M)/SIT)*100.0
410 CONTINUE
    DO 420 M = 1, MN
    I = M
    WRITE(2,10) I(M),SI(M)
 10 FORMAT(10X,F10.6,5X,F13.5)
420 CONTINUE
    WRITE(2,12)
 12 FORMAT(10X,*=====SSSSSSSSS=====*)
    RN = RN + DRN
220 CONTINUE
    GXA = GXA + DGXA
210 CONTINUE
    GXC = GXC + DGXC
    DT=DT+DTS
200 CONTINUE
250 CONTINUE
    GO TO 2
300 STOP
    END
```

```
 VENETION BLINDS THE MIND
 TRANSITION BOUNDARY =     0.0A
25

     CRYSTAL LENGTH = 500.0A      ROTATION ANGLE = 0.0DEGREES

          WC =  .600          N = 100.0
          XC = 120.0          GXC =    120
          XA =  80.0          GXA =    120
             .001000                .61926
             .002000                .58596
             .003000                .92172
             .004000               3.00000
             .005000             -80.42627
             .006000               2.97907
             .007000                .99051
             .008000                .75425
             .009000               1.20244
             .010000              -2.20542
             .011000                .72415
             .012000                .37750
             .013000                .36137
             .014000                .49902
             .015000                .60395
             .016000                .52024
             .017000                .47437
             .018000                .49663
             .019000                .51636
             .020000                .40129
             .021000                .30010
             .022000                .27469
             .023000                .22010
             .024000                .18971
             .025000                .17561
        ----SSSSSSSSSS----
```

TRANSITION BOUNDARY = 96.0A
25

CRYSTAL LENGTH = 500.0A RUTATION ANGLE =12.0DEGREES

WC = .413
XC = 82.6
XA = 117.4
N = 100.0
GXC = 120
GXA = 120

.001000	1.09057
.002000	1.10764
.003000	1.62772
.004000	4.40513
.005000	88.64803
.006000	2.12078
.007000	.39299
.008000	.13007
.009000	.05795
.010000	.00782
.011000	.00422
.012000	.01450
.013000	.03176
.014000	.00467
.015000	.00407
.016000	.00049
.017000	.03812
.018000	.02272
.019000	.00990
.020000	.00174
.021000	.00006
.022000	.00171
.023000	.00399
.024000	.00590
.025000	.00705

=---SSSSSSSSS---=

B. A Semi-Empirical Approach to Lamellae Twisting.*

Let us assume that the distribution of lamellar twist angles (ω) about the radial or b-axis direction in a polyethylene spherulite may be described in terms of

$$P(\omega) = A + B \cos 2\omega \tag{A-10}$$

where A and B are the Fourier coefficients. The function is even and symmetric about zero. The distribution is normalized such that

$$\int P(\omega)\, d\omega = 1 = \int_0^{2\pi} A\, d\omega + B \int_0^{2\pi} \cos 2\omega\, d\omega \tag{A-11}$$

or $A = 1/2\pi$. The average value of the lamellae twist angles, $\overline{\cos^2\omega}$, is given by

$$\overline{\cos^2\omega} = \int P(\omega) \cos^2 \omega\, d\omega$$

*The mathematical derivation was accomplished by Professor R. S. Stein.

which, after substitution of (A-10) and the subsequent mathematical operation, leads to

$$\overline{\cos^2\omega} = \frac{1}{2}(1 + B\pi)$$

which rearranges to

$$B = \frac{1}{\pi}(2\,\overline{\cos^2\omega} - 1) \qquad \text{(A-12)}$$

According to the semi-empirical approach of Yoon (106) the coefficient B is given by

$$B = \frac{1}{\pi}\left[1 - \exp(-\eta\,(\lambda_s^{\,2} - \lambda_s^{\,-1})\sin^2\psi)\right] \qquad \text{(A-13)}$$

where η is a compliance parameter associated with the ease of twisting about the radial direction and is obtained from WAXD methods described in the reference. For random twisting of lamellae, $\eta = 0$. λ_s is the strain ratio and ψ is the particular azimuthal angle of observation of the scattered x-rays.

The SAXS intensity, I, is proportional to the number of lamellae scattering at $\omega = 0$, i.e., at a "Bragg" angle to the incident beam. Thus,

$$I = K\,P(\omega = 0) = K\,(A + B)$$

$$= \frac{K}{\pi}\left[\frac{3}{2} - \exp\left(-\eta\,(\lambda_s^{\,2} - \lambda_s^{\,-1})\,\sin^2\psi\right)\right]$$

Therefore, the ratio of the intensity of scattering from a non-random set of twisted lamellae to a random array is given by

$$\frac{I}{I_{Random}} = \frac{I(\eta)}{I(\eta=0)} = \frac{\frac{K}{\pi}\left(\frac{3}{2} - \exp\left[-\eta\,(\lambda_s^{\,2} - \lambda_s^{\,-1})\,\sin^2\psi\right]\right)}{\frac{K}{\pi}\left(\frac{3}{2} - 1\right)}$$

which reduces to

$$\frac{I}{I_{random}} = F(\psi) = 3\text{-}2\,\exp\left[-\eta\,(\lambda_s^{\,2} - \lambda_s^{\,-1})\,\sin^2\psi\right] \qquad \text{(A-14)}$$

From (A-14) one can see that experimentally determined intensities must be divided by an amount $F(\psi)$ to compensate for the increase in intensity by this amount. Conversely, calculated intensities could be multiplied by this amount.

A plot of Equation (A-14) is given in Figure 58 for various values of strain ratio and for azimuthal angles, ψ, from 0 to 90 degrees. η = 1.2 according to Yoon. The limiting value of 3.0 is readily observed at the higher elongation ratios. As an example, for λ_s = 1.6, the intensity must be corrected by a factor of about 2.8 for lamellae oriented 90 degrees to the strain while at λ_s = 1.1 a factor of 1.6 is necessary. Physically, this is rationalized according to the Yoon theory by the fact that lamellae perpendicular to the strain undergo a "detwisting" in which a greater proportion of lamellae planes in the two-dimensional electron density projection can now scatter x-rays in a constructive manner ($\eta \neq 0$). The greater the strain, the more pronounced the effect. Conversely, lamellae parallel to the strain undergo an untwisting to account for the increase in spherulite length, but retain their twisting randomness ($\eta = 0$). Therefore, $F(\psi) = 1$ throughout the strain range for these lamellae. Intermediate values are obtained for intermediate azimuthal angles and strains as described in the plot.

An attempt was made to incorporate the $F(\psi)$ correction into the Tsvankin intensity relationship given in Equation (37) as

$$I = N \left[|F^2| - |F|^2 \right] + |F|^2 I_1 F(\psi)$$

It was quickly realized that this correction factor would have to be included for each strain and azimuthal angle studied and that a set of calibration curves for each set of conditions (λ_s, ψ) would have to be generated. The task was too large for the results obtained and the attempt was abandoned.

A simpler and more direct approach would seem to be inclusion into the overall intensities calculated by the Hosemann equations or into direct experimental curves. This is mentioned in the Discussion section and will not be repeated here except to say that again the distinction between lamellar twisting and the diffuse boundary effects becomes somewhat difficult to separate. According to this method, however, the intensity is proportional to the number of lamellae scattering at any azimuthal angle, $N(\psi)$. This number is given by

$$N(\psi) = N(\psi)_{\text{apparent}} F(\psi)$$

where the apparent number of lamellae scattering coherently, $N(\psi)_{\text{apparent}}$, is proportional to the intensity of scattering. This would tend to affect the intensity of the entire scattering curve, not just the tail. The latter would be the predominant effect if only the value of E were varying. The line of reasoning is completed in the Discussion section for the particular samples studied.

III. OPTICAL DIFFRACTION ANALOGS

The history and usefulness of optical diffraction analogs to scattering and diffraction processes is well documented in a book by Taylor and Lipson (161) and has been used by many workers (6,162-164). Experimentally, a broad beam of parallel monochromatic light impinges perpendicularly on an opaque mask punched with clear holes or conversely a transparent mask covered with opaque structures. The resulting scattering of light by the holes or structures and the mutual interference of the scattered waves generate the optical transform which is then recorded in some fashion. This technique was used in a very decisive manner (162) to interpret the SAXS from drawn fibers. It was incorporated into this study to verify if in fact the slightly-anisotropic patterns observed photographically from stretched LDPE could be explained by internal changes in the lamellar/interlamellar dimensions. The procedure is as follows.

Chartpak pattern film, type PT055, and graphic tape, type 1501, were used to design the masks. They were chosen because of their very accurate preparation and fine edges when viewed microscopically. The "undeformed" spherulite dimensions were 10 cm in diameter and 1 cm bundles of 5 black lines each. An actual mask is shown in Figure 59. Deformation of the pattern was accomplished using the affine scheme considering constant volume on deformation. Therefore

$$\tan \phi_1 = \lambda_y^{3/2} \tan \phi_0$$

and

$$r_1 = r_0 \lambda_y [\lambda_y^3 \cos^2 \phi_1 + \sin^2 \phi_1]^{-1/2} \qquad \text{(A-15)}$$

where ϕ_0 and r_0 are the original, "undeformed" angle and distance from the origin specified in a polar coordinate system, ϕ_1 and r_1 are the corresponding values after uniaxial deformation by a strain ratio, λ_y along the y axis.

The beginning and end points of each black line were determined by measuring the distances and angles in one quadrant on polar coordinate paper. Thus, the lengths of rods varied as well as the distances between them in the deformed structure. This data was then fed into a program written around Equation (A-15). The program is given at the end of this section. The results for the first quadrant were output to a Calcamp plotter which drew the "deformed" structure and mirrored it to the other three quadrants. Finally, the technician, Mrs. Stanley Baczek, meticulously placed individual pieces of Chartpack tape over each line. A computer printout of a deformed mask is given in Figure 60.

These masks were then photographically reduced thirty-two times using Kodalith 5 x 7 sheet film and a back-lit frosted mylar covered ground glass table as a light source. Reductions were done in steps of 4X, 4X, and finally 2X. Typical exposures were f/16 at 2 to 8 seconds depending on the optical density of the mask being photographed.

Reduced masks were then placed into an apparatus whose diagramatic details are shown in Figure 61 and which resembles that of Taylor and Lipson (see Reference 31, p. 129 for diagram). Scattering patterns were recorded on Polaroid type 57 film at typical exposures of 1/125 sec at f/8 using a 0.9 neutral density filter. The scattering from two masks is shown in Figure 62.

Determination of the repeat period giving rise to the scattering maxima and their orders verified that they were due to interference effects from adjacent parallel lines, i.e., the long period as defined in our one-dimensional models. For the undeformed case, many maxima were noted. In the example shown, only three are visible, but this, of course, depends on the exposure and power of the beam. Visual observation of the pattern revealed at least nine rings.

Upon deformation to 60% strain in the manner prescribed, only a broad, diffuse anisotropic scattering was observed. Obviously since only one or two maxima are commonly seen for polyethylene in the unstretched state, the disorder of lamellae in terms of the bundles as envisioned here and in the Hosemann analysis must be greater than in our simple model. Also, one could predict from the interference pattern

shown in Figure 62 that upon stretching a rather well ordered structure in the prescribed manner, a loss of higher order maxima would occur. Evidence for this is seen in the scattering patterns for HDPE where two orders are visible in the unstretched state while only one remains after about 25% strain at any given azimuth. If the blocks were to deform positionally as entire units, retaining their internal integrity then this should not be the case. In fact, for this extreme case, the pattern would retain its circular symmetry!

No attempt was made to consider the statistics of the scattering centers nor to determine the intensity profiles from these models. Since our laboratory has recently acquired a one-dimensional Optical Multichannel Analyzer (OMA) (Princeton Applied Research), this technique could be extended to a more elaborate study similar to that presented here for the analysis of SAXS data. This indeed would be a controlled situation in which the theoretical models could be scrutinized with respect to a large, fully-characterized physical model.

```
      PROGRAM DEFORM(INPUT,OUTPUT,TAPE5=INPUT,TAPE6)
      CALL PLOTS(6)
      CALL PLOT(4.0,5.0,-3)
      READ(5,10)ELRTIO
   10 FORMAT(F5.2)
   20 READ(5,30)R1,THETA1,R2,THETA2
   30 FORMAT(4F5.2)
      IF(EOF(5))100,40
   40 CONTINUE
      ER=ELRTIO
      IF(THETA1.EQ.90.0)THETA1=89.99
      IF(THETA2.EQ.90.0)THETA2=89.99
      X1=THETA1/57.29578
      X2=THETA2/57.29578
      R1=R1/25.4
      R2=R2/25.4
      X11=ATAN((ER**1.5)*TAN(X1))
      X21=ATAN((ER**1.5)*TAN(X2))
      R11=R1*ER*(ER**3.0*(COS(X11))**2.0+(SIN(X11))**2.0)**(-0.5)
      R21=R2*ER*(ER**3.0*(COS(X21))**2.0+(SIN(X21))**2.0)**(-0.5)
      X12=R11*COS(X11)
      Y12=R11*SIN(X11)
      X22=R21*COS(X21)
      Y22=R21*SIN(X21)
      CALL PLOT(X12,Y12,3)
      CALL PLOT(X22,Y22,2)
      CALL PLOT(-X12,Y12,3)
      CALL PLOT(-X22,Y22,2)
      CALL PLOT(-X12,-Y12,3)
      CALL PLOT(-X22,-Y22,2)
      CALL PLOT(X12,-Y12,3)
      CALL PLOT(X22,-Y22,2)
      GO TO 20
  100 CALL PLOT(0.0,0.0,999)
      STOP
      END
```

IV. ADDITIONAL COMPUTER PROGRAMS

A. TCSC

Hosemann, Telex

```
00160 PROGRAM TCSC(INPUT,OUTPUT,TAPE1,TAPE2,TAPE12,TAPE8=INPUT,TAPE9=OUTPU
00110 DIMENSION SIB(300),SIL(300),F(300),ZS(300),T(300)
00120 DIMENSION IDENT(5),SI(300)
00130 DIMENSION FL(300)
00140 TYPE COMPLEX FC2,FC,FA2,FA,SIC1,SIC2,SIC3,SIC4,SIC0,CEA,CEB
00145 CALL SET(6HTAPE12,6HTAPE12,0,0)
00150 PRINT,*ENTER IDENTIFICATION, 50 SPACES*
00160 READ ,10, IDENT
00170 110 FORMAT(5A10,
00180 PRINT,*ENTER SMIN,SS,SMAX, FREE FLOAT*
00190 READ, SMIN,SS,SMAX
00200 MN=(SMAX-SMIN+.5)/SS
00220 11 FORMAT(6X,F6.0)
00230 READ(12,11)(F(I),I=1,MN)
00235 PRINT,*DO YOU WANT TO LORENTZ CORRECT THIS DATA? Y OR N*
00240 READ 88, IAN
00250 IF(IAN.EQ.1HY) GO TO 450
00260 FIT = 0.0
00270 DO 400 I=1,MN
00280 FIT=FIT+F(I)
00290 400 CONTINUE
00300 GO TO 776
00310 450 FIT = 0.0
00320 DO 555 I=1,MN
00330 F(I) = (SMIN**2)*F(I)*1000.0
00340 FL(I) = F(I)/((SMIN**2)*1000.0)
00350 FIT = FIT + F(I)
00360  SMIN = SMIN +SS
00370 555 CONTINUE
00330 776 CONTINUE
00390 PRINT,*WANT TO NORMALIZE DATA? Y OR N*
00400 READ 88, IAW
00410 IF(IAW.EQ.1HN) GO TO 360
00420 PRINT, *ENTER NORMALIZATION FACTOR, FREE FLOAT*
00430 READ, FNORM
00440 FIT =0.0
00450 DO 355 I=1,MN
00460 F(I) = F(I)*FNORM
00470 FL(I) = FL(I)*FNORM
00480 FIT = FIT+F(I)
00485 355 CONTINUE
00490 360 CONTINUE
00500 777 CONTINUE
00510 PRINT,*ENTER CRYST., AMORPH., AND TRANSITION THICK. IN ANG.*
00520 READ,XC,XA,XB
00530 PRINT,*ENTER GXC1,GXCM,DGXC, FREE FLOAT*
00540 READ,GXC1,GXCM,DGXC
00550 PRINT,*ENTER GXA1,GXAM,DGXA, FREE FLOAT*
00560 READ, GXA1,GXAM,DGXA
00570 PRINT,*ENTER RN1,RNM,DRN, FREE FLOAT*
00580 READ,RN1,RNM,DRN
00590 PI = 3.14159
00600 PI2 = PI*PI
  610 WC =2.0/(XC+XA)
  620 TCM = 1.+(GXCM-GXC1)/DGXC
  630 TCA = 1. +(GXAM-GXA1)/DGXA
  640 IRN = 1 +(RNM-RN1)/DRN
  650 GXC = GXC1
  660 BES(60 = 300.0
```

```
00670 N2 = 2
00680 DO 200 IGX = 1,IGC
00690 DXC = GXC*GXC*XC*XC
00700 GXA = GXA1
00710 DO 210 IGY = 1,IGA
00720 DXA = GXA*GXA*XA*XA
00730 RN=RN1
00740 DO 220 IRNX = 1, IRN
00750 SS CONTINUE
00760 SIT =0.0
00770 SI=0.0
00780 S =SMIN
00790 DO 5 M=1,MN
00800 T(M)=S
00810 FC1=EXP(-2.0*PI2*S*S*DXC)
00820 FC2=COS(2.0*PI*S*XC)-(0.0,1.0)*SIN(2.0*PI*S*XC)
00830 FC=FC1*FC2
00840 FA1=EXP(-2.0*PI2*S*S*DXA)
00850 FA2=COS(2.0*PI*S*XA)-(0.0,1.0)*SIN(2.0*PI*S*XA)
00860 FA=FA1*FA2
00870 SIB1=(1.0-FC)*(1.0-FA)/(1.0-FC*FA)
00880 SIB(M)=SIB1/(2.0*PI2*S*S)
00890 SIC0=(1.0-FC)/(1.0-FC*FA)
00900 SIC1=SIC0*SIC0
00910 SIC3=FA*FC
00920 SIC3=RN*CLOG(SIC3)
00930 SIC4=CEXP(SIC3)
00940 SIC2=FA*(1.0-SIC4)
00950 SIC(M)=(SIC1*SIC2)/(2.0*PI2*S*S)
00960 SI(M)=(SIC(M)/RN)+SIB(M)
00970 IF(XB.EQ.0.0) GO TO 320
00980 FF=-1.0/(4.0*PI2*S*S*XB)
00990 CEA=COS(2.0*PI*S*XB)-(0.0,1.0)*SIN(2.0*PI*S*XB)
01000 CEB=COS(2.0*PI*S*XB)+(0.0,1.0)*SIN(2.0*PI*S*XB)
01010 CE1=(1.0-CEA)*(1.0-CEB)
01020 ZS(M)=FF*CE1
01030 GO TO 330
01040 320 ZS(M) = 1.0
01050 330 CONTINUE
01060 SI(M)=SI(M)*ZS(M)
01070 SIT = SIT+SI(M)
01080 S=S+SS
01090 5 CONTINUE
01100 DO 410 M=1,MN
01110 I=M
01120 SI(M)=SI(M)*FIT/SIT
01130 X = (F(I)-SI(M))/F(I)
01140 SD=SD+ABS(X)
01150 410 CONTINUE
01160 SD=SD/MN
01170 IF(NZ.EQ.1) GO TO 999
01180 IF(SD.LT.BESTSD) BESTGXC=GXC
01190 IF(SD.LT.BESTSD) BESTGXA=GXA
01200 IF(SD.LT.BESTSD) BESTRN=RN
01210 IF(SD.LT.BESTSD) BESTSD=SD
01220 RN=RN+DRN
01230 220 CONTINUE
01240 GXA=GXA+DGXA
```

```
01250 21 CONTINUE
01260 GX1=GXC+DGXC
01270 420 CONTINUE
01280 K=1
01290 T1=(BESTGXC**2)*(XC**2)
01300 T2=(BESTGXA**2)*(XA**2)
01310 MN=BESTRN
01320 GO TO 888
01330 999 CONTINUE
01340 WRITE(2,115) (IDENT(I),I=1,5)
01350 115 FORMAT(1H1,1X,5A10)
01360 PRINT 115, (IDENT(I),I=1,5)
01370 WRITE(2,6) XB
01380 PRINT 6, XB
01390 6 FORMAT(2X,*TRANSITION BOUNDARY = *F4.1,*A*)
01400 GXC=BESTGXC
01410 GXA=BESTGXA
01420 WRITE(2,60) WC,RN,XC,GXC,XA,GXA
01430 PRINT 60, WC,RN,XC,GXC,XA,GXA
01440 60 FORMAT(/,10X,5HWC = ,F5.3,7X,4HN = ,F5.1,/,10X,5HXC = ,F5.1,7X
01450+6HGXC = ,F7.3,/,10X,5HXA = ,F5.1,7X,6HGXA = ,F7.3)
01460 WRITE(2,8) SD
01470 PRINT 8, SD
01480 8 FORMAT(25X,*DEVIATION = *F7.4,//)
01490 IF(IAN.EQ.1HY) GO TO 430
01500 DO 420 M=1,MN
01510 I=M
01520 WRITE(2,10) T(M),F(M),SI(M)
01530 PRINT 10, T(M),F(M),SI(M)
01540 10 FORMAT(10X,F10.6,5X,F13.5,5X,F13.5)
01550 420 CONTINUE
01560 GO TO 441
01570 430 CONTINUE
01580 DO 440 M=1,MN
01590  I=M
01600 WRITE(2,12) T(M),FL(M),F(M),SI(M)
01610 PRINT 12, T(M),FL(M),F(M),SI(M)
01620 12 FORMAT(10X,F10.6,5X,F13.5,5X,F13.5,5X,F13.5)
01630 440 CONTINUE
01640 441 CONTINUE
01650 PRINT,*WOULD YOU LIKE TO CHANGE PARAMETERS? Y OR N*
01660 READ 88, IANS
01670 88 FORMAT(A1)
01680 IF(IANS.EQ.1HY) GO TO 777
01690 CALL REPLACE(5HTAPE2,5HTAPE2,0,0)
01700 STOP
01710 END
READY.
```

B. ECF1 (H109)

Vonk Experimental Correlation Function, Batch;
Adapted by F. P. Warner

```
      PROGRAM HIRY (INPUT,OUTPUT,TAPE1=INPUT,TAPE2=OUTPUT)
      DIMENSION B(500)
      DIMENSION B(500),A(6)
CARD 1
C   (NO) IS THE NUMBER OF RUNS IN I2
CARD 2
C      IDENTIFICATION (5A10)
CARD 3
C   (SS) IS THE ANGULAR STEP IN TERMS OF S IN F9.7
C   (MN) IS THE NUMBER OF INTENSITY POINTS IN I3
C   (PC) IS THE VALUE OF (S**4)*I IN ANGSTROMS IN F8.4
C IF PC=0.0 THEN PC IS COMPUTED BY AVERAGING DATA FROM MP TO MN OR PC MAY BE
C DEFINED IN THE INPUT DATA
C   (FLA) IS THE WAVELENGTH IN ANGSTROMS IN F6.4
C   (RMAX) IS THE MAX VALUE TO WHICH THE ECF IS CALCULATED IN ANGSTROMS IN F6.1
C   (DR) IS THE STEP OF THE ECF IN ANGSTROMS IN F4.1
C   (MX) IS THE NO. OF POINTS CALC. FROM MN ONWARDS ASSUMING PORODS LAW IN I3
C   (MP) IS THE POINT FROM WHICH PC IS CALCULATED
C   (E) IS THE BOUNDARY WIDTH IN ANGSTROMS IN F4.1
CARDS 4, ETC.
C   (B(M)) IS THE LORENTZ CORRECTED I*S**2 DATA IN F6.1
      READ (1,1) NO
    1 FORMAT (I2)
      DO 84 NRUN=1,NO
      READ (1,2) A
    2 FORMAT(6A10)
      WRITE (2,3) A
    3 FORMAT(1H1,6A10)
      READ (1,4) SS,MN,PC,FLA,RMAX,DR,MX,MP,E
    4 FORMAT (F9.7,I3,F8.6,F6.4,F6.1,F4.1,I3,I3,F4.1)
      WRITE (2,11) SS,PC,FLA,MX,E,MP
   11 FORMAT (20X,5HSS = ,F9.7/20X,5HPC = ,F8.6/19X,6HFLA = ,F6.4/20X,5H
     1MX = ,I3/21X,4HE = ,F4.1/20X,5HMP = ,I3//)
    6 READ(1,5) (B(M),M=1,MN)
    5 FORMAT(10F8.1)
      WRITE (2,8)
    8 FORMAT (5X,27HINTENSITY*(S**2) AS READ IN)
      WRITE (2,12)
   12 FORMAT (//)
      DO 10 M=1,MN,10
      M1=M+9
      WRITE (2,7) M,M1,(B(M2),M2=M,M1)
   10 CONTINUE
    7 FORMAT (5H M , ,I4,2H -,I5,5X,10F8.1)
      IF (PC.EQ.0.0) GO TO 14
      PI2=(3.14159**2)/3.0
      E2=E**2
      WRITE (2,13)
   13 FORMAT (//5X,25HPORODS CORRECTED INTENSITY//)
      DO 9 M=1,MX
      S1=SS*M
      S2=S1*S1
      CF=1.0-(PI2*E2*S2)
    9 B(M)=B(M)/CF
      DO 15 M=1,MX,10
      M1=M+9
      WRITE (2,17) M,M1,(B(M2),M2=M,M1)
```

```
15 CONTINUE
17 FORMAT (2H M  ,I4,3H -,I5,5X,10F8.1)
14 CONTINUE
   IF (PC.NE.0.0) GO TO 20
   PCS=0.0
   DO 13 M=MP,MN
   S=SS*M
   PCI=P(M)*S*S
13 PCS=PCS+PCI
   PC=PCS/(MN-MP+1)
20 CONTINUE
   R=0.0
   GAM=1.0
   WRITE (2,83)
83 FORMAT (//3X,1HR,7X,6HF1-DECF,7X,4HSOMA,2X,5HSUMAP,6X,4HSOMB,6X,5HS
  1OMBP,/)
   IMAX=RMAX/DR+1.0
   DO 82 I=1,IMAX
   SOMA=0.0
   SOMB=0.0
   SOMAP=0.0
   SOMBP=0.0
   IF (I.EQ.1) GO TO 80
   DO 75 M=1,MN
   S=M*SS
   FIH=P(M)
   FIHS=COS(R*2.0*3.141592*S)*FIH
   SOMA=SOMA+FIHS
75 SOMB=SOMB+FIH
   SOMA=SS*SOMA
   SOMB=SS*SOMB
   MY=MN+1
   DO 77 M=MY,MX
   S=M*SS
   FIHP=PC/(S**2)
   FIHSP=COS(2.0*3.141592*S*R)*FIHP
   SOMAP=SOMAP+FIHSP
77 SOMBP=SOMBP+FIHP
   SOMAP=SS*SOMAP
   SOMBP=SS*SOMBP
   GAM=(SOMA+SOMAP)/(SOMB+SOMBP)
80 CONTINUE
   WRITE (2,86) R,GAM,SOMA,SOMAP,SOMB,SOMBP
86 FORMAT (F9.1,5X,F5.3,5X,F8.5,2X,F8.5,2X,F8.5,2X,F8.5)
   R=R+DR
82 CONTINUE
84 CONTINUE
   STOP
   END
```

C. TCF1 (H112)

Vonk Theoretical Correlation Function, Batch;
Adapted by F. P. Warner

```
      PROGRAM H112 (INPUT,OUTPUT,TAPE1=INPUT,TAPE2=OUTPUT)
C     THEORETICAL CORRELATION FUNCTION
      DIMENSION PA(300), PC(300), TEKST(20), S(300,4), T(4), B(300,19)
      DIMENSION PCA(300), PAA(300)
      DOUBLE X,C,Y,B
      READ (1,1) NO
    1 FORMAT (I2)
      DO 36 KK=1,NO
      READ (1,2) TEKST,LZ,C,BA,CA,BCA,CB,BCB
    2 FORMAT (10A8,/10A8,/I4,6F8.4)
      VV=10.0**LZ
      READ (1,4) NDC,NDA,NABC,NC,NA
    4 FORMAT (5I2)
      DO 3 I=1,300
      PA(I)=0.0
    3 PC(I)=0.0
      WRITE (2,32) TEKST,C,BA,CA,BCA,CB,BCB
   32 FORMAT (1H1,10A8,/1X,10A8,//,1X,13HSPECIFIC DATA,//10X,6H  C = ,F
     10.6/10X,6H BA = ,F10.6,/10X,6H CA = ,F10.6,/10X,6HBCA = ,F10.6,/1
     2X,6H CB = ,F10.6,/10X,6HBCB = ,F10.6)
      IF (NDC.NE.4) GO TO 49
      WRITE (2,50)
   50 FORMAT (//,2X,2HYC,8X,3HPCI,/)
      YC=0.0
      DO 42 N=1,NC
      DO 43 M=1,300
   43 PCA(M)=0.0
      PCS=0.0
      PCXS=0.0
      DO 41 M=1,300
      X=FLOAT(M-1)*0.01
      PCA(M)=DISTBN(BCA,C,X,YC)
      PCS=PCS+PCA(M)
      PCX=PCA(M)*X
      PCXS=PCXS+PCX
   41 CONTINUE
      PCI=(PCS-0.5*PCA(1))*0.01
      PCXI=PCXS*0.01
      AVXC=PCXI/PCI
      YC=YC+(AVXC-C)
      WRITE (2,45) YC,PCI
   45 FORMAT (2F8.4)
   42 CONTINUE
      SCALE1=PCI
   49 IF (NDA.NE.2) GO TO 44
      WRITE (2,51)
   51 FORMAT (//,2X,2HYA,8X,3HPAI,/)
      YA=0.0
      DO 46 N=1,NA
      DO 47 M=1,300
   47 PAA(M)=0.0
      PAS=0.0
      PAXS=0.0
      DO 48 M=1,300
      X=FLOAT(M-1)*0.01
      PAA(M)=DISTBN(BA,1.0-C,X,YA)
      PAS=PAS+PAA(M)
```

```
      PAX=PAA(M)*X
      PAXS=PAXS+PAX
   48 CONTINUE
      PAI=(PAS-0.5*PAA(1))*0.01
      PAXI=PAXS*0.01
      AVXA=PAXI/PAI
      YA=YA+(AVXA-(1.0-C))
      WRITE (2,52) YA,PAI
   52 FORMAT (2F8.4)
   46 CONTINUE
      SCALE2=PAI
   44 DO 14 I=1,300
      X=FLOAT(I-1)*0.01
      IZ=I
      GO TO (6,7,8,5), NDC
    5 CONTINUE
      PC(I)=DISTBN(BCA,C,X,YC)
      PC(I)=PC(I)/SCALE1
      GO TO 9
    6 CONTINUE
      IF (I.EQ.1) GO TO 9
      PC(I)=DALOG(BCA,C,X)
      GO TO 9
    7 CONTINUE
      PC(I)=DISTBNC(C,CA,BCA,CB,BCB,X,YC)
      PC(I)=PC(I)/SCALE1
      GO TO 9
    8 CONTINUE
      PC(I)=SQDISB(BCA,C,X)
    9 CONTINUE
      GO TO (10,11,12,13), NDA
   10 CONTINUE
      IF (I.EQ.1) GO TO 14
      PA(I)=DALOG(BA,1.0-C,X)
      GO TO 13
   11 CONTINUE
      PA(I)=DISTBN(BA,1.0-C,X,YA)
      PA(I)=PA(I)/SCALE2
      GO TO 13
   12 CONTINUE
      PA(I)=SQDISB(BA,1.0-C,X)
   13 CONTINUE
      IF (PC(I).LT.VV.AND.PA(I).LT.VV.AND.X.GT.C) GO TO 15
   14 CONTINUE
   15 I=IZ
      DO 17 I1=1,4
      DO 16 I2=1,300
      S(I2,I1)=0.0
   16 CONTINUE
      T(I1)=0.0
   17 CONTINUE
      DO 19 I1=1,300
      DO 18 I2=1,19
      B(I1,I2)=0.0
   18 CONTINUE
   19 CONTINUE
   20 I=I-1
```

```
      X=FLOAT(I-1)*0.01
      GO TO (22,23,24,21), NDC
   21 CONTINUE
      FC=DISTBN(BCA,C,X+0.005,YC)
      FC1=DISTBN(BCA,C,X+0.0025,YC)
      FC3=DISTBN(BCA,C,X+0.0075,YC)
      FC=FC/SCALE1
      FC1=FC1/SCALE1
      FC3=FC3/SCALE1
      GO TO 25
   22 CONTINUE
      FC=DALOG(BCA,C,X+0.005)
      FC1=DALOG(BCA,C,X+0.0025)
      FC3=DALOG(BCA,C,X+0.0075)
      GO TO 25
   23 CONTINUE
      FC=DISTBNC(C,CA,BCA,CB,BCB,X+0.005,YC)
      FC1=DISTBNC(C,CA,BCA,CB,BCB,X+0.0025,YC)
      FC3=DISTBNC(C,CA,BCA,CB,BCB,X+0.0075,YC)
      FC=FC/SCALE1
      FC1=FC1/SCALE1
      FC3=FC3/SCALE1
      GO TO 25
   24 CONTINUE
      FC=SQDISB(BCA,C,X+0.005)
      FC1=SQDISB(BCA,C,X+0.0025)
      FC3=SQDISB(BCA,C,X+0.0075)
   25 CONTINUE
      IF (NABC.NE.1) GO TO 27
      D1=0.0025*(PC(I)+PC(I+1)+2.0*FC+4.0*(FC1+FC3))/3.0
      D3=0.0025*(X*PC(I)+(X+0.01)*PC(I+1)+2.0*FC*(X+0.005)+4.0*FC1*(X+0
     10025)+4.0*FC3*(X+0.0075))/3.0
      GO TO 28
   27 CONTINUE
      D1=0.0025*0.5*(PC(I)+FC1+FC1+FC+FC+FC3+FC3+PC(I+1))
      D3=0.0025*0.5*(X*PC(I)+(X+0.01)*PC(I+1)+2.0*FC*(X+0.005)+2.0*FC1*
     1X+0.0025)+2.0*FC3*(X+0.0075))
   28 CONTINUE
      T(1)=T(1)+D1
      T(3)=T(3)+D3
      DO 29 L=1,4
   29 S(I,L)=T(L)
      IF (I.NE.1) GO TO 20
      DO 30 L=1,IZ
      X=FLOAT(L-1)*0.01
      S(L,1)=S(L,1)/C
      S(L,3)=S(L,3)-C*S(L,1)*X
   30 CONTINUE
      CALL CONV (S(1,1),PA,B(1,2),0.01)
      CALL CONV (S(1,2),S(1,1),B(1,3),0.01)
      CALL CONV (PA,PC,B(1,6),0.01)
      CALL CONV (B(1,6),B(1,6),B(1,7),0.01)
      CALL CONV (B(1,6),B(1,3),B(1,10),0.01)
      CALL CONV (B(1,7),B(1,3),B(1,13),0.01)
      CALL CONV (B(1,13),B(1,6),B(1,14),0.01)
      CALL CONV (B(1,14),B(1,6),B(1,15),0.01)
      F=C*(1.0-C)
```

```
      DO 31 I=1,300
      SC=S(I,3)/C**2
      S2=B(I,3)+B(I,10)+B(I,13)+B(I,14)+B(I,15)
      B(I,19)=(C/(1.0-C))*(SC+S2-1.0)
   31 CONTINUE
      IF (NDC.NE.4) GO TO 37
      WRITE (2,39) YC,SCALE1
   39 FORMAT (/10X,6H YC = ,F10.6,/10X,10H SCALE1 = ,F10.6)
   37 IF (NDA.NE.2) GO TO 38
      WRITE (2,40) YA,SCALE2
   40 FORMAT (/10X,6H YA = ,F10.6,/10X,10H SCALE2 = ,F10.6)
   38 K=1
      KV=1
      WRITE (2,33)
   33 FORMAT (1H1,2X,1HX,6X,2HPC,8X,2HPA,8X,2HQC,8X,2HIC,8X,2HB2,8X,2HB
     1,8X,2HB6,8X,2HB7,7X,3HB10,7X,3HB13,7X,3HGAM)
   34 K=K+KV
      X=FLOAT(K-1)*0.01
      WRITE (2,35) X,PC(K),PA(K),S(K,1),S(K,3),B(K,2),B(K,3),B(K,6),B(K
     1,7),B(K,10),B(K,13),B(K,19)
   35 FORMAT (1X,F5.2,2X,11F10.6)
      IF (K.EQ.11) KV=2
      IF (K.EQ.31) KV=5
      IF (K.EQ.81) KV=10
      IF (K.LT.291) GO TO 34
   57 CONTINUE
   58 CONTINUE
      IF (KK.EQ.NO) STOP
   36 CONTINUE
      END
```

D. SAXSC

Schmidt Slit Desmearing Program, Batch

```
 PROGRAM SAXSC(INPUT,OUTPUT,TAPE60=INPUT,TAPE61=OUTPUT,PUNCH,
1TAPE62=PUNCH)
 SLIT-LENGTH COLLIMATION CORRECTION FOR GAUSSIAN WEIGHTING FUNCTION
       (REVISED MARCH, 1969)

 THIS PROGRAM SAXSC IS USED FOR CORRECTING SMALL ANGLE X-RAY  SCATTERING
 INTENSITY FROM A FINITE SLIT SYSTEM WITH A GAUSSIAN WEIGHTING  FUNCTION
 THE USER IS REFERED TO  (P.W.SCHMIDT,ACTA CRYSTA.19,938 (1965))
 THE PROCEDURE AND INPUT DATA ARE EXPLAINED AS FOLLOWS.
 THE ANGULAR DATA INCREMENT IS ,A, MINUTES. THE INTENSITY VALUES F(I)
 ARE GIVEN FOR SCATTERING ANGLES FROM A THROUGH A*IMAX.  (THE FORTRAN
 SYMBOL * WILL BE USED TO DENOTE MULTIPLICATION.  ZEROES ARE USED FOR F(I)
 FOR INTENSITIES AT WHICH EXPERIMENTAL DATA ARE NOT AVAILABLE.)  FIVE
 INTENSITY VALUES ARE PUT ON EACH CARD IN (5E13.7) FORMAT
      THE PROGRAM CALCULATES CORRECTED INTENSITIES FROM J0*A MILLIRADIANS
 THROUGH N1*A MILLIRADIANS WITH AN ANGULAR INCREMENT N2*A MILLIRADIANS.
 CORRECTED INTENSITIES ARE COMPUTED NEXT FROM (N1 + N4)*A MILLIRADIANS
 THROUGH N3*A MILLIRADIANS WITH AN INCREMENT N4*A, AND THEN FROM
 (N3 + N6)*A MILLIRADIANS THROUGH N5*A MILLIRADIANS WITH AN INCREMENT N6*A,
 PROVIDED N5 DOES NOT EXCEED IMAX.  CORRECTED INTENSITIES ARE NOT CALCUL-
 ATED FOR ANGLES EXCEEDING IMAX*A MILLIRADIANS, REGARDLESS OF THE VALUES
 OF THE NUMBERS ON CARD 3 BELOW.  (THIS IMAX VALUE IS THE VALUE FOR THE
 CURVE BEING CORRECTED.)
      IN THE USE OF THIS PROGRAM, THE CARDS ARE ARRANGED AS FOLLOWS.
           CARD 1. A
           CARD 2.  J0 AND IMAX.  (THE VALUE OF J0 ON THIS CARD MUST EQUAL
                THE SMALLEST J0 VALUE USED WITH ANY OF THE SCATTERING
                EQUAL THE LARGEST IMAX VALUE USED FOR ANY OF THE CURVES
                BEING CORRECTED.)
           CARD 3. N1, N2, N3, N4, N5, N6
           CARD 4. J0 AND IMAX FOR THE FIRST CURVE
           CARD 5.  THE FIRST CARD OF THE SET OF CARDS WITH THE INTENSITIES
                F(I)
 THE OTHER CARDS FOR THIS CURVE THEN FOLLOW.  FOR EXAMPLE, IF THERE ARE 80
 F(I) IN THE FIRST CURVE, IMAX = 80, AND THERE 16 CARDS IN THE SET.  FOR
 EACH SUCCEEDING CURVE, THE SET OF F(I) CARDS IS PRECEDED BY A CARD GIVING
 J0 AND IMAX FOR THIS CURVE.
      AFTER THE LAST CURVE HAS BEEN CORRECTED, THE COMPUTER GIVES A STATE-
 MENT INDICATING THAT THE END OF THE DATA HAS BEEN REACHED.
      USUALLY IT IS MOST CONVENIENT TO HAVE THE VALUES OF N3 AND N5 BE AT
 LEAST AS LARGE AS N1 AND N3, RESPECTIVELY, WITH N2 AND N4 BEING NO LESS
 THATN N4 AND N6, RESPECTIVELY.  HOWEVER, THESE CONDITIONS ARE NOT NECES-
 SARY.  FOR EXAMPLE, IF CORRECTED VALUES ARE DESIRED ONLY FOR A SINGLE
 ANGULAR INCREMENT, THE APPROPRIATE VALUES OF N1 AND N2 CAN BE CHOSEN, AND
  N3, N4, N5, AND N6 CAN ALL BE SET EQUAL TO ZERO, OR THESE POSITIONS CAN
 BE LEFT BLANK ON CARD 3.
      THE LARGEST VALUES ALLOWED FOR THE NUMBERS ON CARDS 2, 3, AND 4 ARE
  DETERMINED BY THE DIMENSION STATEMENT AT THE BEGINNING OF THE PROGRAM.
 (THIS STATEMENT CAN BE CHANGED WHEN NECESSARY.)  NO IMAX VALUE ON CARDS
  2 OR 4 CAN EXCEED J00, AND NO INPUT CURVES CAN HAVE MORE THAN 400 DATA
 POINTS, ACCORDING TO THE DIMENSION STATEMENT USED IN THIS PROGRAM.  WITH
 THE NUMBER 50 USED IN THE SECOND SUBSCRIPT OF T(I,JJ) IN THE DIMENSION
 STATEMENT, CORRECTED INTENSITIES CAN BE CALCULATED AT UP TO 50 ANGLES.
```

THE ANGLES AT WHICH CORRECTED DATA ARE OBTAINED ARE SPECIFIED BY THE NUMBERS ON CARDS 2, 3, AND 4.

THE WIDTH OF THE GAUSSIAN WEIGHTING FUNCTION IS DETERMINED BY THE CONSTANT SL DEFINED EARLY IN THE PROGRAM. FOR A BEEMAN-TYPE FOUR-SLIT COLLIMATION SYSTEM WITH 50 CM. BETWEEN SUCCESSIVE SLITS AND WITH THE X-RAY BEAM UNIFORMLY ILLUMINATING THE ENTIRE LENGTH OF THE ENTRANCE SLIT, SL IS EQUAL TO THE SLIT LENGTH IN CENTIMETERS. THE CONSTANT SL MUST BE SPECIFIED FOR EACH SLIT SETTING FOR WHICH CORRECTIONS ARE CALCULATED.

IN OUR CASES, THE WIDTH OF THE GAUSSIAN WEITHTING FUNCTION IS THEORETICALLY CALCULATED BY THE METHOD REPORTED BY R.W.HENDRICKS AND P.W. SCHMIDT (1966). WE HAVE A SEPARATED PROGRAM CALLED WEIGHT FOR THIS CALCULATION.

THE CONSTANTS L0, L1, AND L2 IN THE INPUT AND OUTPUT STATEMENTS MUST BE DEFINED AT THE BEGINNING OF THE PROGRAM.

IN STEP 103, ALOG IS A NATURAL LOGARITHM. THIS NOTATION MAY HAVE TO BE CHANGED FOR SOME COMPUTERS.

THE ANGLE S=2*SIN(THETA)/SLAM WHERE SLAM = LAMBDA IN ANGSTROMS

```
C
C     COMPUTATION OF LEAST SQUARES FIT TIJ
      DIMENSION T(220,100), F(200)
      COMMON T
      DIMENSION FA(200)
      DIMENSION IMA(4),JJM(4),AT(4)
      DIMENSION IDENT(5)
      DOUBLE PRECISION SL, PDELH, SQPI, A, SJ1(220), SJ2(220),
     1 SJ3(220), B, C, D, E, DD, EE, H, UIJ, V32IJ,V33IJ,
     2 T31IJ, DEL51, DEL52, DEL53, DEL42, VV
      L0=60
      L1=61
      PI=3.14159270 00
      A1=2.00*180.00*60.00
      SQPI = 1.77245385100
      PDELH = SQPI*11.00800
      SLAM = 1.5417
    1 FORMAT(F6.4,I4)
    2 FORMAT(2I4)
    3 FORMAT(6I4)
    4 FORMAT(/,4X,10HANGLE( S ),9X,10HANGLE(MIN),8X,14HCORRECTED INT.,
     19X,14HMEASURED INT.,28HLORENTZ-GEOM. CORRECT. INT.      )
    5 FORMAT(5E13.7)
    6 FORMAT(/1X,F12.6,6X,F12.6,4X,E20.8,2X,E18.6,5X,E18.6)
    7 FORMAT(5X,F10.6,E15.6,5X,F10.6,2E15.6)
      READ(L0,1) A,IFA
      READ (L0,2) JO, IMAX
      READ (L0,3) N1, N2, N3, N4, N5, N6
      A = (2.00*A*PI)/A1
      N = N1
      NN = N2
      JOO = JO
      NJ = 0
C     IF IFA .GT., 0 YOU WANT DATA LORENTZ CORRECTED ONLY
      IF(IFA.GT.0) GO TO 200
```

```
100 DO 105 J = JC, N, NN
    IM = IMAX - J + 12
    JJ = JJ + 1
    DO 102 I = 6, 10
    SJ1(I) = 0.0
    SJ2(I) = 0.0
102 SJ3(I) = 0.0
    B = J
    IM1 = IM + 1
    DO 104 I = 11, IM1
    C = I - 10
    D = C*C + 2D0*C*B
    E = (C-1D0)*(C-1D0)+2D0*B*(C-1D0)
    DD=DSQRT(D)
    EE= DSQRT(E)
103 SJ1(I)=DLOG((C+B+DD)/(C+B-1D0+EE))
    SJ2(I)=(C+B-0.5D0)*SJ1(I)-DD+EE
104 SJ3(I)= 0.5D0*((C+B)**2-1D0/3D0+0.5D0*B**2)*SJ1(I)
   1  -0.75D0*(C+B)*DD+(0.75D0*(C+B)+0.25D0)*EE
    H = A * PDELH
    KA=0
    DO 605 I = 10, IM
    C = I - 12
    UIJ=DEXP(-(H*H)*(C*C+2D0*B*C))/(H*SQPI)
    V32IJ=SJ2(I-1)  -2D0*SJ2(I-2)  +SJ2(I-3)
    V33IJ=SJ3(I)-3D0*SJ3(I-1  )+3D0*SJ3(I-2  )-SJ3(I-3  )
    T31IJ=UIJ* (SJ1(I-1  )-SJ1(I-2  )+V32IJ+V33IJ)
    DEL51= SJ1(I+1  )-5D0*SJ1(I)+10D0*SJ1(I-1  )-10D0*SJ1(I-2  )+5D0*
   1 SJ1(I-3  )-SJ1(I-4  )
    DEL52 = SJ2(I+1  )- 5D0* SJ2(I)+10D0*SJ2(I-1  )-10D0*SJ2(I-2  )
   1 + 5D0*SJ2(I-3  )-SJ2(I-4  )
    DEL53=SJ3(I+1)-5D0*SJ3(I)+10D0*SJ3(I-1)-10D0*SJ3(I-2)
   1 +  5D0*SJ3(I-3)-SJ3(I-4)
    DEL42=SJ2(I)-4D0*SJ2(I-1)+6D0*SJ2(I-2)-4D0*SJ2(I-3)+SJ2(I-4)
    VV=-2D0*DEL51+DEL52+9D0*DEL42+7D0*DEL53
    T(I,JJ) = T31IJ + (5.*UIJ*VV)/126.
    KA=0
    IF(KA.LT.4) GO TO 605
    KA=KA+1
    IMA(KA)=I
    JJN(KA)=JJ
    AT(KA)=T(I,JJ)
401 FORMAT(5X,2I4,E15.8)
605 CONTINUE
105 CONTINUE
    IF (N - N3) 110, 111, 111
110 N = N3
    NN = N4
    JC = N1 + N4
    JJ1 = JJ - 1
    GO TO 100
111 IF (N - N5) 112, 200, 200
112 N = N5
```

```
      NN = N6
      JO = N3 + N6
      JO2 = JJ - 1
      GO TO 100
C     SLIT LENGTH CORRECTION
  200 READ (L0,2) JO, IMAX
      IF(EOF(L0)) 700,701
  701 READ(L0,1001)  STRATE,NAZIM
 1001 FORMAT(F5.2,I4)
      WRITE(L1,1000) STRATE,NAZIM
 1000 FORMAT(1H1,*STRETCH RATIO =*F6.3,5X,*AZIMUTHAL ANGLE =*I4)
      READ(L0,1002) (IDENT(I),I=1,5)
 1002 FORMAT(5A10)
      WRITE(L1,1003) (IDENT(I),I=1,5)
      WRITE(62,1003) (IDENT(I),I=1,5)
 1003 FORMAT(1X,5A10)
      READ (L0,5) (F(I), I = 1, IMAX)
C     SLIQ IS VALUE OF CONSTANT LIQUID SCATT. VIA VONK
C     SET SLIQ=0.0 IF NO SUBTRACTION DESIRED, AT END OF INT. SET
C     IF PUNCHED DATA FOR H109 IS DESIRED PUT 1 IN COL. 10 OF LAST CARD
C     IF IS SAMPLE TRANSMN, SINT IS INTY VALUE OF KRATKY STANDARD MEAS.
      READ(L0,8) SLIQ,NPNCH,TR,SINT
    8 FORMAT(F5.3,I5,F5.3,F6.3)
C     THE VALUE OF 20.0 IN CFAC IS AN ARBITRARY NORMALIZNT CONSTANT
      CFAC = (1.0/TR)*(20.0/SINT)
      DO 800 I= 1,IMAX
  800 F(I) = (F(I) - SLIQ)*CFAC
      IF(IFA.GT.0) GO TO 600
      WRITE (L1,4)
      IF (JO - N1) 201, 204, 204
  201 NN = N2
      JJ = (JO - JO2)/N2
      IF (N1 - IMAX) 202, 203, 203
  202 N = N1
      GO TO 220
  203 N = IMAX
      GO TO 220
  204 IF (JO - N3) 205, 208, 208
  205 NN = N4
      JJ = J01 + (JO - N1)/N4
      IF (N3 - IMAX) 206, 207, 207
  206 N = N3
      GO TO 220
  207 N = IMAX
      GO TO 220
  208 NN = N6
      JJ = JO2 + (JO - N3)/N6
      IF (N5 - IMAX) 209, 210, 210
  209 N = N5
      GO TO 220
  210 N = IMAX
  220 DO 230 J = JO, N, NN
      IMAX1 = IMAX + 12 - J
```

```
      JJ = JJ + 1
      SUM = 0.0
      DO 225 I = 10, IMAX1
      K = J + I - 12
  225 SUM = SUM + F(K)*T(I,JJ)
      X = J
      XA = A*X
      X = XA/SLAM
      Y = XA*57.29578*60.0
      FA(J)=SUM
      AC=(FLOAT(J)*A)**2
      FA(J)=FA(J)*AC
      WRITE (L1,6) X,Y,SUM,F(J),FA(J)
C     PUNCHED OUTPUT FOR H109, CORR. FUNCT. ANAL.
      IF(NPNCH.EQ.1) 235,230
  235 CONTINUE
      FA(J) = FA(J)*103000.0
      IF(FA(J).LT.0)240,245
  240 FA(J) = 0.0
  245 CONTINUE
      WRITE(62,504) FA(J)
  504 FORMAT(10F6.1)
  230 CONTINUE
      IF (N - IMAX) 251, 200, 200
  251 IF(N - N3) 252, 261,261
  252 JJ = N1 + N4
      GO TO 205
  261 IF(N - N5) 262, 200, 200
  262 JJ = N3 + N6
      GO TO 208
  600 WRITE(L1,601)
  601 FORMAT(* PCKGD CORR. INT.*,5X,*LORENTZ-GEOM. CORR. INT. *)
  500 DO 503 I=JJ,N,NN
      AB=(FLOAT(I)*A*2.0)**2
      FA(I)=F(I)*AB
  501 WRITE(L1,502) F(I),FA(I)
  502 FORMAT(/E18.6,7X,E18.6)
  503 CONTINUE
      GO TO 200
  700 CONTINUE
      STOP
      END
```